Pulsed Laser Deposition of Doped Sesquioxide Films for Planar Waveguide Lasers

Tina L. Parsonage
Optoelectronics Research Centre,
University of Southampton,
Southampton,
SO17 1BJ, UK

tlp1g08@soton.ac.uk

Supervisor: R. W. Eason

August 25, 2016

Abstract

The sesquioxides Y_2O_3, Lu_2O_3 and Sc_2O_3 have been identified as promising laser host materials due to their excellent thermo-mechanical properties and ability to be doped with rare-earth ions. However, crystals of these materials are problematic to grow due to their high melting points of $\sim$2500°C, which means standard methods of crystal growth from a melt need to be modifed to deal with such high temperatures and become more expensive. Pulsed laser deposition (PLD) has the capability to grow these materials, without requiring a melt of material to grow from. Sintered ceramic targets of the sesquioxides, often doped with rare-earth ions, are ablated with a UV laser pulse and material is ejected. This plume of material travels through a vacuum chamber to a carefully chosen substrate where material is deposited and forms a crystalline film.

Planar waveguide lasers are structures of interest due to their low lasing thresholds in comparison to bulk material, owing to the greater overlap of the pump and laser modes, and their large aspect ratio that allows efficient heat removal from the laser crystal. This, combined with the high thermal conductivity of the sesquioxides, should allow for power scaling of these waveguide lasers with minimal thermal affects. The laser results in this thesis are for progressively higher powers, and no detrimental heating affects are witnessed.

This thesis reports on the growth of single and multilayer sesquioxide waveguides grown by PLD, including growth optimisation, sample analysis and laser experiments. The first sample of this project to be successfuly lased was a single layer Tm:Y_2O_3 waveguide on a YAG substrate, which produced a maximum output power of 35 mW with 9% slope efficiency at a wavelength of 1.95 μm, and, to the best of our knowledge, was the first Tm:Y_2O_3 planar waveguide laser. Next, Yb:Y_2O_3 was the material of choice and a multilayer sample was fabricated, where the Yb:Y_2O_3 core was sanwiched between two undoped Y_2O_3 layers, again on a YAG substrate. Laser experiments with this waveguide gave a maximum output power of 1.2 W at 1030 nm, with a slope efficiency of 20%. The highest laser output power of any of the doped sesquioxide waveguides in this project is 8.5 W, achieved using a Yb:Lu_2O_3 sample.

Contents

List of Figures

List of Tables

Symbols and abbreviations

PLD Pulsed laser deposition

HTC High temperature superconductor

RE Rare-earth

λ_{pump} Pump wavelength

λ_{laser} Laser wavelength

$\sigma_{emission}$ Emission cross-section

$\sigma_{absorption}$ Absorption cross-section

$\sigma_{reabsorption}$ Reabsorption cross-section

NA Numerical aperture

PVD Physical vapour deposition

SEM Scanning electron microscope

MBE Molecular beam epitaxy

UHV Ultra-high vacuum

LPE Liquid-phase epitaxy

CVD Chemical vapour deposition

NK Nacken-Kyropolous

RF Radiofrequency

HEM Heat-exchanger method

TSSG Top-seeded solution growth

cw Continuous wave

LHPG Laser heated pedestal growth

μ-PD Micro-pulling-down

FWHM Full width at half maximum

E_g Band gap

dn/ dT Thermo-optic coefficient

SESAM Semiconductor saturable absorber mirror

DBR-TDL Distributed Bragg-reflector tapered diode laser

HR High reflection

AR Anti-reflection

L_a Absorption length

L_d Diffusion length

α Absorption coefficient

κ Thermal Diffusivity

τ_d Laser pulse duration

d_a Depth (of ablated material)

F Fluence

F_{th} Threshold fluence

EDX Energy dispersove x-ray analysis

FCC Face-centred cubic

BCC Body-centred cubic

f Lattice mismatch

a_0(s) Unstrained lattice parameter of substrate

a_0(f) Unstrained lattice parameter of film

M Number of modes

d_{WG} Waveguide thickness

λ Wavelength

n Refractive index

θ_{max} Maximum acceptance angle

P Power

x Waveguide length

α_L Propagation loss coefficient

$R_{1/2}$ Reflectivities of input/ output coupling mirrors

h Planck's constant

v Frequency

$w_{lx/px/ly/py}$ $1/e^2$ radii of the intenisty of pump and laser spots

τ Fluorescence lifetime

L Propagation loss

η_s Slope efficiency

η_0 Limiting slope efficiency

C Output coupling fraction

η_p Pumping efficiency

λ_p Pump wavelength

λ_0 Output wavelength

σ_{eff} Effective gain cross-section

σ_{ea} Excited state absorption cross-section

P_{pth} Threshold pump power

l Crystal length

T Transmission

R Reflectivity

N_1 Population density of the lower laser level

XRD X-ray diffraction

d Lattice spacing

m Diffraction order

a Lattice constant

h, k, l Miller indices

VP Variable pressure

OSA Optical spectrum analyser

THOX Thermal oxide

BSD Backscatter detector

BADL Broad area diode laser

IL Insertion loss

OC Output coupler

APCVD Atmospheric pressure chemical vapour deposition

PMMA Poly-(methyl methacrylate)

Declaration of Authorship

I, Tina Louise Parsonage, declare that this thesis, titled "Pulsed laser deposition of doped sesquioxide films for planar waveguide lasers", and the work presented in it are my own and has been generated by me as the result of my own original research. I confirm that:

- This work was done wholly or mainly while in candidature for a research degree at this university;
- Where any part of this thesis has previously been submitted for a degree or any other qualifications at this University or any other institution, this has been clarly stated;
- Where I have consulted the published work of other, this is always clearly attributed;
- I have acknowledged all main sources of help;
- Where the thesis is based on work done by myself jointly with others, I have made clear exactly what was done by others and what I have contributed myself;
- Parts of this work have been published before submission of this thesis and are listed in the appendices.

Signed: .....

Date: .....

Acknowledgements

There are many people to whom I owe credit for guiding me through the past few years, helping in various ways that have made this thesis possible. I would like to begin with thanking Kate Sloyan, for getting me started by teaching me how to use the setup in the pulsed laser deposition lab and the considerations one has to make when performing these depositions, for the training she provided on various analytical equipment, and general support and friendship she showed me from the start.

For the work conducted and presented in this thesis, I owe credit to Jakub Szela for obtaining our first set of laser results from a sesquioxide sample and to Amol Choudhary for characterising some of my waveguide samples with his setup using a single-mode diode pump laser and for extending the work to include pulsed operation of my samples, in collaboration with S. Dhingra and B. D'Urso.

I would also like to thank Tim May-Smith for imparting knowledge of the lab setup to me, and to Alberto Sposito, Matthias Feinäugle and James Grant-Jacob for assistance in the lab when necessary and its general upkeep.

Stephen Beecher has been a key part of the work conducted in this project, working with me to perform spectroscopic characterisation experiments on my samples, as well as the higher power laser experiments reported, teaching me along the way. He has always been helpful and supportive in both experimental work and by engaging in conversations regarding all aspects of the project, which has been invaluable.

Thanks must also be given to Neil Sessions for training on clean room equipment and the SEM (plus EDX), continued support using these pieces of equipment and the polishing lab, and for the upkeep of these shared facilities. Similarly, Mark Light has been extremely helpful, providing training on the x-ray diffractometers and helping with pole figure analysis, as well as performing a few of the pole figure measurements displayed in this thesis (the others being performed by James

Grant-Jacob).

Ping Hua has also been part of the team working on this project and has performed the majority of the sample facet polishing, which is key to the laser experiments that followed. Thanks also goes to Lewis Carpenter who investigated the dicing of our waveguides on YAG substrates in an attempt to achieve an optical quality finish that would be far quicker than the polishing process.

Thanks must also go to our collaborators in Hamburg for donating sesquioxide substrates, and to Jacob Mackenzie for the silica sputtering of some of the YAG substrates reported in this thesis. Jacob and David Shepherd have also discussed aspects of the project with me and given their thoughts and feedback in group meetings, which I thank them for.

The last of my project-related thanks go to my supervisor, Rob Eason, who has supported me from day one, through highs and lows, making sure the project is on track, and being awarded grants to keep this project alive. Rob has been amazingly efficient in getting back to me whenever I've needed help, especially with various drafts of conference submissions, journal papers and this thesis. I would also like to acknowledge EPSRC for funding me and this project through grant numbers EP/L021390/1, EP/N018281 and EP/J008052/1.

Finally, I would like to thank my family and friends - those who have been there for me throughout my PhD, and those gained in the past few years, both in the department and those who I have met through my hobbies who have helped keep me sane and made life more fun.

Chapter 1

Introduction

1.1 Pulsed Laser Deposition

Pulsed laser deposition (PLD) is a relatively simple, low cost method of fabricating thin films on substrates for a range of applications. The setup requires a pulsed laser source, usually in the ultra-violet (UV), incident on a target of the material to be deposited. Each pulse ablates the target surface causing a highly directional plume, normal to the target surface, containing constituent atoms, ions, electrons and particles from the target. A substrate is positioned opposite the target to receive the material, and is usually heated to aid crystalline material growth. This technique can provide a deposition rate of several microns per hour.

For ablation to occur, it is a requirement that the material to be ablated must absorb light at the laser wavelength being used for ablation. UV wavelengths are commonly used for this reason, but some materials, particularly organic molecules and polymers, ablate well with infra-red wavelengths that correspond to vibrational modes of molecules [1].

With several variables that can be changed, PLD is a versatile technique that can be implemented for a wide range of materials and is suitable for fabricating samples of multiple layers with relative ease. In this thesis the variables changed during optimisation experiments are limited to laser ablation fluence and repetition rate, background oxygen pressure and the temperature of the substrate being deposited onto. Other variables in PLD are the target to substrate distance, the substrate material, the ablating laser wavelength and choice of background gas. Having many variables to adjust can, however, make finding optimum growth conditions a time-consuming process. Changing variables can also affect the stoichiometry of the deposited film. Optimisation in

this thesis is mainly towards achieving samples with few surface particulates while maintaining a reasonable growth rate.

The majority of samples created during this PhD have been on YAG substrates, as this material has good thermal conductivity, although lower than the sesquioxides (see table 1.1 that compares properties), a similar thermal expansion coefficient and a lower refractive index than the sesquioxides, allowing for waveguiding to occur in the films, and as these substrates are readily available at low cost.

Particulates are a notable problem in PLD-grown films as they can be detrimental to waveguiding due to increased scattering and therefore higher losses. These particulates can occur in a variety of ways; for example, target surfaces are modified during the ablation process and the features formed can be ablated and transferred to the growing film, and particles in the ablated plume can combine to form particulates, particularly for higher background gas pressures. More information on the origin of particulates in PLD-grown films is presented in section 3.2.4.

PLD properly began to take off in 1987 as a method for growing high temperature superconducting (HTC) thin films. As the technique developed, research extended to using PLD for many different materials including high temperature superconductors, oxides, semiconductors, dielectric materials and refractory metals, with a wide range of applications [2, 3].

1.2 Sesquioxides

Sesquioxide materials of the chemical formula X_2O_3, especially the rare-earth (RE) sesquioxides Y_2O_3, Sc_2O_3 and Lu_2O_3, have been identified as very promising host materials for high power lasers due to their high thermal conductivity and excellent thermo-mechanical properties [4]. The isotropic crystalline structures of these materials can be doped with other rare-earth ions. Higher dopant concentration usually reduces the thermal conductivity due to greater disruption in the crystal lattice from the dopant ions having a different mass to that of the host it's replacing [5].

Studies on Yb-doped sesquioxides have found the splitting of the ground state to be larger than for YAG, as well as having a larger gain bandwidth, making these materials very promising for efficient, short-pulse operation [5, 6]. Many relevant physical and spectroscopic properties of these materials are displayed in table 1.1, below.

Property	Yb-doping	YAG	Y_2O_3	Lu_2O_3	Sc_2O_3	Reference
λ_{pump} (nm)	3% at.	968.8	976.7	976.0	975.1	[4]
λ_{laser} (nm)	<1%	1030	1031	1032	1041	[6,7]
$\sigma_{emission}$ (10^{-21} cm^2)	<1%	19	10.6	12.8	14.4	[6]
$\sigma_{absorption}$ (10^{-21} cm^2)	3% at.	8	24	30	45	[4]
$\sigma_{reabsorption}$ (10^{-21} cm^2)	<1%	1.2	0.8	0.7	0.7	[6]
Thermal conductivity,	undoped	9.8	12.8	12.2	15.5	[4]
κ (W m^{-1} K^{-1})	3% at.	7.1	7.4	10.8	6.4	[4]
Fluorescence lifetime	<1%	950	850	820	800	[6]
(μs)	3% at.	1040	850	820	800	[4]
Melting point (^{o}C)	undoped	1930	2430	2500	2430	[4,8]
Mohs hardness	undoped	8.5	6.8	∼7	<6.8	[8,9]
$^2F_{7/2}$ splitting (cm^{-1})	<1%	785	874	903	1017	[6]
Lattice constant (Å)	undoped	12.0	10.6	10.4	9.8	[10]

Table 1.1: Comparison of YAG and sesquioxide properties

1.3 Planar waveguide lasers

Planar waveguide lasers are of interest as they are compact devices with the potential for use in integrated optical circuits and have various geometrical advantages. The large aspect ratio of a planar material provides a large surface area for efficient heat removal, which is important for quasi-three-level systems and advantageous for high power devices [11]. Another advantage of the planar geometry over bulk systems is the greater overlap of pump and laser modes, leading to lower lasing thresholds [11, 12].

The structure of waveguides can be designed to be single-mode or multi-mode by tuning their thickness and numerical aperature (NA), by selection of materials to be used as the substrate, waveguide and cladding layers. Thin, low NA guides promote single-mode operation, but suffer problems from the difficulty of efficient pump beam coupling. Thicker, high NA guides promote multi-mode operation, and are much easier to couple pump light into and can therefore be pumped by high-power diode bars, rather than lower power single stripe higher beam quality lasers (lower

M^2 values, close to 1). It has been found that by careful selection of waveguide layer thicknesses, of doped and undoped regions, preferential selection of the fundamental laser mode can be achieved and therefore the laser output in the guided direction can be almost diffraction limited [13, 14]. This allows the potential for small, high power devices with high beam quality in the guided axis.

1.4 Structure of Thesis

Following a brief introduction to pulsed laser deposition, the materials being studied in this project and the laser cavity geometries to be employed, this thesis begins with an overview of various different techniques available for thin film deposition, waveguide fabrication and methods that have been used for growth of crystalline sesquioxides. This chapter ends with an overview of some of the best laser results achieved to date from rare-earth-doped sesquioxide crystals, in bulk, thin disk and planar waveguide configurations.

The theory section, chapter 3, covers both the processes involved in pulsed laser deposition, from the laser ablation process through to the crystal growth, and laser theory. Some specifics for waveguides are covered as well as general laser theory and details of the particular dopant species studied within this project. A brief introduction to thin disk lasers is provided before the section concludes with mechanisms for pulsed laser operation, to accompany the results presented in chapter 10.

Chapter 4 details the experimental and analytical methods used throughout the subsequent results chapters. This begins with the setup used for pulsed laser deposition and the method employed for substrate heating before covering the various material analysis techniques, polishing, spectral characterisation and finally some considerations in the construction of planar waveguide laser setups.

The experimental and results chapters of this thesis, chapter 5 onwards, begin with some optimisation experiments performed with (doped) scandia, yttria and lutetia, where the aim was to grow crystalline films with as few particulates as possible, while maintaining a reasonable deposition rate. Studies performed depositing these sesquioxides onto different substrate materials are then presented in chapter 6.

Laser results achieved with these pulsed laser deposited sesquioxides are reported in the following chapters, beginning with the first published results of a Tm:Y_2O_3 planar waveguide laser

in chapter 7, then results achieved from single and multilayer Yb-doped samples as we attempt to power scale the output of these planar waveguide lasers. Results obtained using Yb:Y_2O_3 are presented first, and then the more recent, higher power results from a Yb:Lu_2O_3 waveguide sample. The experimental results chapters finish with pulsed operation of Yb:Y_2O_3 waveguides using graphene as a saturable absorber in two different configurations - on the output coupler and on the waveguide surface, which interacts with the evanescent field.

This thesis concludes with some comments on the results acheived in this project so far and ideas for future work to be carried out with the hope of continuing to improve crystal growth, power scale these PLD-grown planar waveguide lasers and expand the range of dopants used to provide a wider range of operational wavelengths.

1.5 Summary of Achievements

A brief summary of the main achievements in this project is listed below:

- Growth and characterisation of a single layer Tm:Y_2O_3 waveguide on YAG, which provided the first laser results of this project and was, to the best of our knowledge, the first reported Tm:Y_2O_3 planar waveguide laser. This laser had a slope efficiency of 9%, maximum output power of 35 mW and operated at a wavelength of 1.95 μm.

- The growth of an Yb:Y_2O_3 multilayer waveguide sample, its analysis and subsequent lasing experiments. A maximum output power of 1.2 W was obtained at an operating wavelength of 1030 nm, with a slope efficiency of 20%.

- Growth of an Yb:Lu_2O_3 single layer waveguide on YAG, analysis of the sample and involvement with laser experiments. An output of 8.5 W was achieved, which was the highest output of any PLD-grown wavguide laser at the time.

Chapter 2

Background

2.1 Introduction

This chapter explores a range of competing techniques for thin film deposition, waveguide fabrication and crystal growth methods with specific reference to the sesquioxides studied in this thesis. A brief review of results achieved, to date, with the sesquioxides in terms of lasing performance in bulk, thin disk and waveguide laser configurations is given.

2.2 Techniques for thin film deposition

2.2.1 Physical Vapour Deposition (PVD)

Physical vapour deposition is a general term for those techniques that involve particles being ejected from a solid target material in a vacuum chamber and transported to a substrate where the material can deposit and form a thin film [15]. Particle ejection can occur due to resistive heating, electron beam heating, ion bombardment or laser ablation. PLD is therefore a form of PVD, discussed in detail in this thesis. Below are details of two alternative PVD methods.

2.2.1.1 Sputtering

Sputtering of material from a target occurs when it is bombared by high energy ions (∼30 eV to ∼2 keV) [16]. Ejected atoms travel away from the target and are deposited on a substrate and grow uniform thin films, typically at deposition rates of 1 - 10 nm/ s [15]. There are two

commonly used methods of generating high energy ions for sputtering, both of which usually use argon, or sometimes neon or krypton, depending on the mass of atoms to be sputtered. The use of inert gases avoids contamination of the deposited layer. Firstly, a discharge plasma can be created by a high voltage being applied between an anode and cathode inside a vacuum chamber filled with a background gas, usually to a pressure of about 2 to 20 mTorr [16]. The ions in the plasma (usually Ar^+) are accelerated towards the negatively biased target where bombarment occurs. The relatively high background pressure in the deposition chamber results in many collisions of the ejected atoms on their journey to the substrate, which causes a loss of energy. The second method commonly employed uses an ion gun incident on a target in a high vacuum. In this case the energetic ions strike only the target, so contamination of the film due to sputtering of material from the chamber walls is avoided. Fewer collisions of ejected atoms occur using this method due to the high vacuum used, resulting in higher energy atoms reaching the substrate for film growth. High energy particles arriving at the growing film can have the positive effect of knocking loosely bound atoms off the film, including impurities, which improves adhesion and causes the film to become more dense. However, higher energy atoms can also cause damage to the growing film as they collide with it.

Reactive ion sputtering uses reactive gases, namely oxygen or nitrogen, in the vacuum chamber, usually mixed with an inert gas. Sputtered atoms can then react with these gas molecules on route to the substrate, which is useful when the desired film is an oxide or nitride. Sputtering is most commonly used for fabrication of metal and dielectric films. Yttria, along with a few other oxides, has been deposited by plasma-assisted magnetron sputtering with the aim of using them for planar waveguiding applications [17]. Y_2O_3 samples had losses of 2 - 4 dB/ cm at 1.3 and 1.5 μm, but no waveguiding at the shorter wavelengths trialled of 633 nm and 833 nm. Scanning electron microscope (SEM) images of a cross-section through an Y_2O_3 sample grown on SiO_2 show a columnar structure, similar to what is seen in SEM images of the PLD-grown samples reported in this thesis.

2.2.1.2 Evaporation

Evaporation is a simple technique that can be used to deposit a thin film of material. The desired material is placed in a crucible inside a vacuum chamber and heated electrically until it melts and vapourises. A substrate is positioned above the crucible to recieve the vapourised

material and a thin film forms. This technique requires high or ultra-high vacuum, is only suitable for materials that vapourise at a fairly low temperature, and provides very slow deposition rates of 0.1 - 1 nm/ s [15]. This simple method has a line-of-sight transport of material, so is not good for coating around corners, side walls or ridges, and has very few parameters to adjust to tailor film properties. The subtrate can be heated to improve the quality of the growing film, as the extra energy allows deposited atoms to migrate into energetically favourable sites and can cause impurities to be desorbed.

Materials with higher melting points, such as refractory metals, require a different method of heating in order for vapourisation to occur. Localised electron-beam heating can be employed for this purpose, which is even capable of vaporising tungsten (with a melting point of 3650 K), but deposition rates are very low. Sesquioxides have been grown on α-Al_2O_3 substrates by electron-beam evaporation and results compared with PLD [18]. While results are fairly similar, the apparent differences highlighted are that the packing density of the films grown by electron-beam evaporation are typically lower than those grown by PLD due to the kinetic energies of the atoms being deposited being much higher in PLD (up to 100 eV, compared to some 100 meV for evaporation), and the change in the fluorescence spectra over time for the e-beam evaporated Eu-doped samples, where PLD-grown samples showed no significant changes.

While simple, this technique has problems and limitations. Films grown by evaporation can suffer from contamination as molten metals may react with the crucible and be incorporated in the growing film. This is minimised by a suitable choice of crucible material, such as refractory metals. Contamination is less likely from evaporation by localised e-beam heating but still possible in the case of misalignment. Evaporation of compounds and alloys is problematic as components may evaporate at different rates.

2.2.2 Molecular Beam Epitaxy (MBE)

Molecular beam epitaxy is a deposition technique that requires ultra-high vacuum (UHV) but can produce very high quality thin films of accurate thickness due to atomic layer-by-layer growth. Source materials are evaporated/ sublimated and form beams of atoms or molecules, depending on the source, which are incident on a heated substrate of suitable material for the desired growth [19]. Two methods used for source heating are winding a filament around the source crucible for Ohmic heating or electron beam heating. The variables to adjust are the source

and substrate temperatures and the incident flux rate. Typical growth rates for MBE are $1\mathring{A}$ (1 atomic layer) per second.

2.2.3 Liquid-phase epitaxy (LPE)

Liquid phase epitaxy is a method of growing a single crystal layer onto a single crystal substrate. This involves dipping a rotating substrate into a crucible of a solution of the molten constituents, which seeds the crystal growth [20]. Extra constituents can be added into the solution to help compensate for lattice mismatch between the substrate and growing crystal, or to increase the refractive index difference.

This technique can produce good quality films, including multiple layers, and can be economical for mass production. However, high temperatures (typically $\sim$1000°C) are required, along with crucibles that can withstand them such as platinum, and setup for new depositions is slow [20].

2.2.4 Chemical Vapour Deposition (CVD)

Chemical vapour deposition has been used to deposit a wide selection of materials, with high purity results at a relatively high deposition rate, around 0.1 - 10 nm/s [15]. Precursors, often halides or hydrides of the elements to be deposited, are mixed and react on and near heated surfaces to form thin films. This means films can be uniformly deposited on shaped surfaces as well as flat ones. It is also common to use small organic radicals, such as methyl or ethyl groups, bound to the desired elements as precursors, and sometimes larger functional groups. When the pre-cursors react, by-products are formed which are removed from the deposition chamber. Both precursors and by-products can be hazardous due to high toxicity, tendency to explode and corrosiveness. CVD often requires fairly high temperatures (typically ranging from 200-1600°C), limiting the materials that can be deposited onto due to thermal expansion coefficient differences [21]. The temperatures required are, however, modest in comparison to the melting points, sometimes allowing depositions to be performed at less than half the melting point of the deposited material, but is a limitation with respect to the substrates that can be deposited onto [22].

2.3 Techniques for waveguide fabrication

2.3.1 Thermal Bonding

Thermal bonding involves precision finished materials being brought into contact and heated to increase bonding strength. Van der Waals intermolecular forces hold components securely together. This technique can be used to bond both crystals and glasses, including to each other, allowing high NA (>0.8) waveguides to be fabricated [23]. Spectral properties of the bulk materials used for the core are unaffected, which is often not the case for other thin film deposition techniques.

2.3.2 Indiffusion

Indiffusion is a relatively simple process where a thin film is evaporated or sputtered onto a substrate surface that is then heated, which triggers a complex diffusion process that is not fully understood [24]. While some other materials have been trialled with this method, the best results have been achieved from diffusing titanium into $LiNbO_3$. For this material, a thin film of 50 - 100 nm of Ti is deposited onto the surface of a $LiNbO_3$ crystal, which is then placed in a quartz tube oven for several hours at ∼1000°C with a flowing atmosphere of oxygen, argon or air, and diffusion takes place [25]. The diffusion of the titanium into the $LiNbO_3$ crystal causes an increase in refractive index near the surface, creating a waveguide. Very low propagation losses of 0.1 dB/ cm at 1.5 μm has been achieved using this method.

2.3.3 Ion exchange

Ion exchange is a simple and cheap method of increasing the refractive index of a crystal to form a waveguide layer at the surface by immersing the crystal in an ion source, often high temperature molten salts for metal ion exchange or acids for proton exchange [24, 25]. Migration of ions can be encouraged by use of an electric field by placing a cathode opposite the substrate surface to attract the positive ions to the surface to undergo exchange, while the back side of the crystal is negatively biased [16]. Proton exchange is a low temperature process (T<250°C) that can be used to exchange lithium ions for hydrogen ions in $LiNbO_3$ and $LiTaO_3$ crystals. This exchange causes an increase in the extraordinary refractive index and a decrease in the ordinary refractive index, meaning that a waveguide is formed only for extraordinary waves [24, 25]. Acids commonly used

for proton exchange include benzoic acid, sulphuric acid and phosphoric acid [24], and sufficent exchange occurs over a period of an hour or less [16].

2.3.4 Ion Implantation

Ion implantation requires an ion source of the desired dopant and electrodes in an accelerator capable of accelerating those ions to energies of, typically, 20 - 300 keV, and a beam deflector to allow the collimated ion beam to be raster scanned over the substrate, all of which must be in vacuum [16]. The penetration depth of the dopant ions depends on their mass, energy and the substrate material used. Ions slow on entering the crystal substrate due to energy loss from interactions with electrons and nuclei of the crystal. For higher energy incoming ions electronic excitation is the dominant energy loss mechanism and scattering centres can be formed in the crystal. Annealing of samples following ion implantation is sometimes performed to reduce optical losses by providing energy for implanted ions to move to substitutional sites and remove lattice damage caused by implantation [16]. For lower energy ions, in the keV range, nuclear collision is the main mechanism for energy loss. For the implantation of light ions such as H^+ and He^+, nuclear collision can cause amorphisation of the crystal and a reduction in the refractive index. A sharp maximum of the nuclear damage per crystal volume occurs at about 5 μm below the surface. This well-defined damaged layer with reduced refractive index creates a barrier that can be used to guide light by total internal reflection [24]. The refractive index profiles created by ion implantation are almost step-like, particularly when higher energy ions are used, and lower energy implantation results in shallower implantation that has a wider distribution of damage in the crystal [24].

2.4 Methods of sesquioxide growth

2.4.1 Nacken-Kyropoulos method (NK)

The Nacken-Kyropoulos method of crystal growth is a simple method that requires a stationary crucible in a furnace containing a melt of material. Crystal growth is initiated by dipping a rod with a seed crystal attached to it into the melt. An alternative method to using a seed crystal that is sometimes employed is dipping an air-cooled tube into the surface of the melt, allowing

a few crystallites to nucleate, then pulling it back out until contact is only just maintained, and using this to seed subsequent growth [26]. There are two approaches to proceeding with crystal growth, the first being to gradually cool the melt and the alternative is to further cool the inserted rod [27]. This technique provides growth rates of order millimeters per hour with cooling rates less than 1°C/h, and is capable of growing crystals up to 90% of the crucible diameter [26] and single crystals of several kg [27].

In the case of sesquioxides, the Nacken-Kyropoulos technique has been reported as a growth method resulting in crystals of several cubic mm, grown in crucibles of 20 mm diameter and 20 mm in height, but with a stressed structure [28]. Rhenium was the material of choice for the crucible due to its ability to withstand the high temperatures required for sesquioxide melts. The background atmosphere for the crystal growth was chosen to be a reducing atmosphere, to avoid oxidation of the crucible and contamination of the melt, of 94.97% N_2 and 5% H_2, and 300 ppm of O_2 with respect to the nitrogen concentration to avoid oxygen deficiency in the growing crystal.

2.4.2 Czochralski Technique

The Czochralski technique is a well-established, widely used method for crystal growth that involves pulling a crystal from the melt. Research was required to be able to use this method for sesquioxide production due to their high melting points, meaning setups that can withstand such high temperatures are needed. Investigation into suitable crucible materials revealed rhenium, with a melting point of 3180°C, to be the best fit to the requirements of being mechanically stable at temperatures high enough to achieve a sesquioxide melt and resistant to chemical reactions with the melt and surroundings. Rhenium rods are welded to the crucible so that it can be suspended in a thermally insulating tube of zirconia felts, avoiding contact between the two materials, and surrounded by gas, while inductively heated, for example, by a radiofrequency (RF) source at 230 kHz, at a power of 20 kW [29]. Sesquioxides grown by the Czochralski process have been reported to be pulled at 1-3 mm/h and a rotation rate of 10 rpm in an inert He atmosphere, leading to 2-5 mm of crystal growth before problems start to occur, such as the crystal losing contact with the melt or growth becoming asymmetrical.

2.4.3 Bridgman Technique

The Bridgman technique for crystal growth requires a crucible to hold a melt of material, which means using a crucible formed from a material with a higher melting point than the sesquioxides, as in the Czochralski method. In the Bridgman technique, the crucible is moved slowly through a temperature gradient to cool the melt, causing crystalisation to occur from one end, usually from a seed crystal, through the melt.

As in the Czochralski technique, the crucible material used for sesquioxide growth by the Bridgman technique is rhenium, and zirconia felts are used as thermal insulation around the crucible but are kept out of direct contact with it. The reported growth atmosphere used was Ar with 10% H_2 [30]. Using a cooling rate of 3°C/h, it was possible to make large crystal boules with single crystalline domains of order cm^3, which was an improvement from the single crystals with mm scale dimensions obtained using the Nacken-Kyropoulos and Czochralski methods. These larger crystals do however require annealing in air to become transparent, as the as-grown crystals are black due to oxygen deficiencies and colour centres.

2.4.4 Heat-exchanger method (HEM)

The heat-exchanger method is a modification of the Bridgman technique for growth of bulk crystals. Instead of moving a crucible through a temperature gradient, the HEM uses a crucible in a fixed position and is cooled from the centre of the bottom of the crucible by a variable gas flow. The crucible is kept in an isothermal insulation setup, with the walls kept at constant temperature until the end of the growth process so that the crystal doesn't reach the edges and create secondary nucleation sites during the growth, and ensures low strain in the crystal. This setup is surrounded by insulating zirconia felts, and the background atmosphere of choice is dependant on the crystal being grown and crucible used.

As for sesquioxide growth using the Czochralski technique, the crucible material found to meet the necessary requirements best was rhenium. Rhenium is sensitive to oxidising atmospheres, so the background gas composition used contained very little oxygen, but is resistant to RE-oxide melts; the best growth atmosphere reported by Peters et al. in [9] is 0.01% O_2, 10-15% H_2 and 85-90% N_2 at a pressure of 1 bar. Crystal growth can be seeded by a crystal placed in the bottom of the crucible that is heated until the seed is partially molten, with a low gas flow being used, before increasing the gas flow through the heat exchanger to begin the crystallisation of the melt.

The crucible is heated by induction throughout the growth process, with an RF-generator that can provide a maximum power of 36 kW at a frequency of ∼400 Hz, until most of the melt has crystallised. The heating is reduced near the end of the process until the crystallisation reaches the crucible walls. More than 95% of the melt can be made into high-quality crystalline material using this method.

2.4.5 Flux Method

The flux method involves combining the constituents of the desired material to be grown with a solvent, so that a solution can be made at a temperature far less than the melting point of the crystal components alone. The mixture sits in a crucible, made of a highly stable, non-reactive material, and is heated just beyond the saturation temperature so that a complete solution is formed. The crucible is then cooled, and crystal begins to form, either by spontaneous nucleation or by introduction of a seed crystal to encourage single crystal growth in a particular orientation.

In the case of the sesquioxdes, the use of a non-toxic solvent that allows a growth setup that requires reaching only 1200°C, half the melting point of the cubic rare-earth sesquioxides, and that can be operated in air has been reported [31]. This technique involved first preparing the solvent and solute materials, that were commerical powders, by a combination of heating in air to dry them and mechanically mixing and grinding correct amounts together. The solvent, $Li_6(Y_{0.95}Yb_{0.05})(BO_3)$, and solute, $(Y_{0.95}Yb_{0.05})_2O_3$, were mixed together in a platinum crucible and heated to 1200°C inside a furnace. The molten solution was stirred by a platinum spatula attached to a rotating alumina rod, at 30 rpm for 4 hours, to ensure a homogenised melt. The platinum spatula was drawn up so that just the tip was left inserted a few mm into the melt, which continued to rotate at 20 rpm to avoid sedimentation as the growth stage began, by slowly cooling the content of the crucible by 0.5°C/h down to 1035°C. Following this, the spatula was fully removed and the cooling rate increased to 42°C/h. A similar process was applied for the preparation and formation of Yb:Lu_2O_3 crystals, which also resulted in crystals with perfect visual transparency, but typically of smaller dimensions and lower dopant concentration.

2.4.6 Top-seeded solution growth (TSSG)

Top-seeded solution growth is sometimes referred to as a modified flux technique, which combines Czochralski and solution growth processes to pull crystals from a high temperature flux. A

suitable solvent needs to be selected and quantities of compounds to be mixed decided upon. These quantities are chosen following the study of a phase diagram of the compounds being used, as is the temperature to be used in order to achieve the desired crystal growth. The physiochemical properties of density, viscosity, thermal conductivity and surface tension of the solution are used to configure the parameters to be used in the setup for crystal growth. The parameters to be changed in this growth technique include the aspect ratio of the crucible used (as well as appropriate choice of crucible material, as always), the axial and radial thermal gradients in the solution, and the rotation and pulling rates. Heating of the crucible is performed by an electrical resistance coil and a seed is inserted into the solution to initiate crystal growth. The seed crystal is attached to a rod connected to rotation and pulling systems that consist of high precision mechanisms that allow for simultaneous rotation and pulling of the crystal [32].

2.4.7 Floating Zone Technique

The floating zone technique is a crucible-free method of single crystal growth that involves a cylindrical polycrystalline rod, held vertically by the ends, being passed through a heat source, such as an induction coil [27]. Starting with the middle region, the polycrystalline rod is heated until melting occurs a few mm along the length of the rod, which holds together due to surface tension. The rod is slowly moved up and down through the heated area, causing melting and conversion into single crystal throughout the rod. This process is performed under high vacuum or a protective gas atmosphere.

For the growth of sesquioxides, and other oxides with high melting points, a floating zone technique using CO_2 gas lasers as the heat source has been reported [33]. These lasers emit at a wavelength of 10.6 μm, which is almost completely absorbed by the oxides, and have a relatively small beam diameter and divergence that allow for a relatively simple setup with long focal length lenses to be used. The power output from these lasers is continuous wave (cw) and can be controlled over the range 50 to 400 W, and is focussed down to a spot size of 1 to 2 mm at the surface of the floating zone, which provides a maximum power density of 50 kW/ cm^2. The rods used for this process are 0.5 to 0.7 cm in diameter and up to 10 cm long, and formed from powders that are pressed and sintered. Two rods are employed for this growth process, one held from the top and the other from the bottom, positioned with their ends approximately 0.1 cm apart and rotated in the same direction at 5 to 10 rpm. The lasers are aligned such that one is incident on each rod

end, forming molten tips that expand and join together to form a stable molten zone, at which point the lasers are aligned level with each other in the floating zone. This two rod approach helps to avoid severe buckling or fracture due to the thermal expansion of the material. Once the floating zone is established, the rods are traversed through the laser beams at 1 to 3 cm/ h. This process is performed in an auxiliary furnace at 1700°C and produces crystals 5 mm in diameter and several cm long. However, despite the 1700°C background temperature there is still a large thermal gradient present in this process, particularly with the sesquioxides with melting points ∼2500°C, which leads to strained crystals being formed that frequently crack.

2.4.8 Laser heated pedestal growth (LHPG)

Laser-heated pedestal growth is another crucible-free crystal growth method that allows high purity crystal fibres to be pulled. A molten zone is created at the top of a feed rod by a focussed laser beam. A seed crystal is dipped into the molten zone and pulled back upwards to start drawing the crystal fibre at a higher rate than the source rod is fed into the molten zone, as is required to achieve a thinner structure due to conservation of the melt volume [34]. The pulled fibre and feed source remain in contact due to surface tension through the molten zone.

Various rare-earth doped Y_2O_3 fibers have been formed using LHPG, pulled from rods typically cut from crystal or polycrystalline ceramics to a size of 1 x 1 x 12 mm^3 [35]. A 50 W CO_2 laser is symmetrically focussed to form a small molten region from which a fiber is drawn. The pulling and feed mechanisms are computer-controlled and pulling rates of 0.5-2 mm/min used to obtain fibers of 300-700 μm diameter, with a maximum pulling length of 6 cm in this reported example. This technique has resulted in production of good quality fibers, is inexpensive and rapid, and does not require the feed and seed rods to be rotated, as in some other growth techniques such as the Czochralski method.

2.4.9 Micro-pulling-down Technique (μ-PD)

The micro-pulling-down technique [36] is another method of crystal growth that requires a melt of the desired material in a crucible, but with a hole in the centre of the bottom of the crucible (or multiple outlets) to allow material to be drawn out. The growth is seeded by bringing a crystal into contact with the capillary outlet, then pulling it back down slowly to proceed with the crystal growth. Contact is kept between the grown crystal and the melt as it exits the crucible

by surface tension, and a melt meniscus is formed just outside the capilliary tube. The crystal growth is controlled by the rate of pulling down and the heating of the melt via a RF coil [37]. This technique is suitable for bulk rods of crystalline material and crystal fibres.

As with other growth techniques, sesquioxide growth requires some modifications to the standard micro-pulling-down setup. Rhenium crucibles are chosen due to their excellent mechanical properties at the melting temperature of the sesquioxides, and as it does not react chemically with the melt. However, rhenium is easily oxidised so a reducing atmosphere is used; reports of 3-4% H_2 by volume in an argon background have been reported [37, 38], to keep below the lower explosve limit of H_2. Near isothermal temperature distributions are achieved by surrounding the crucible with zirconia felts, kept out of contact with the crucible to avoid reactions between the two, within a quartz tube with a lid. Pure RE-oxide powders are the starting materials that are ground together and placed in the crucible, which is heated by RF induction coils to form the melt. The pulling down is kept at a constant velocity, and the best speed reported is approximately 0.1 mm/min [37]. Yb:Y_2O_3 rods of 4.2 mm diameter and 10-20 mm in length have been reported, which are gray-blue crystals, with colour intensity being dependant on Yb-concentration, before annealing in air, and seeded by high quality ceramic yttria, due to lack of a single crystalline seed [37]. The colouration is put down to the reducing atmosphere, leading to some of the Yb^{3+} ions being reduced to Yb^{2+}, and possibly oxygen vacancies in the crystal. Similarly, Yb:Lu_2O_3 crystals were grown, but with a less smooth surface and less colouration, with a diameter of 4.2 mm and lengths of 8-10 mm. Annealing in air resulted in transparent, colourless, defect-free crystals in both cases. Results with scandia were less good, thought to be due to the lack of availability of a scandia seed, but the crystals produced were still transparent and colourless following annealing. Another attempt at sesquioxide growth by the micro-pulling-down method reported the use of 3% H_2 in the argon background atmosphere and the resulting rods being gray or black from deposition of Re from the crucible on the surface, suggesting the background atmosphere used didn't completely prevent oxidation of the crucible [38]. In this case it was the Yb:Lu_2O_3 that had the worst results, judged by comparison of the full width at half maximum (FWHM) of X-ray rocking curve measurements, put down to a lower purity of the starting powder. However, once annealed, cut and polished to a thickness of 1 mm, these crystals were each found to have optical transmittances of nearing 80%.

2.5 Sesquioxide properties

Properties of materials determine what applications they may be useful for. The sesquioxides yttria, scandia and lutetia have been identified as very promising laser host materials for high power lasers, mostly due to their high thermal conductivity and ability to be doped with rare-earth ions. In addition to this, these sesquioxides are chemically stable, transparent across a large wavelength range, mechanically hard and display optical isotropy [39]. Various physical and optical properties of these materials have already been displayed in the introduction to this thesis in table 1.1, in comparison to YAG. The greater Stark splitting seen in the sesquioxides due to a larger crystal field results in emission from Y_2O_3, Lu_2O_3 and Sc_2O_3 being shifted to longer wavelengths, with this effect being most prominent in Sc_2O_3 [40]. In addition to the data provided in table 1.1, the absorption and emission spectra of Yb-doped sesquioxides are shown below, in figure 2.1, taken from reference [40].

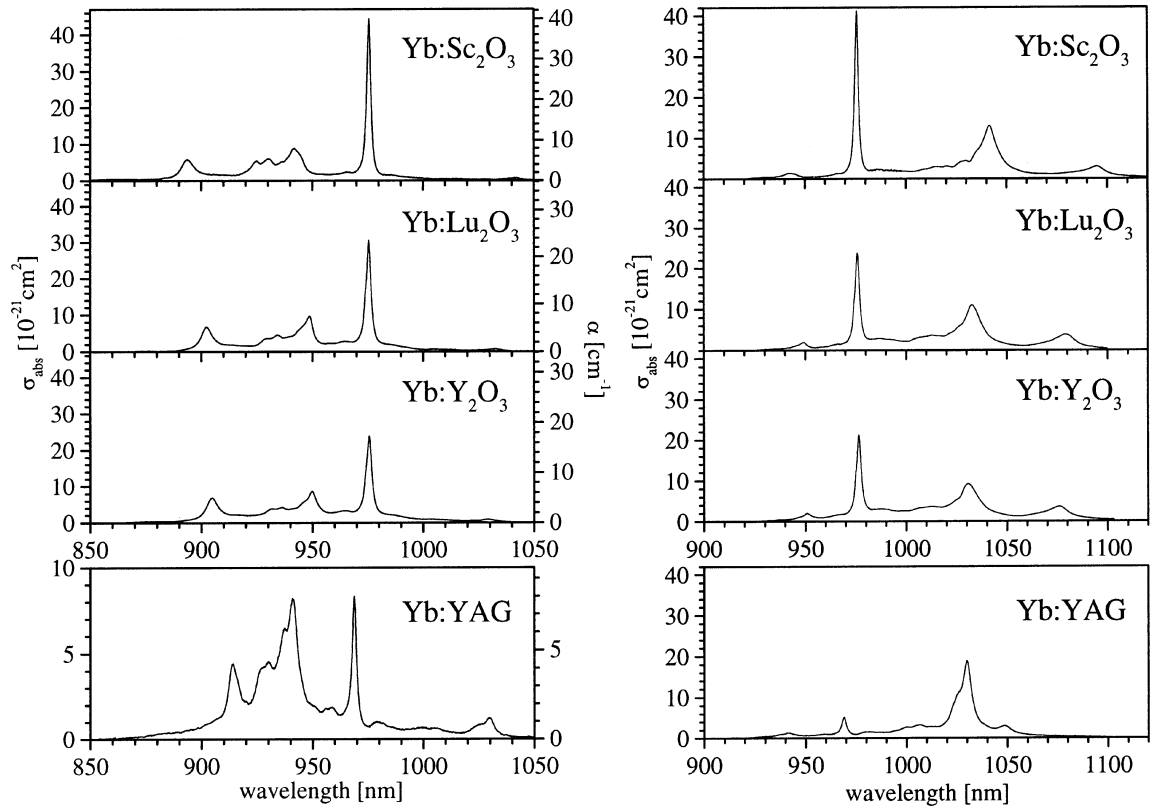

Figure 2.1: Absorption (a) and emission (b) spectra of Yb-doped sesquioxides.

As can be seen from these spectra, the peak emission cross-sections are slightly smaller than those obtained from Yb:YAG but the absorption line at the zero phonon line is considerably higher, which is useful for pumping with commercially available high power diode laser sources around 976 nm. Furthermore, the fluorescence lifetimes of the $^2F_{5/2}$ state reported in this paper are 800 μs in Sc_2O_3, 820 μs in Lu_2O_3, and 850 μs in Y_2O_3, which is also in line with those in table 1.1 from reference [6].

Sesquioxide crystals have a body-centred cubic bixbyite structure and belong to the cubic space group $Ia\bar{3}$ [39,41], the unit cells of which are shown in figure 2.2. Until fairly recently lutetia was only assumed to be isomorphous with yttria, but this has been confirmed experimentally in reference [39]. The structure of these sesquioxides have two independant cation sites for the 32 ions in a unit cell, and the O^{-2} anions occupy 48 general positions. The cation sites with local symmetries are the centrosymmetric C_{3i} sites (figure 2.3(a)) and noncentrosymmetric c_2 sites (figure 2.3(b)), which occur in a 1:3 ratio (C_{3i}:C_2), meaning there are 8 ions occupying the C_{3i} sites and 24 occupying C_2 [39]. It was also confirmed that the structure of polycrystalline Lu_2O_3 is the same as that for single crystal and has advantages in the size of the material that can be produced, mechanical strength and production costs.

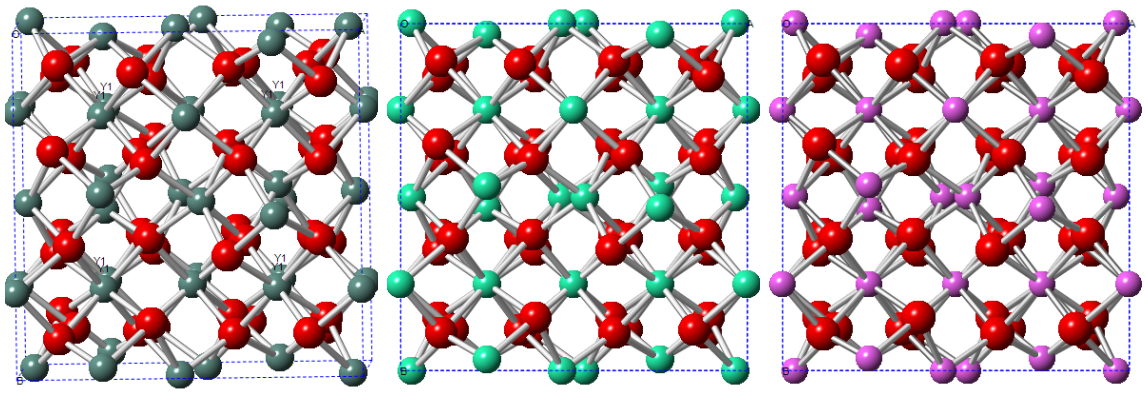

(a) Y_2O_3 (b) Lu_2O_3 (c) Sc_2O_3

Figure 2.2: Unit cells of sesquioxides. The yttria cell, (a), is slightly offset from a direct side-on view to provide a better view of the Y1 sites, labelled. The other 24 Y atoms occupy the Y2 sites. The lutetia (b) and scandia (c) unit cells are displayed directly from one side of the cubic unit cell.

A recent study of the thermo-optic properties of Yb:Lu_2O_3 single crystals [42] has reported the thermal expansion coefficient of lutetia as 5.880 $\pm$ 0.014x10^{-6} K^{-1}, at room temperature, and

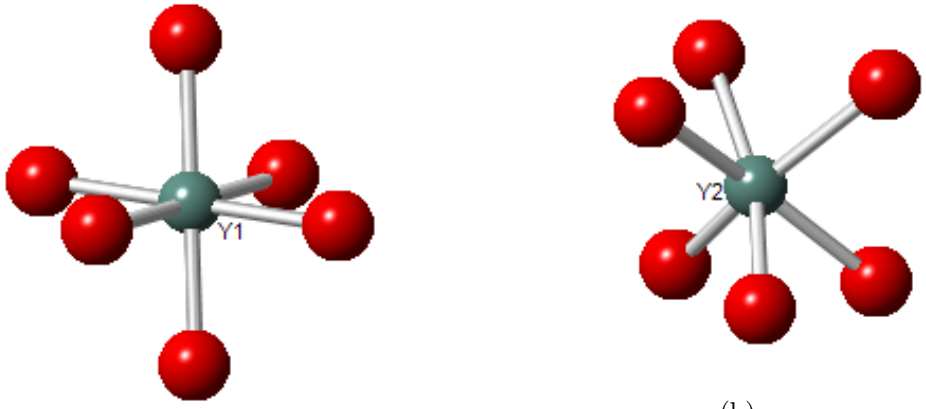

(a) (b)

Figure 2.3: Y1 and Y2 atoms in their local symmetries, known as (C_{3i}) and (C_2) sites, respectively.

the band gap, E_g, to be 5.15 eV for Yb:Lu_2O_3 and 5.41 eV for the undoped crystal. The main factors affecting thermal lensing in materials is their thermal expansion, which causes end-bulging, and temperature dependance of the refractive index, known as the themo-optic coefficient, dn/dT. This quanity, dn/dT, was determined to be 5.8x10^{-6} K^{-1} at the typical Yb lasing wavelength of 1.03 μm. Thermal lensing in Yb:Lu_2O_3 crystals is weaker than that seen in Yb:YAG, mainly due to the high thermal conductivity of this material.

2.6 Previous Sesquioxide Laser Results

The last section of this chapter reports on some of the best results of sesquioxide-based laser systems in the literature in bulk, thin disk and waveguide configurations. The majority of such results to date have been with bulk and thin disk laser setups, leaving a gap in the development of rare-earth doped sesquioxide waveguide lasers that the work carried out in this project begins to fill.

2.6.1 Bulk laser crystals

Experiments performed using Yb:Sc_2O_3 as the laser medium provided efficient operation in both cw and pulsed operating regimes [6]. A maximum output power of 1 W was achieved with a slope efficiency of 65% and threshold of 250 mW of absorbed pump power, using a Ti:sapphire

laser as the pump source. There was no active cooling of the laser crystal, but no problems due to thermal effects were observed. Passive mode-locking was achieved by inserting a semiconductor saturable-absorber mirror (SESAM) into the system, which resulted in a maximum pump efficiency of 47% (this was the highest reported optical-to-optical efficiency for a mode-locked laser at the time of publication), and 54% efficiency with respect to absorbed pump power. This setup gave pulses as short as 1.33 ps at an operating wavelength of 1041.5 nm and maximum average output power of 0.8 W. The pulse duration was reduced down to the femtosecond time-scale by the addition of prisms for dispersion compensation. With the prisms inserted, the maximum average output achieved was 540 mW with a pulse energy of 6.3 nJ, which gives a peak power of 27.6 kW. The pump efficiency was reduced to 30% (35% with respect to absorbed pump power) and the pulses had a FWHM of 230 fs at a central wavelength of 1044.5 nm. Experiments were also performed using a tapered diode laser as the pump source with a bandwidth of 1 nm, stabilised at 976 nm by feedback of a small amount of radiation (<0.02%) from a reflection grating. This setup allowed for 120 mW of output power with 1 W of incident power using a 2.8% output coupler, for which the laser threshold was at an absorbed pump power of 250 mW and the slope efficiency with respect to absorbed pump power was 15%. At maximum power, the repetition rate was 86 MHz and the pulses produced were 255 fs long. Roughly the same pump power was available from the Ti:sapphire and the tapered diode laser, but the slightly reduced performance using the diode pump is due to the lower beam quality and consequently imperfect matching of the pump and resonator modes. However, both pump setups gave results that surpassed the limit of 340 fs pulses reported for Yb:YAG due to the larger gain bandwidth of Yb:Sc_2O_3.

Another report uses an Yb-doped mixed sesquioxide host in the form of single crystal Yb:$LuScO_3$ to obtain mode-locked pulses with a duration of 74 fs [43]. 1 at. % Yb doped $LuScO_3$ crystals were grown by the HEM, along with 0.7 at. % Yb doped Sc_2O_3 for comparison. The mixed host has the same crystal structure as the pure sesquioxides but is locally disordered due to the random distribution of Lu and Sc cations in the rare earth lattice sites. The Yb dopant ions that replace some of these cations experience a variation in their environment and therefore the crystal field, which causes inhomogeneous broadening of the absorption and emission spectra. The cross-sections are, however, about 35 % lower than that obtained from Yb:Sc_2O_3. This mixed sesquioxide, along with Yb:$YScO_3$, is reported to have the broadest emission spectrum of sesquioxides known so far, at 22 nm FWHM [44]. Yb:$LuScO_3$, however, is easier for growing good quality crystals and was

therefore chosen for mode-locked laser experiments. The pinhole method [45] was used to measure the fluorescence lifetime of the Yb:$LuScO_3$, which was found to be ~850 μs, close to the values of 800 μs and 820 μs obtained for Yb:Sc_2O_3 and Yb:Lu_2O_3 respectively. For laser experiments, crystals of 2.9 mm in thickness with a 3 x 3 mm aperture were inserted into a Z-cavity laser setup, in turn, at Brewster's angle with no active cooling. Dispersion compensating prisms were included in the cavity and an output coupler of 1% transmission used initally, and a semiconductor saturable absorber mirror (SESAM) formed the other end of the cavity. A 50 μm broad-stripe diode-pump laser that could deliver up to 6 W at 975 nm (with spectral linewidth of about 5 nm) was used as the pump source, and the laser results obtained using an incident pump power of 2 W. The Yb:Sc_2O_3 crystal produced 227 fs pulses at a repetition rate of 83 MHz, providing an average output power of 39 mW. The laser spectrum was centred at 1040 nm and had a FWHM bandwidth of 5 nm. The average power obtained was increased to 280 mW by changing the output coupling to 5%, which caused only a slight change in pulse duration to 230 fs. The crystal was then swapped for the mixed sesquioxide, Yb:$LuScO_3$, which then gave shorter pulses of 125 fs, at a repetition rate of 91 MHz. The central wavelength of the laser spectrum was at 1037 nm and the spectral bandwidth FWHM was 9.2 nm. The significantly shorter pulse duration obtained with the mixed sesquioxide crystal is attributed to the larger gain bandwidth. Both of these crystals absorbed about 85% of the incident pump power. A second, thinner Yb:$LuScO_3$ crystal of 1.7 mm in thickness was also trialled in the laser cavity. Shorter pulses of duration 111 fs were obtained at a repetiion rate of 92 MHz. Despite the lower pump absorption of about 65%, the average output power was similar to the previous experiments at 34 mW. The spectrum obtained was centred at 1036 nm and had a FWHM of 11 nm. Lastly, the pump source was replaced by a two-section distributed Bragg-reflector tapered diode laser (DBR-TDL), operating on a single longitudinal mode at 975 nm with a spectral linewidth FWHM of less than 13 pm and capable of producing up to 10 W in a nearly diffraction-limited beam, and the SESAM was replaced by a curved mirror. This setup produced laser pulses of 74 fs via Kerr-lens mode locking at a repetition rate of 84 MHz, while the output was 40 mW for a pump power of 2.33 W. The central wavelength was 1048 nm and its FWHM bandwidth was 22.4 nm, demonstrating a strong broadening in comparison with the SESAM mode-locked pulses.

Longer wavelength laser operation has been reported using Tm:Sc_2O_3 [46], produced using the heat-exchanger method (described in section 2.4.4). The Tm(1%):Sc_2O_3 crystal was barrel

polished and had final dimensions of 15 mm in length and a 3 mm diameter. The end facets of the rod were anti-reflection coated for both the pump and laser wavelengths. The fluorescence lifetime was measured to be 3441 ± 25 μs using the pinhole method. The best results achieved with this laser crystal, which was water cooled to 20°C, were an output power of 26.2 W with 41% slope efficiency, with respect to absorbed pump power, using a 3% output coupler. The free running laser wavelength was 2116 nm, but tunability over the range 1975 - 2168 nm was achieved. The output power was only limited by the pump power available.

2.6.2 Thin Disk Lasers

The majority of sesquioxide laser results have been obtained in thin disk laser setups, where power scaling can be achieved by increasing the diameter of the pump spot used (pumping a larger area of the gain medium while maintaining the photon density). More information about thin disk laser setups and the advantages of this configuration can be found in section 3.4.4. The following paragraphs give details of some of the best results acheived in this configuration for both cw and mode-locked operation.

In reference [4], the HEM is employed to grow high purity, optical quality, Yb:Lu_2O_3 crystals with doping concentrations between 1 and 3 at. %. The thin disks formed from these crystals had a diameter of 5 mm and the thicknesses ranged between 0.08 mm and 0.45 mm. Fluorescence lifetime measurements performed on these disks gave values between 820 and 905 μs. For laser experiments, the disks were high reflection (HR) coated on the back-side for the wavelength range 900-1150 nm and soldered to a water-cooled copper heat sink. The front side of the disk was anti-reflection (AR) coated for the same spectral range. The thin disk configuration used provides 24 passes of the pump beam through the gain medium and a plane-concave resonator of about 70 mm. The Yb:Lu_2O_3 disks were each pumped at 976 nm and the best results achieved were with a 0.25 mm thick, 3 at. % doped disk. An output power of 32.6 W was achieved for an incident power of 45.3 W in cw operation, with a slope efficiency of 80%, and optical-to-optical efficiency of 72%. Laser operation occurred at 1034 nm and 1080 nm. Further experiments were performed to investigate the tuning capability of this material. The best results were a continuous tuning from 987 nm to 1127 nm, with more than 10 W of output power obtainable over a 90 nm tuning range. The tuning range and output power achieveable were dependent on the dopant concentration and output coupler used.

A comparison to Yb:YAG, the usual material of choice for high power (kW range) operation, is also made. The maximum doping level of Yb in YAG is around 10 at.% as there is a strong decrease in quantum efficiency as the dopant concentration is further increased due to energy migration and transfer to impurities in the material. Thinner disks are preferable for heat removal from the crystal, but this requires the dopant concentration to be higher to acheive the same absorption of the pump. The very similar masses of Lu and Yb allows for higher dopant concentration, and therefore thinner disks, as the crystal lattice is affected very little by the substitution of Lu for Yb, meaning there is nearly no scattering of propagating phonons and the high heat conductivity of the material is maintained. The lack of decrease in slope efficiency for thicker disks trialled in the experiments reported here [4] is evidence of the high thermal conductivity of Lu_2O_3. Further to this, the absorption of Yb:Lu_2O_3 around 976 nm, with a FWHM of 2.1 nm, is around 4 x larger than for Yb:YAG, so disks can be thinner for a given dopant concentration and have the same pump absorption. This is also convenient for high power operation as high power diode lasers (in the 100 W range) are commercially available around 976 nm. Yb:Lu_2O_3 also brings promise of shorter pulses than Yb:YAG, owing to its broader, although lower, emission cross-section, and the possibility of the operation at 1080 nm that is not possible in Yb:YAG.

Further experiments using Yb-doped sesquioxides in the thin disk laser configuration have given output powers exceeding 300 W, in cw operation [47, 48]. Improved growth of the sesquioxides using the HEM has led to higher efficiencies than for any other gain material in the thin disk geometry. This improved crystal growth combined with using a volume Bragg-grating stabilised diode laser with up to 410 W output power available at 976 nm (FWHM bandwidth of <0.6 mm) as a pump source has led to some excellent results. Yb:Lu_2O_3, Yb:Sc_2O_3 and Yb:$LuScO_3$ crystals were used to form thin disks, each of which was HR coated for the pump and laser spectral range on the back surface and soldered to a water-cooled heat sink. The 24 pump pass system led to above 95% of pump light being absorbed for all crystals tested here. The best results obtained with Yb:Lu_2O_3 were from a disk of 250 μm in thickness and with 2 at. % doping. Using a pump spot diameter of 2.6 mm and an output coupler with 2.7 % transmission, 301 W of output power was achieved at 1034 nm from an incident pump power of 413 W. The slope efficiency was 85% and optical-to-optical efficiency 73%. A slight decrease in slope efficiency was observed above 370 W pump power, which is likely due to thermal rollover. A smaller pump spot size of 1.9 mm led to a slight increase in efficiency, with the optical-to-optical efficiency going up to 74% and slope

efficiency reaching a record high of 88%. For Yb:Sc_2O_3, the best results were achieved with a 2.4% doped, 200 μm thick disk and 1.2% output coupling. In this case, the output power reached 264 W for 380 W pump power, with a slope efficiency of 80% and optical-to-optical efficiency of 70%. Experiments with the mixed sesquioxide, Yb:$LuScO_3$, were also performed on a 200 μm thick disk with a doping concentration of 3 at. %. 250 W of output power was achieved with an input power of 365 W in a pump spot diameter of 4 mm. The slope efficiency was 81% and the optical-to-optical efficiency 69%. Mode-locking experiments were also performed with the Yb:Lu_2O_3 thin disk and a SESAM. The pump spot diameter used was 2.6 mm and an output coupler with 9% transmission. The optical-to-optical efficiency obtained from this setup was 40.4%, and the average output power was 141 W, which was believed to be the highest reported from a mode-locked laser. The pulses had a duration of 738 fs (FWHM) at a repetition rate of 60 MHz, and an energy of 2.4 μJ.

Continuing now with mode-locked sesquioxide lasers, the first report of the mixed sesquioxide Yb:$LuScO_3$ as a mode-locked thin disk laser was reported to give 227 fs pulses [49]. Mixing of the two sesquioxides as the host combines the emission peaks seen from the two separate Yb-doped materials, giving a gain bandwidth of more than 20 nm to allow shorter mode-locked pulses than from a single sesquioxide host. A SESAM was used as the cavity end mirror to achieve passive mode-locking. The average output power achieved was 7.2 W when pumped with 34 W input power and a 4.2% output coupler used. An optical-to-optical efficiency of 21% is reported for this mode-locked laser, whose bandwidth is 5.2 nm, centred near 1041 nm. These results are reported to be limited by defects in the crystal, therefore further improvements are expected with the use of higher quality disks of material.

More Yb-doped mixed sesquioxide hosts in the form of Yb:$LuScO_3$, Yb:$YScO_3$ and Yb:(Y, Sc, Lu)$_2O_3$ have had their emission cross-sections investigated and subsequent laser experiments performed [44]. The broader emission cross-sections achieved with mixed sesquioxide hosts provide the potential for shorter mode-locked laser pulses, results of which have been reported in reference [44] for Yb:$LuScO_3$ and Yb:(Y,Sc,Lu)$_2O_3$, along with results from Yb:Lu_2O_3. Yb:$LuScO_3$ and Yb:$YScO_3$ have the same FWHM bandwidth but the former has the best potential for future power scaling of pulses <100 fs because of growth difficulties of Y_2O_3 due to a phase transition near the melting point. The aforementioned crystals were used in a thin disk laser configuration with a SESAM to achieve mode-locking, and group delay dispersion compensation mirrors so that shorter pulses could be achieved. A 150 μm thick, 3 at. % doped Yb:Lu_2O_3 thin disk glued

to a diamond heat sink and in a 24 pump pass setup, pumped with a volume Bragg grating stabilised diode laser operating at the 976 nm absorption line, gave stable mode-locked pulses up to an average power of 7 W for an input power of 47 W. Nearly transform-limited pulses of 142 fs were obtained at a repetition rate of 64 MHz, using 75% of the gain bandwidth available. A 4% transmission output coupler was used and the laser spectrum was centred at 1035 nm. Power scaling to 25 W resulted in longer pulses of 185 fs and a reduction in the locked gain bandwidth, but still at least 59%. Similar experiments were performed using the mixed sesquioxide thin disk samples. A 200 μm thick, 3 at. % doped Yb:$LuScO_3$ thin disk gave 96 fs pulses at a repetition rate of 77.5 MHz with 5.1 W average output power when a 2.6 % transmission output coupler was used. The output wavelength was centred at 1039 nm and 61 % of the gain bandwidth was modelocked. Lastly, the Yb:$(ScYLu)_2O_3$ thin disk gave 101 fs pulses at a repetition rate of 75 MHz with an average output power of 4.6 W and central wavelength of 1037 nm, when a 1.8 % transmission output coupler was used. 76% of the gain bandwidth was mode-locked. These results are the shortest pulse durations ever achieved from mode-locked thin disk lasers.

Investigation has also been made into using dual-gain setups to increase the gain bandwidth available to allow shorter mode-locked pulses to be achieved, while maintaining the excellent thermal properties of each disk [50].

2.6.3 Sesquioxide Waveguide Lasers

While waveguide lasers provide a good overlap of pump and laser modes to provide low thresholds, and a geometry with a large surface area to volume ratio for effective heat management, there are very few reports of rare-earth doped sesquioxide waveguide lasers prior to those in this thesis. This is presumably due to the difficulty of fabricating thin sesquioxide films of sufficiently low loss to be used as a laser medium.

The first report of a waveguide laser based on a rare-earth doped sesquioxide was a 2 μm-thick Nd(0.5%):(Gd, Lu)O_3 film, epitaxially grown by PLD and lattice matched to a Y_2O_3 substrate [51]. This film was structured by reactive ion etching [52] to form rib channel waveguides of widths of about 2 - 5 μm and 300 nm deep. These dimensions were chosen such that only one transverse mode at the operating laser wavelength of 1079 nm would be supported. This post-processing causes the propagating light to be guided in two dimensions, meaning tighter confinement than in a planar waveguide and consequently lower threshold for laser operation. The film had a 1.8

μm-thick layer of amorphous Al_2O_3 sputtered onto it to reduce scattering and prevent damage and edge rounding during polishing. The final length of the waveguide following polishing was 6 mm.

Light was coupled into this waveguide, of NA = 0.34, and losses determined by comparing the power going into the waveguide and the power emerging from it. The upper limit for the waveguide loss was determined to be 4.8 dB, taking into account the Fresnel reflections and transmission of the output coupling objective. These losses are mainly attributed to scattering in the waveguide due to small imperfections in the crystal and particulates of micron scale generated by the ablation process.

The end facets of the waveguide were coated for laser experiments; the incoupling facet with a highly reflective coating for 1000 - 1100 nm and about 1 - 2% transmission for this wavelength range on the outcoupling facet. The results achieved by pumping this waveguide with 820 nm light from a Ti:Al_2O_3 laser were a maximum output power of 1.8 mW for 370 mW of pump power, and a slope efficiency of 0.5% with respect to the incident pump power. The absorbed power could not be calculated as the waveguide losses were high and the coupling efficiency was unknown. The laser threshold was very low due to the tight confinement and could not be determined reliably from the input-output curve, but is reported to have been found to be about 0.8 mW. The laser spectrum revealed that lasing occurred at 1075 nm and 1079 nm simultaneously. The main requirement for improved performance of such lasers is improved crystal growth to provide higher quality, lower loss waveguides, but also using higher output coupling to achieve higher output powers and slope efficiencies.

A second report of a rare-earth doped sesquioxide waveguide laser followed shortly after the first, this time with Yb^{3+} as the dopant of choice [53]. The Yb(3%):(Gd, Lu)$_2O_3$ was also grown epitaxially by PLD, and again lattice-matched to a Y_2O_3 substrate, resulting in a 2 μm-thick film with an almost atomically flat surface. Reactive ion etching was used to form rib-channel waveguides with a depth of 725 nm and widths of 4 μm, which simulations show to support two transverse modes at the laser wavelength of 796.8 nm. The waveguide length was reduced to 6 mm following polishing.

As in the previous report, this waveguide also had an NA = 0.34 and the waveguide loss was determined via transmission measurements. A transmission of 20%, following corrections for Fresnel reflections and losses incurred from the objectives used, corresponds to a loss of 7.0 dB from the coupling and propagation through the waveguide. The fluorescence lifetime was measured,

using a Yb(1%) doped sample to supress reabsoprtion, and found to be 680 μs, a little shorter than that of Y_2O_3 at 790 μs. The emission spectra of these two Yb-doped materials are almost identical due to them having the same lattice constant and almost identical crystal field.

For the laser experiments with this Yb(3%):(Gd, Lu)$_2O_3$ sample, the incoupling facet had a coating applied that had 50% transmission for the Ti:Al_2O_3 pump wavelength of 905 nm used and about 0 - 1 % transmission for 950 - 1100 nm. The outcoupling facet was left uncoated to make use of the Fresnel reflections of about 10%, meaning 90% would be outcoupled. The laser oscillated on several modes simultaneously, around 976.8 nm, and had a maximum output of 12 mW for 200 mW of pump power, a threshold of 17 mW and 6.7% slope efficiency with respect to the input power. The significantly higher threshold is due to the quasi-three-level nature of the Yb^{3+} ion that exhibits reabsorption at the laser wavelength, compared to the four-level system of Nd which does not, as well as the high output coupling losses of 90%. This laser displayed a diffraction-limited beam and was the first Yb-doped sesquioxide waveguide laser. Further reports of sesquioxide waveguide lasers are found in the experimental chapters of this thesis, which are mostly Yb-doped waveguides operating at significantly higher powers.

2.7 Conclusions

This chapter has given an overview of alternative techniques for thin film deposition, waveguide fabrication and methods of crystal growth, focussing on sesquioxide growth. PLD comes under the broader heading of PVD and, as seen throughout the rest of this thesis, allows thin waveguiding crystalline films to be manufactured. Plasma-assisted magnetron sputtering has been used for depositing thin films of sesquioxides but not of sufficiently high optical quality for use as laser crystals. Use of evaporation is limited to materials that vaporise at fairly low temperatures so is obviously unsuitable for the sesquioxides with their high melting points. Although MBE is used to produce high quality films, it requires UHV, is very expensive and deposition rates acheived are low. LPE is a widely used technique for achieving high quality crystalline layers on substrates, including the possibility of manufacturing multilayers, and coatings on a surface of any shape. However, this is not a viable technique for sesquioxides due to their high melting points. CVD can also be used to coat shaped surfaces as well as flat ones, but involves the use of chemical precursors and generates by-products, both of which can be toxic, explosive and corrosive, so often is not a

good choice.

Various crystal growth techniques, many of which have been modified for growth of sesquioxides, have been described in this chapter along with an indication of the crystal sizes achievable in each case. The N-K, Czochralski, Bridgman and μm-PD methods all require a melt of material in a crucible and have provided crystals with single crystalline domains of order mm^3. The HEM, modified from the Bridgman technique, also requires a crucible of molten material to begin with, but growth is initiated by a seed at the bottom of the crucible and crystal growth continues due to cooling by a variable gas flow. Secondary nucleation at crucible walls is prevented by keeping them at constant temperature until the crystal growth is almost complete. High quality, low strain material with crystalline domains of order cm^3 have been acheived using this method.

The flux method has allowed sesquioxide growth at 1200°C, about half the melting point of the sesquioxides, by use of a non-toxic solvent, so is a promising option that avoids the temperatures high enough to form sesquioxide melts. TSSG combines the flux method with the Czochralski technique to pull crystals from a high temperature flux.

Finally, the floating zone and LHPG techniques are crucible-free methods that use lasers to create a molten zone which converts rods of material to single crystal as it is moved through the heated area or has a fibre drawn from the molten material, respectively, and are both limited to producing mm-size crystals. The large temperature gradients present in the floating zone method tend to result in strained crystals that often crack, and the LHPG method has allowed rapid growth of high purity, good quality fibres with a simple system that does not require rotation as the crystal is pulled.

High power outputs of up to ∼300 W have been achieved from sesquioxide crystals in bulk and thin disk configurations with high efficiencies (up to 74% optical-to-optical and slope of 88%). This demonstrates the excellent capabilities of sesquioxides as laser hosts. However, very minimal studies of sesquioxide waveguides have been reported. The work undertaken in this project expands the use of sesquioxides as laser hosts to the planar waveguide configuration, which have the potential to also provide high power outputs but in smaller, simpler systems.

Chapter 3

Theory

3.1 Introduction

This chapter explores the theory behind the work carried out for this thesis. Pulsed laser deposition has various parts to consider, from laser ablation, through plume dynamics and target modification, to crystal growth of the deposited material. Waveguide theory is then considered, before moving on to various aspects of laser theory. Details of the dopant ions used for the samples in this thesis are given, including their electronic structure and uses of the wavelengths they can produce. The parameters affecting laser threshold and the slope efficiency are studied, and lastly a look at Q-switching for pulsed laser operation.

3.2 Pulsed Laser Deposition Theory

3.2.1 Laser Ablation

Various mechanisms can lead to particle emission when a surface is bombarded by incident electrons, ions or photons. The main sputtering mechanisms that occur are outlined below, with particular focus on the effects of laser pulses.

- **Thermal**

  In thermal ablation the laser pulse causes the irradiated area of the target to be heated and vapourised, forming a plume of ejected material, as shown by the diagrams in figure 3.1. This process leaves structures on the target surface where it has been melted and re-solidified,

usually in the form of ridges or droplets (see section 3.2.4). Thermal ablation requires the target material to absorb light at the laser wavelength being used for ablation, and then the heated area is dependant on the absorption and diffusion lengths, L_a and L_d, respectively, the equations for which are as follows [54, 55]:

$$L_a = \frac{1}{\alpha} \tag{3.1}$$

where α is the absorption coefficient of the target material at the laser wavelength and

$$L_d = 2\sqrt{(\kappa\tau_d)} \tag{3.2}$$

where κ is the thermal diffusivity of the target material (in m^2/s) and τ_d is the laser pulse duration. This ablation process is more effective when the absorption length, L_a, is short so that the energy is absorbed in a tightly confined area near the target surface and the thermal diffusivity, κ, is low so that energy is not wasted due to being conducted away from the ablation site. When the absorption length is greater than the diffusion length, the depth of material ablated can be described by equation 3.3:

$$d_a = \frac{1}{\alpha} ln \left| \frac{F}{F_{th}} \right| \tag{3.3}$$

where F and F_{th} are the laser fluence and threshold ablation fluence, respectively.

Considering the above, desirable properties of a laser to be used for ablation are short pulses, minimising the time available for the target material to react to the pulse and therefore reducing the heat diffusion, and a short operating wavelength as shorter wavelengths have a smaller absorption depth in most materials. Nanosecond UV lasers such as excimer lasers are therefore a common choice to use for ablation. A KrF excimer laser with a pulse duration of 20 ns and operating wavelength of 248 nm was used for the work in this thesis.

- **Electronic**

  On very short time scales, such as when femtosecond pulses are used, electronic effects are dominant. Multi-photon absorption causes direct ionization of target atoms, and the free electrons produced can be accelerated by repulsion from bound electrons to interact with

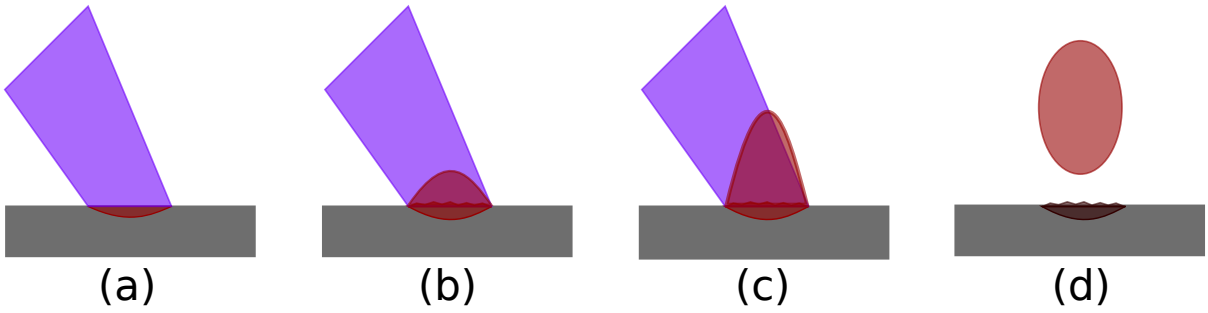

Figure 3.1: Schematic representation of the ablation process. (a) the incident laser beam strikes the target and heating begins, (b) the energy from the laser pulse is absorbed further and the target material begins to vapourise, (c) towards the end of the pulse the vapourised material expands further, (d) the laser pulse has ended and the vapourised material travels away from the target, leaving the surface modified.

more atoms and cause further ionisation, and this is referred to as avalanche ionisation. Another electronic process leading to the release of energetic ions is Coulomb explosion, where a build up of positive charge on the target surface, due to electrons escaping, results in Coulomb repulsion of ions away from the target on a very short time scale of ∼100 fs [56].

- **Collisional**

  Collisional sputtering is associated with particles transferring momentum to a target and causing material to be ejected. This, therefore, is not a direct mechanism in laser ablation, but occurs due to backscattered ions from the ejected plume of material bombarding the target surface [57].

- **Exfoliational**

  Exfoliational sputtering is caused by repeated thermal shock to the target surface, causing flakes to detach. This effect is more prominent when using target materials with high melting points, such as the sesquioxides used in this project, as damage caused by thermal shock is not relaxed due to melting and eventually flakes break off [57].

- **Hydrodynamic**

  Transient melting caused by laser pulses allow droplets to form on the target surface, which

are then expelled due to subsequent laser pulses. This effect doesn't occur for sputtering via particle bombardment [57].

3.2.2 Plume Dynamics

The direction and angular spread of the plume of material ejected from a target during PLD is important to study to be able to obtain films uniform in thickness and composition. These properties of the plume are analysed by methods that fit into two categories, namely probe or film-based measurement techniques. Probe-based techniques involve direct measurement of the plume by use of a small-area detector in the setup, which would disrupt any actual film growth. Film-based techniques are effective and far simpler. Following deposition, thin films can be analysed using tools such as a surface profilometer (see section 4.3.2) to measure the thickness variation of the deposited layer across the substrate and energy-dispersive x-ray analysis (EDX) for compositional variation.

Parameters that have been considered when studying the plume generated by a laser pulse include the laser parameters of wavelength, fluence and pulse length, as well as geometrical considerations of the setup such as the size and aspect ratio of the laser spot, and the target-substrate distance and orientation, as well as the background gas pressure. The main, most consistent findings have been from looking at how the shape of the plume changes with laser spot size. Smaller spot sizes give a wider angular distribution of ejected material, and as the spot size is increased, with the fluence kept constant, the plume becomes more peaked, as illustrated in figure 3.2. Therefore, a larger incident laser spot size leads to a higher deposition rate when the substrate is positioned perpendicular to the plume axis.

The axis of the ablated plume material is oriented normal to the target surface for normal laser incidence. In PLD the incident laser pulse usually approaches the target material at an angle to its normal to allow for a substrate to be positioned opposite the target. However, the plume axis is often normal to the target surface, independent of the angle of incidence (at least up to an angle of 45° to the target normal). The direction of the plume axis has been reported to deviate from the target normal for some materials ablated at a non-normal angle, particularly when high ablation fluences (>100 J/ cm^2) were employed [58].

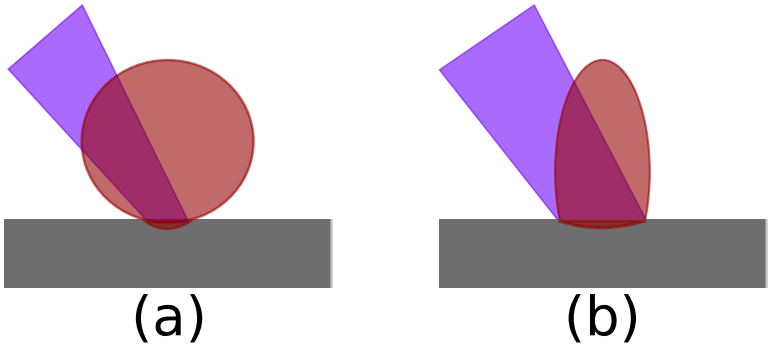

Figure 3.2: Schematic of how the ejected plume of material changes with the ablating laser spot size: (a) a small laser spot incident on the target provides a widely spread plume, (b) a larger laser spot causes the ejected material to form a more directional plume.

3.2.3 Crystal Growth

3.2.3.1 Growth Mechanisms

Crystalline growth via PLD is affected by many parameters, meaning there are lots of options to change to improve sample quality, but also that finding the best conditions can be a long process. The growth mode that occurs in PLD as the plume of material reaches the substrate surface is dependant on the energy available, and therefore on the properties of the plume of ejected material and the substrate: the material, its cut, roughness and the temperature it is heated to. The background gas pressure and laser ablation spot size and fluence affect the angular distribution of the plume and its kinetics, and therefore the deposition rate, stoichiometry, stress and crystallinity of the deposited film. The presence of particulates also affects the properties of PLD-grown thin films, and the processes by which they occur are discussed in section 3.2.4. The nucleation and growth of thin films can be separated into three conventional modes of growth:

- **Three-dimensional island growth (Volmer-Weber)** Deposited material forms clusters on the substrate surface and outwards from there, so predominantly by the processes of atom deposition on cluster and atom diffusion to cluster, as shown in figure 3.3.

- **Two-dimensional full-monolayer growth (Frank-van der Merwe)** The film thickness builds up monolayer by monolayer.

- **Two-dimensional growth of full monolayers followed by three-dimensional island growth (Stranski-Krastanov)** Growth begins with the formation of monolayers on the substrate and then clusters begin to form on the surface.

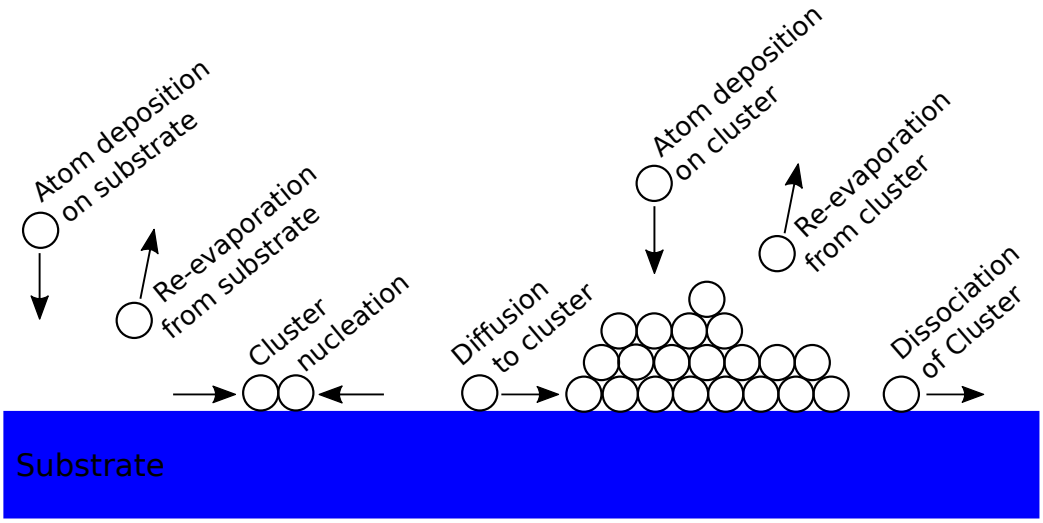

Figure 3.3: Different processes by which nucleation can occur: atom deposition on substrate, re-evaporation from substrate, cluster nucleation, diffusion to cluster, atom deposition to cluster, re-evaporation from cluster and dissociation of cluster [59].

The dominant processes for thin film growth will depend on the parameters mentioned above, affecting the available energy. Substrates are usually heated in PLD to encourage crystalline growth. While the formation of a film isn't slowed by low temperature, the formation of crystalline material can be; the lower the temperature the more likely the deposited material is to be in an amorphous state. However, high temperatures can, in some cases, lead to some species being boiled off from the substrate surface and therefore lead to films deficient in that species. Deposited material can also be removed again due to sputtering effects of the incident material from the plume bombarding the growing thin film.

3.2.3.2 Crystal Defects

Crystal defects can be categorised into three different types [60]:

- **Point defects** include lattice vacancies and interstitials, meaning that there is either an atom missing from the structure or an extra atom where it should not be. Interstitial atoms

can either be self-interstitials, where the extra atom is of the same species as the atoms forming the lattice, or interstitial impurities, which are other atoms that have made their way into the structure. Both vacancies and interstitials cause a distortion in the lattice, the degree of which is determined by the comparative size of the missing or extra atom with respect to its surroundings.

- **Linear defects** are groups of atoms in irregular positions, which distort the crystal lattice. These defects are referred to as dislocations and can be described by a group of atoms shifting with respect to neighbouring atoms.

- **Planar defects** occur between homogeneous regions of the material, as found in polycrystalline material at the grain boundaries. Stacking faults can also occur within crystals, where there's an error between planes.

  Defects are an inherent property of crystalline materials and play a strong role in their properties, which can be both positive and negative. For example, diffusion in crystals only occurs due to the presence of vacancies, the number of which increase exponentially with absolute temperature as more energy is available for atoms to move from their equilibrium position. The structure of a material and the ease of dislocation formation has a strong role in whether a material is ductile or brittle. Dislocations tend to occur between densest planes, where the least movement is required for atoms to reach a new similar site. There are lots of dense planes in metals with face-centred-cubic (FCC) and body-centred-cubic (BCC) lattices, which makes them highly ductile, meaning they will deform significantly before breaking. In contrast, ionically bonded materials require ions to move past repulsive sites to relocate to a similar position to the one it came from, which requires more energy, so these materials tend to be brittle instead. Similarly, covalently bonded materials are also brittle due to their lower density and, therefore, lack dense planes along which dislocations can occur.

  Perhaps most relevant to this work is the effect of grain boundaries in crystals, which can cause scattering within materials. This scattering in otherwise transparent materials can make them appear cloudy or even opaque, which is obviously detrimental for the propagation of light. Grain boundaries also affect the mechanical properties of materials due to limiting the size and motion of dislocations that can occur; smaller grains with more boundaries strengthens materials. In general, for crystals grown from the melt the size of the crystal

grains can be controlled via the cooling rate - rapid cooling produces crystals with small grains and slower cooling leads to larger grains, and even single crystal growth.

As discussed in section 2.5, the sesquioxides Y_2O_3, Lu_2O_3 and Sc_2O_3 have a BCC structure. This means they have dense planes along which dislocations can occur, making them resistant to breaking. Evidence of crystal grain boundaries can be seen in the samples grown in this project via SEM images of both polished end facets and sample surfaces, and in some cases by eye, where the deposited film appears cloudy. Such cloudy samples are discarded as they scatter too much light to be useful as waveguides.

3.2.3.3 Lattice Matching

A small lattice mismatch between a substrate and the film being deposited is always desirable. Epitaxial growth will occur where possible and it has been reported that for a lattice mismatch of less than ∼9% the inital growth, or very thin films, will be elastically strained such that the interatomic spacing of the growing crystal matches that of the substrate [61], which is illustrated in figure 3.4. As the film thickness is increased, the elastic strain energy also increases until misfit dislocations form to relieve the strain. These dislocations relax the crystal lattice and allow subsequent growth to occur with the usual lattice constant of the material. For larger lattice mismatches, more dislocations occur and are more likely to continue throughout the deposited crystal, decreasing its quality.

Lattice matching can be achieved by controlling the composition of materials. Epitaxial growth can also be achieved by a match between different crystal orientations and/or materials having lattice constants such that one is, more or less, an integer multiple of the others, known as harmonic lattice matching, as shown in figure 3.4.

The lattice mismatch, *f*, between a deposited film and a substrate can be calculated using the equation:

$$f = (a_0(s) - a_0(f))/a_0(f) \tag{3.4}$$

where a_0(s) and a_0(*f*) are the unstrained lattice parameters of the substrate and film, respectively. If *f* is positive it implies that the layers are stretched in tension and if *f* is negative it means there is compression of the layers. The growth parameters of a film also have an affect on the stress in deposited thin films, with the substrate temperature and ablation fluence being found to be the most significant in the case of PLD [62]. The strain in the grown crystal due to lattice mismatch can

cause a curvature of the sample, as can strain due to a difference in thermal expansion coefficent between the substrate and deposited film.

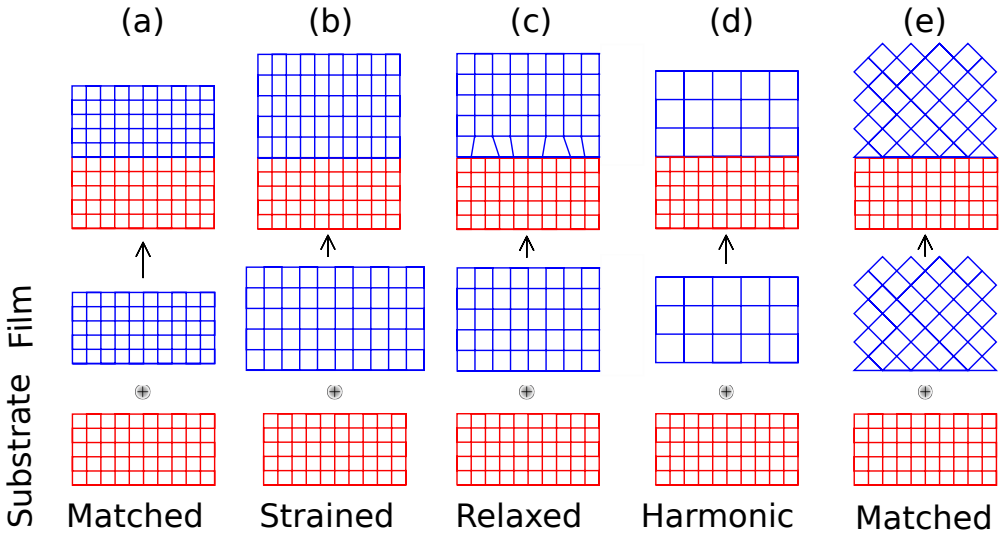

Figure 3.4: Ways lattice matching can occur, from left: (a) substrate and film lattice constants are the same and match; (b) film lattice constant is different to that of the substrate so film grows strained to compensate; (c) film lattice constant is different to that of the substrate and grown crystal relaxes after an initial layer; (d) the lattice constant of the grown film is a multiple of the substrate lattice constant so matches harmonically; (e) the film grows in a different orientation to the substrate that matches the two.

3.2.3.4 Thermal Expansion Coefficient Mismatch

As substrates are heated during depositions to provide energy for crystal growth, the amount the film and substrate materials contract on cooling is a factor that needs to be considered. Films that are grown heteroepitaxially and unstrained on a heated substrate may become strained on cooling. If the thermal expansion coefficient of the substrate is larger than that of the film, $\alpha_s > \alpha_f$, then the strain is compressive, or if the film has the larger thermal expansion coefficient, $\alpha_f > \alpha_s$, then the strain is tensile [55], as depicted in figure 3.5. The effect the thermal expansion coefficient mismatch has on the final sample falls into a range of possibilities; thinner films may be able to flex sufficiently, whereas thicker films are at greater risk of cracking or delamination from the substrate. The layer thickness at which the elasticity in the film allows bending without cracking

for a GGG on YAG is a film approaching 5% of the substrate thickness [62]. For PLD-grown GGG on YAG substrates the limit of how thick films could be grown without cracking or delamination during either cooling or post-processing of the sample (such as during polishing) was found to be $\sim$40 μm [62].

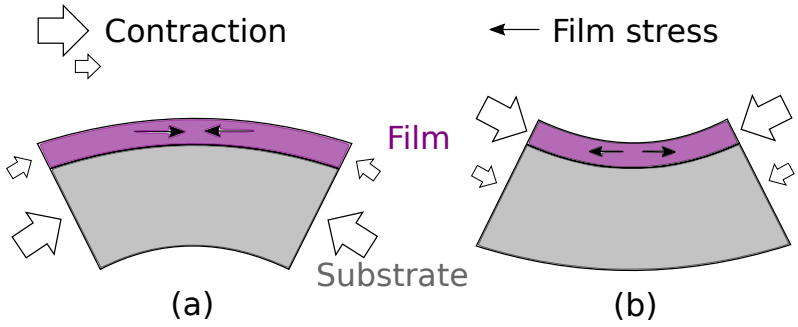

Figure 3.5: A schematic of how thermal mismatch affects samples on cooling [55]. (a) The substrate contracts more than the film, $\alpha_{substrate} > \alpha_{film}$ causing compressive strain in the film, (b) the film contracts more than the substrate, $\alpha_{film} > \alpha_{substrate}$, causing tensile strain in the film.

3.2.4 Target Modification and Particulates

While PLD is a versatile technique with many positive attributes, its one major drawback is what is referrred to as "splashing". The repetitive laser ablation of a target surface leads to it being modified, and larger, micron-sized, particulates are ejected into the plume along with atomic and molecular-sized constituents. These particulates can cause defects in crystal growth and scattering centres, which is detrimental to their use as waveguides, and can also lower the damage threshold of materials. The mechanisms by which splashing occurs are outlined below [2]:

- **Subsurface boiling**

  Subsurface boiling occurs if the time required to transfer heat energy into the target material is shorter than that needed to evaporate the surface layer. This leads to subsurface boiling, where material below the surface is superheated before the surface is in vapour phase, causing micron-sized globules to be ejected into the plume. However, higher power densities than those usually employed for PLD are required for this effect to occur, meaning it is an insignificant cause of splashing compared to the two following mechanisms.

- **Expulsion**

  The liquid layer left on the target surface following an ejected pulse experiences recoil pressure from the shock wave of the plume, which can cause expulsion of micron-sized globules that may end up in the growing film. This effect can be reduced by lowering the ablation fluence.

- **Exfoliation**

  Repetitive laser ablation leaves the target surface eroded, particularly for sintered ceramic targets (such as those used throughout the work in this thesis). Features of a few microns in dimension are formed and are broken off due to the thermal shock of laser irradiation. These microstructres are carried towards the substrate in the plume of material and are incorporated into the growing film. These particulates vary in size and shape depending on the form of the microstructures; for example, needle-shaped microstructures pointing towards the incoming laser beam have been reported [63], as well as ridges. More information on target modification, including the formation of needles/ cones and ridges, and the variation in microstructures seen over an ablated target surface can be found in [55, 57, 64].

These mechanisms are all affected by the ablation fluence used. Subsurface boiling is non-existent unless particularly high power density is used, while expulsion by recoil pressure from the shock wave of the plume is decreased by lowering the ablation fluence, and the rate of exfoliation and size of particulates formed by this process is also affected. While the particulate density in a film can therefore be reduced by decreasing the ablation fluence, this is at the expense of the deposition rate.

Various methods have been trialled to decrease the number of particulates that end up in pulsed-laser-deposited thin films. Details of some of these methods are provided below, including some variations that fit into each category. These are:

- **Mechanical particle filters**

  Mechanical particle filters act as velocity selectors, removing slow-moving particulates from the plume of material. The smaller, faster moving contituents are allowed to continue to the substrate to be deposited, while larger, slower particles are blocked. Setups have been trialled with multiple fin rotary velocity filters and with a mechanical shutter synchronzied to the plume of ejected material. The limiting factor of this method is the rotor frequency/

shutter speed compared with the particulate velocity. While mechanical particle filters are effective devices, they are bulky and lower the deposition rate.

- **Plume manipulation**

  The ejected plume of material can be manipulated in a number of innovative ways to attempt to diminish the number of particles reaching the growing film, including modifying the geometry of the setup. One method employed has been to have two intersecting synchronized beams [65]. The high density of molecular and atomic species in the plumes interact and scatter along a new direction, bisecting the initial trajectories. The substrate to deposit on was therefore positioned along a line that bisects the axes of the two plumes. Micron-sized particulates would be present in a much lower density and mostly interact with the lighter plume constituents, rather than other similar sized particulates, meaning they would not be redirected towards the substrate. A collimator was placed in front of the substrate to allow through the redirected particles and block others.

  Another configuration used, with just one plume, was to position the substrate to grow on at a wide angle from the axis normal to the target surface. This setup takes advantage of the angular distribution of the different sized species that form the plume. Smaller, lighter components are ejected over a wider angle than slower, heavier, micron-sized particulates, which travel more directionally along and close to the normal from the target. Growth at a wide angle therefore produces films with lower particulate density, but also significantly lowers the growth rate. This method may also cause non-stoichiometric transfer of material for multicomponent targets.

  The usual PLD setup can also undergo plume modification by other additions to the setup, such as a pulsed gas jet or a second laser pulse to interact with the plume. The gas jet or laser pulse can be synchronized with the laser ablation process to push the particulates out of the plume of material, so that they don't reach the growing film [66, 67]. The timing of the pulse is critical to the effectiveness of this technique.

- **Target surface improvement**

  Ideally, targets being ablated should be high density and have a smooth surface to minimize splashing and therefore the occurence of particulates in grown films. One method employed for Ge deposition was to use a molten Ge target. Heating the target to just above its

melting point, where thermal evaporation is negligible, caused the target surface to remain smooth and therefore eliminate the problem of particulate formation due to exfoliation of microfeatures. Unfortunately, this isn't possible with the majority of materials.

A method of target surface improvement that is simple is to polish the surface prior to each deposition. This process is fairly time-consuming, but effective in minimising particulates. Target reconditioning was routinely used as a means to minimise particulates in this work.

3.2.5 Variables

This section on PLD theory concludes with an overview of the main parameters that can be changed in a PLD setup. Firstly, different lasers can be employed for the ablation process but all the work presented here has been performed using an excimer laser filled with KrF. The angle of incidence of the laser pulses on the target surface is kept constant, and would be impossible to adjust much in the setup used due to the fixed position of the windows to the deposition chamber. The ablation fluence, however, is changeable and set to a chosen value for each deposition; the spot size is fairly constant and the fluence is therefore adjusted by changing the pulse energy, which is measured prior to each deposition. The substrate is always positioned as parallel as possible to the target surface at a fixed distance between the two of $\sim$7 cm. While a few different target materials are used in this project, all targets used are sintered ceramics (single crystal targets are also sometimes used for PLD). As the target surface is ablated away and then reconditioned, it gradually gets thinner, marginally changing the target to substrate distance. As well as the laser fluence, the other variables adjusted in this work were the substrate temperature and the background gas, which was always oxygen for work in this thesis, and its pressure. These three variables, for a given target material, are likely to make the most difference to the deposited film, and are easily changed one at a time to analyse trends in the effects, as in chapter 5. A much more complete study of the effects of changing PLD parameters could be carried out, but would become a lengthy process.

3.3 Waveguide Theory

Planar waveguides are structures consisting of a layer of higher refractive index material than the surrounding media, thereby providing the ability to guide light in one dimension by total

internal reflection. These structures can be made to lase if the guiding layer is doped with active ions, and designed and manufactured to have particular acceptance angles and thicknesses, and therefore number of modes, M, supported. For symmetric waveguides, this can be calculated as follows [74],

$$M = \frac{2d_{WG}}{\lambda} NA \tag{3.5}$$

where d_{WG} is the waveguide thickness, λ is the wavelength of the propagating light and NA is the numerical aperture, defined as

$$NA = \sqrt{n_2^2 - n_1^2} = n_0 \sin\theta_{max} \tag{3.6}$$

where n_1 and n_2 are the refractive indices of the cladding and waveguide core respectively, and n_0 is the refractive index of the medium surrounding the structure. This determines the maximum acceptance angle, θ_{max}, at which light can enter the waveguide. Multilayer structures provide the ability to engineer waveguides to have a particular NA by selection of the materials used for each layer. The NA and thickness of a waveguide is important for efficient launching of pump light into the waveguide core.

The result of equation 3.5 should be rounded up to the nearest integer value. Therefore, if $(2d_{WG}/\lambda)NA < 1$ the waveguide will only support a single mode. While high NA and thicker wavguides are preferable for easy launching of pump light they also promote multimode operation and lower output beam quality. Multilayer structures can be manufactured to allow single-mode operation of thicker structures. A cladding pumping scheme can be used, where light is launched into the cladding of the waveguide and only absorbed in the doped core region. It has been demonstrated, by Bhutta et al, that the spatial dopant profile in a waveguide affects the allowed modes and, in a step function profile, preferential selection of the fundamental mode can be achieved with a central dopant profile of up to 60% of the waveguide thickness [13]. A schematic of this type of structure is shown in figure 3.6, and results from such a multilayer sample can be found in chapter 8.

An important characteristic of a waveguide is its loss. Various methods of loss measurement have been developed, each with advantages and limitations depending on the geometry of the waveguide and the material it's made from. A few commonly used methods are outlined below [75], and the methods used in this thesis are highlighted.

A simple method of obtaining the propagation loss coefficient, α, through a waveguide is using the cut-back method, where single pass transmission measurements are taken for the waveguide

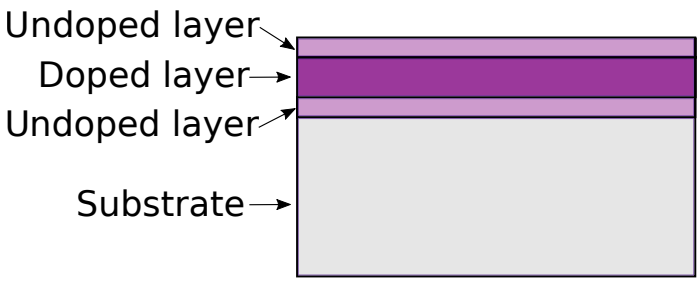

Figure 3.6: Schematic of a multilayer waveguide structure, with the doped region of the deposited layer constituting half of the total waveguide thickness.

at decreasing lengths. The power transmission ratio is given by

$$\frac{P(x)}{P_0} = 10^{\frac{-\alpha x}{10}} \tag{3.7}$$

where P_0 is the incoupled power, taken to remain constant, $P(x)$ is the out-coupled power for the waveguide of length x. This can be written as

$$log[P(x)] = log(P_0) - \left(\frac{\alpha}{10}\right) x. \tag{3.8}$$

By plotting the outcoupled power as a function of x the propagation loss coefficient can be determined from the gradient. This method is useful to apply to fibers that are relatively long and easy to cleave, which can be done without touching the input coupling arrangement. Planar waveguides, however, require removal from the setup to be cut and re-polished, which makes the process lengthy and less reliable due to coupling efficiency variation each time the waveguide is put back into the setup. In addition to this, the nature of this method is destructive and therefore no good when futher use of the waveguide may be desired.

Similarly, the sliding prism method [76] provides a means of measuring the transmission loss through different lengths of a waveguide. A pair of prisms, of higher refractive index than the waveguide, are clamped to the surface of a waveguide and used as input and output couplers.The incoupling prism is kept fixed and the output coupling prism moved along the waveguide to provide the different effective waveguide lengths for the loss measurements. The propagation loss coefficient can then be determined from a plot of the outcoupled power against the effective waveguide length, as above. While less destructive than the cut-back method, some damage can be incurred to the waveguide surface from clamping the prisms to it. The sliding prism method has limitations

concerning the sample size that can be used, and the waveguide surface needs to be flat, so may not work effectively on PLD-grown waveguide samples.

Streak imaging [77,78] determines the loss of a waveguide by analysing the intensity of the laser light as it propagates through a waveguide. This can either be done by using an optical fibre to collect light at various positions along the streak or by using a CCD camera to image it and then analyse it. This technique requires the scattering centres in the waveguide to be homogeneously distributed, which isn't necessarily the case in PLD-grown samples. One problem this technique suffers from is that light coupled into the substrate rather than the waveguide is also detected once scattered, giving incorrect measurements. Higher optical quality materials with fewer scattering centres have lower streak intensities making it difficult to detect and accurately measure the change in intensity as light propagates through such guides, meaning this technique is less precise for lower loss waveguides.

To measure the losses of the PLD-grown waveguides in this project a simple insertion loss measurement is taken, with a setup resembling that of the cut-back method (but without cutting the samples back for multiple measurements), allowing the loss in dB to be determined. Details of this method can be found in section 4.5.

There are also methods of determining loss from laser-based experiments. The Findlay-Clay method [79] uses the dependancy of the absorbed pump power threshold for lasing, P_{th}, on the level of output coupling for 4-level laser systems, where the relation is as follows:

$$P_{th} = K[(2\alpha_L l) - ln(R_1 R_2)] \tag{3.9}$$

where α_L is the propagation loss coefficient, l is the waveguide length and R_1 and R_2 are the intensity reflectivities of the input and output coupling mirrors, respectively. K is a constant given by

$$K = \frac{\pi h v_p}{4\tau\sigma_e}\sqrt{w_{lx}^2 + w_{px}^2}\sqrt{w_{ly}^2 + w_{py}^2} \tag{3.10}$$

for a longitudinally pumped sytem, where h is Planck's constant, v_p is the frequency of the pump light, and the w values correspond to the $1/e^2$ radii of the intensity of the pump (p) and laser (l) modes in the horizontal (x) and vertical (y) directions, respectively. τ is the fluorescence lifetime and σ_e is the emission cross-section. These equations can be compared with equation 3.16 in section 3.4.3, which is for incident pump power threshold so has a modification for the pump power absorbed and also an additional term to account for reabsorption losses in a quasi-three-level system.

For the Findlay-Clay method, $P_{th}/2l$ is plotted against -ln(R_1R_2)/2l, giving a straight line, from which the propagation loss coefficient, α_L, can be determined. An upper limit for the propagation loss, L, can then be calculated using equations

$$L\,[dB] = 10log_{10}\left[\frac{I_{out}}{I_{in}}\right] \tag{3.11}$$

in dB, where I_{in} is the input intensity and $I_{out} = I_{in}$exp(-αl), is the output intensity of the waveguide, or directly in dB/cm using the equation

$$L\left[\frac{dB}{cm}\right] = 10log_{10}[exp(-\alpha_L)] \tag{3.12}$$

where the value of α_L has been taken from the Findlay-Clay plot [75].

Another means of deducing the loss of a laser material is to see how the slope efficiency acheiveable for cw operation changes with output coupling. The Caird method [82] uses the inverse linear relationship between the slope efficiency η_s, and output coupling fraction, C, as follows:

$$\frac{1}{\eta_s} = \frac{1}{\eta_0}\left(1 + \frac{L}{C}\right) \tag{3.13}$$

where L is cavity loss per pass, and

$$\eta_0 = \eta_p.\frac{\lambda_p}{\lambda_0}.\frac{\sigma_{eff}}{\sigma_e} \tag{3.14}$$

is the limiting slope efficiency, which is achieveable in the absence of passive losses. η_p is the pumping efficiency, λ_p and λ_o are the pump and output wavelengths, respectively, σ_e is the emission cross section and σ_{eff} is the effective gain cross-section, given by

$$\sigma_{eff} = \sigma_e - \sigma_{ea} \tag{3.15}$$

where σ_{ea} is the excited state absorption cross section. Using a linear fit to points on a graph of inverse slope efficiency against inverse output coupling the value of the limiting slope efficiency, η_0 can be determined by extrapolating to the point where the inverse output coupling is equal to zero and the gradient represents the passive loss, L. One of the benefits of this method is that the losses from excited state absorption and passive losses can be separated. This is important as the excited state absorption is intrinsic to the material whereas the passive losses, ie. losses due to scattering, can be minimised by improved crystal growth, which is important here where the aim is to improve sesquioxide crystal growth by PLD to achieve more efficient, higher power lasers.

3.4 Laser Theory

3.4.1 Three- and four-level lasers

Laser operation arises due to stimulated emission, for which a gain medium is needed where a population inversion can be achieved. There are different operational laser schemes, all of which have an upper and lower laser level within the structure of the active ions, that have different characteristics, such as the threshold pump power required to achieve laser action. These schemes can be split into three-level and four-level lasers systems, however, in practice, most lasers are something between the two and referred to as quasi-three-level (or quasi-four-level) lasers. These energy level schemes are illustrated in figure 3.7 [80, 81].

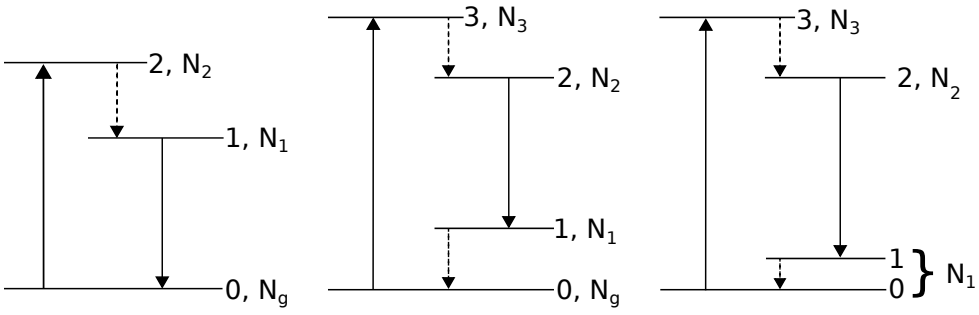

Figure 3.7: From left, three-, four- and quasi-three-level laser schematics.

3.4.1.1 Three-level lasers

Three-level lasers consist of a ground state, which is the lower laser level, an upper laser level and a higher energy level with a short lifetime, labelled 0, 1 and 2 respectively in figure 3.7. Energy is required to pump electrons from the ground state (0) to an energy level above that of the upper laser level. A rapid, usually non-radiative, energy transfer occurs leaving the excited electron in the upper laser level (1). Beyond a threshold pump value, more active laser ions are in this excited state than are in the ground state (half or more are required to be excited), meaning a population inversion is achieved and laser action can begin. In this three-level scheme the threshold pump power is therefore fairly high. The difference in pump energy required to get into the higher excited state (2) and the energy emitted as laser radiation as a result of the transition from the

upper laser level (1) to lower laser level (0) prevents stimulated emission being caused by the pump wavelength.

3.4.1.2 Four-level lasers

Four-level lasers have a lower laser level that is above and separate from the ground state, from which electrons decay rapidly into the ground state, meaning that this lower laser level has negligible population. Having a population of effectively zero in the lower laser level makes it much easier to achieve a population inversion and therefore four-level lasers have lower threshold pump powers than three-level lasers. As shown in figure 3.7, the operation of a four-level laser requires pumping electrons from the ground state to the highest level shown (3), from which they quickly transfer to the upper laser level via a (generally) non-radiative process and create a population inversion. The laser transition occurs between the levels labelled 2 and 1 in figure 3.7 and the lower laser level (1) depopulates to the ground state, ready to absorb pump energy again. This scheme of laser operation therefore also avoids reabsorption of the laser radiation.

3.4.1.3 Quasi-three-level lasers

Quasi-three-level lasers operate in a manner in between that of the three-level and four-level schemes. The lower laser level is an upper manifold of the ground state, or an energy level very close to the ground state, as displayed in figure 3.7. This means that, unlike in the four-level situation, the lower laser level is partially populated. The population of this level is dependent on the thermal equilibrium temperature, and allows reabsorption losses to occur. This intermediate scheme therefore allows a population inversion to be achieved more easily than for three-level lasers, and the threshold to be lower, but with reabsorption losses. As the lower laser level is more populated at higher temperatures, the pump threshold can be lowered by cooling the laser gain medium and making it behave more like a four-level-laser system.

Both the thulium and ytterbium-based lasers reported in the results chapters of this thesis are quasi-three-level laser systems.

3.4.2 Dopants

The dopants used in these studies are ytterbium and thulium, and their properties are discussed below. Laser action in sesquioxides doped with other rare-earth ions have also been reported, such

as with holmium [68], erbium [69] and neodymium [28], as well as co-doping [70]. While these dopants are not studied here, the reports of their usage in the literature makes expansion of these studies to fabricate PLD-grown sesquioxide planar waveguide lasers with a wider range of dopants, and therefore operating wavelengths, promising.

3.4.2.1 Ytterbium

Ytterbium is widely used as a dopant in various host materials for creating lasers. Yb is a trivalent ion that replaces other ions, often yttrium (eg. in YAG), in crystal lattices. Yb^{3+} ions provide quasi-three-level laser systems that typically lase around 1030 nm, where reabsorption losses are prominant. However, there are benefits to the simple electronic structure of Yb, a schematic of which is pictured in figure 3.8 [80], such as the small quantum defect, meaning high efficiency can be acheived, and minimal thermal effects, making Yb^{3+} appealing for high power lasers. In the sesquioxide host lattices, of Y_2O_3, Sc_2O_3 and Lu_2O_3, the absorption of Yb is highest around 976 nm [40], the zero phonon line, and is therefore normally the pump wavelength of choice. High-power laser diodes operating around this wavelength are readily available, with InGaAs-based diode lasers producing kilowatts of pump power. However, these diode lasers have a broad spectral bandwidth of 2-3 nm, which is wider than the absorption bandwidth of the Yb ions, and therefore not all of the energy emitted by them is absorbed. To improve the absorption of these diode laser pump sources they can be stabilised with volume Bragg gratings [73], to achieve bandwidths of less than 1 nm, making them ideal pump sources.

Yb-doped gain media can have relatively high lasing thresholds due to the thermal population of the lower lasing level, but this can be improved upon by cooling the laser crystal, thereby decreasing the population of the lower lasing level and making a population inversion easier to achieve, as in a four-level system. The laser transition that occurs is from the lowest stark level of the upper $^2F_{5/2}$ manifold to one of the upper stark levels of the lower $^2F_{7/2}$ manifold [69]. The highest emission cross-sections for these materials have been reported to be at 1030 nm for Yb:Y_2O_3, 1033 nm for Yb:Lu_2O_3 and 1041 nm for Yb:Sc_2O_3.

Additionally, Yb-doped materials tend to have large gain bandwidths making them suitable for tunable lasers and generation of ultrashort pulses from mode-locked lasers. The relatively long upper level lifetime, of around 850 μs in sesquioxide hosts [40, 69], is also benefical for high power pulse generaion via Q-switching.

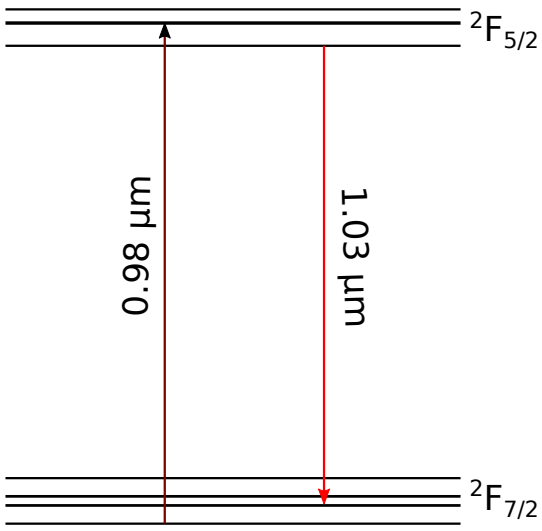

Figure 3.8: Ytterbium energy level diagram [69].

3.4.2.2 Thulium

Thulium is another rare-earth element that can be doped into material to be used as a quasi-three-level laser medium. The energy level structure of Tm^{3+}, shown in figure 3.9, has a strong splitting of the ground state, providing a large gain bandwidth of over 200 nm, and allows for a cross-relaxation pumping mechanism in which two Tm^{3+} ions are left in the upper laser level for every pump photon absorbed, giving a potential quantum efficiency of nearly two (typical for 3 - 12% Tm^{3+}) [71]. Excitation to the $^3H_4$ manifold is achieved with 800 nm pump photons. Cross-relaxation with a neighbouring Tm ion in the ground state ($^3H_6$ manifold) results in two Tm ions in the first excited state, $^3F_4$, which is the upper laser level for the 2 μm transition. This mechanism is dependent on the concentration of thulium ions present in the crystal lattice - fewer Tm^{3+} ions (<3%) result in a weakening of this effect and a larger proportion of fluorescence observed in the visible range [72], while detrimental energy transfer processes increase with the dopant concentration. Using the cross-relaxation process, the theoretical limit of the slope efficiency of a Tm laser is as high as 80%. The $^3F_4$ upper manifold of the Tm^{3+} ion has a lifetime of about 3.5 ms in the sesquioxides, compared with about 10.5 ms in YAG, and peak absorption cross-sections that are about an order of magnitude lower than Yb-doped sesquioxides.

High performance laser diodes are available around 800 nm that can be used as pump sources for the aforementioned Tm transition. The ability to pump with high power combined with a lasing

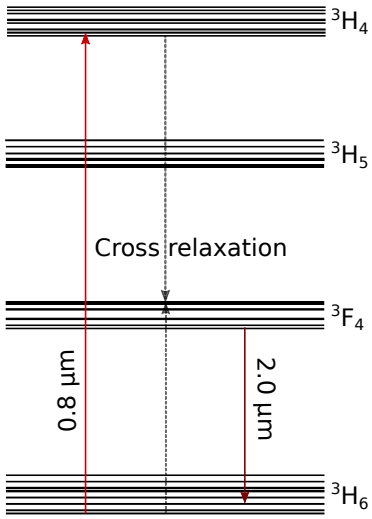

Figure 3.9: Thulium energy level diagram [69].

wavelength in the 2 μm region makes Tm^{3+} a dopant of interest for development of lasers to be used for coherent radar systems, remote sensing and medical applications. Thulium-based lasers that emit at other wavelengths can also be formed with the appropriate dopant concentration, pump scheme and optics. However, the pump scheme detailed above with a laser output around 2 μm is the only one trialled in the work detailed in this thesis.

3.4.3 Waveguide lasers

Waveguides doped with active ions can be used as a laser medium. In this project, planar waveguide lasers (also known as slab lasers) are fabricated using PLD and then have opposing edges polished to become the input and output facets of the waveguide, which can have mirrors brought into close proximity to them to form a quasi-monolithic plane-plane laser cavity. A schematic of such a waveguide is shown in figure 3.10. More details on planar waveguide laser construction can be found in section 4.7. Presented below are equations for the incident pump power required to achieve laser action from a planar waveguide laser and the theoretically obtainable slope efficiency.

The incident threshold pump power for a waveguide laser is [83]

$$P_{pth} = \frac{\pi h v_p \left(w_{px}^2 + w_{lx}^2\right)^{\frac{1}{2}} \left(w_{py}^2 + w_{ly}^2\right)^{\frac{1}{2}}}{4\left(\sigma_e + \sigma_\alpha\right)\tau\left(1 - exp\left(-\alpha_p l\right)\right)} \left(L + T + 2N_1\sigma_\alpha l\right) \tag{3.16}$$

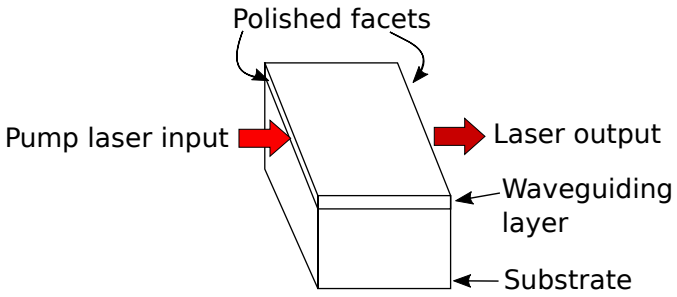

Figure 3.10: Waveguide schematic highlighting the polished facets for the pump laser input and output, where input and output coupling mirrors (not shown) are positioned to form a quasi-monolithic plane-plane laser resonator. Heat leaves the waveguide through the substrate into a heat sink and also radiates into the surrounding air-cladding.

where h is Planck's constant, v_p is the frequency of the pump radiation, w_{px}, w_{lx}, w_{py} amd w_{ly} are the beam spot sizes of the pump and laser modes in the x and y directions in the waveguide, resepectively, where the x direction is in the plane of the waveguide and y is perpendicular to this (leaving z as the propagation direction), σ_e is the effective emission cross-section and σ_α is the effective absorption cross-section of the pump radiation in the laser medium, τ is the upper laser level lifetime, α_p is the absorption coefficient of the pump radiation in the laser medium, l is the crystal length, L is the round-trip loss (equal to $2\alpha_L$l, where α_L is the propagation loss coefficient), T is the output transmission and N_1 is the population density of the lower laser level. Average values through the length of the waveguide should be used in the x direction due to the divergence of the beams in this axis. The last term, $2N_1\sigma_\alpha$l, represents the reabsorption losses in quasi-three-level lasers and (1 - exp(-α_pl)) is the quantum efficiency, η_q, which describes how efficiently pump photons are absorbed.

This equation has been modified from that presented by W. P. Risk [83] to account for the pump and laser beams not necessarily being of equal size in both axes and to use the effective emission and absorption cross-sections, which can be experimentally measured.

The slope efficiency of a laser is an important quantity to be optimised for achieving high-power output and can be described by the following equation [83]:

$$\frac{dP_{out}}{dP_p} = \frac{T}{L+T}\frac{v_L}{v_P}\eta_a\frac{dS}{dF} \tag{3.17}$$

where T/(L+T) is the fraction of photons lost from the cavity through the output coupler, v_L/v_P

represents the quantum defect associated with the conversion of pump photons to laser photons, η_a is the quantum efficiency and dS/dF is the efficiency with which the absorbed pump photons are converted to laser photons and incorporates geometrical factors affecting this conversion, such as the pump and laser beam spatial overlap.

3.4.4 Thin Disk Lasers

The thin disk laser is another kind of laser configuration that has potential to be used in conjunction with PLD-grown samples. A disk-shaped active medium, typically around 100 - 200 μm thick, is coated with a highly reflective layer on the back side of the disk, for both the pump and laser wavelengths, and an anti-reflection coating on the front side, also for both wavelengths. The back side of the disk is soldered to a water-cooled heat sink, as shown in a basic schematic of a thin disk laser in figure 3.11, and the laser cavity formed between the high reflection (HR)-coated back face of the disk and an output coupling mirror positioned opposite the disk.

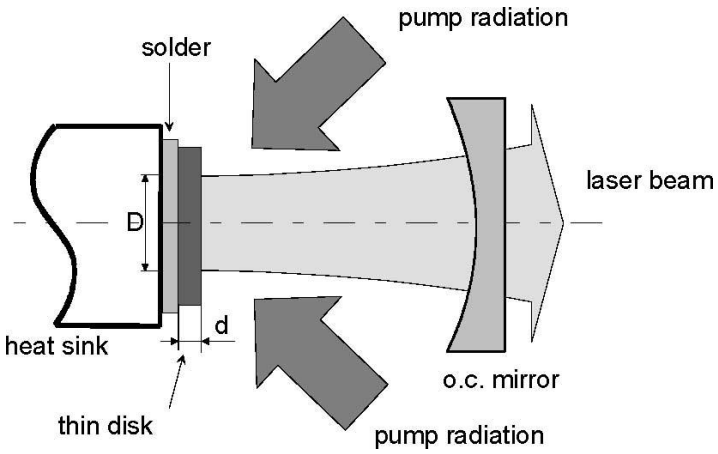

Figure 3.11: Thin disk laser setup, taken from [84]

The thickness required for a thin disk laser depends on what the laser active material is, the doping concentration and the pump design. Obviously a thicker disk and/or higher dopant concentration results in more of the pump light being absorbed, but thinner disks are preferable for heat management. The large surface area to volume ratio of thin disks allows effective heat dissipation into the heat sink. This efficient heat removal minimises temperature gradients and thermal effects such as lensing, compared to that seen in rod lasers, which allows excellent beam quality to be acheived and operation at very high power densities (up to MW/cm^3 absorbed pump

power density).

An elegant solution has been developed to allow for thinner disks and/or a lower dopant concentration to be used while achieving efficient absorption of the pump. In a quasi-end-pumped setup the pump beam enters the disk at an angle and exits it again after being reflected back off the HR-coated back face of the disk. To increase the absorption, and therefore the efficiency of the system, the beam is successively redirected back into the thin disk. This is done by homogenising the pump beam and imaging it onto the disk using a collimating lens and a parabolic mirror, providing a homogenous pump profile. The unabsorbed pump radiation is collimated again and reflected off the opposite side of the parabolic mirror, redirected to another spot on the parabolic mirror and back into the thin disk. This can be repeated several times, with the number of positions on the parabolic mirror that can be used depending on the size of the pump beam incident on it and therefore on the beam quality of the pump laser. Up to 32 passes has been reported using this method and more than 90% of the pump power absorbed [84]. A homogenous pump spot is necessary for good beam quality, and can be provided by this method. Power scaling of thin disk lasers can be achieved simply by increasing the size of the pump spot, while keeping the power density constant.

While the setup for thin disk lasers can become quite complex, they have many advantages. The combination of their large surface area to volume ratio and active cooling allow for excellent beam quality, efficiency and high power operation, while avoiding thermal problems. An output of more than 5 kW has been achieved from a single disk in cw operation, and more than 9 kW from a resonator containing four thin disks. Power levels of up to 8 kW are commercially available from thin disk lasers and make them excellent choices for high power materials processing. Another advantage applicable for this use is that the beam quality is better than that achieveable from a rod laser with a similar output power, meaning a smaller focus can be achieved for more precise processing. Thin disk lasers with up to 100 W output power operating in the fundamental mode ($M^2 < 1.2$) are available for such purposes. Ultrashort pulsed thin disk laser systems are also employed for materials processing.

The first material to be used in the thin disk laser configuration was Yb:YAG. Ytterbium has many advantages for high power laser operation (see 3.4.2.1) and most of the high power and high pulse energy results from thin disk lasers have therefore been achieved with Yb:YAG.

3.4.5 Q-switching

Q-switching is a method of obtaining short, high peak power laser pulses by modulating the Q-factor of a laser resonator [80,85]. A gain medium is pumped, as per usual, but with a shutter in the cavity that prevents laser oscillation occurring. The population inversion therefore continues to grow beyond the usual threshold value reached as more energy is stored in the gain medium. The amount of energy that can be stored is often only limited by spontaneous emission. When the shutter in the cavity is opened, the Q-factor of the resonator becomes high, which corresponds to a low loss, and a large gain is seen such that the spontaneous emission triggers the onset of laser oscillation and the power builds up in the cavity very fast. An intense pulse of light is emitted from the laser resonator as the gain becomes saturated, and the peak of the pulse occurs when the gain is equal to the resonator loss (in the high q-factor, low loss state). The timing of these processes can be seen in the graphs in figure 3.12 [86]. The duration of this pulse is similar to the photon decay time, which is usually on a nanosecond time scale, and corresponds to several round trips of the resonator.

A long upper state lifetime is required for Q-switched lasers to allow a sufficiently large population inversion to build up. Solid-state lasers operating on electric-dipole-forbidden transitions (with millisecond timescale lifetimes) and with high gain saturation energies are therefore most commonly used for Q-switching. Yb is a common active ion used for Q-switched lasers, and is used in the work presented in chapter 10. Gain media with shorter lifetimes can be used in Q-switched systems if the pump source is pulsed as this reduces the amount of spontaneous emission, but this regime is not used in the work in this thesis. Bulk lasers are preferable to fibre lasers for Q-switching as they have a larger mode area, allowing more energy to be stored, and shorter resonators provide shorter pulses.

There are various methods used for modulating the cavity losses in a laser resonator to create this Q-switching effect, which can be separated into active and passive Q-switching. The most commonly used methods are use of electro-optical shutters, rotating prisms, acousto-optical switches and saturable absorbers [85]. The former three are active methods of Q-switching, where there is external operation involved - for example, changing the voltage applied on an electro-optical shutter to open and close the Q-switch. Saturable absorbers are a passive method of Q-switching, where the losses in the resonator change automaticaly due to nonlinear absorption. Saturable absorbers absorb the laser wavelength and have low saturation intensity; once saturated, the cav-

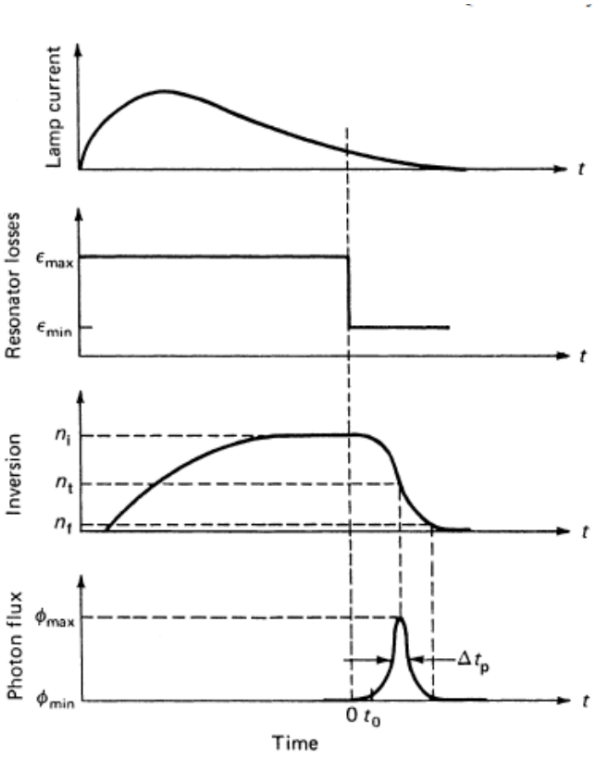

Figure 3.12: Development of a Q-swtiched laser pulse over time. The four plots show how the pump lamp current, resonator losses, population inversion and photon flux change over time and how they are linked together to form Q-switched pulses, taken from [86].

ity Q-factor switches to a higher value and the laser pulse is created. The recovery time of the saturable absorber should ideally be longer than the pulse duration and preferably sit between this and the upper state lifetime of the gain medium. The pulse energy and duration are often fixed for passively Q-switched lasers, and it is the repetition rate that varies with pump power (typically in the kHz regime or higher).

Passive Q-switching is simple and cost-effective in comparison with active Q-switching, with the laser parameters determined by the characteristics of the Q-switch. This can be convenient, but also a potential downfall as there is less control over the system; for example, the pulses cannot be triggered externally. Passively Q-switched systems are suitable for achieving high repetition rates and tend to have lower pulse energies than actively Q-switched systems.

The peak powers achieved with Q-switched laser systems can be orders of magnitude higher than that from the laser in cw operation. The high peak powers and pulse energies can cause safety issues, even with fairly low average power output, as well as damage to the intracavity

optical elements, such as mirrors. The damage thresholds of the components used needs to be taken into consideration and can be a limiting factor of the output achieveable with a Q-switched laser system.

The Q-switched laser experiments reported in this thesis (see chapter 10) use graphene as a saturable absorber. Graphene is a zero bandgap semiconductor and can therefore have resonant absorption at any wavelength, making it suitable for use with a range of laser materials, and an ultrashort recovery time, meaning high pulse repetition rates can be achieved [87]. Use of carbon in the form of both graphene monolayers and single-walled carbon nanotubes as saturable absorbers has been reported [87, 88]. While both forms can endure high optical power, graphene is believed to have a higher damage threshold, which is obviously desirable for Q-switched lasers to be able to achieve higher power outputs [89]. Power-induced damage to a saturable absorber can be avoided, or at least minimised, by positioning it outside of the laser cavity, in the evanescent field of the laser mode, and taking advantage of evanescent field coupling [90]. This technique is reported in reference [91] where single-walled carbon nanotubes have been employed as the saturable absorber.

3.5 Conclusions

This chapter has given an overview of various theoretical aspects that need to be taken into consideration when employing PLD to grow thin films for use as planar waveguide lasers, right through from laser ablation and crystal growth to the theory of waveguides, lasers, methods of determining loss, and the dopants used for work reported in this thesis. Details of thin disk lasers are also given as this is another possible laser configuration to consider using with PLD-grown samples. The chapter finishes with the qualitative theory behind Q-switching, and details of graphene as a saturable absorber, to support the final experimental chapter, chapter 10, in this thesis.

Chapter 4

Experimental and analytical methods

4.1 Introduction

This chapter outlines practical techniques used throughout this project, from the fabrication of samples to the final stages of the process where they are used as the gain media in laser setups. I begin with the pulsed laser deposition setup and detail of how the substrate being deposited on is heated, then give overviews of the techniques used for the material analysis; how we assess the crystallinity of a sample, measure its thickness and estimate the surface particulate density, as well as imaging the surface and polished end facets, and measurement of the dopant concentration within a sample or target. The latter part of the chapter looks at the optical and spectroscopic properties, and using these samples as lasers.

4.2 Pulsed Laser Deposition

4.2.1 Single beam PLD

Single beam PLD involves a relatively simple setup; a UV light pulse from an excimer laser is guided into a vacuum chamber where it is incident on a target, mounted in a rotating holder driven by a motor, with a substrate positioned opposite, which is laser heated from the rear, for the material to be deposited onto, as shown in figure 4.1. PLD has many variables that can be changed in attempts to optimise growth conditions. In this thesis, optimisation is explored mainly through changing the ablation fluence, background gas pressure in the vacuum chamber and the temperature of the substrate being grown upon. Other parameters that can be investigated are

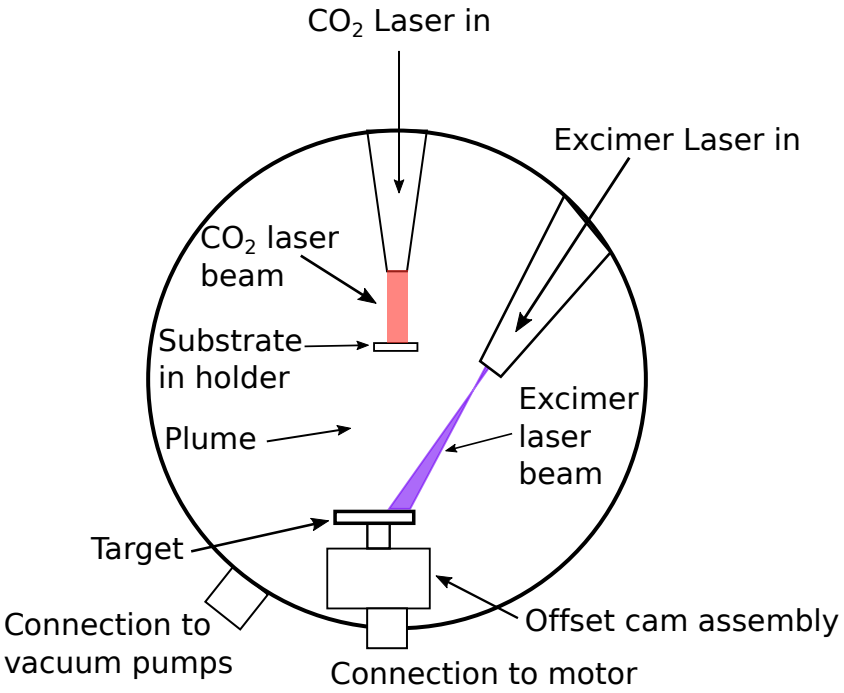

Figure 4.1: Pulsed laser deposition setup.

the target to substrate distance, ablation spot size and the repetition rate of the ablating laser.

4.2.2 Substrate Heating

Heating of the substrate provides extra energy to the particles being deposited on the surface of the substrate, which allows them to migrate to the correct locations in the growing crystal lattice, thereby aiding crystalline growth. In this setup, the heating is done using a CO_2 laser, capable of delivering 30 W into the vacuum chamber. To increase the efficiency and uniformity of the substrate heating, and minimise heating of the surroundings, the Gaussian beam from the CO_2 laser is directed through a system of lenses and a ZnSe tetra-prism that folds the beam, giving it a square profile of approximately equal size to the substrate, 1 cm^2, at the position of the substrate within the vacuum chamber [94]. Previous work on temperature calibration, performed by Tim May-Smith [54], indicates that the temperature the substrate can reach is approximately 1200°C at the maximum incident laser power (∼30 W) available.

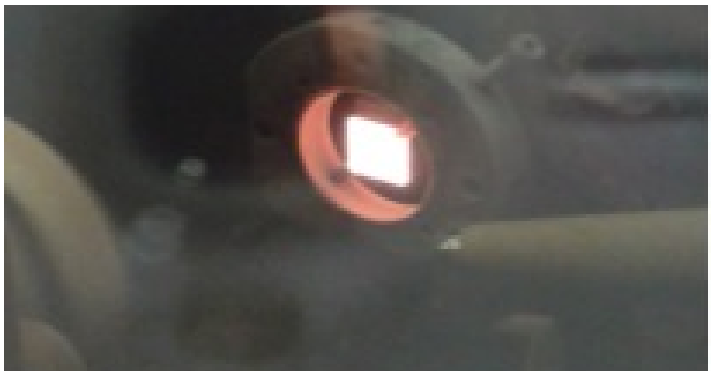

Figure 4.2: Photograph of a YAG substrate in the deposition chamber, heated by the CO_2 laser.

The substrate temperature in the work carried out as part of this thesis is determined by the CO_2 laser power percentage on the control box, and consequently the laser power incident on the substrate. The table below gives average readings of the CO_2 laser power for a range of percentage values on the control box, as well as the estimated corresponding substrate temperature (for 1 mm-thick, 1 cm^2 YAG substrates).

CO_2 power %	Incident heating power (W)	Error (W)	YAG substrate temperature (°C)
10	2.23	± 0.03	350
20	6.97	± 0.18	460
30	11.27	± 0.12	570
40	15.40	± 0.15	680
50	18.37	± 0.27	790
60	22.47	± 0.24	900
65	23.83	± 0.26	960
70	25.00	± 0.36	1015
75	27.23	± 0.12	1070
80	28.47	± 0.15	1125
85	29.10	± 0.15	1180
90	30.77	± 0.15	1240
95	33.33	± 0.50	1290

Table 4.1: Relation between the CO_2 laser power percentage value and the power incident on the substrate, and estimates of the corresponding substrate temperature. The incident power readings are an average of three measurements at each power % taken consecutively, and the error is that associated with the variation in these readings. Further power fluctuations are likely on a day to day basis, and an overall degredation of the power output over time (this data is from measurements by K. A. Sloyan, in conjunction with temperature calibration data from T. May-Smith [54]).

4.3 Analysis Techniques

This section provides an overview of the analysis techniques used to study various properties of the pulsed laser deposited thin films in this project, as well as some substrates prior to deposition and the target materials used.

4.3.1 X-ray Diffraction

X-ray diffraction (XRD) is a quick and easy way of establishing the crystallinity of a sample, in this case thin films grown by PLD. A source of x-rays and a detector rotate in opposite directions

about the mounted sample, as shown in figure 4.3(a), in order to measure the angles at which x-rays constructively interfere; this happens at

$$2d \sin\theta = m\lambda \tag{4.1}$$

known as the Bragg condition (see 4.3(b)), where d is the lattice spacing, θ is the angle of incident x-rays, m is the diffraction order and λ is the wavelength of the incident x-rays. Data collected

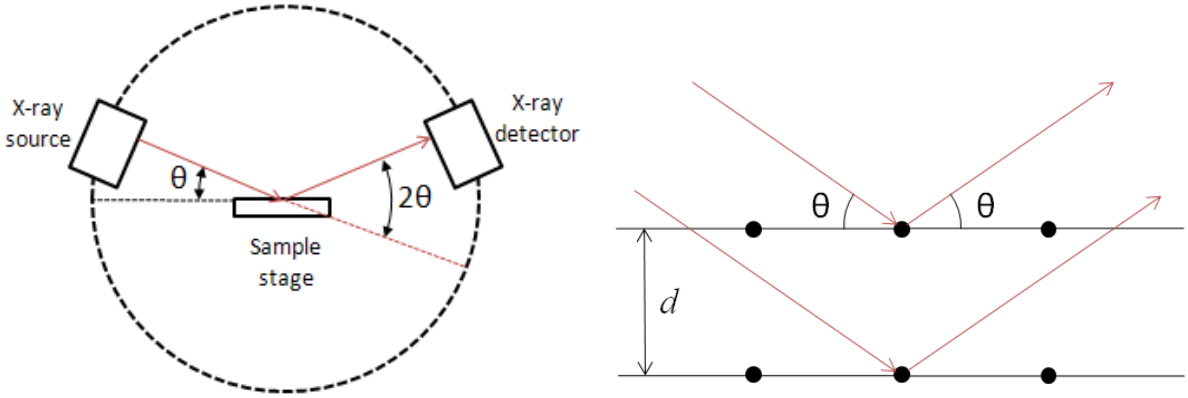

(a) XRD schematic, taken from [92].

(b) Bragg's law, taken from [92]

Figure 4.3: (a) A diagram of the basic geometry used for XRD and (b) x-rays incident on a crystal with lattice spacing d, from which equation 4.1 is derived.

is the number of counts as a function of angle, 2θ. Using the above equation, the lattice spacing of the film can be determined. Crystal orientation can be determined by comparing the peaks in the spectrum against a database of known values. Shifts from these values may be observed due to a difference in stoichiometry or strain in the lattice, resulting in a change of lattice spacing. These factors can also cause peak broadening, so the width of peaks is a good indication of the quality and uniformity of a film. Once the lattice spacing of a crystal has been determined and its orientation identified, the lattice constant, a, can be calculated by rearrangement of the following equation:

$$d_{h,k,l} = \frac{a}{\sqrt{h^2 + k^2 + l^2}} \tag{4.2}$$

for cubic crystal lattices. In this equation, h, k and l are the Miller indices corresponding to the crystal plane in question. The diffractometer used to analyse films in this report is a Bruker D2 Phaser, and scans are typically taken from 2θ values of 10° to 80° at intervals of 0.02°.

Other x-ray diffraction techniques are available for further analysis with the use of the SmartLab facility. Pole figure measurement can be used to determine the degree of preferred crystal orientation in a sample. Intensity measurements are taken at a fixed 2θ angle while varying the tilt angle, from the sample surface normal, α, and the rotation around the sample, β. This forms a hemisphere of data showing the diffracted intensity variation, which is typically viewed as a stereoscopic projection with polar coordinates α and β [93], examples of which can be seen in figures 6.4 and 6.9, amongst others.

4.3.2 Stylus Profiler

A KLA Tencor P-16 surface profiler is used to measure the thickness and curvature of films, to a height resolution of about 1 nm. A 2 μm stylus tip on the end of a cantilever rests on the sample and records vertical measurement as the sample moves under the tip.

4.3.3 ZeScope Surface Analysis

The quality of a film can be observed by eye to some extent for a qualitative assessment only. Poor quality films with many particulates tend to look cloudy and speckled, whereas better films look more transparent and reflective. To quantitatively analyse this, a sophisticated optical microscope (Zemetrics ZeScope) and Scanning Probe Image Processor (SPIP) software package are used to measure the number of particulates and pores there are over chosen threshold values on a sample surface. Such three-dimensional images are constructed from interference data that can provide sub-nanometre vertical resolution.

4.3.4 Scanning Electron Microscopy

A focussed beam of electrons is incident on a sample and an image is accumulated from detecting inelastically scattered secondary electrons. Samples usually need to be conducting or coated in a conductive layer to prevent the build up of charge on the sample, but this requirement can be bypassed by variable pressure (VP) mode where there is some background gas to allow the sample to discharge; however, this is at the cost of a slightly lower resolution. The model used here is a Zeiss EVO SEM.

4.3.5 Energy Dispersive X-ray Analysis

Energy dispersive x-ray analysis is an add-on to the SEM, which allows compositional analysis. High-energy electrons bombard the sample causing inner shell electrons to enter an excited state and then emit characteristic x-rays on de-excitation. The abundance of elements present is determined by the intensity of the peaks detected at different wavelengths. The determination of elements present can, however, be inaccurate due to some elements having very similar gaps between energy levels; this problem can be minimised using the software when analysing a sample of known elemental composition to eliminate peaks from elements that shouldn't be present in the film (and/or substrate, depending on sample thickness). Information recorded is from, approximately, the top 2 μm of a sample.

This technique is non-destructive but with limited accuracy of about $\pm 2\%$ and detection limits in the region of 1000 ppm by weight, so is poor at detecting low mass elements ($Z<11$).

4.4 Polishing

Lapping and polishing is an important part of the production of our planar waveguide lasers, as polished facets are required for end-launching laser pump light into the waveguide and forming the laser cavity. Where plane and parallel polishing is achieved on opposing end facets it is possible to achieve lasing using the Fresnel reflection at the facet without the requirement of an external output coupler.

This process is fairly lengthy and labour intensive as it requires lapping back an end facet, using Al_2O_3 grits of decreasing size, starting with 9 μm, through 3 μm, and down to 1 μm, to level and smooth the surface before the final step of polishing it. The sample then has to be turned around and aligned to be plane-parallel using a system that requires a laser reflection off the already polished facet, and the lapping and polishing process repeated for the second facet.

The lapping process is also used in the process of reconditioning targets, to remove the top layer of material that has been modified through laser ablation, before it is used again.

4.5 Waveguide Loss Measurements

Following polishing, insertion loss measurements can be performed using a HeNe laser beam launched into the waveguide through an end facet, then capturing the light exiting the other end facet and imaging the transmitted light onto a photodiode, as illustrated in figure 4.4. A comparision of the light transmitted through the waveguide and the HeNe laser beam travelling through the optics but not the waveguide allows a loss value to be calculated by providing a percentage loss that can be converted into loss in dB via the equation:

$$L = -10 \log_{10} \frac{P_{waveguide}}{P_{without}} \tag{4.3}$$

where $P_{waveguide}$ is signal captured when the laser beam travels through the waveguide and $P_{without}$ is the signal obtained when the waveguide is removed from the system (c.f. equation 3.11). The waveguide sits on a 5-axis translation stage so that position can be altered in three dimensions, as well as the angle through roll and yaw adjustments, to optimise the coupling of the HeNe laser beam into the guide. The telescope formed by the aspheric lenses, A1 and A2, expand the beam to then allow a smaller focus to be achieved for coupling into the waveguide. The losses calculated using equation 4.3 assume 100% launch efficiency and the measurement taken with the waveguide in the system is adjusted to account for the Fresnel loss at each waveguide facet. Multiple measurements are taken across the waveguide to get an idea of the uniformity of the internal structure across it, and seek areas of lowest loss.

The photodiode can be replaced by a CCD camera and the mode viewed. This gives further information on the uniformity of the sample and its internal structure.

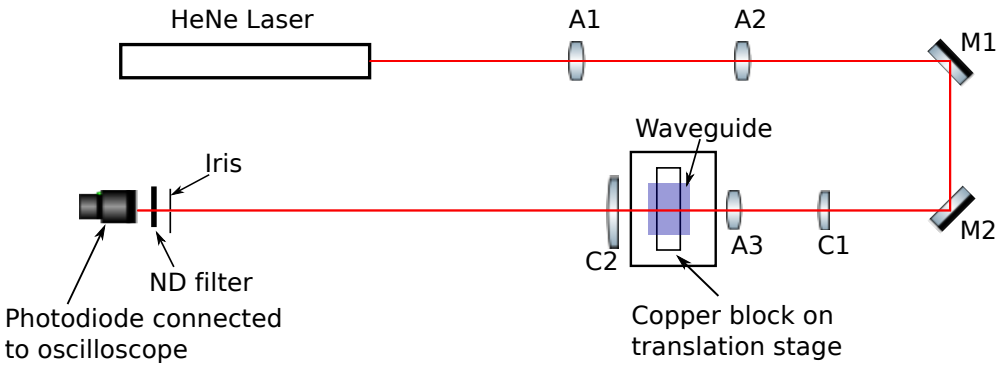

Figure 4.4: A schematic of the setup used for insertion loss measurements. Components A1, A2 and A3 are aspheric lenses, C1 and C2 are cylindrical lenses and M1 and M2 are mirrors.

4.6 Spectral Characterisation

Spectral characterisation is performed on samples to obtain information that helps determine what components will be required when building a laser system that uses it as the gain medium and to compare them to reports in the literature of the same materials and see if the behavior is as expected.

Fluorescence measurements involve a laser beam incident on the sample, at a wavelength that is known to be absorbed by the dopant ions in the sample material, and collecting the emerging fluorescence light with an optical fibre that carries the signal into an optical spectrum analyser (OSA). This measurement can be performed by the pump light being incident on the sample surface and collecting the fluorescence output at an angle to the surface, as shown in figure 4.5, or once the sample's end facets have been polished the pump light can be coupled into the guide and the optical fibre positioned perpendicular to the sample surface to collect the emerging light, as in figure 4.6. The latter of these configurations is preferred as a higher signal is achieved due to the pump light being coupled into the sample, and any systematic errors as a result of reabsorption tend to be lower.

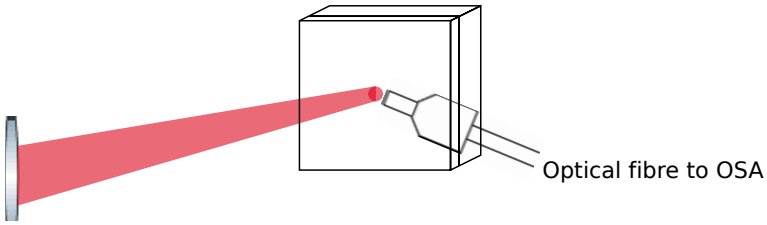

Figure 4.5: A schematic of the experiemental setup used for taking fluorescence measurements from unpolished samples

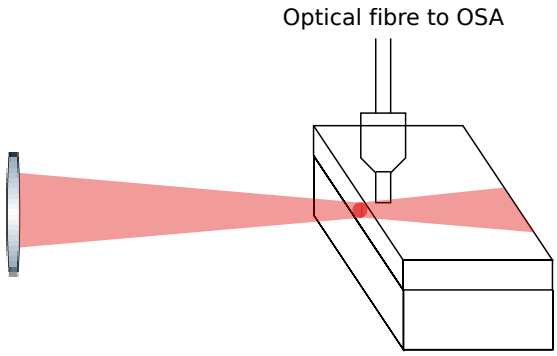

Figure 4.6: A schematic of the experiemental setup used for taking fluorescence measurements from polished samples

4.7 Waveguide Laser Construction

Firstly, a pump laser of suitable wavelength and beam quality needs to be selected for pumping the waveguide sample to be used. A variety of diode lasers are used as pump sources for the work in this thesis, from a single mode diode laser, grating-stabilised to the 976 nm zero phonon line for the Yb-doped sesquioxide samples, to broad area diode lasers and diode bars for high power pumping. The broad area diode laser and diode bars fit a wavelength specification around the desired pump wavelength, and are tuned to the correct wavelength to maximise the absorption in the sample by adjustment of the driving current and operating temperature. To achieve the maximum pump power available, the driving current is set to the full recommended ampage and wavelength tuning controlled by the temperature of the base plate the diode is mounted on via a water cooling system, and in some cases a Peltier patch with a temperature feedback loop. A sample of the light emerging from the laser being tuned is captured with an optical fiber and sent

to an OSA for analysis, the results of which can be compared with the results of the spectral characterisation of the sample material to be used.

For the grating-stablised diode the pump power can simply be controlled via the driving current, but in the case of the high power diodes that are wavelength tuned by driving current and temperature an alternative method is required. A half wave-plate and polarising beam splitter are inserted into the beam path to control how much power is sent through to the waveguide and how much is steered away to a beam dump, so that the pump wavelength can be kept constant.

The basic setup for the waveguide lasers built in this project require the pump beam to be focussed down to a spot size similar to that of the thickness of the sample being tested, using a system of lenses that involves expansion and collimation of the beam prior to focussing into the guide, as well as control of the focussing in the unguided axis in the case of the high power diode lasers. A suitable mirror is selected for the pump input, such that the pump light can enter the waveguide but the light generated inside the sample at the laser wavelength is trapped, and a selection of output coupling lenses trialled. Both bulk mirrors are mounted and brought into close proximity to the polished facets of the waveguide, with angular and distance alignment performed by eye. The waveguide itself is mounted on a water cooled platform, connected to a 5-axis translation stage for adjustments in position and angle to allow for optimisation of the system. The waveguide could be moved horizontally to scan across the crystal layer in search of regions of lowest loss, unlike in the channel waveguide lasers mentioned in chapter 2, reported in references [51, 53].

More lenses are positioned after the waveguide to collect the emerging laser light, and a dichroic mirror used to separate out the laser light from the emerging pump light so that just the ouput power of the waveguide laser is incident on a power meter.

4.8 Conclusions

The experimental setup for PLD has been discussed, along with the variables that can be changed to optimise growth conditions, as well as the method used in this setup for heating of the substrate. Various analysis techniques are employed for material characterisation, to determine trends in growth and to assess which samples are worth putting forward for polishing and subsequent laser experiments. Insertion loss measurements performed using a HeNe laser give further

indication of which samples are more promising to use as gain media, both by quantitative loss measurements and looking at the mode profiles.

Chapter 5

Optimisation of Sesquioxide Crystal Growth

5.1 Introduction

Optimisation experiments were performed for each of the sesquioxides, Sc_2O_3, Y_2O_3 and Lu_2O_3, with the aim of lowering waveguide losses by minimising surface particulates, while achieving highly crystalline samples at relatively high growth rates. The main two parameters adjusted to optimise the sesquioxide growth were the ablation fluence and background gas pressure, which in combination affect the size of the ejected plume of material and the energy with which the matter reaches the substrate. In some cases, the CO_2 laser power that is incident on the substrate to heat it was varied to determine whether the temperature variation, and therefore energy available, at the substrate surface being deposited on has an affect on the crystallinity of the grown thin film. The target-substrate distance was set to 7 cm throughout all depositions, and YAG substrates used throughout these sets of experiments. Changes in fluence and background pressure were done out of sequence to minimise the chance of any systematic variations in the number of surface particulates due to target degredation over time, as the target surface is modified by the ablation process.

Analysis was performed on the samples using X-ray diffraction, a KLA Tencor surface profiler and Zemetrics ZeScope with SPIP software, as described in section 4.3.

5.2 Scandia (Sc_2O_3)

The first set of sesquioxide optimisation experiments were performed using a Tm:Sc_2O_3 target, the results of which are displayed in table 5.1. Ablation fluence was the first parameter to be changed in this set of experiments, while keeping all other conditions constant. As shown in figure 5.1(a), the growth rate, calculated from the sample thickness and deposition time, increased with higher fluence, as would be expected due to more material being ejected from the target by each pulse. The oxygen background pressure was then changed, which also had an affect on the growth rate, as seen in figure 5.1(b), with a general trend of lower pressure providing a higher growth rate as there are fewer gas molecules between the target and substrate to interact with the plume of material.

Sample ID	Fluence	Pressure	CO_2 laser	Thickness	Particulates (x10^4) /cm^2		(222) peak
	J/cm^2	mBar	power %	μm	>100 nm	> 50 nm	XRD counts
TP23	1.5	4 x 10^{-2}	62.5	1.5	3.9	9.2	24411
TP24	1.9	4 x 10^{-2}	62.5	2.3	7.8	19	845542
TP25	1.3	4 x 10^{-2}	62.5	–	9.7	12	28898
TP26	1.7	4 x 10^{-2}	62.5	2	7.3	18	44067
TP27	1.5	1 x 10^{-2}	62.5	2.3	2.2	4.2	87668
TP28	1.5	8 x 10^{-2}	62.5	1.4	6.5	14	8908
TP29	1.5	2 x 10^{-2}	62.5	2.1	1.5	1.8	65246

Table 5.1: Tm:Sc_2O_3 optimisation deposition conditions and analysis. Number of particulates greater than 50 and 100 nm are averages of measurements from five 134 x 179 μm^2 areas on the surface of each sample, converted into the number of particulates present in 1 cm^2.

Particulate analysis of these samples is displayed in figure 5.2, with figure 5.2(a) showing results from samples grown using different ablation fluence with a constant background pressure of 4x10^{-2} mbar and figure 5.2(b) showing the results of depositions performed at varying background pressure, with a constant ablation fluence of 1.5 J /cm^2. This analysis revealed a minimum number of surface particulates at a fluence of 1.5 J /cm^2 and background pressure of 2x10^{-2} mbar, where the particulate density is 1.5x10^4 / cm^2 for particulates of >100 nm and 1.8x10^4 /cm^2 for particulates

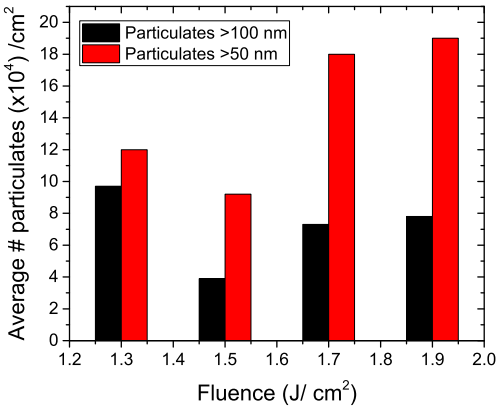

(a) Constant background pressure of 4x10^{-2} mbar.

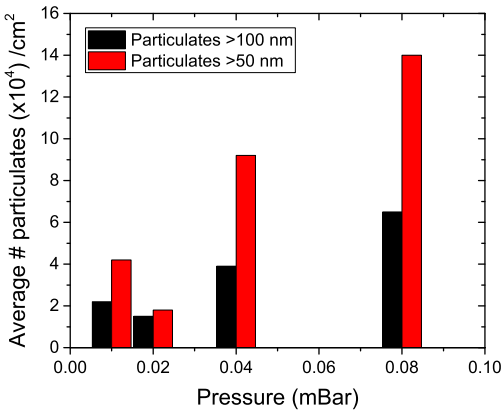

(b) Constant ablation fluence of 1.5 J/cm^2.

Figure 5.1: Growth rate dependancy on (a) ablation fluence and (b) background gas pressure.

of >50 nm. Roughness measurements were also taken of the five positions over the sample surface that particulate counts were performed on, and the average roughness for the sample calculated. The average Sa roughness measurements for the samples grown at different fluences are plotted in figure 5.3(a), and results for samples grown under different background pressures in figure 5.3(b). These show an increase in roughness when higher fluence is used, and an increase in roughness for higher background pressures.

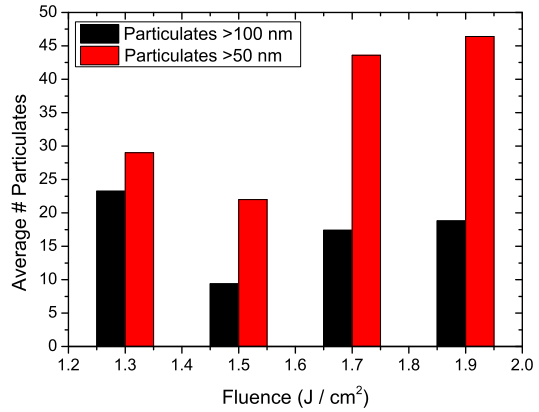

(a) Constant background pressure of 4x10^{-2} mbar.

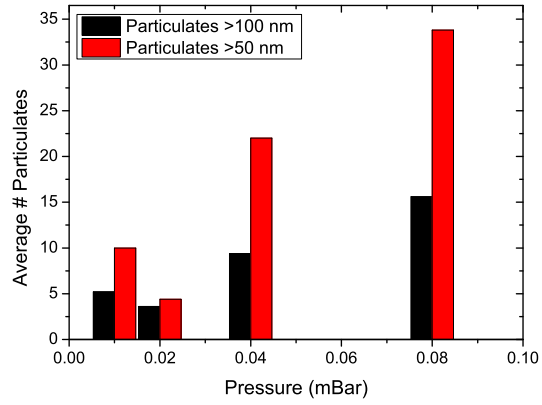

(b) Constant ablation fluence of 1.5 J /cm^2.

Figure 5.2: Average number of particulates on the surfaces of samples grown at (a) a range of ablation fluences, (b) a range of background pressures.

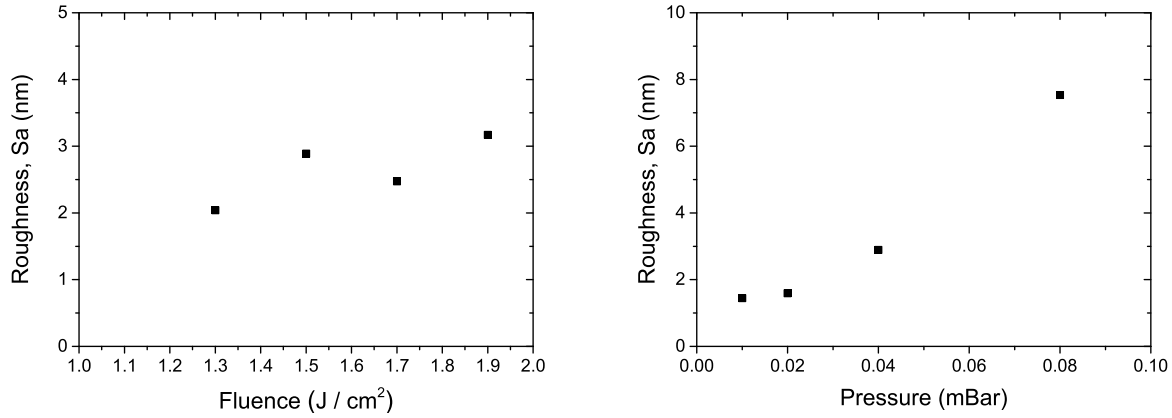

(a) Constant background pressure of 4x10^{-2} mbar. (b) Constant ablation fluence of 1.5 J /cm^2

Figure 5.3: Average roughness values of the sample surfaces for (a) samples grown using different ablation fluences, at constant background pressure, (b) samples grown with the same ablation fluence under different background pressures.

Analysis of the XRD spectra for these films, plotted together in figure 5.4, revealed that the (222) Sc_2O_3 peak was present, and therefore that <111>-oriented Sc_2O_3 had grown on the YAG <100> substrate. This peak along with other identified orientations of scandia and those seen from the YAG substrate are labelled in figure 5.4. The <222> peak height from the Sc_2O_3 samples varies, and when compared to other parameters it is found that, over this range of sample thicknesses, a higher signal is obtained from a thicker sample, as seen by the data plotted in figure 5.5 along with a trend line.

Comparing the position of the (222) Sc_2O_3 peak obtained by XRD of these samples against values in the crystal database [10] highlights a slight negative shift, indicating a marginally bigger lattice constant in our crystal. This change is likely to be due to the incorportation of the Tm dopant ions, that have a slightly larger ionic radius than the host ions being replaced in the crystal lattice (102.0 pm versus 88.5 pm [95]), or because the growth is under strain due to the lattice constant mismatch and difference in thermal expansion between the substrate and grown material, or a combination of the two. In figure 5.6, the points at 0 and 100% are the lattice constants of Sc_2O_3 and Tm_2O_3, respectively, and the lattice constant calculated from the XRD spectrum against the dopant concentration as measured by EDX of a Tm:Sc_2O_3 sample is the point plotted in between. This point sits on a line between the points for the lattice constant of the pure Sc_2O_3 and Tm_2O_3 values. This indicates that the change in lattice constant, and therefore the XRD

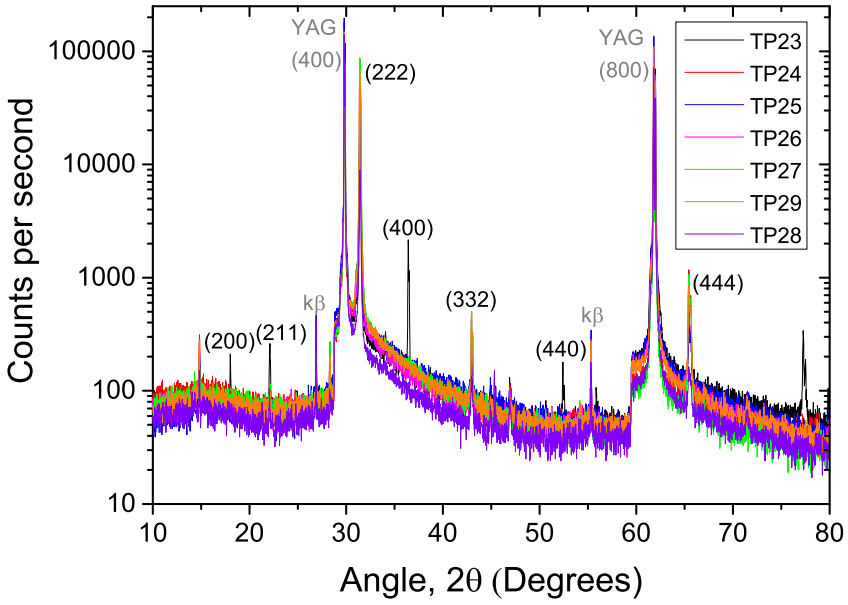

Figure 5.4: XRD spectra of the Sc_2O_3 samples grown in this set of optimisation experiments. Sc_2O_3 peaks are labelled in black and those associated with the YAG substrate in grey.

spectrum shift, is due to the incorporation of the dopant ions, which is in keeping with Vegard's law [96].

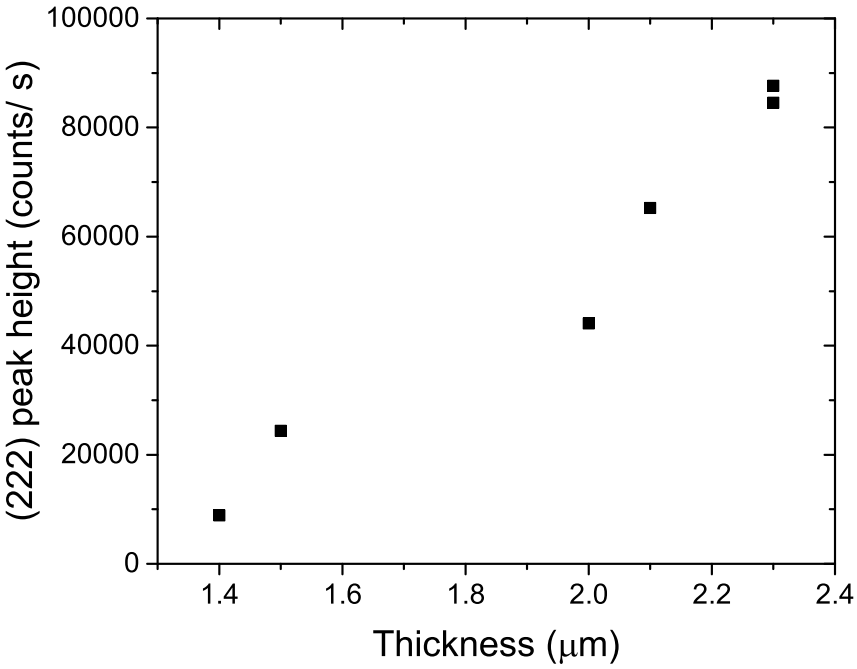

Figure 5.5: XRD peak height variation with film thickness.

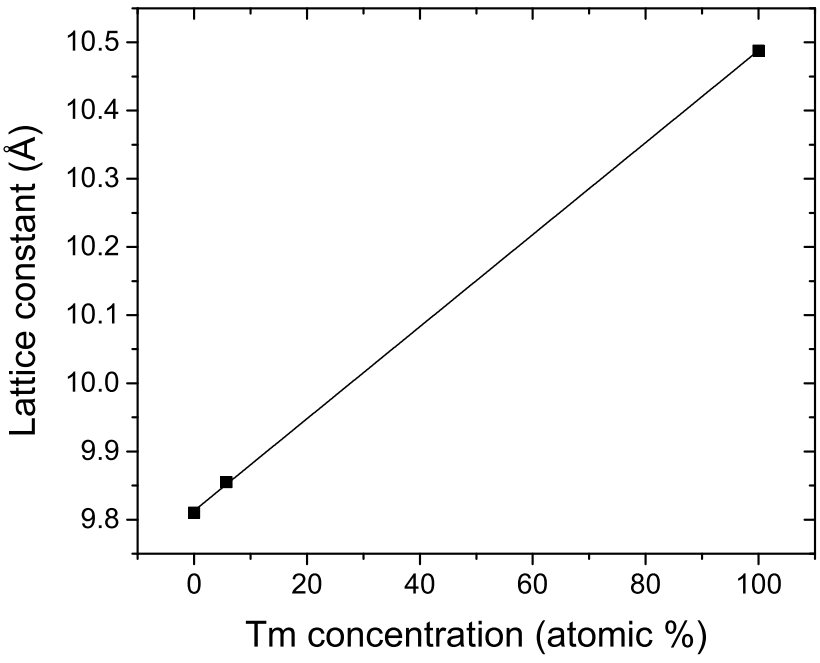

Figure 5.6: Lattice constant variation for Tm-doped Scandia, showing that the lattice constant of the grown sample sits on the line between the points representating pure Sc_2O_3 and pure Tm_2O_3.

5.3 Yttria (Y_2O_3)

An investigation into the optimum conditions for Y_2O_3 was performed, similar to that for Sc_2O_3. However, having found from the optimisation experiments with Sc_2O_3 in section 5.2 that having a higher background pressure, of $8x10^{-2}$ mbar, decreases the growth rate and increases the average number of surface particulates present, growths of Y_2O_3 at this pressure were not trialled. Similarly, growths at the other end of the pressure range previously used, $1x10^{-2}$ mbar, were not investigated either as they did not give fewer particulates than depositions at $2x10^{-2}$ mbar. Futhermore, the growth rate wasn't higher by a great enough margin to accept the higher particulate count, and the ablated material spreading out more in the chamber would likely coat the vacuum chamber windows faster. Similarly, when changing the fluence, 1.9 J/cm^2 was discounted for Y_2O_3 optimisation as it had previously resulted in a higher number of surface particulates.

Consequently, for this set of experiments, the fluence was varied between 1.3 and 1.7 J/ cm^2 and the background oxygen pressure only set to $2x10^{-2}$ mbar or $4x10^{-2}$ mbar. In addition to this, the temperature of the substrate being deposited onto was also investigated, controlled by the CO_2 laser power incident on the substrate (the CO_2 laser power percentages of 55%, 62.5% and 70% roughly correspond to temperatures of 800°C, 875°C, and 950°C, respectively). The conditions for each deposition and some results of the analysis are detailed in table 5.2.

Sample ID	Fluence J/cm^2	Pressure mBar	CO_2 laser power %	Thickness μm	Particulates (x10^4) /cm^2 >100 nm	> 50 nm	(222) peak XRD counts
TP37	1.7	4 x 10^{-2}	62.5	2.25	9.4	13	906449
TP38	1.3	4 x 10^{-2}	62.5	1.75	2.2	6.8	587832
TP39	1.5	4 x 10^{-2}	62.5	2	7.7	78	727120
TP40	1.3	2 x 10^{-2}	62.5	1.5	0.67	1.2	645450
TP41	1.5	2 x 10^{-2}	62.5	2	3.9	8.1	710105
TP42	1.3	2 x 10^{-2}	70	2	1.4	3.9	874983
TP43	1.3	2 x 10^{-2}	55	1.75	1.8	2.7	506950

Table 5.2: Yb:Y_2O_3 optimisation deposition conditions and analysis. Number of particulates greater than 50 and 100 nm are averages of measurements from 134 x 179 μm^2 areas on the surface of each sample.

Analysis of the average number of surface particulates was, in this case, done for different ablation fluences at two background pressures. Figure 5.7(a) shows the results of the particulate counts for samples deposited under a background pressure of 4x10^{-2} mbar, and figure 5.7(b) the results of the particulate counts for samples deposited under a background pressure of 2x10^{-2} mbar. In both cases, using an ablation fluence of 1.3 J/ cm^2 gave the fewest particulates, with the fewest overall being for the deposition performed at this fluence and with a background pressure of 2x10^{-2} mbar.

As with the Sc_2O_3 depositions, the growth rate was plotted as a function of the ablation fluence used for growing the samples, as shown in figure 5.8. Again, the growth rate was found to increase with higher fluence.

The (222) Y_2O_3 peak height obtained by XRD analysis was again found to loosely correlate with the thickness of the sample being analysed, as can be seen in figure 5.10.

Finally, the growth rate achieved using different fluences to ablate doped Y_2O_3 targets is plotted along with the results obtained using the doped Sc_2O_3 targets in figure 5.11. It is obvious from this plot that, at least within the range of ablation fluences used here, the growth rate is higher for Y_2O_3 at a given fluence than for Sc_2O_3.

Following these optimisation experiments, longer depositions were performed at the optimised

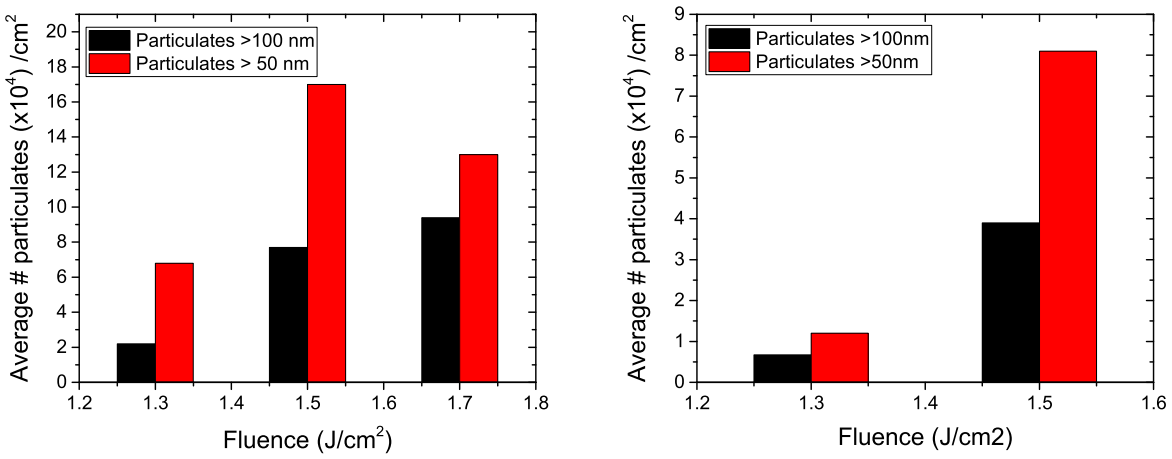

(a) Constant background pressure of 4x10^{-2} mbar. (b) Constant background pressure of 2x10^{-2} mbar.

Figure 5.7: Average number of particulates on the surfaces of samples grown at a range of fluences and background pressures of (a) 4x10^{-2} mbar and (b) 2x10^{-2} mbar.

conditions. Analysis of these samples, including laser experiments performed using them, can be found in chapters 6 and 8.

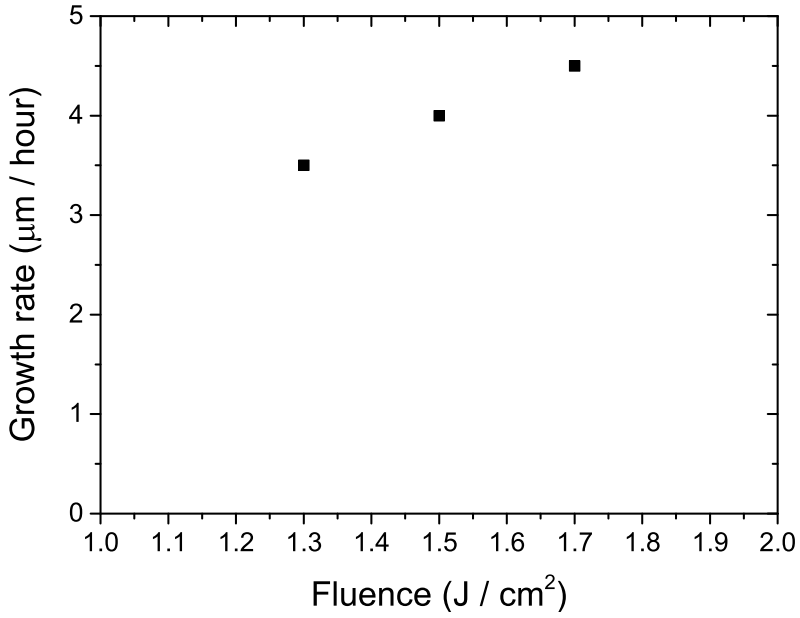

Figure 5.8: Growth rate dependency on ablation fluence

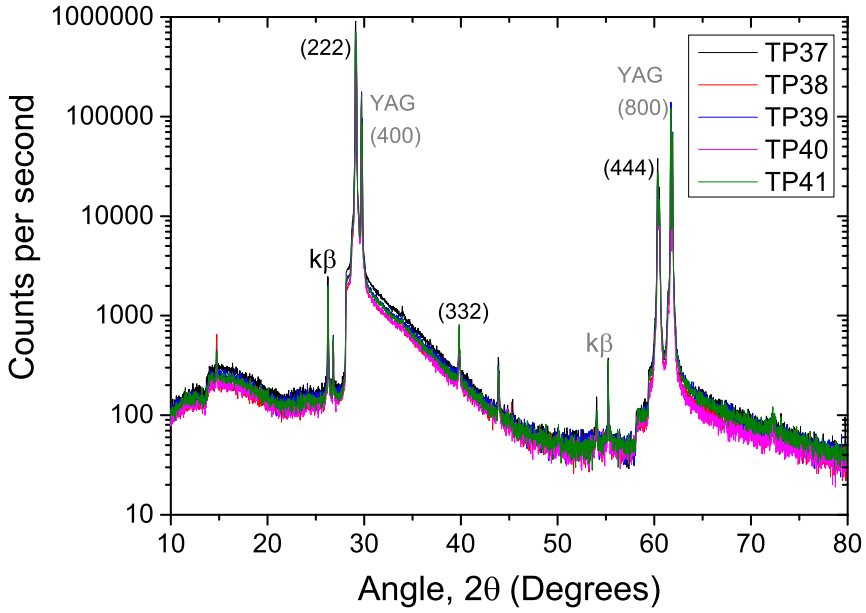

Figure 5.9: XRD spectra of Yb:Y_2O_3 samples deposited at the same growth temperature in these optimisation experiments.

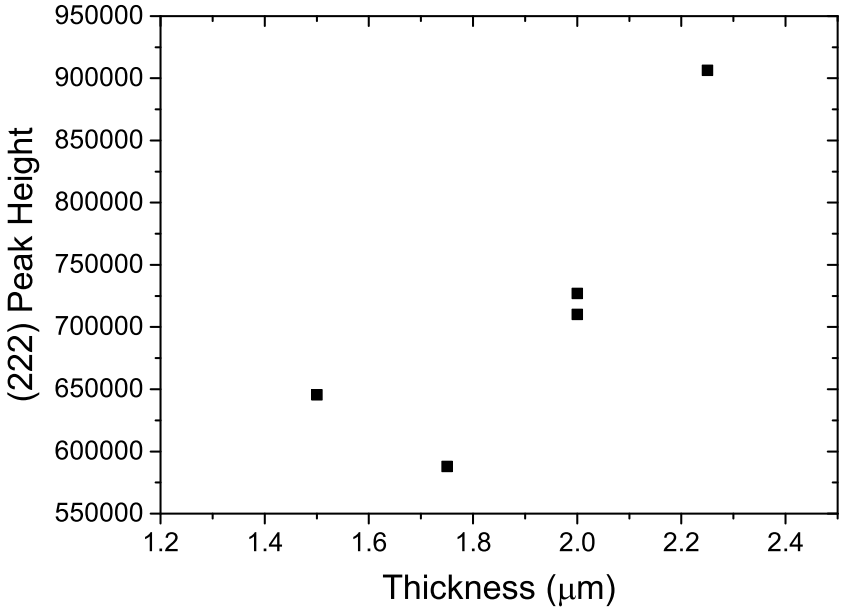

Figure 5.10: XRD peak height variation with film thickness.

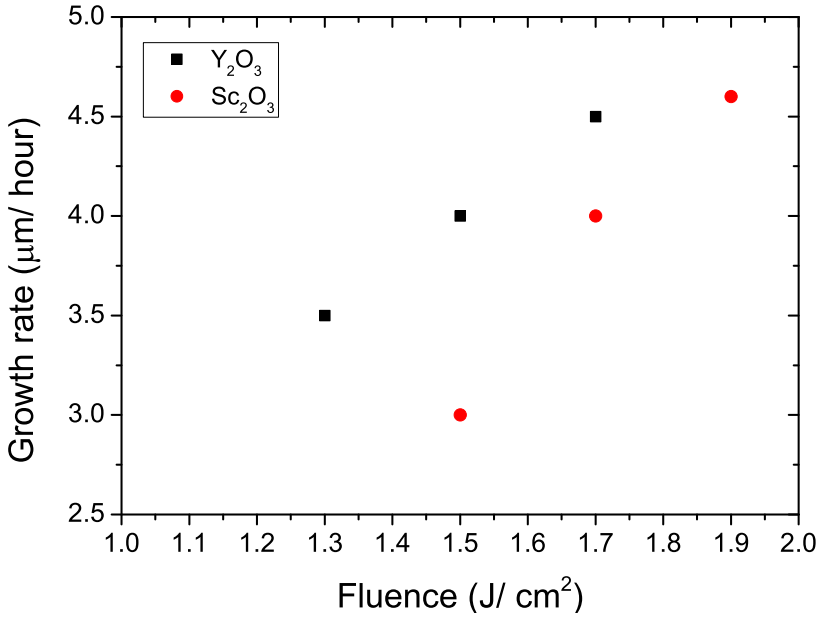

Figure 5.11: Growth rate comparison between Y_2O_3 and Sc_2O_3 depositions performed at a range of ablation fluences and constant background pressure of $4x10^{-2}$ mbar.

5.4 Lutetia (Lu_2O_3)

Optimisation experiments were performed using a Yb:Lu_2O_3 target, again using a range of ablation fluences and background oxygen pressures, and the resulting samples anlysed as for the Sc_2O_3 and Y_2O_3 optimisation experiments. A list of samples and their deposition conditions are given in table 5.3. The CO_2 laser power used for substrate heating was constant throughout this set of depositions, while the fluence and background oxygen pressure were varied.

Sample ID	Fluence	Pressure	CO_2 laser	Thickness	Particulates (x10^3) /cm^2		(222) peak
	J/cm^2	mBar	power %	μm	>100 nm	> 50 nm	XRD counts
TP95	1.5	2 x 10^{-2}	75	1.4	1.7	5.8	102821
TP96	1.3	2 x 10^{-2}	75	1	2.5	8.3	296751
TP97	1.9	2 x 10^{-2}	75	2.3	2.5	25	430836
TP98	1.7	2 x 10^{-2}	75	1.7	0.83	2.5	541915
TP99	1.7	4 x 10^{-2}	75	1.7	7.5	16	247961
TP100	1.7	1 x 10^{-2}	75	1.8	17	26	356497

Table 5.3: Yb:Lu_2O_3 optimisation deposition conditions and analysis. Number of particulates greater than 50 and 100 nm are averages of measurements from five 134 x 179 μm^2 areas on the surface of each sample.

Results of the surface particulate count analysis can be found in figure 5.12, this time showing a minimum number of particulates for an ablation fluence of 1.7 J/ cm^2 (figure 5.12(a)), and a background pressure of 2x10^{-2} mbar (figure 5.12(b)). Figure 5.13 shows how the surface roughness of Yb:Lu_2O_3 changes with the ablation fluence used; the points plotted are the average surface roughness of each sample, calculated from measurements taken at the same five areas on the sample surfaces that the particulate counts were performed on. There is a positive linear correlation, as seen in figure 5.3(a) for growth of Tm:Sc_2O_3, but the growths here are smoother.

The thickness of each sample was measured using a stylus profiler and the data converted to growth rate. The growth rate was then plotted against the ablation fluence used for the range of depositions that were performed under the same background pressure, and, as before, a positive linear correlation is observed. These results are displayed in figure 5.14 along with growth rate

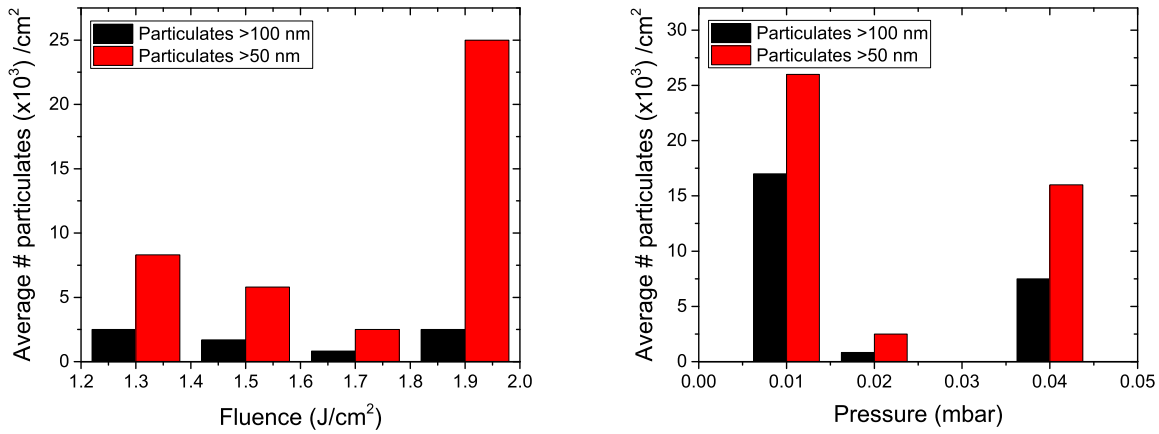

(a) Constant background pressure of 2x10^{-2} mBar. (b) Constant ablation fluence of 1.7 J/ cm^2.

Figure 5.12: Average number of particulates counted on sample surfaces for samples deposited at (a) a selection of fluences, (b) a range of background pressures.

results from Y_2O_3, performed at the same background pressure, for comparison. The slope formed by each set of points appears to be very similar, but again Y_2O_3 has the higher growth rate.

XRD was used to analyse these samples, the peak heights of which are included in table 5.3, but showed no significant trends with the growth conditions. Due to the almost perfect match between the <111>-oriented Lu_2O_3 and <100> YAG substrate the (222) Lu_2O_3 and (400) YAG XRD peaks are indistinguishable and therefore the listed (222) peak heights may well not be fair representation of the signal from the sample. An example of an XRD spectrum collected from a Yb:Lu_2O_3 sample can be found later in this thesis, in chapter 9 (figure 9.1) along with further characterisation of the sample, including laser results.

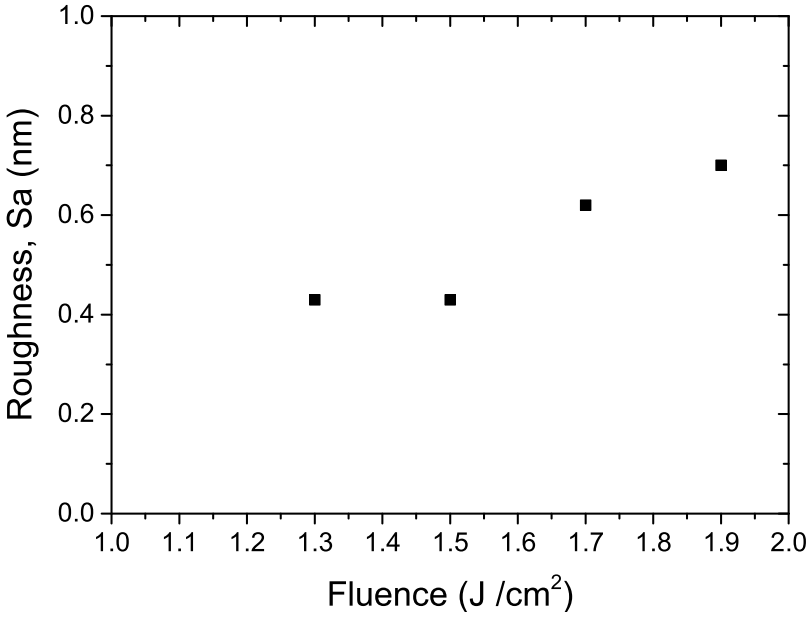

Figure 5.13: Roughness dependency on fluence.

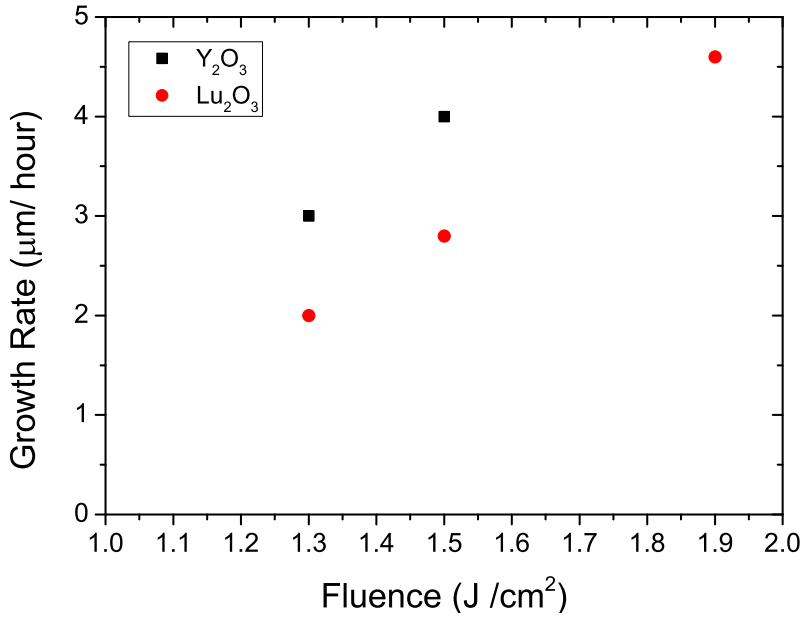

Figure 5.14: Growth rate comparison between Y_2O_3 and Lu_2O_3 samples, all deposited under a background oxygen atmosphere at 2x10^{-2} mBar.

5.5 Conclusions

In this chapter the results of sets of optimisation experiments performed with the doped sesquioxides Tm:Sc_2O_3, Yb:Y_2O_3 and Yb:Lu_2O_3 are presented. The main focus was to minimise the number of surface particulates while maintaining good crystal quality and high growth rate. Minima were found in results of particulate counts for samples grown using different ablation fluences and background pressures, and a trend was identified between ablation fluence and growth rate. The increasing growth rate with higher fluence was similar in each material, but Y_2O_3 showed higher growth rates for a given fluence than the other two materials trialled, which suggests it is more strongly absorbing at the ablation laser wavelength of 248 nm.

The optimum growth conditions for Scandia, Yttria and Lutetia were ablation fluences of 1.5 Jcm^{-2}, 1.3 Jcm^{-2}, and 1.7 Jcm^{-2}, respectively, and a background oxygen pressure of $2x10^{-2}$ mbar in each case.

Chapter 6

Sesquioxide Deposition on Different Substrates

6.1 Introduction

This chapter covers sesquioxide film growth by PLD on a variety of different substrates trialled, and the pros and cons of each. Aspects such as crystallographic orientation, thermal expansion and lattice match are considered and evaluated using the analysis performed following depositions. Where possible, the laser performances of similar samples on different substrates is also compared.

Tables 6.1 and 6.2 provide information on the lattice constants [10] of the cubic substrate and target materials along with the dominant lattice plane detected from them by XRD and the corresponding plane spacing, and the lattice mismatch between these planes (harmonic lattice mismatch, section 3.2.3.3), respectively. It is obvious that some combinations used here provide a very good match, whereas others do not. These differences will be commented on throughout this chapter as different material combinations are presented.

	Material	Lattice constant (Å)	Dominant detected plane	Plane spacing (Å)
Substrate	YAG	12.00	(400)	3.00
			(444)	1.73
Film material	Y_2O_3	10.60	(222)	3.06
	Lu_2O_3	10.40	(222)	3.00
	Sc_2O_3	9.84	(222)	2.84

Table 6.1: Comparison of the lattice constants of the cubic materials used in this thesis and the corresponding plane spacing for the dominant detected planes in the XRD spectra, determined experimentally. These values are calculated using equation 4.2.

		Deposited material		
		Y_2O_3	Lu_2O_3	Sc_2O_3
Substrate	YAG <100>	-1.96%	0%	5.63%
	YAG <111>	13.1%	15.3%	21.8%

Table 6.2: Lattice plane mismatch between substrate and deposited material for the cubic materials used within this thesis. For the sesquioxides on <100>-oriented YAG the calculated lattice mismatch is between the YAG (400) plane and sesquioxide (222) planes, and in the case of <111>-oriented YAG the mismatch has been calculated between the (444) planes of each.

6.2 Growth on Silica

Reports in the literature suggest that it is energetically favourable for these sesquioxides, or at least yttria, to grow in a <222> orientation, even when grown on an amorphous substrate such as silica [72]. This is often not the case for crystal growth, where many materials need to have their crystalline formation seeded either by a small amount of that material in crystalline form or another crystal with similar lattice constant. The energetically favourable <222> growth of yttria on amorphous material provides the benefit of not undergoing strain induced by lattice mismatch and the dislocations required for the crystal lattice to relax (see section 3.2.3). However, the thermal expansion coefficient of silica is $\sim$0.5x10^{-6} /°C [98], which is very different to that of the sesquioxides (8.1x10^{-6} /°C for yttria [97]). This causes significant strain in the samples on cooling as the deposited material and silica substrates contract by different amounts.

The strain induced by thermal contraction was the main concern for these growths, so a number of depositions were performed at different temperatures and the crystallinity and surface morphology subsequently analysed. These depositions were each 1 hour long (72000 excimer shots at 20 Hz) and performed in a background oxygen atmosphere of 4x10^{-2} mbar. Two different fluences, calculated to be $\sim$0.66 J/ cm^2 and $\sim$1.22 J/ cm^2, were used. XRD was performed on each sample and the growth temperature decreased to assess the lowest temperature the deposition could be performed at while still producing crystalline material, as lower growth temperature means less strain would be induced on cooling due to the smaller change to reach room temperature. XRD spectra of such samples are shown in figure 6.1; the spectra displayed are those with the highest and lowest peak counts recorded from this set of samples, showing that the samples with higher peak counts have a higher degree of crystallinity and fewer crystal orientations present within them.

Crystalline growth could be seen at relatively low CO_2 laser heating powers, much lower than those typically used. Crystalline peaks in the XRD spectrum still occured when samples were grown using only 20% of the CO_2 power available to heat the substrate, corresponding to around 450°C [54] (assuming the silica substrates reach a similar temperature to the YAG substrates, which were used in temperature calibration experiments, as they both absorb strongly at the laser wavelength of 10.6 μm). Analysis of the yttria crystal peaks seen in the XRD spectra was performed to see how the peak height and width varied with substrate temperature during growth, the results of which are displayed in figures 6.2 and 6.3, respectively. It is apparent that there is

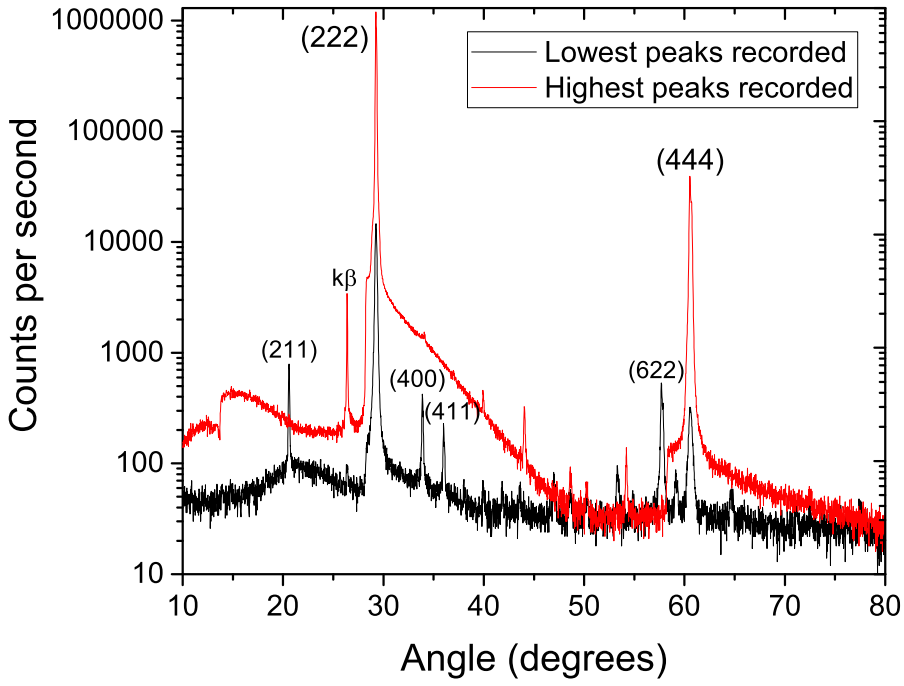

Figure 6.1: Examples of XRD spectra of Y_2O_3 grown on silica.

an optimum point corresponding to 40% CO_2 laser power for heating the substrate (to ~650°C) in the case where the lower of the two fluences was used, which is possibly true for the higher fluence used too, but there is insufficient data to draw this conclusion. The higher peak counts and smaller FWHM indicates that the samples fabricated using a higher ablation fluence are higher quality crystals.

A pole figure measurement was also performed on one of the samples about the (222) peak 2θ angle to determine the orientation of the crystallites on the amorphous substrate. The stereoscopic projection of the data obtained is shown in figure 6.4. The complete ring suggests the crystal grows at all angular orientations, which isn't unexpected given there is no lattice to match to and influence the orientation when an amorphous substrate such as silica is used.

The surfaces of these samples were analysed by an optical interferometric microscope and software (section 4.3.3), and stylus profiler. While the XRD had revealed the samples to be crystalline, the surface analysis showed cracking of the films, making them unsuitable for waveguide applications.

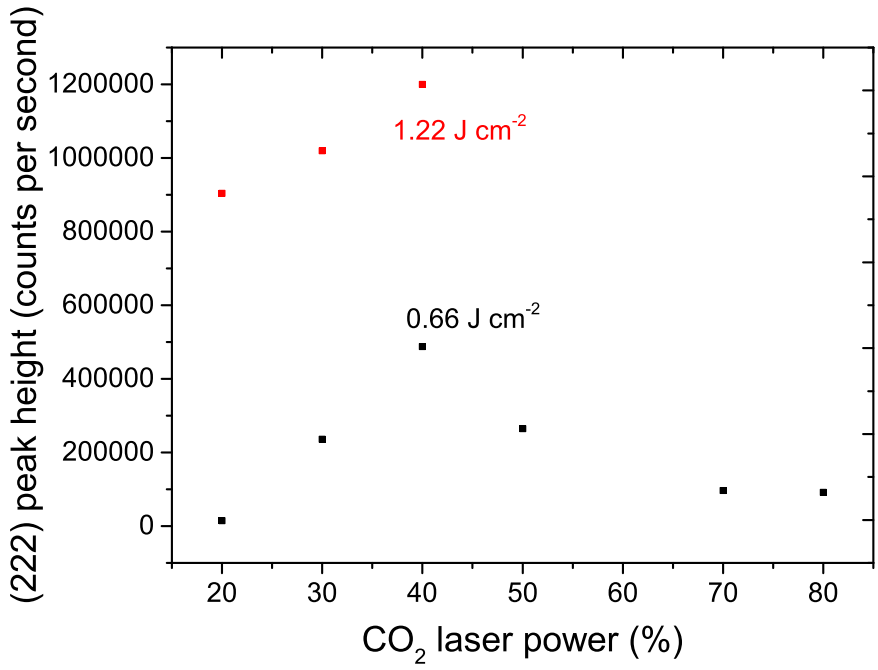

Figure 6.2: XRD peak height variation of Y_2O_3 grown on silica with different CO_2 laser heating power incident on the substrate.

More samples were grown by K. A. Sloyan on silicon substrates with a 15 μm thermal oxide (THOX) layer on either side. The aim of this was to establish whether even lower substrate temperatures could be used. As the thermal expansion coefficent of silicon (2.6x10^{-6} / °C) is ∼5x larger than for silica this was also slightly more promising for yeilding fewer cracks. These depositions were just 30 minutes each (36000 excimer shots at 20 Hz) and performed using an ablation fluence of ∼1.7 J /cm^2 and background oxygen pressure at 4x10^{-2} mbar. As can be seen in figures 6.5 and 6.6, the thin films produced were still highly crystalline down to just 15% CO_2 laser power heating the substrate, corresponding to a substrate temperature of ∼ 400°C, and mostly amorphous at lower temperatures (see plot of XRD peak heights in figure 6.6), although the (222) peak is still visible for the growth at 10% CO_2 laser power in figure 6.5. The large peak around 69° in figure 6.5, labelled A, is unidentified, but as it is present in all scans and not showing the same systematic decrease in magnitude for the lower temperature depositions it may not be coming from the crystal film. However, there are multiple, indistinguishable peaks around 2θ = 69° corresponding to other orientations of yttria.

Images of these films were taken using the ZeScope to check for cracking and it was found that,

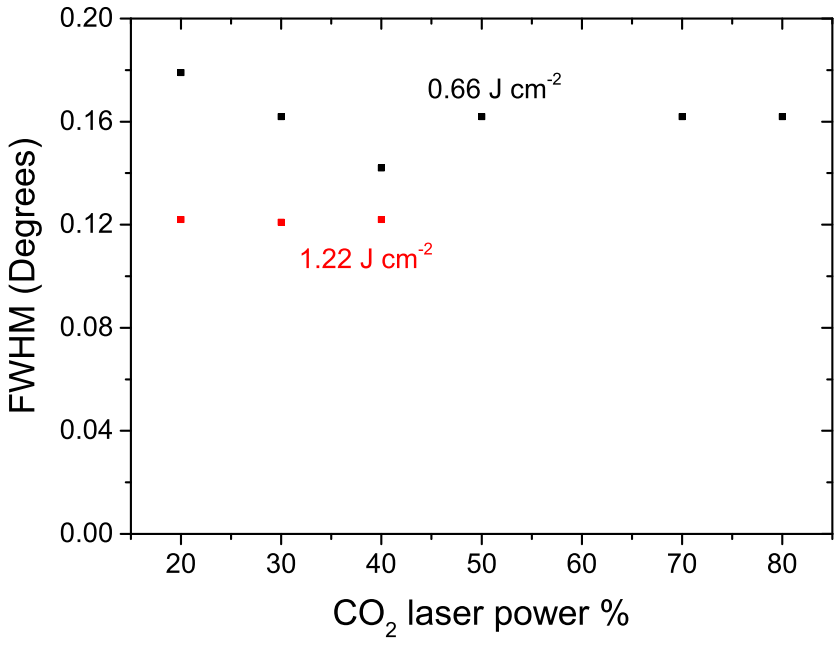

Figure 6.3: XRD peak width variation of Y_2O_3 on silica with incident CO_2 laser heating power.

despite the low temperature growth, the films still cracked, as shown in figure 6.7. The silicon substrates with THOX layers of equal thickness on either side were used with the idea that this symmetry may make the substrates more resistant to flexing under the growth of the depositing film and on cooling when the materials are contracting by different amounts. As the yttria films deposited on these substrates cracked, further experiments were done in an attempt to compensate the stress on one side by matching it on the other. Depositions of crystalline yttria on both sides of the substrates were trialled, as well as an amorphous yttria layer on one side (deposited at room temperature) and crystalline layer on the other. This attempt at making the samples symmetrical to eliminate cracking failed. Therefore, while the crystalline quality of the yttria on silica/ silicon is good (even when deposited at relatively low temperatures), this combination isn't viable for waveguides and therefore was not pursued further.

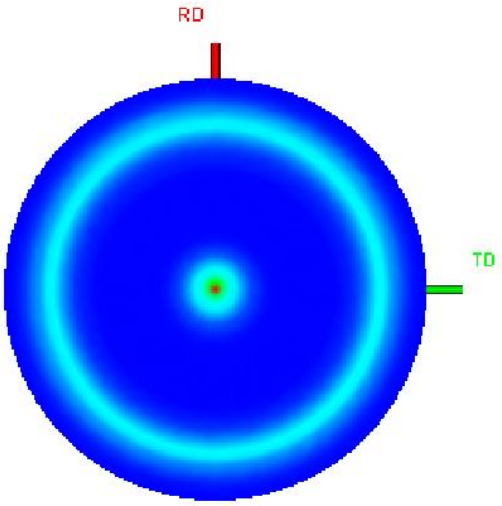

Figure 6.4: Pole figure of Y_2O_3 on silica.

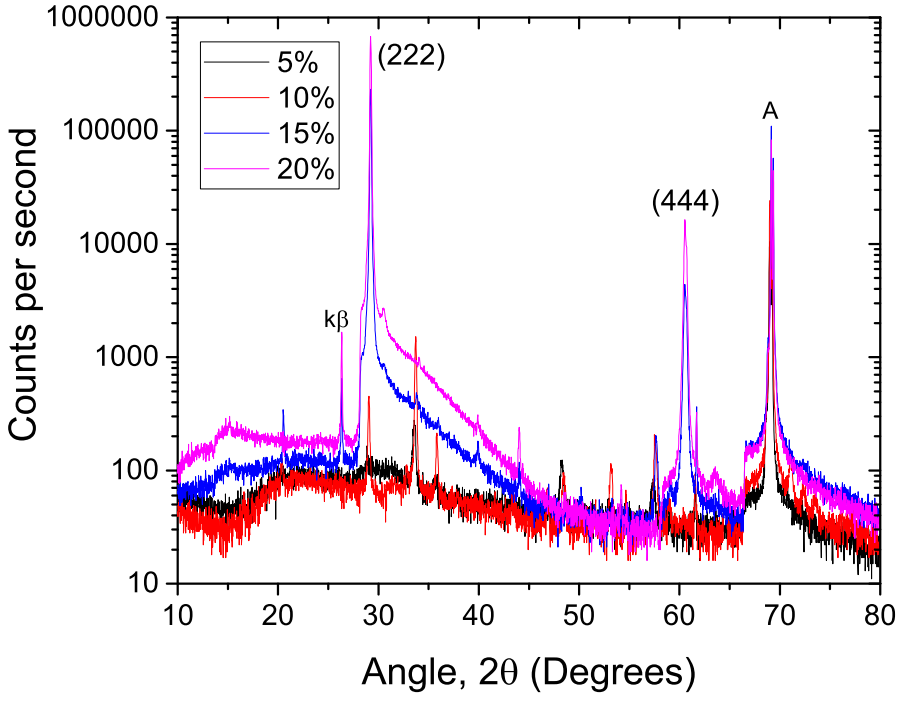

Figure 6.5: XRD of yttria deposited on Si substrates with THOX layer at different temperatures.

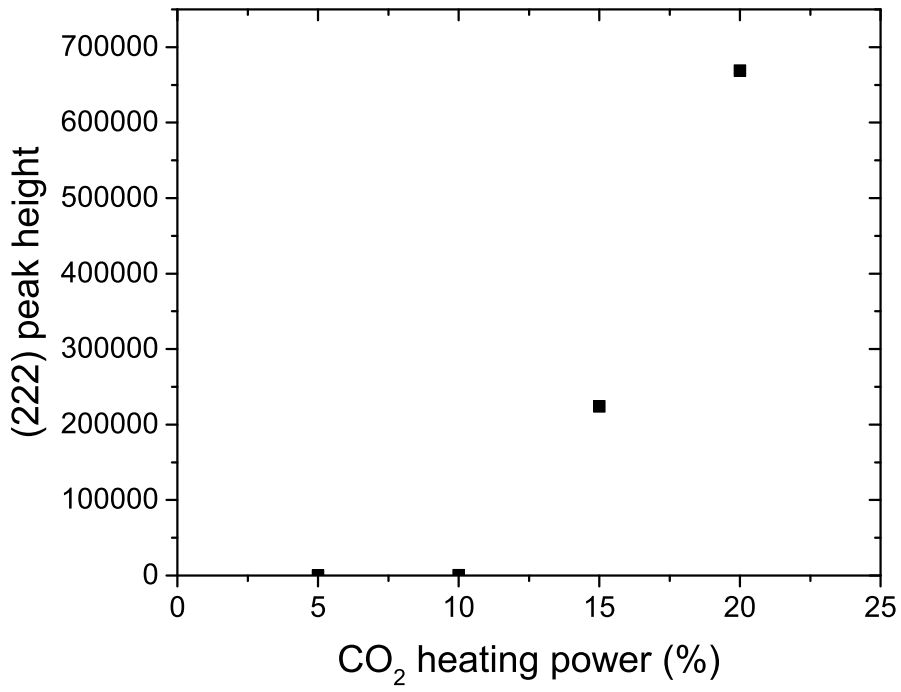

Figure 6.6: (222) peak height variation, corresponding to the XRD in figure 6.5, for yttria deposited on Si substrates with THOX layer at different deposition temperatures.

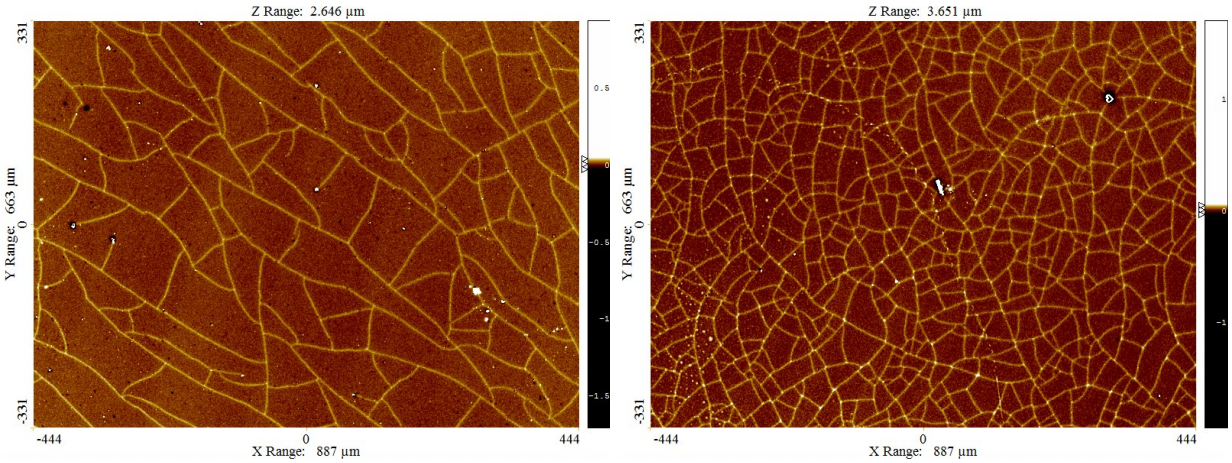

(a) 20% CO_2 power.

(b) 15% CO_2 power.

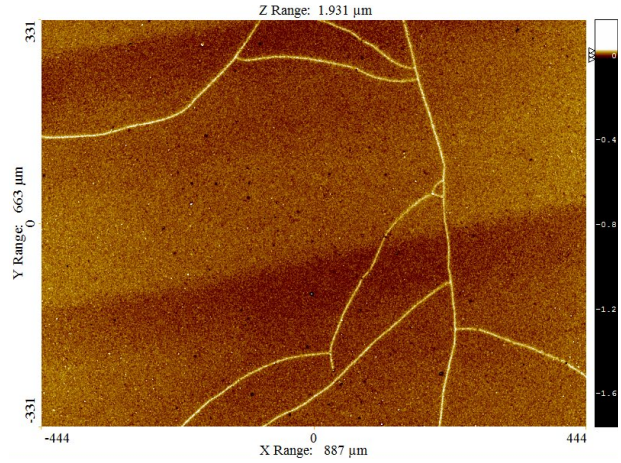

(c) 10% CO_2 power.

Figure 6.7: ZeScope images of yttria deposited on Si substrates with THOX layer, all at 10x magnification. The % CO_2 power label for each image corresponds to the percentage of the available CO_2 power incident on the substrate during the deposition; these values are approximately 10.3 W for 30%, 6.6 W for 20%, 4.6 W for 15%, and 2.5 W for 10%.

6.3 Growth on YAG

The majority of samples created during this PhD have been on YAG substrates, as stated in the introduction, chapter 1. This section looks at growth on YAG substrates of two different orientations, <100> and <111>-cut YAG.

6.3.1 YAG <100>

In the case of Y_2O_3 growth on <100>-oriented YAG, a near lattice match is achieved between the (222) Y_2O_3 plane and (400) YAG, as indicated by the overlapping peaks seen in the XRD spectrum shown in figure 6.8. The lattice match here is like that pictured on the far right of figure 3.4 in chapter 3, between different crystal planes. XRD peaks that correspond to the (332) and (440) yttria planes have also been identified, but are orders of magnitude smaller, and peaks labelled kβ are artifects of the x-ray radiation source used (associated with the very large (222) and (444) yttria peaks).

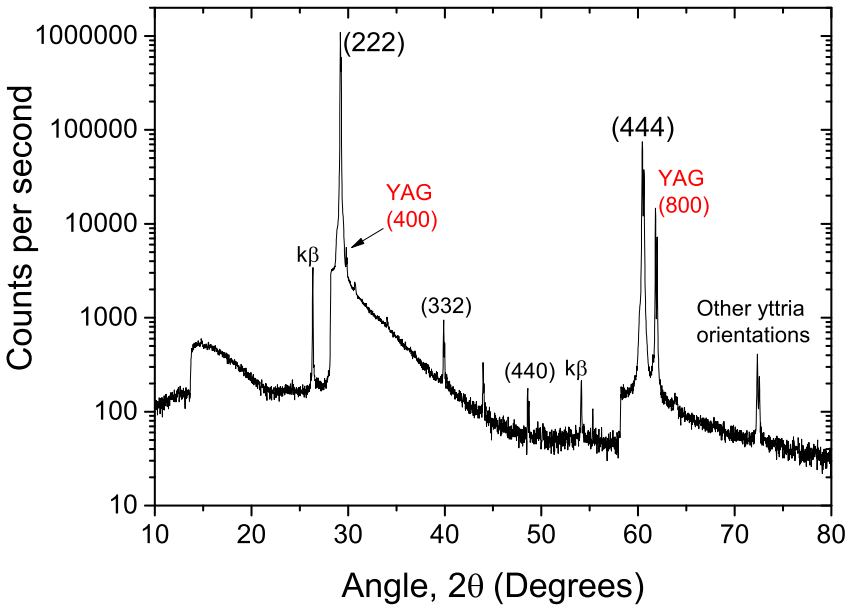

Figure 6.8: XRD of Y_2O_3 on YAG <100>.

A pole figure measurement of an Yb:Y_2O_3 film deposited on a YAG <100> substrate was performed about the 2θ angle corresponding to the dominant (222) yttria peak. A stereoscopic

projection of the data collected is displayed in figure 6.9. The theoretical expectation for single crystal <111>-oriented yttria is to obtain a central maximum and three evenly spaced spots around it at an α angle of 19.5°. However, there are clearly 12 peaks surrounding the central maximum in the pole figure in figure 6.9. This suggests that the <111>-oriented yttria has grown in four rotational orientations on the <100>-oriented YAG substrate, a representation of which is also shown in the right hand image of figure 6.9. The theoretical positions of the peaks for the <111>-oriented yttria in these four rotational orientations are marked on the pole figure as black dots, over the stereoscopic projection of collected data. The weak signal between these peaks suggests there is a small amount of the grown crystal in other rotational orientations and the splitting in α indicates tilt in the crystal growth, away from the ideal <111> orientation.

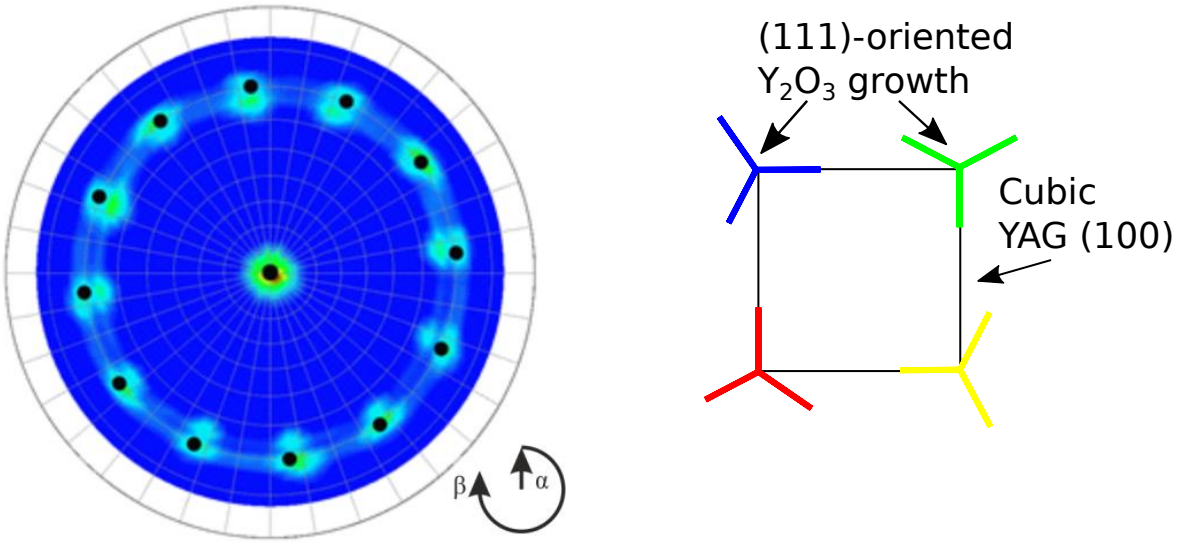

Figure 6.9: (222) pole figure of Yb:Y_2O_3 on a YAG <100> substrate. The image to the right represents four rotational orientations the <111>-oriented yttria growth may be sitting in on the YAG substrate.

A selection of depositions of Y_2O_3 on <100>-oriented YAG were performed at varying substrate temperatures for comparison, using an ablation fluence of 1.3 J/ cm^2 and background oxygen pressure of $2x10^{-2}$ mbar, as determined as optimal for minimising particulates while maintaining a reasonable growth rate through optimisation experiments, presented in section 5.3.

The SEM image displayed in figure 6.10 shows a backscatter detector (BSD) image of a sample surface. This surface appears to be smooth and largely free from particulates, but shows patterning

that is likely to be associated with crystal domains of different rotational orientations of the (222) Y_2O_3 growth and other growth orientations. The following collection of SEM images in figure 6.11 show BSD images of sample surfaces on the left, in (a), (c) and (e), and corresponding end facets on the right, in (b), (d) and (f). These images are displayed in order of increasing incident CO_2 power for substrate heating, and therefore in order of increasing deposition temperature. These samples all display patterning on the surface, but on a smaller scale than in figure 6.10, which suggests the crystal domain sizes in these growths are smaller. Smaller domain sizes means there

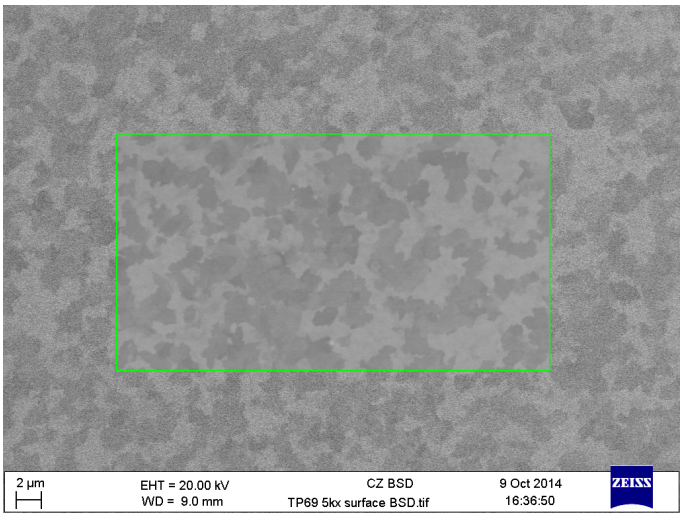

Figure 6.10: SEM images of Y_2O_3 on YAG <100>.

are more grain boundaries that will potentially act as scattering centres and increase loss. These domains can be seen as internal structure through the waveguide layer in the images taken of the polished facets; detail in the structure generally appears finer close to the substrate where the growth is initiated and then gradually relaxes away from the substrate and the domains, seen as columns, become larger and more defined.

These samples also had their surfaces examined using a ZeScope and particulate count measurements were performed in five positions over the sample surface, each covering an area of 134 x 179 μm^2. Few particulates were found on each of the three sample surfaces, with average counts of between one and two particulates >100 nm and between 3 and 6 particulates >50 nm in diameter in each case. Laser experiments were performed on some of the better Yb:Y_2O_3 samples grown in this project, the results of which can be found in chapter 8.

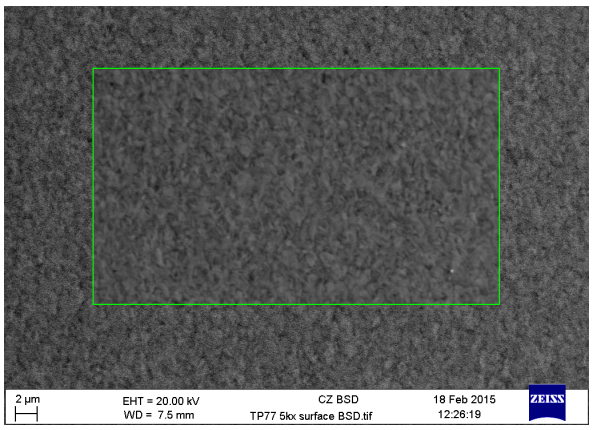

(a) 70% CO_2

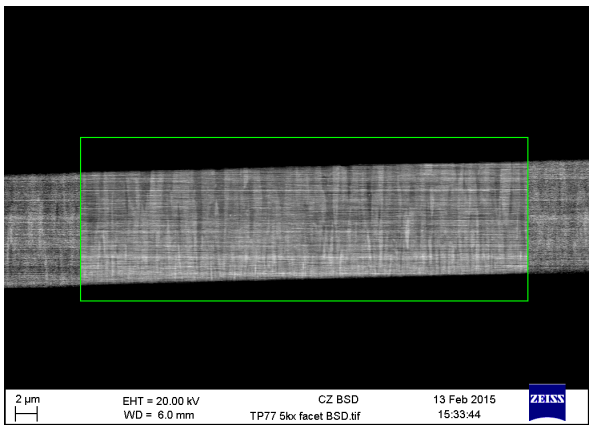

(b) 70% CO_2

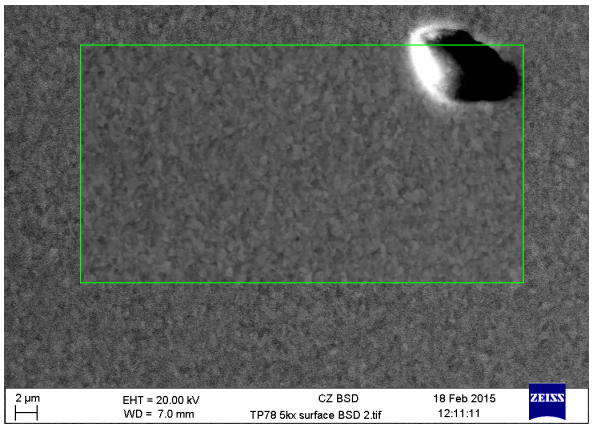

(c) 75% CO_2

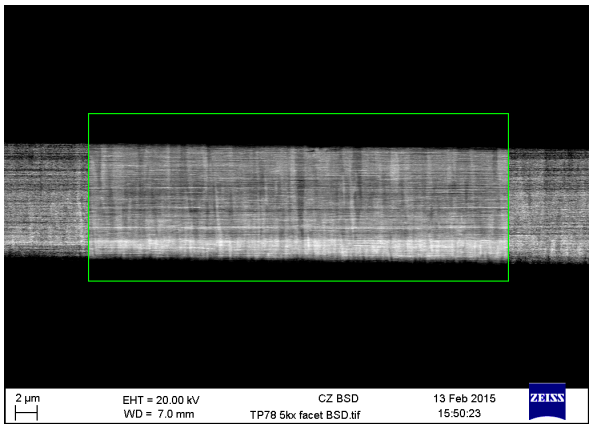

(d) 75% CO_2

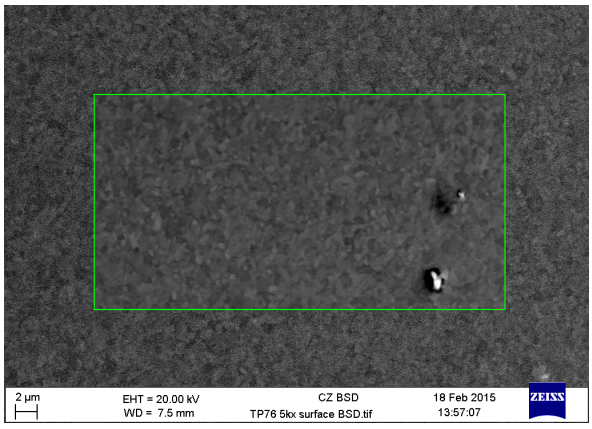

(e) 80% CO_2

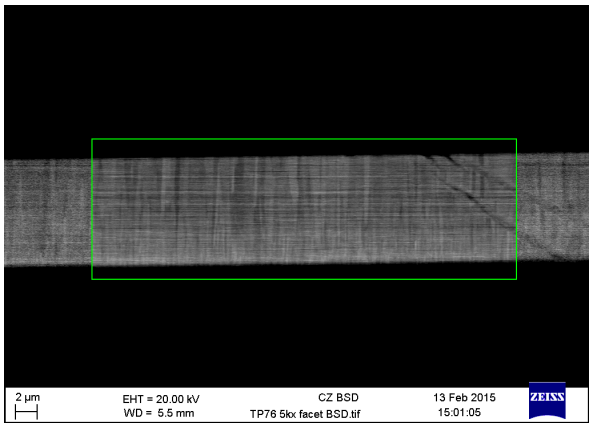

(f) 80% CO_2

Figure 6.11: SEM images of the surfaces and facets of Yb:Y_2O_3 on YAG <100> samples, deposited at 3 different substrate temperatures. The horizontal lines in the images are artifacts from the settings that were required to see the columnar detail in these films.

6.3.2 YAG <111>

As the sesquioxides grow preferentially in the <111> orientation, growth of Y_2O_3 was trialled on <111>-oriented YAG substrates at four different growth temperatures. However, as suggested in table 6.2 at the beginning of this chapter, the lattice mismatch between this substrate-film combination is large. Comparison of the (444) peaks for both YAG and Y_2O_3, as seen in the XRD spectrum in figure 6.12, suggests a lattice mismatch of 13.2% between these two crystals, which is in keeping with the data in table 6.2.

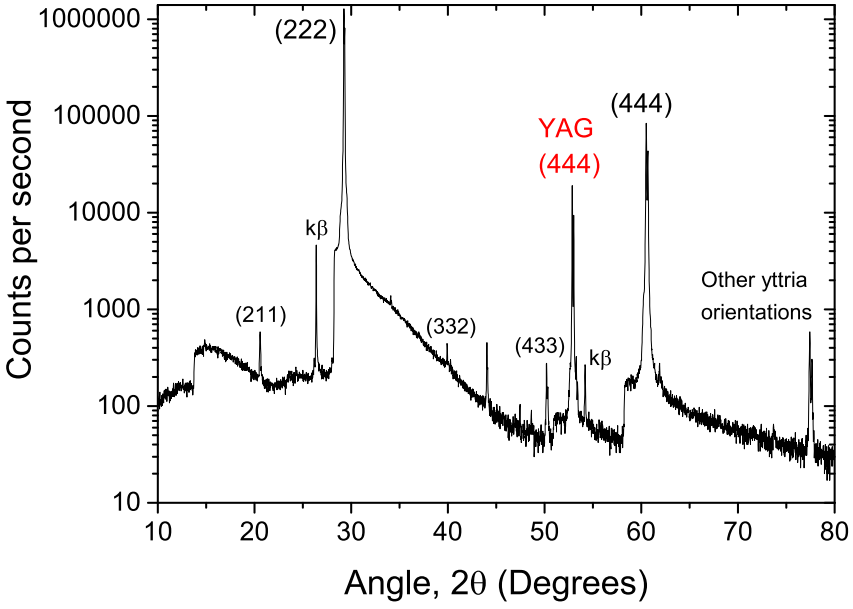

Figure 6.12: XRD spectrum of Yb:Y_2O_3 on YAG <111>.

Pole figure measurements were also taken on these samples about the dominant (222) peak seen in the standard XRD scan. Examples of these pole figures can be seen below in figure 6.13. As previously stated, the expected pattern from <111>-oriented crystalline material is a central spot and three other evenly spaced peaks surrounding it at an α angle of 19.5° from the centre. However, while the peaks present do sit around a ring at an α value of 19°, there are again far more than three peaks. In figure 6.13(a), taken from a sample deposited with the highest substrate temperature achieveable, estimated from previous work (by T. C. May-Smith) to be nearing 1200°C, there are 18 peaks separated by 20° in β, in an alternating pattern of three being distinctly separate from each other and three being blurred together. Another sample grown at a slightly cooler deposition

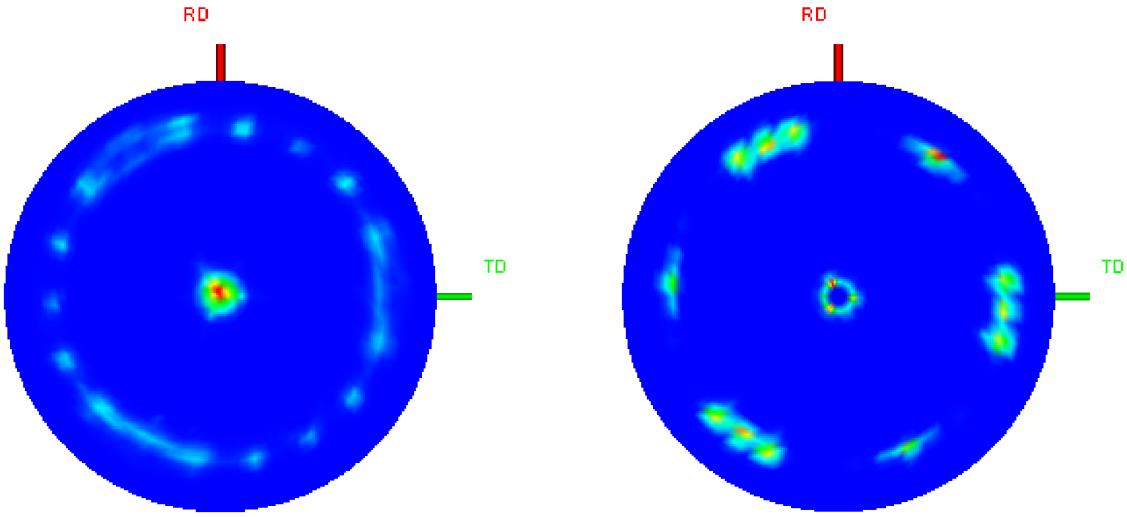

(a) (b)

Figure 6.13: Pole figure data from Yb:Y_2O_3 samples on <111>-oriented YAG.

temperature, estimated to be ∼1100°, also had a pole figure measurement taken that produced the stereoscopic projection seen in figure 6.13(b). The ring of peaks again falls around 19° in α but this time with three groups of three closely spaced peaks (10° between them), and three more peaks evenly spaced in between these. The ring in the centre of this image instead of a spot suggests misalignment of the sample during the measurement.

SEM images of the surfaces of the four depositions of Y_2O_3 on YAG <111> substrates performed under the same conditions, bar the CO_2 laser heating power on the substrate, and therefore the substrate temperature, are displayed in figure 6.14. These images were produced using the BSD and are arranged in order of increasing substrate temperature during deposition. In the case of Y_2O_3 growth on YAG <111> substrates the surface morphology appears to change fairly dramatically between the sample grown at the coolest temperature estimated to be around 900°C in part (a) of figure 6.14 and the sample grown at an estimated 1200°C in part (d). These temperature estimates are likely to be a little high, owing to the use of a different substrate holder (the one used in these experiments is likely to have caused greater heat sinking of the substrate, compared to those used in the temperature calibration experiments [54]). The sample surfaces appear to become increasingly rough for hotter growth temperatures, and are therefore likely to have higher waveguide losses. While the surface morphology, as seen by an SEM, changes, the

number of surface particulates for each of these samples is consistently low (average measurements of <10 particulates >50 nm within the 134 x 179 μm^2 area viewed), as detected using a ZeScope.

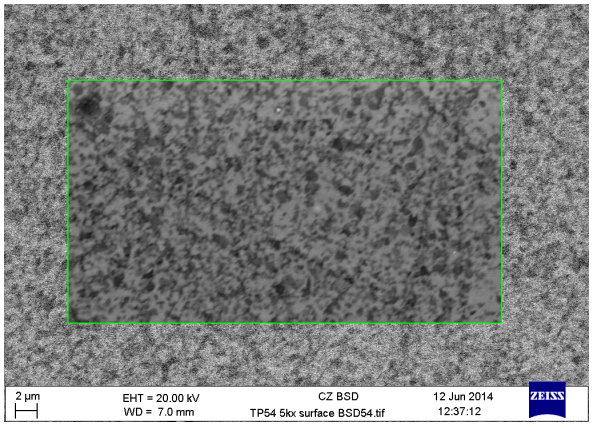

(a) 65% CO_2

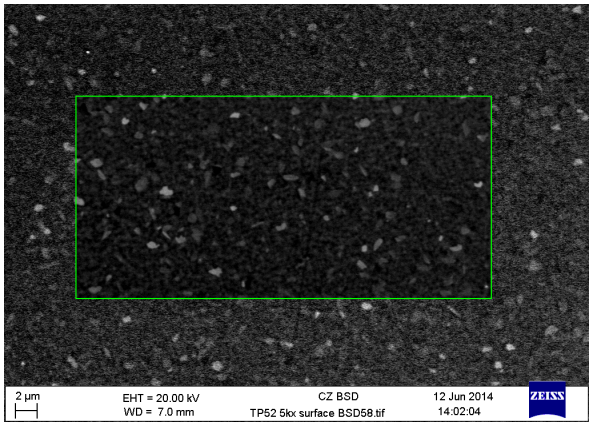

(b) 75% CO_2

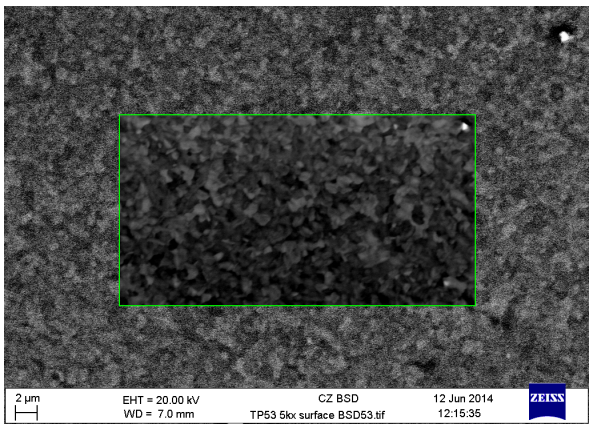

(c) 85% CO_2

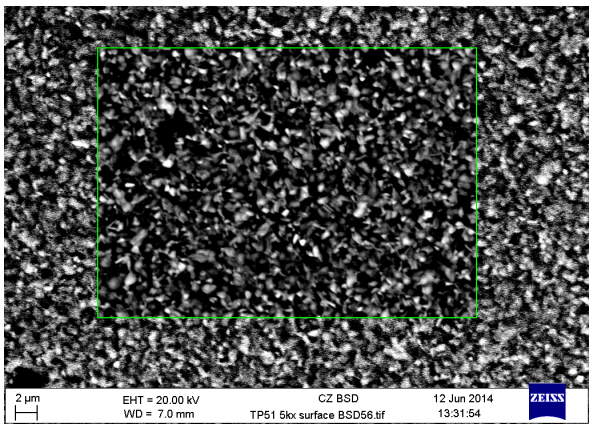

(d) 95% CO_2

Figure 6.14: SEM images of Y_2O_3 on YAG <111> at a range of substrate temperatures during growth, increasing from (a) to (d).

Laser experiments were carried out on these samples so that their performance could be compared with that acheived from growths on <100>-oriented YAG. The samples were pumped with a single-mode fibre-coupled laser diode, with a grating-stabilised wavelength of 975.1 nm, in a setup similar to that seen later in figure 10.1. The laser characterisation curves are plotted in figure 6.15. The best result achieved from the sample grown at the highest temperature, the sample surface of which is shown in figure 6.14(d), had the worst slope efficiency of this group of samples, likely due to scattering loss at the textured surface. The best results achieved with two of the other samples are very similar in their maximum output powers and slope efficiencies. In these experiments, the

waveguides were translated to search for the best areas for laser operation, but these low slope efficiencies of <4% were the best that could be achieved. Laser characterisation experiments performed prior to this with samples grown on YAG <100> substrates had consistently higher slope efficiencies, so no further growths on <111>-oriented YAG substrates were performed.

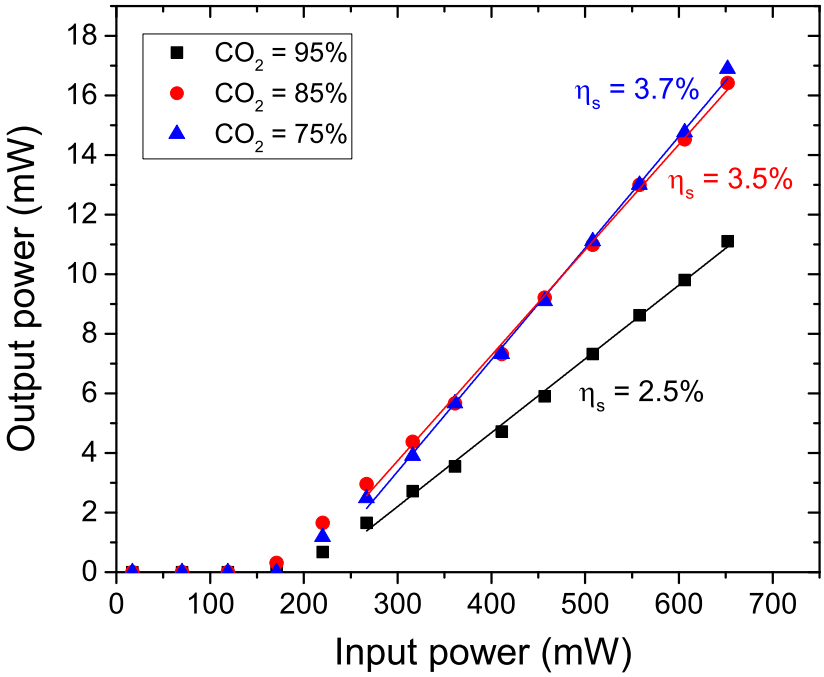

Figure 6.15: Laser characterisation of samples grown on <111>-oriented YAG substrates.

6.3.3 Intermediate layers

Following the results of the crystal growth on the YAG substrates, both <100> and <111>-oriented, and on amorphous substrates, a number of growths were performed on YAG substrates that had had a thin layer of silica sputtered onto it. The aim of this amorphous intermediate layer was to disrupt the lattice match so that the growing crystal wouldn't form in the four rotational orientations suggested by the pole figure of yttria on YAG <100>, and would prevent the large lattice mismatch seen with growth on YAG <111> substrates, providing the intermediate layer was thick enough. This section displays the results of these growths as a comparison to the growths directly on the <100> and <111> substrates in sections 6.3.1 and 6.3.2, respectively.

A pole figure measurement was performed on a sample that had been grown under comparable conditions to those used for the growth of the sample whose pole figure is shown in figure 6.13(a), the only difference being that an intermediate silica layer had been sputtered onto the YAG <111> substrate prior to the Yb:Y_2O_3 deposition. Figure 6.16 displays the results of this pole figure measurement twice, with two different peak intensity levels. In figure 6.16(a), there are clearly 12 peaks present, again in a ring sitting at an α angle of around 19°. These 12 maxima do not have equal spacing between each of them, but appear to have six pairs of peaks. This is clearly different from the pole figures of the growth directly onto the <111>-oriented YAG substrates, but the patterns arising from each of these samples is not fully understood. In figure 6.16(b) the signal intensity has been increased to reveal that there is a faint ring at $\alpha = 19°$, intersecting the 12 maxima, suggesting a small amount of growth in all rotational orientations. A solid ring, as seen in figure 6.4, was the expected result if the lattice match was completely disrupted by the intermediate layer. The low intensity ring implies the silica interemediate layer has had some effect on the crystal growth, but was not sufficient to completely disrupt the crystal lattices trying to match during growth.

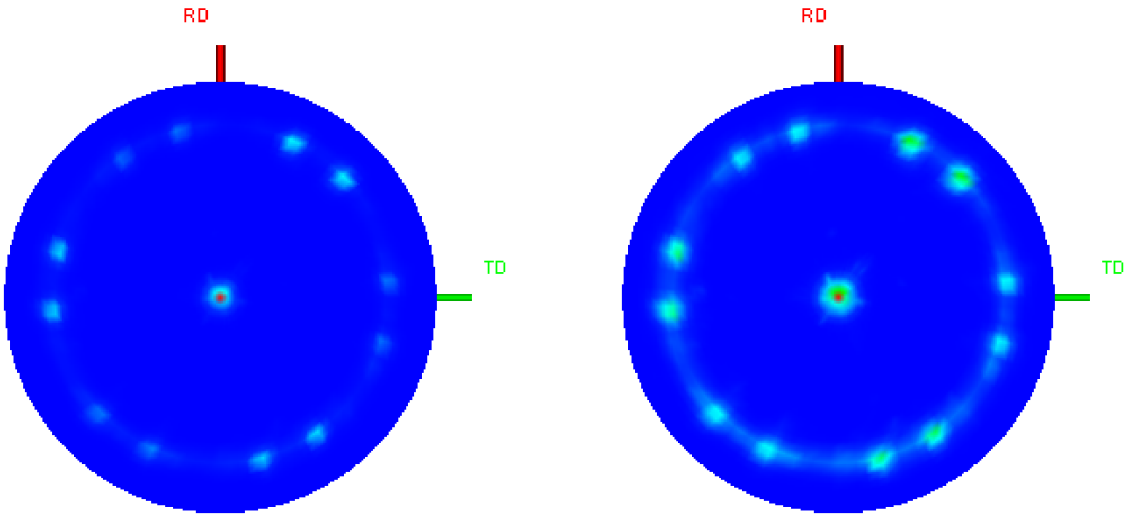

(a) (b)

Figure 6.16: Pole figure plots of an Y_2O_3 sample deposited on a YAG <111> substrate with silica intermediate layer (shown in figure 6.18 (h)).

Results of another pole figure measurement are displayed in figure 6.17. The sample from

which this data was obtained was a PLD-grown Yb:Y_2O_3 layer deposited on a <100>-oriented YAG substrate with a sputtered intermediate layer of silica on the surface. In figure 6.17(a), 12 evenly spaced peaks at 30° separation in β are present, again in a ring at an α angle around 19°. This fits with the analysis of Yb:Y_2O_3 on <100>-oriented YAG presented in figure 6.9. Increasing the signal intensity of the collected pole figure data in figure 6.17(a) gives the pattern shown in figure 6.17(b). While there was some signal at rotational orientations other than at the 12 peaks seen in figure 6.9, the ring seen in figure 6.17(b) appears more complete due to higher signal at all rotational orientations. Unsurprisingly, this result is part way between what was seen for growth on silica, shown in figure 6.4, and that seen when growing straight onto <100>-oriented YAG, seen in figure 6.9. As with the growth on <111>-oriented YAG, this pole figure supplies evidence that the silica intermediate layer has partially disrupted the lattice match between substrate and grown material.

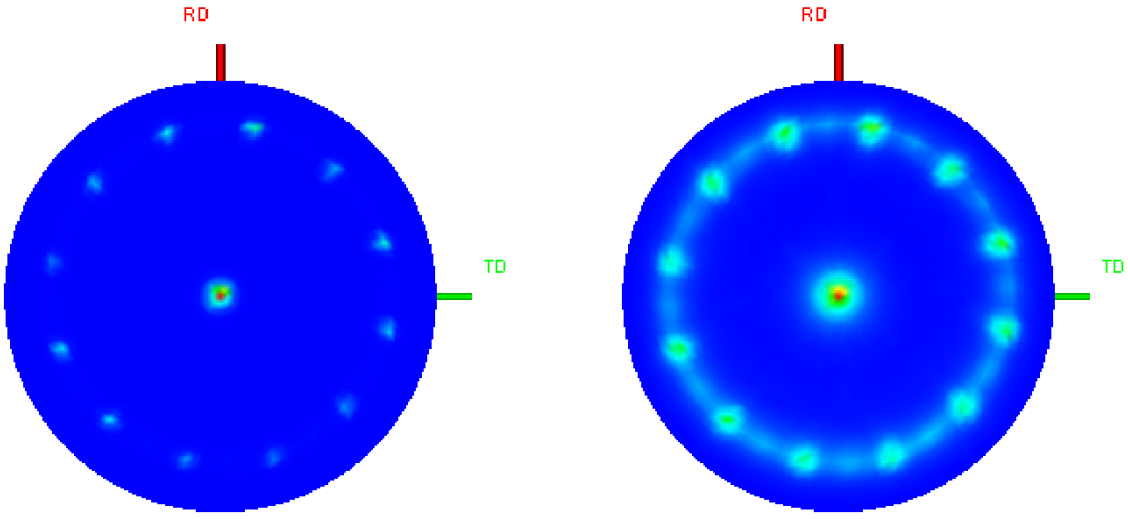

(a) (b)

Figure 6.17: Pole figure plots of an Y_2O_3 sample deposited on a YAG <100> substrate with silica intermediate layer (shown in figure 6.19 (f)).

SEM BSD images have been taken of the surfaces and the polished end facets of the samples grown on <111> and <100> YAG with a silica intermediate layer, and can be seen in figures 6.18 and 6.19 respectively. Despite all of the substrates having undergone the same treatment of having a layer of silica sputtered onto the surface, this layer is only obviously visible in three out

of eight of the SEM BSD images of the polished facets, images 6.18(h) and 6.19(f) and (h). The columnar structure through these samples appears to be broader than that seen previously in the growths directly on YAG <100>, referring back to figure 6.11, and compared to the other growths supposedly on a silica intermediate layer but where it is not visible in the SEM images. As well as being broader, the columns in 6.18(h) and 6.19(f) and (h) run, on the whole, all the way through the sample, whereas they mostly merge part way in the other, more finely structured, samples. As for the sample surfaces, all appear to have some patterning most of which is reasonably uniform, however there are some variations. In figure 6.18(c) the sample imaged has structure running in lines across the surface; this doesn't seem to be a systematic change with growth conditions (only temperature has been changed here) as it is a solitary case within this set of depositions. The next sample, in figure 6.18(e), appears to have a smoother, more finely textured surface, but with various features that have potentially arisen due to target degredation that has resulted in particulates that have either been deposited on the surface or caused damage to the material already deposited. These features are counted as clusters of particulates by the ZeScope and SPIP software, which gave particulate counts that, on average, translate to 1.9x10^5 /cm^2 for particulates >50 nm and 2.6x10^5 /cm^2 for particulates >100 nm. These values are in the region of two orders of magnitude greater than the average particulate density for the samples displayed in images 6.18(a) and (g). In figure 6.19, the surfaces shown in (a) and (c), corresponding to the facet images in (b) and (d), respectively, where the intermediate silica layer isn't visible are very similar. The surfaces in (e) and (g) are also very similar to one another, corresponding to facet images (f) and (h) where the silica layer can be seen, but appear rougher than the surfaces in (a) and (b), which is supported by surface roughness measurements taken using the ZeScope and software. Sa roughness measurements and particulate counts were again performed at five locations on the sample surfaces and averages calculated. The roughness of the sample surface seen in image 6.19(a) was 4.0 nm, and 8.2 nm for the sample seen in (g). The average particulate densities for these sample surfaces were calculated to be 1.3x10^4 /cm^2 for particulates >100 nm and 2.3x10^4 for particulates >50 nm, and 8.3x10^4 /cm^2 >100 nm and 8.8x10^5 /cm^2 >50 nm for the samples seen in images 6.19(a) and (g) respectively.

Laser characterisation experiments were performed using the same setup as for the Yb:Y_2O_3 waveguides deposited directly on YAG <111> substrates, with the single-mode fibre-coupled diode laser as the pump source. The results of these experiments are displayed in figure 6.20, where each

set of results is identifiable by the underlying substrate orientation and the CO_2 laser power % used for substrate heating during deposition (see table 4.1 for corresponding temperature estimates). For these samples with an intermediate layer of silica, no laser results were achieved using the samples deposited at the highest growth temperature, hence there are only six characterisation curves present in figure 6.20. The samples grown at the higher temperatures had very similar slope efficiencies, independent of the underlying substrate, with those deposited with 85% CO_2 heating displaying slopes of around 2% and those deposited with 75% CO_2 heating displaying slightly higher slopes in excess of 4%. The two samples deposited with 65% CO_2 laser power heating the substrate display high slope efficiencies with a bigger difference between them than for the other samples. This difference could be due to the effects of the substrate and silica layers, but not necessarily as the results acquired from any given waveguide fluctuate, sometimes fairly dramatically, depending on the lateral position of the waveguide in the pump beam. However, the results obtained here suggest that a lower growth temperature leads to better waveguides in the case of growths on an intermediate silica layer. A plot of how the slope efficiencies obtained with samples at different growth temperatures can be seen in figure 6.21. There is clearly a correlation between the growth temperature and slope efficiencies obtained in laser characterisation experiments. Further experiments could have been performed using less CO_2 power for substrate heating, to enable an optimum growth temperature to be determined for the growth on YAG substrates with an intermediate silica layer and the maximum achievable slope efficiency. Looking back to the SEM images in figures 6.18 and 6.19, the better laser results were acheived from the samples whose surfaces appear smoother, and not from those with bigger domains (larger columns in the facet images).

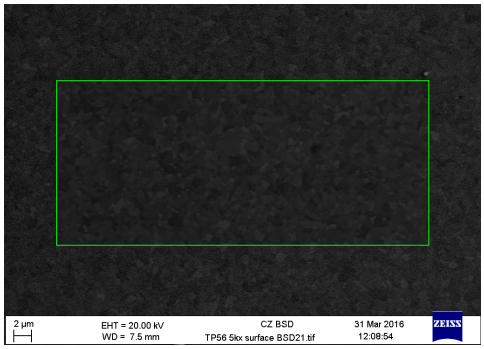

(a) 65% CO_2, surface.

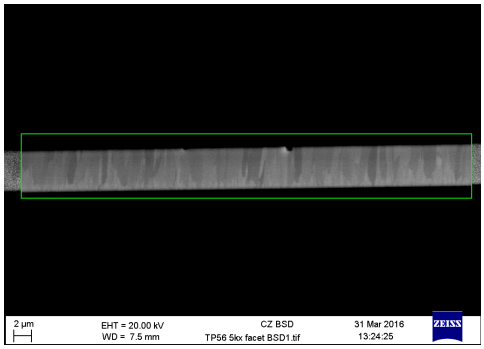

(b) 65% CO_2, facet.

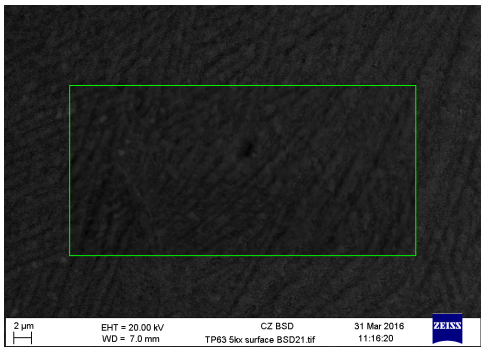

(c) 75% CO_2, surface.

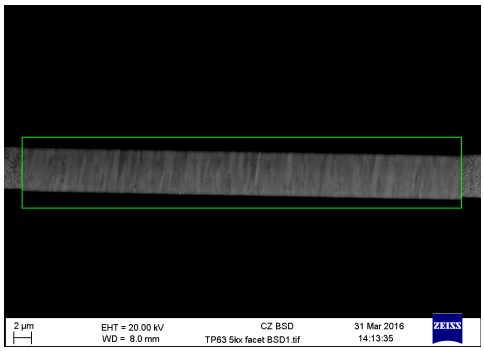

(d) 75% CO_2, facet.

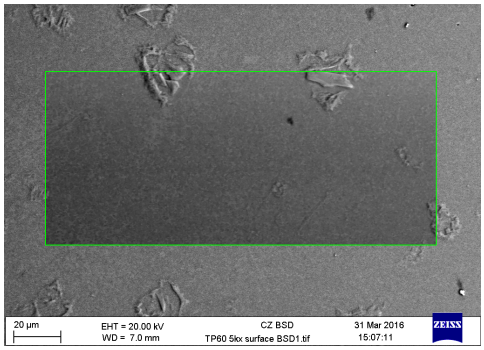

(e) 85% CO_2, surface.

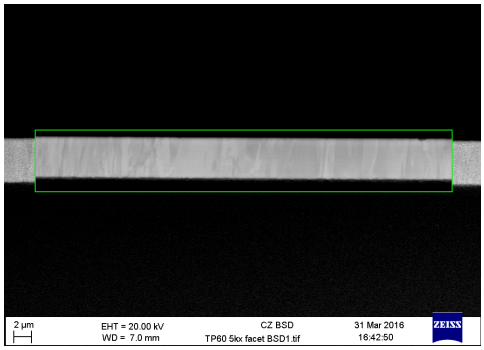

(f) 85% CO_2, facet.

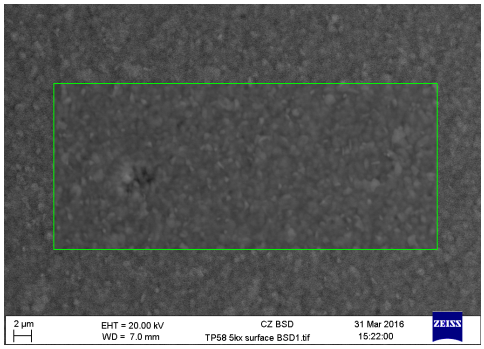

(g) 95% CO_2, surface.

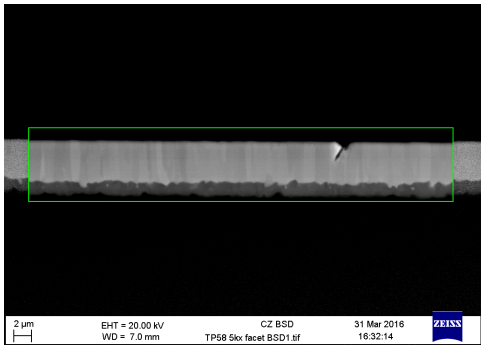

(h) 95% CO_2, facet.

Figure 6.18: SEM images of Y_2O_3 on YAG <111> with a silica intermediate layer.

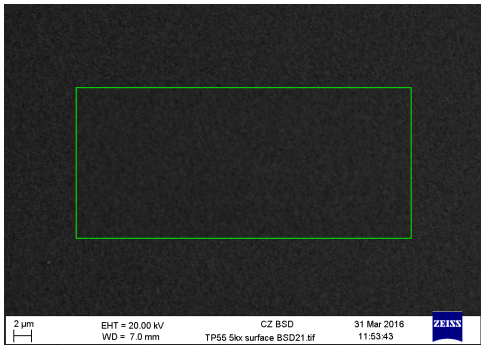

(a) 65% CO_2, surface.

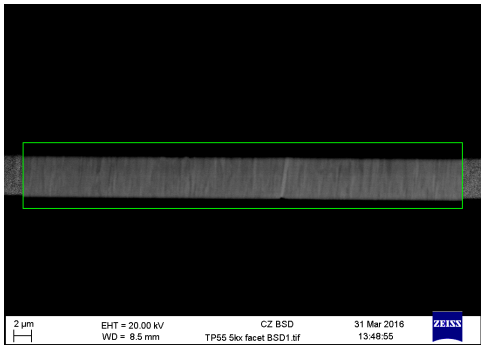

(b) 65% CO_2, facet.

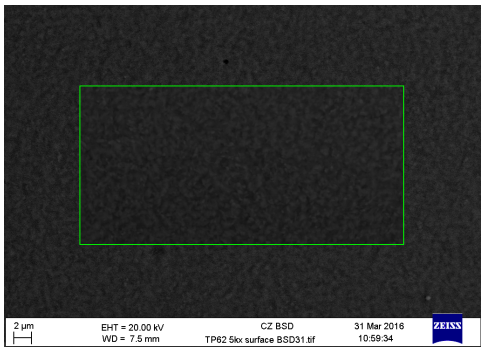

(c) 75% CO_2, surface.

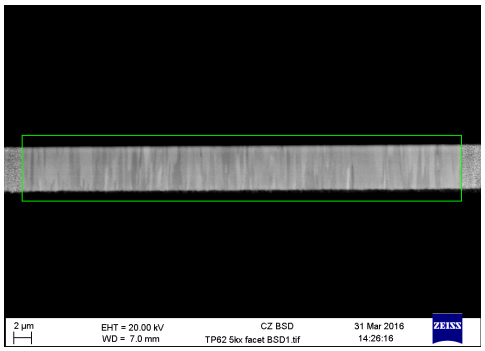

(d) 75% CO_2, facet.

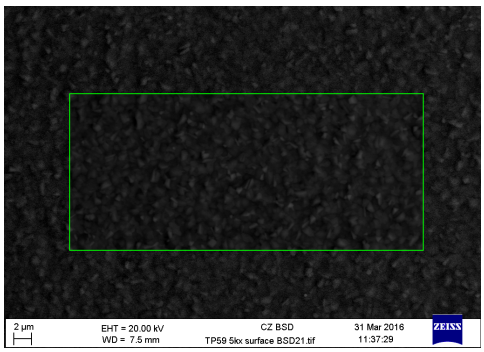

(e) 85% CO_2, surface.

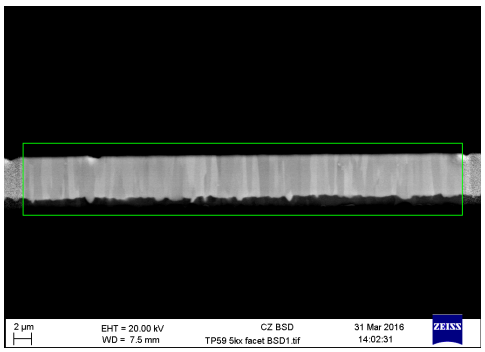

(f) 85% CO_2, facet.

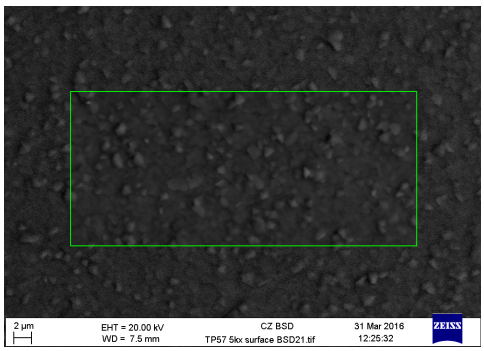

(g) 95% CO_2, surface.

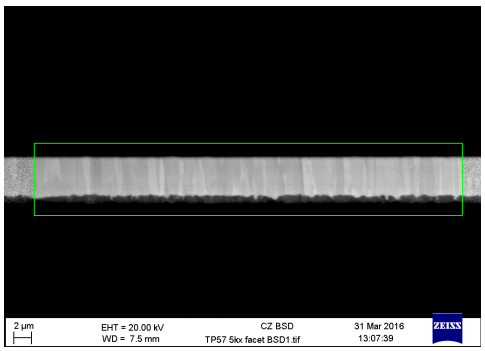

(h) 95% CO_2, facet.

Figure 6.19: SEM images of Y_2O_3 on YAG <100> with a silica intermediate layer.

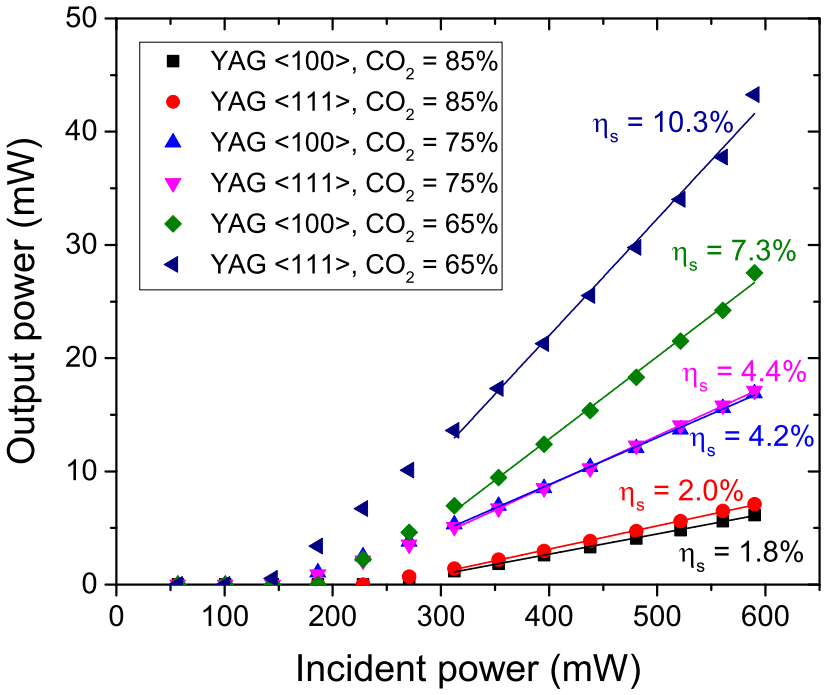

Figure 6.20: Laser characterisation of Yb:Y_2O_3 waveguides deposited on YAG <100> and <111> substrates with an intermediate silica layer. Results obtained from waveguides grown at three different temperatures are shown, where higher temperatures are associated with greater CO_2 laser power percentage used.

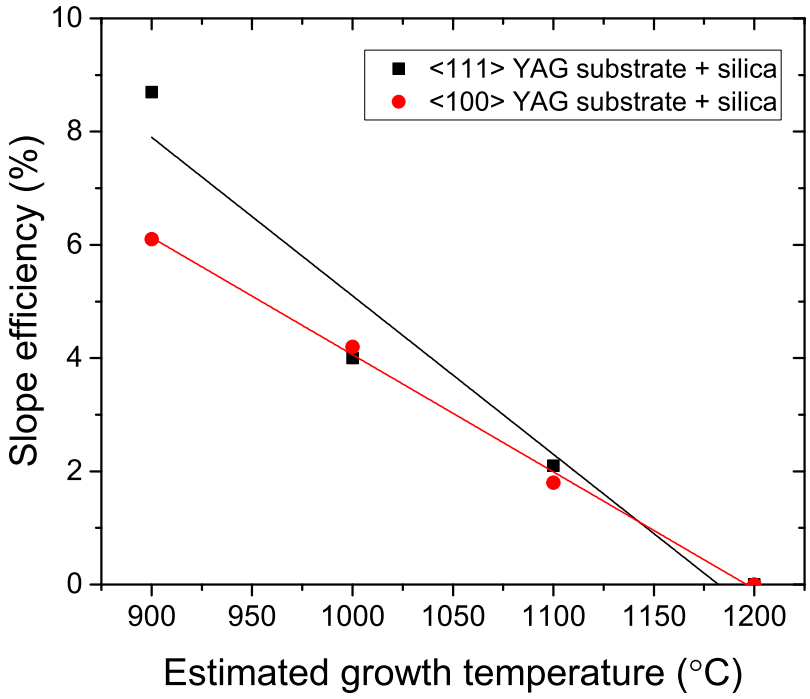

Figure 6.21: Laser slope efficiencies achieved with the waveguide samples on an intermediate silica layer as a function of growth temperature.

6.4 Growth on c-cut Sapphire

Sapphire is another readily and cheaply available substrate with high thermal conductivity (30.3 W/(m.K) perpendicular to the c-plane and 32.5 W/(m.K) parallel to the c-plane at room temperature [99]) and, when c-cut, with a lattice constant of 4.76 Å (at 295K) [10,99] that provides a fairly close lattice match between the sesquioxide crystal lattices and 3 units of the sapphire crystal lattice (mismatch of 4.7%, 2.9% and 2.6% with <111>-oriented Y_2O_3, Lu_2O_3 and Sc_2O_3, respectively). With a refractive index of 1.76 (at 1.03 μm) [100], sapphire is also suitable as a substrate material for depositing sesquioxide films that will act as waveguides. However, sapphire is a very hard crystal (Mohs hardness of 9 [99]) which results in an even longer, more labour intensive polishing process (and diamond-based grit for the lapping process). The work using sapphire reported in this thesis is therefore fairly minimal, and revolves around investigation of the material growth and the possibility of growing thicker layers of the sesquioxides on sapphire to be used in a thin disk laser setup, which avoids the need to polish end facets.

Depositions of Yb:Y_2O_3 on sapphire were performed and the growths analysed. Two samples were grown using an ablation fluence of 1.7 J/ cm^2 and background oxygen pressure of 4x10^{-2} mbar, each for 4 hours. Very similar temperatures of around 900°C and 875°C were used, the XRD spectra of which are presented in figures 6.22(a) and 6.22(b), respectively. These spectra are very similar, as would be expected from growths performed under such similar conditions, but the most notable difference is that the spectrum from the sample grown at a slightly higher temperature (figure 6.22(a)) is lacking the (006) sapphire peak. These growths show it is possible to grow crystalline Y_2O_3 on sapphire substrates. However, due to the hardness of the sapphire these samples were not polished for use as waveguides and lasing experiments.

A deposition of Yb:Lu_2O_3 on sapphire was also performed, using just one Yb:Lu_2O_3 target surface for 5 hours, resulting in a sample thickness of 10 μm. This deposition was performed under a background oxygen atmosphere at 2x10^{-2} mbar and using an ablation fluence of 1.3 J/cm^2. The sapphire substrate was sat in a sample holder that loosely held it around the edges. The XRD spectrum obtained from this sample is shown in figure 6.23. The (222) lutetia peak is dominant, as with the growths on YAG, but has a fairly low peak intensity in comparison to most of the other XRD spectra in this thesis (including yttria on sapphire), and the XRD spectrum features many more peaks, most of which can be identified as other orientations of lutetia (as labelled in figure 6.23). The lower signal obtained for the growth of Yb:Lu_2O_3 on sapphire compared to Yb:Y_2O_3

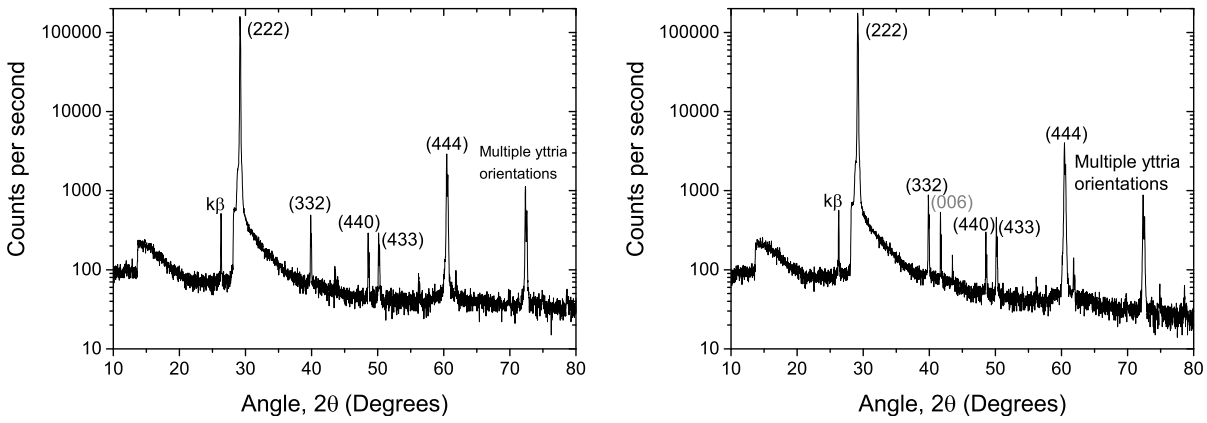

(a) (b)

Figure 6.22: XRD of Yb:Y_2O_3 samples on sapphire substrates. The sample the spectrum in (a) was taken from was slightly more heated (+∼25°C) during deposition than the sample whose XRD spectrum is shown in (b).

on sapphire suggests lower quality growth, despite the match between three unit cells of sapphire and the sesquioxide in the <111> orientation being being closer for the lutetia (2.9% versus 4.7% for yttria).

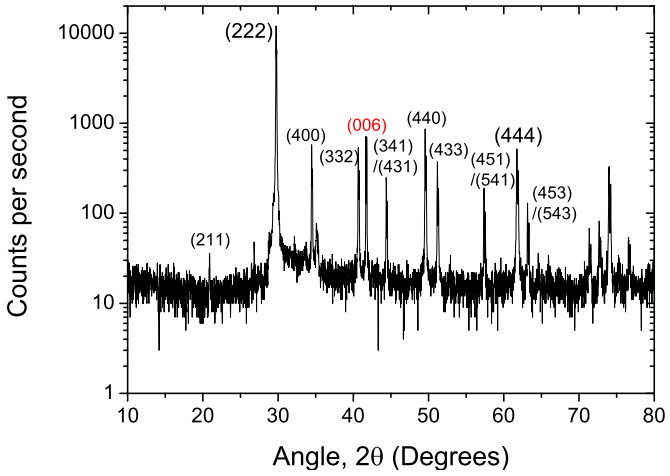

Figure 6.23: XRD spectrum of Yb:Lu_2O_3 on sapphire.

The sample surface was analysed using both an SEM and ZeScope; images taken using each of these can be seen in figures 6.24 and 6.25, respectively. The surface texture is visible in each of these images, as well as sub-micron particulates and voids (best seen in figures 6.24(a) and 6.24(b),

respectively). Particulate count analysis on this sample translates to average particulate densities of 1.1x10^5 /cm^2 for particulates >100 nm and 1.3x10^5 /cm^2 for particulates >50 nm.

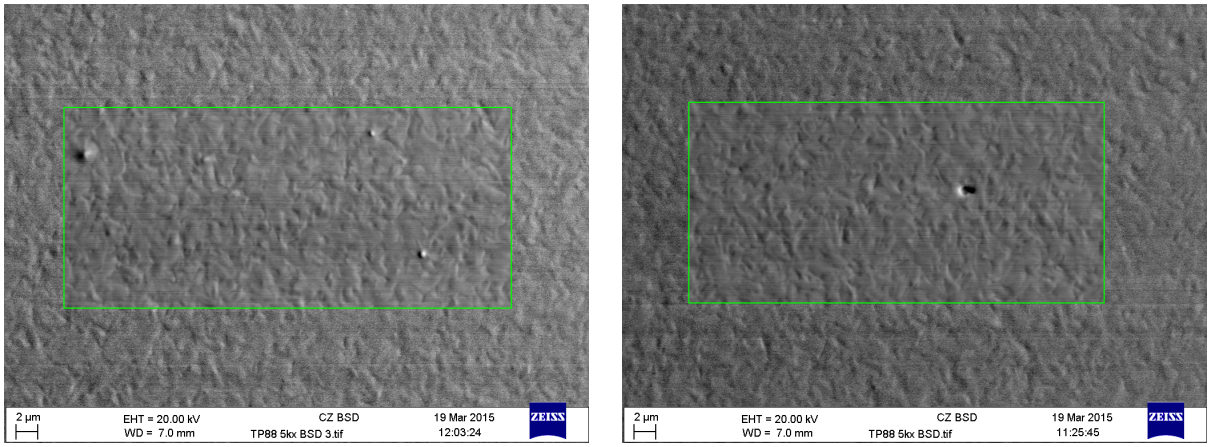

(a) (b)

Figure 6.24: SEM images of the surface of Yb:Lu_2O_3 on sapphire

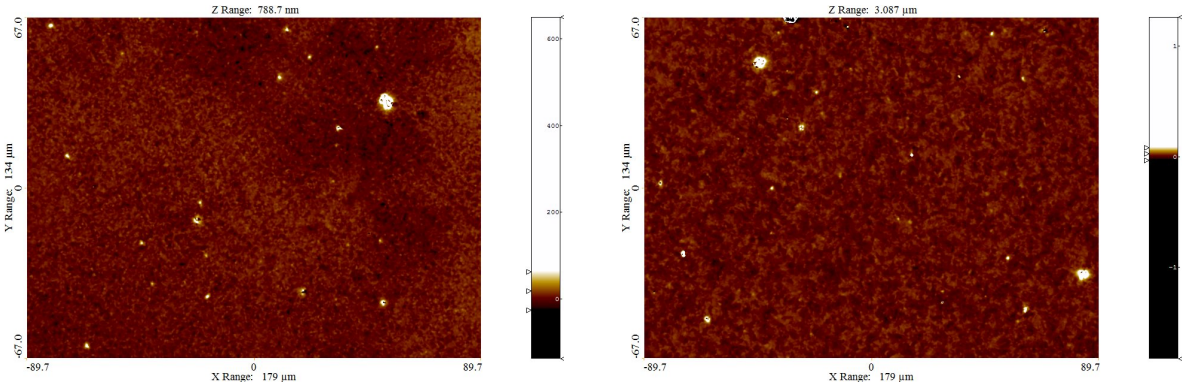

Figure 6.25: ZeScope images of the surface of Yb:Lu_2O_3 on sapphire

6.5 Sesquioxides on Sesquioxides

Sesquioxide substrates are not readily available due to their very high melting points that cause difficulties in the production of high quality bulk materials. However, multiple methods have been modified in an attempt to achieve optical quality bulk sesquioxides, as discussed in section 2.4, with mixed results. A group at the University of Hamburg have employed the heat-exchanger method to make bulk sesquioxides, which have then been cut and polished to form substrates.

Some of these substrates have kindly been donated to us for use in our PLD setup, to epitaxially grow doped sesquioxides on the corresponding sesquioxide substrates. These substrates are all 0.5 mm thick, and are of varying surface area, depending on the crystal size and quality achieved in the growth process.

6.5.1 Yttria

An yttria substrate was analysed by XRD to check the crystal orientation prior to deposition of Yb:Y_2O_3. The substrate was found to be <100>-oriented. To ensure the substrate was clean before being loaded into the vacuum chamber for deposition, it was sonicated sequentially in acetone, isopropanol, methanol and DI water for 2 minutes each and then dried with a N_2 flow.

The yttria substrate was mounted in a substrate holder that held it loosely with ceramic posts in opposite corners, to minimise heat sinking of the substrate. The deposition chamber was evacuated and then filled with oxygen to provide the desired background atmosphere at $4x10^{-2}$ mbar for the sesquioxide deposition. The CO_2 laser power was gradually increased up to 62.5% of its maximum power to heat the substrate. Again from previous calibration experiments, this heating power was found to correspond to a temperature of around 875°C for 1 cm^2, 1 mm-thick YAG substrates; these Y_2O_3 substrates will be hotter for the same heating power as they are only 0.5 mm-thick. These Y_2O_3 substrates also appeared brighter to the naked eye than YAG substrates had with the same incident laser heating power, suggesting a higher temperature. The ablation fluence on the Yb:Y_2O_3 target, provided by the incident excimer laser beam, was 1.7 J/cm^2.

The deposition was approximately 12 hours long; performed in three stages of 288000 excimer laser shots at 20 Hz, taking 4 hours each, but with the middle stage unintentionally interrupted by the interlock being broken. The substrate was reheated and the excimer set to run for a period of time such that the target surface was used for an estimated 4 hours, as originally intended. This material showed no signs of cracking or other detrimental damage due to the sudden loss of CO_2 laser heating, demonstrating a resiliance to quite extreme (and unintentional) temperature change.

The XRD spectra of this sample, overlaid with the measurement of the substrate prior to deposition of the Yb:Y_2O_3 is displayed in figure 6.26. These spectra show that both substrate and film are highly crystalline and that the film has grown epitaxially on the substrate, also growing in the <100> orientation. While the data from the two XRD scans do overlap very well, there

is a slight shift in the 2θ positions of the peaks. For the (400) peaks, the substrate peak is at a 2θ angle of 33.40° and film at 33.44°, both scans performed with a step size of 0.02°. These peak positions correspond to lattice constant values of 10.73 Å and 10.72 Å for the substrate and film, respectively. Data obtained from the crystal database for the (400) yttria peak puts it at 33.78°, which corresponds to a lattice constant of 10.61 Å. The results from the XRD of the substrate and film suggest that the Yb-doping in the film is at a low enough concentration to not disrupt the epitaxial growth and increase the lattice constant of the grown crystal. The slight discrepancy between the results reported here and those found on the database could be due to misalignment of the sample during measurement by XRD, slight error in the cut and polish of the yttria substrate or differences in the yttria crystals due to different growth conditions and methods used to produce them.

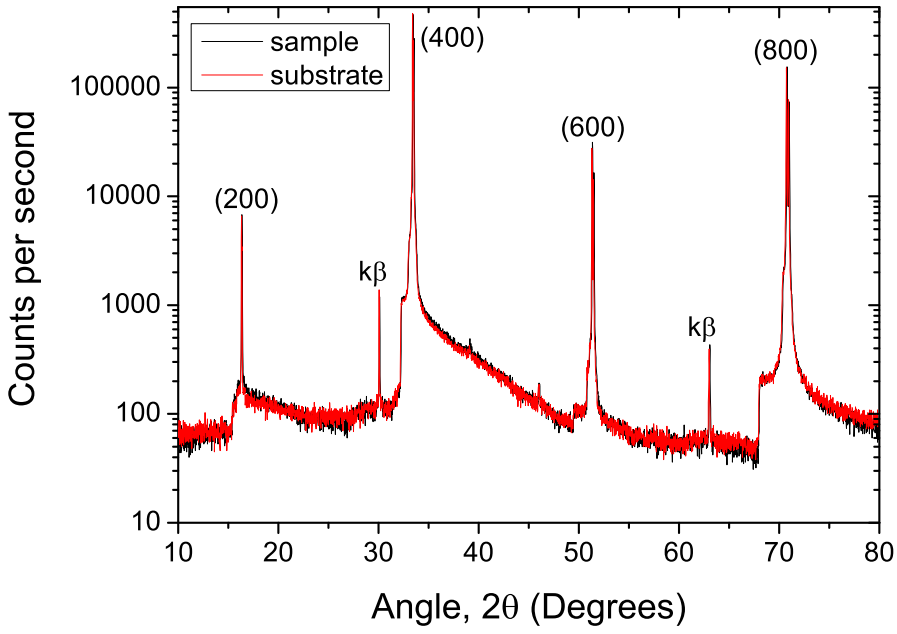

Figure 6.26: XRD spectra of Yb:Y_2O_3 on Y_2O_3.

A pole figure measurement of this sample was performed, the results of which are displayed in figure 6.27. This is further evidence of the epitaxial growth of Yb:Y_2O_3 on the <100>-oriented Y_2O_3 substrate, and actually matches with the theoretically expected output (four evenly spaced peaks around the central maximum).

This sample is estimated to be 30 - 35 μm thick. Measurement of the thickness using the stylus profiler was less reliable than usual as the sample had broken prior to this measurement

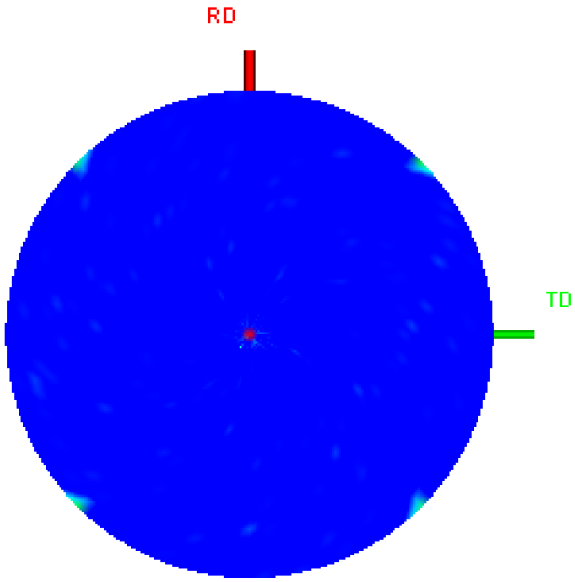

Figure 6.27: Yb:Y_2O_3 on Y_2O_3 pole figure.

being taken, meaning that only around half a profile could be taken, and the result could not be levelled corner-to-corner as it usually would be. The sample surface was also studied using an SEM, which produced the BSD image in figure 6.28. Lots of square-edged features can be seen here, characteristic of the cubic lattice of the yttria in the <100> orientation.

EDX analysis was performed and revealed the Yb concentration to be 2.3 at. %. A fluorescence spectrum and lifetime measurement were also performed. A 965 nm laser was used to illuminate a spot on the surface of the deposited Yb:Y_2O_3 layer, and the emitted fluorescence signal captured by a multimode fibre positioned facing the surface, very close to the pump laser spot, connected to an OSA, the results of which are displayed in figure 6.29. The shape of the fluorescence spectrum matches up well to that reported in the literature, taken from bulk Yb:Y_2O_3 [40]. To obtain the fluorescence lifetime the setup was modifed by modulating the incident laser beam and sending the decaying signal to an oscilloscope. The data collected is displayed in figure 6.30 on a logarithmic scale with an exponential fit used to determine the fluorescence lifetime, which resulted in a value of 862 μs. This is in line with a lifetime measurement of 850 μs reported in the literature [40].

Further Yb:Y_2O_3 depositions on yttria substrates were performed once substrates were available. These substrates were also <100>-oriented, confirmed by XRD analysis. The growth con-

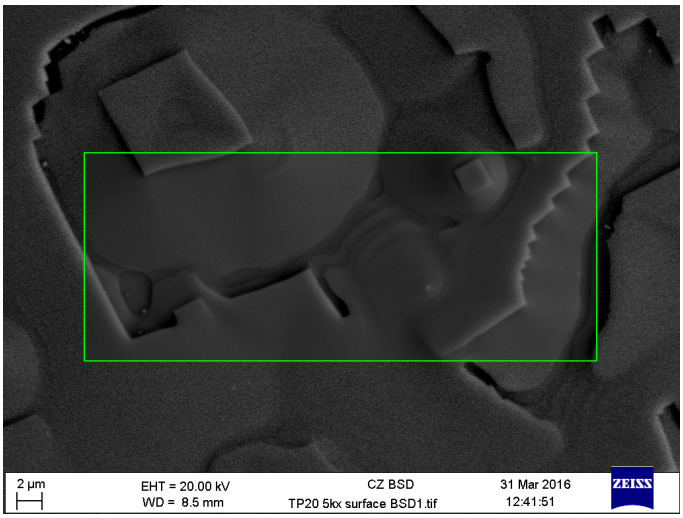

Figure 6.28: Yb:Y_2O_3 on Y_2O_3 SEM BSD image of the sample surface.

ditions were the same as for the previous sample, apart from a slightly lower oxygen background pressure of 2x10^{-2} mbar being used with the aim of slightly increasing the growth rate. Two samples were grown from two Yb:Y_2O_3 targets; one with a Yb concentration measured by EDX to be ∼2 at. % and the other 4 at. %. Both samples were grown in two stages, with 360000 excimer laser pulses ablating each side of the target used, totalling 10 hours of deposition time for each sample.

The first of these two samples was found, by EDX, to contain 1.9 at. % Yb and appeared to have grown in two sections, visible to the naked eye. Two XRD scans were performed with the sample positioned differently for each scan, to take data from each of the two visually different areas, the results of which are displayed in figure 6.31. Both sections appear to have grown homoepitaxially in the <100> orientation, but one half has considerably higher (200) and (400) peaks, and the other has higher (600) and (800) peaks, suggesting variation in the dominant planes detected, and therefore domain sizes. This difference may have been seeded by imperfections in the substrate, formed during its growth. Measurement using the stylus profiler revealed this film to be 40 μm thick.

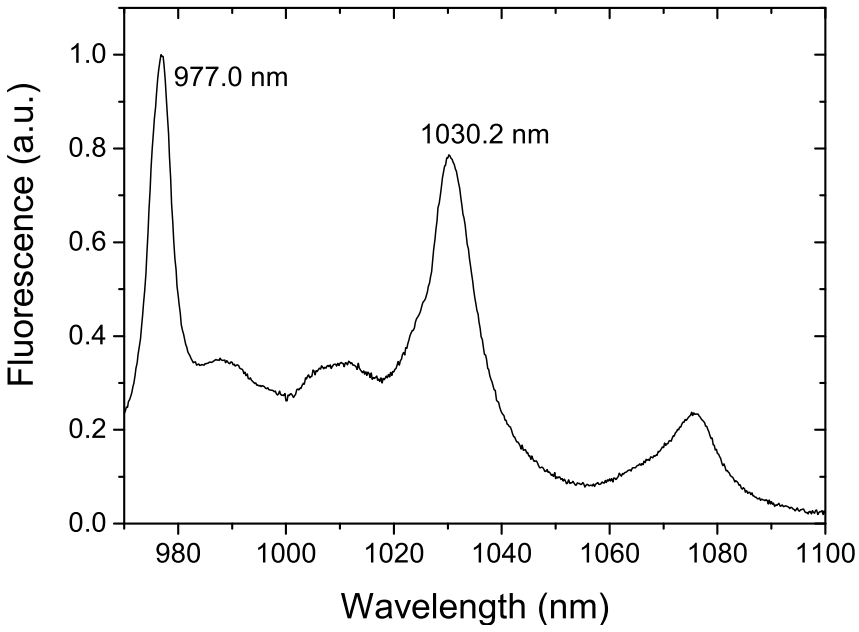

Figure 6.29: Fluorescence spectrum of Yb:Y_2O_3.

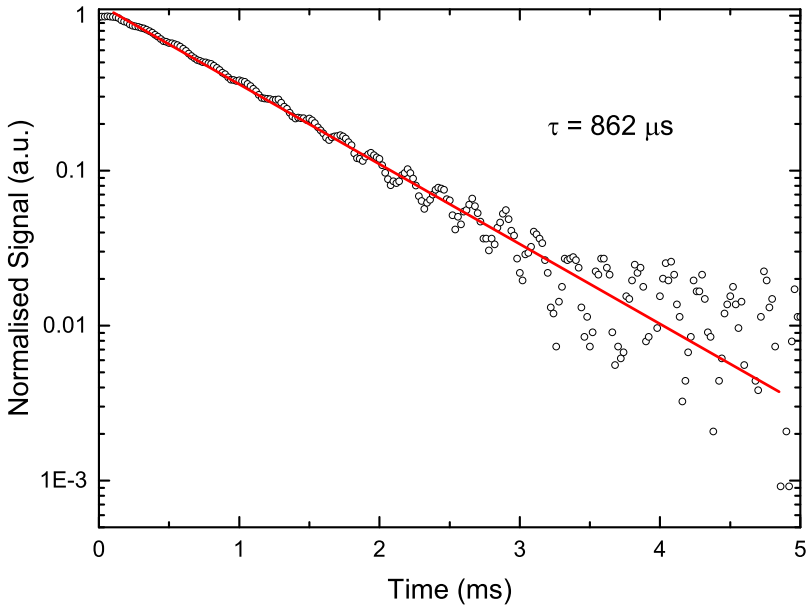

Figure 6.30: Fluorescence lifetime of Yb:Y_2O_3.

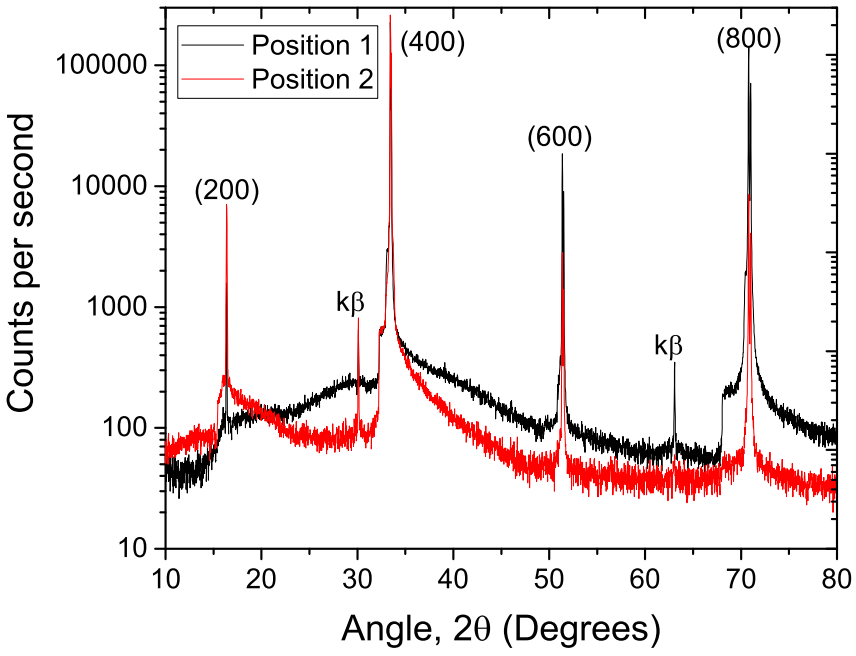

Figure 6.31: XRD of Yb(5 at.%):Y_2O_3 on Y_2O_3.

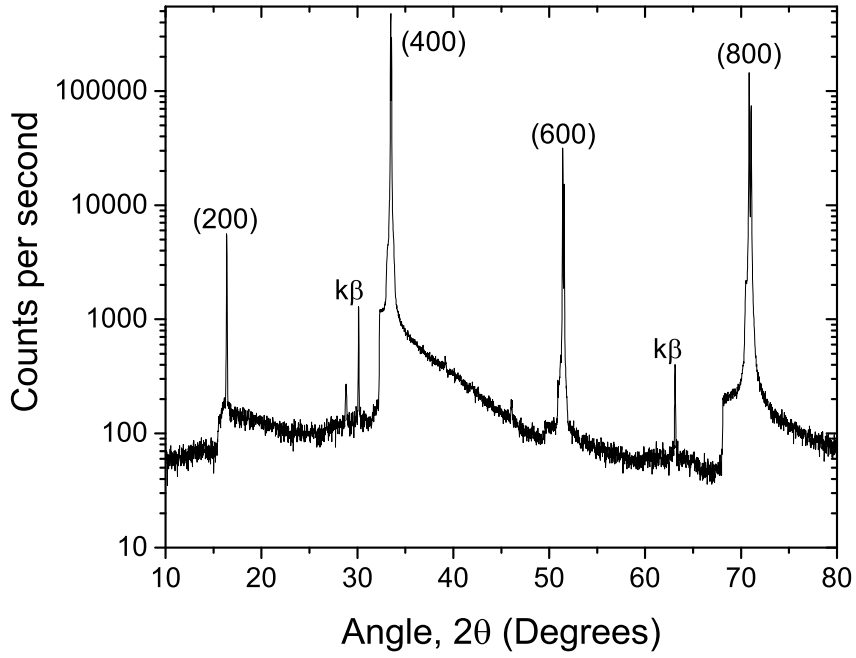

Figure 6.32: XRD of Yb(10 at.%):Y_2O_3 on Y_2O_3.

6.5.2 Lutetia

Following the homoepitaxial growth seen with Yb:Y_2O_3 on yttria, a thicker layer of Yb:Lu_2O_3 on a lutetia substrate was deposited. The lutetia substrates available were not 1 cm^2 like other substrate materials, but around 10 mm x 7 mm and 0.5 mm thick. This substrate therefore did not match the CO_2 laser beam heating profile but still sat within it, and was held in position by the substrate holder that supports the substrate by two opposing corners. As the substrate is of different dimensions and different material to that used in the calibration experiments referred to in this thesis, a temperature estimate based on this is likely to be inaccurate, but assumed to be about 1000°C. This deposition was conducted under the conditions established for growth with low surface particulate count while also achieving a reasonable growth rate, as discussed in section 5.4, which were an ablation fluence of 1.7 J/cm^2 and an oxygen atmosphere at a pressure of 2x10^{-2} mbar. The CO_2 laser was again set to 75% of the maximum power, heating the substrate to ∼1100°C). The deposition was performed in three stages, using target surfaces for 5 hours at a time (360000 shots per run), with a total deposition time of 15 hours. Analysis revealed this film to be ∼ 40 μm thick, compared to an estimated ∼ 50 μm that was hoped to be achieved from the deposition rates seen in optimisation experiments in section 5.4.

Analysis of this sample by XRD is shown in figure 6.33 along with a measurement performed on the substrate prior to deposition. The crystal orientation was found to be <100> for both the substrate and the deposited Yb:Lu_2O_3 film. Using the 2θ positions of the (400) peaks and equations 4.1 and 4.2 in section 4.3.1, the lattice constant of the substrate was calculated to be 10.4 Å, and a lattice constant of 10.6 Å for the grown film. This increase implies the PLD-grown material may be slightly strained, and have grown with dislocations in the crystal lattice. Sitting side by side on the periodic table, Yb and Lu are very similar in size (both reported to have an (empirical) atomic radius of 175 pm [95]) and ionic radius (112.5 pm for Yb and 111.7 pm for Lu [95]), so the substitution of Lu with Yb ions in the crystal lattice is unlikely to have caused this change.

The difference in the 2θ values of various orientations of lutetia seen in the XRD spectrum of this PLD-grown film, the substrate it was deposited on and values from the crystal database [10] are displayed in table 6.3. It can clearly be seen that the shift in 2θ of the film is greater than that of the substrate, when compared to database values. The shift does however appear to be fairly systematic for both the substrate and film, with the variation in shift for peaks corresponding

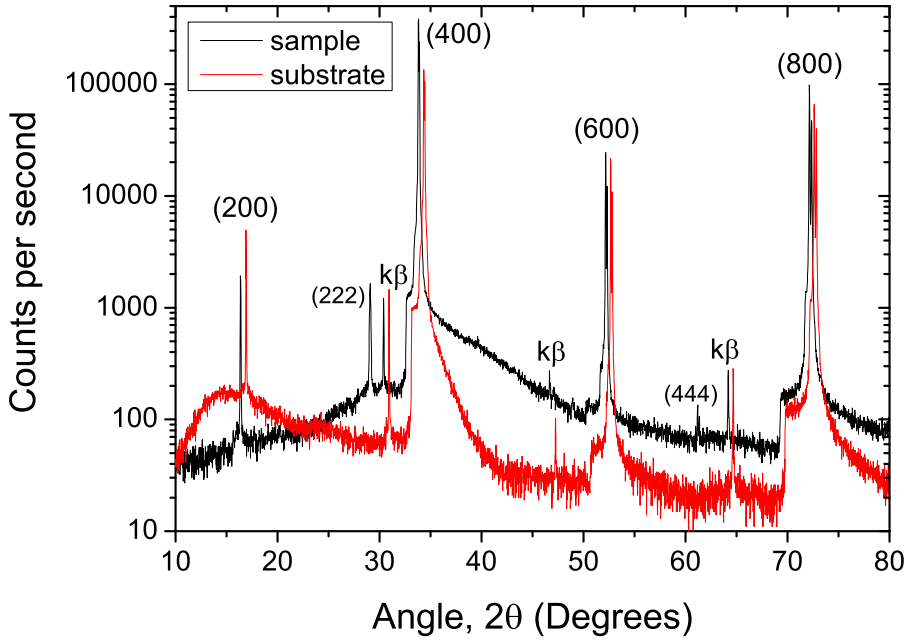

Figure 6.33: XRD spectrum ofYb:Lu_2O_3 on a Lu_2O_3 substrate. The spectrum displayed in black is of the sample, and the data in red is from an XRD scan of the substrate, prior to deposition.

to different crystal orientations being within 0.03° for the substrate and 0.05° for the film peaks. Calculating the lattice constant from the 2θ angles of the different lattice planes suggests the substrate lattice constant lies between 10.41 Å and 10.49 Å, and the sample lattice constant between 10.47 Å and 10.84 Å, all larger than the figures reported in the crystal database [10].

A pole figure measurement was performed on this sample, the result of which is shown in figure 6.34. As with the Yb:Y_2O_3 on Y_2O_3, the pattern seen here matches the theoretical expectation for a pole figure of <100>-oriented cubic material, with a central maxima and four evenly spaced peaks around the edge of the stereoscopic projection.

Surface analysis using the ZeScope and SPIP software were used to analyse the number of surface particulates and roughness. The results gave an average particulate density of 7.0x10^5 /cm^2 for particulates >100 nm and 9.1x10^5 /cm^2 for particulates >50 nm, which is amongst the highest seen on any sample during this project, possibly due to the thickness of growth and target degredation. The surface was also inspected using an SEM, and one of the resulting BSD images is displayed in figure 6.35. Some of the surface appears very flat, and some with an interesting

Crystal	Database	Substrate		Sample		Lattice Constant (Å)		
Orientation	$2\theta^{\circ}$	$2\theta^{\circ}$	$\delta 2\theta$	$2\theta^{\circ}$	$\delta 2\theta$	Database	Substrate	Sample
(200)	17.08	16.91	-0.17	16.36	-0.72	10.38	10.49	10.84
(222)	29.78	-	-	29.08	-0.70	10.39	-	10.64
(400)	34.52	34.35	-0.17	33.82	-0.70	10.39	10.44	10.60
(600)	52.86	52.66	-0.2	52.18	-0.68	10.39	10.43	10.52
(444)	61.86	-	-	61.19	-0.67	10.39	-	10.49
(800)	72.82	72.62	-0.2	72.15	-0.67	10.39	10.41	10.47

Table 6.3: Yb:Lu_2O_3 on Lu_2O_3 analysis.

patterning to it with square-edges, attributed to the cubic nature of the material and its <100> orientation. This surface morphology may have also added to the particulate count performed using the ZeScope and software.

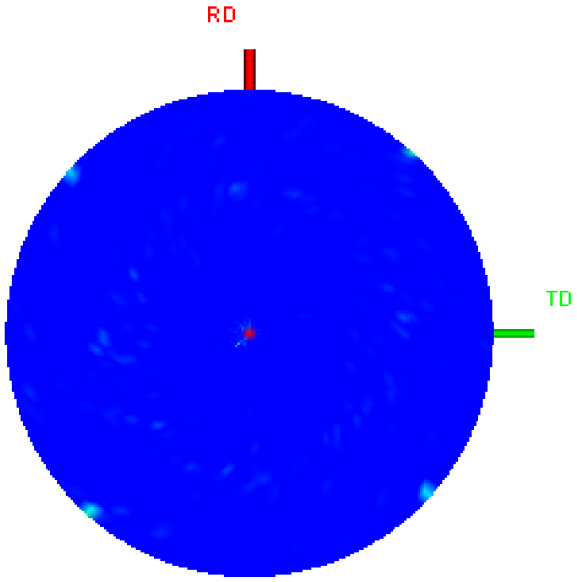

Figure 6.34: Yb:Lu_2O_3 on Lu_2O_3 pole figure.

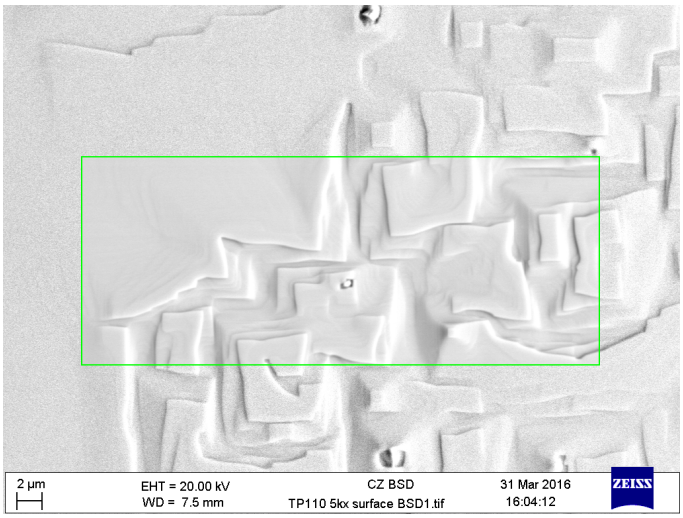

Figure 6.35: SEM BSD image of Yb:Lu_2O_3 deposited on a Lu_2O_3 substrate.

6.5.3 Scandia

Scandia substrates of surface area 1 cm^2 and a thickness of 0.5 mm were analysed by XRD prior to being deposited on. The substrates were cleaned in the lab with methanol, mounted in the substrate holder that suspends the substrate by opposing corners, and blasted with an air gun before being loaded into the deposition chamber along with a Tm:Sc_2O_3 target. The deposition conditions used were based on the optimisation experiments previously performed with this material, as reported in section 5.2. These were a background oxygen atmosphere at $2x10^{-2}$ mbar, an ablation fluence of 1.4 J/cm^2 (1.5 J/cm^2 was desired but 1.4 J/cm^2 was the maximum available at the time) and 62.5% of the total available power from the CO_2 laser for heating the substrate, and a second at 95% CO_2 laser power. This corresponded to substrate temperatures of around 875°C and 1200°C, respectively, for the 1 mm-thick YAG substrates - these scandia substrates are likely to have exceeded these temperatures due to the power being absobed in half the volume (0.5 mm compared to the 1 mm-thick YAG). Each of these depositions ran for 2 hours, consisting of 144000 shots at 20 Hz.

The results of the XRD scans performed prior to deposition are displayed in black in figures 6.36(a) and 6.36(b) along with the data collected by XRD following depositions, shown in red. The largest substrate peaks, associated with the (222) and (444) planes of Sc_2O_3, are at 31.21°and 31.19°in plots 6.36(a) and 6.36(b) respectively. These 2θ values are smaller than those found for the same scandia peaks in the crystal database [10], where the (222) peak is reported to be at 31.6°. This translates to a larger lattice constant of 9.90 or 9.89 Å for these substrates compared to 9.81 Å calculated from the database data, all given to 3 significant figures.

In both cases, the XRD spectra obtained following deposition of the Tm:Sc_2O_2 layer revealed a further shift in the 2θ values of the peaks, to 31.21° and 31.19°. This implies the lattice constant of the grown crystal is 9.93 Å, to 3 significant figures, in both cases. Attempted measurement of the thickness of the samples with a stylus profiler revealed rather convex surfaces, making determination of the thicknesses of the samples by this method very unreliable; at the peak of the curvature they appeared to be ∼1.5 μm and ∼1.3 μm thick (corresponding to the samples in figures 6.36(a) and 6.36(b), respectively), whereas they were each expected to be 5 - 6 μm thick, using growth rates from previous depositions as a guide. The surface profiles also revealed fairly rough surfaces, with lots of spiking rather than a smooth line representing the sample surface, and the on-screen view of the each sample during measurement showed what appeared to be porous

samples.

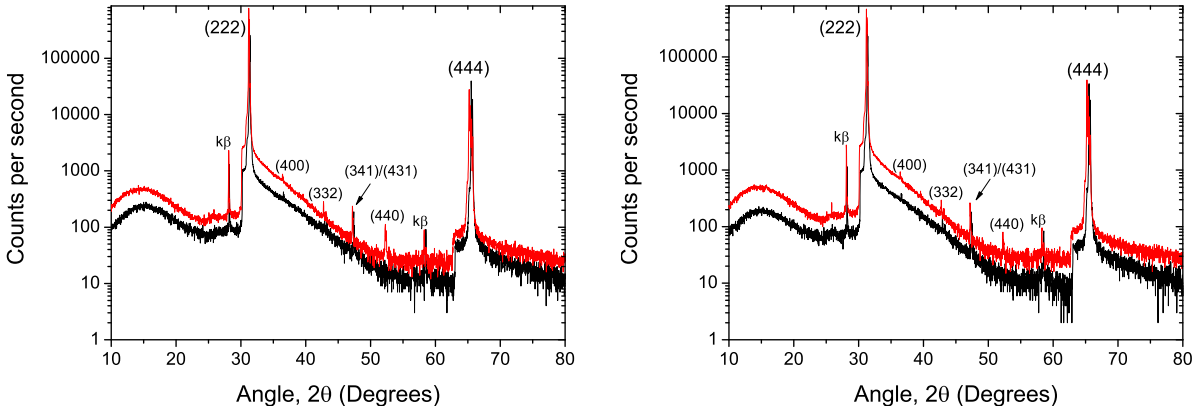

(a) CO_2 = 62.5%. (b) CO_2 = 95%.

Figure 6.36: XRD of Tm:Sc_2O_3 on <111>-oriented Sc_2O_3.

As the Sc_2O_3 is <111>-oriented, the expected pole figure has three evenly spaced peaks surrounding a central maxima, as mentioned in section 6.3.1. In this case, where Tm:Sc_2O_3 has been deposited epitaxially on a <111> Sc_2O_3 substrate, this is in line with the pole figure measured, displayed in figure 6.37.

The two Tm:Sc_2O_3 samples were also viewed under the ZeScope, see section 4.3.3, and software was used to count the number of surface particulates present and take roughness measurements. As with other samples, particulates were counted over a threshold value of >100 nm and >50 nm. However, in this case the number of particulates counted by the software over each of these threshold values was very similar in each location measured on both samples, so only one particulate density will be quoted for each sample. The first of these two samples, grown with 62.5% CO_2 laser power heating the substrate, was found to have a particulate density of $\sim$ 1.88x10^6 /cm^2 an average Sa roughness of 16.7 nm. The second, grown at a higher temperature provided by 95% CO_2 laser power, had considerably fewer particulates, which corresponds to a particulate density of 7.09x10^5 /cm^2 and also a lower Sa roughness value of 11.3 nm. The sample surface was also studied using an SEM. A BSD image of the sample is shown in figure 6.38 that very obviously shows many particulates, as well as a void, and no sign of angular patterning similar to that seen on the surfaces of the <100>-oriented sesquioxide on sesquioxide samples.

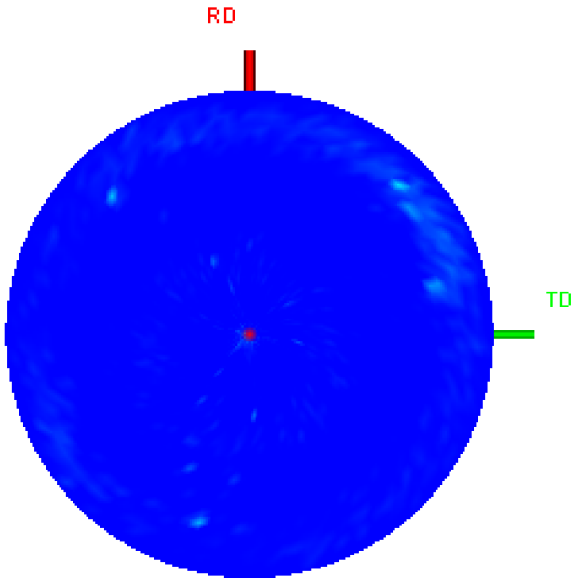

Figure 6.37: Pole figure of Tm:Sc_2O_3 on Sc_2O_3.

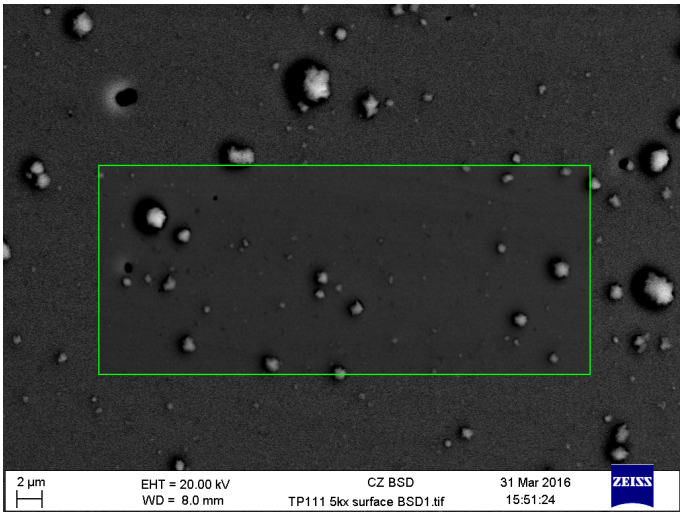

Figure 6.38: SEM BSD image of Tm:Sc_2O_3 on a Sc_2O_3 substrate.

6.6 Conclusions

This chapter has reported the results of the analysis of several samples deposited onto different substrates, often at a selection of growth temperatures. Beginning with growth on silica (and silicon with a thermal oxide layer), where there is no lattice match, crystalline growth of Y_2O_3 is seen in the <111> direction, but in domains at all rotational orientations (deciphered by the pole figure analysis). However, these films all showed signs of cracking, even at the lowest deposition temperatures trialled, due to the large thermal expansion mismatch.

The next section looks at growth on YAG substrates, of both <100> and <111> cuts. In the case of <100>-oriented YAG, a close lattice match is achieved with the sesquioxides, but due to the different orientations of the growth the sesquioxide layer appears to grow mostly in four distinct rotational orientations. In the case of <111>-oriented YAG, while the orientation of the substrate and grown material is the same, there is a large lattice mismatch. In an attempt to disrupt the lattice mismatch and the related lattice relaxation, YAG <100> and <111> substrates were sputtered with silica prior to sesquioxide deposition. Analysis by XRD, particularly the pole figure measurements, suggests the lattice matching was only partially disrupted, and the slope efficiencies achieved in laser experiments were lower than those with samples grown directly on YAG <100>, discussed in the following chapters.

A limited number of depositions of sesquioxide on sesquioxide were performed and the samples analysed. This work is limited by the availability of sesquioxide substrates. The substrates used were <100>-oriented Y_2O_3, <100>-oriented Lu_2O_3, and <111>-oriented Sc_2O_3. XRD analysis revealed epitaxial growth had occurred in each case, and pole figures were as theoretically expected. Further work needs to be done to optimise the growth rate and test how thick these films can be grown, in a reasonable amount of time and sufficiently high quality. This may have application in manufacturing thin disk lasers, if films of 50 - 100 μm can be achieved.

Chapter 7

Tm:Y_2O_3 Planar Waveguide

7.1 Introduction

Pulsed laser deposition was used to deposit a Tm:Y_2O_3 layer on a YAG <100>-oriented substrate with the aim of making the first planar waveguide laser of this material, to the best of our knowledge. Details of the energy-level structure of thulium and its operation as a lasing ion can be found in section 3.4.2 This chapter goes through the details of the deposition and analysis of the sample, and then onto the laser experiments, performed by J. W. Szela, and the results achieved, reported in [101].

7.2 Fabrication

A Tm:Y_2O_3 sintered ceramic was rotated, driven by an offset cam assembly, and repeatedly ablated by KrF excimer laser that operates at a wavelength of 248 nm, at a repetition rate of 20 Hz, resulting in an epitrochoidal ablation path on the target, for efficient, relatively even usage of the surface. The ablated material was deposited on a YAG <100>-oriented substrate, heated from the rear by a CO_2 laser beam, as described in section 4.2.2. The ablation fluence used was 1.7 J/cm^2 and the background oxygen pressure in the deposition chamber was 4x10^{-2} mbar. Following analysis, two opposing facets were polished plane and parallel for laser experiments, resulting in a final waveguide length of $\sim$8 mm.

7.3 Sample Analysis

7.3.1 Material Characterisation

The sample thickness was measured using a stylus profiler (section 4.3.2) and found to be ∼12 μm. A Zemetrics Zescope optical profiler and SPIP software (section 4.3.3) were used to obtain 3D surface profile maps and allow a surface particulate count to be performed. The average density of particulates of height >100 nm and >50 nm on the film surface was measured to be (9.8 ± 1.3)x10^3 /cm^2 and (15 ± 2.4)x10^4 /cm^2, respectively. The average thulium concentration in the sample was measured by EDX (section 4.3.5) to be ∼2.3 at.% in a ∼1 mm^2 area in the center of the sample surface. The thulium concentration across a wider area of this sample was not measured, but characterisation of previous Tm:Y_2O_3 samples grown under the same conditions suggests there is no systematic variation of the dopant concentration across the film surface.

XRD was performed on both the sample and a bare YAG substrate, allowing peaks in the spectra from the sample to be identified as either coming from the substrate or from the grown film. The XRD spectrum obtained from the sample indicates that the film was crystalline and is displayed in figure 7.1. The largest peaks observed correspond to the (222) and (444) orientations of the Y_2O_3 film and the (400) and (800) orientations of the underlying YAG substrate. A number of other smaller peaks were observed, most of which could be identified as likely to be other cubic orientations of yttria, as labelled in figure 7.1.

Another deposition of Tm:Y_2O_3 on YAG was performed under the same conditions for comparison of the XRD spectra from the 12 μm-thick film and a much thinner 50 nm-thick film, to assess the early stages of the crystal growth. The XRD data collected from the 50 nm-thick sample is displayed in figure 7.2. In this case the signal from the substrate is, as expected, larger than the signal from the thin layer of yttria, but the strong presence of the (222) and (444) yttria peaks and lack of other cubic orientaions suggests growth is primarily in the (222) orientation from the outset. Other orientations appear to become more prevalent as the sample thickness increases, but it may also be that the signal from these other orientations in the 50 nm-thick film is so small that it is lost in the noise.

The peaks in figures 7.1 and 7.2 labelled with letters have a few different origins: B and C perhaps correspond to the (211) and (440) orientaions of cubic yttria, G may correspond to the (221) orientation of $YAlO_3$ (YAP), A is the kβ peak (artifact of the x-ray radiation source) linked

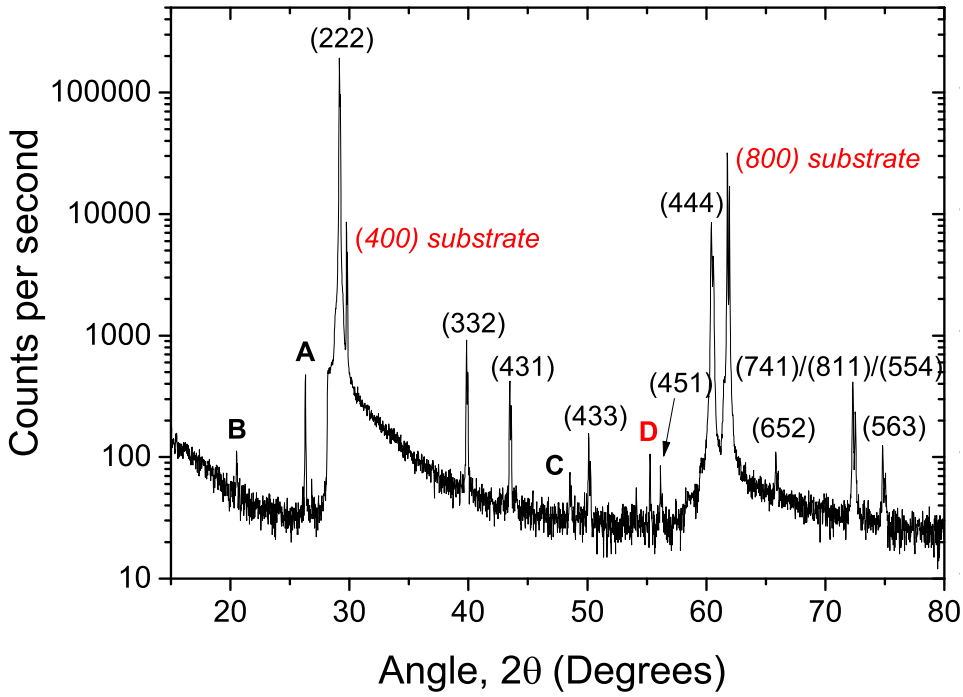

Figure 7.1: XRD spectrum of the 12 μm-thick Tm:Y_2O_3 waveguide layer deposited onto a YAG substrate. Most peaks have been identified as various orientations of yttria by comparison with data from the crystal database [10]. Peaks from the YAG substrate are also present.

with the main (222) yttria peak, F and D are kβ peaks associated with the (400) and (800) YAG peaks, and E is unidentified. It should be noted that the XRD spectrum collected from blank YAG substrates include more than peaks from just the (400) and (800) orientations of YAG, indicating the substrates are not perfect single crystal, which may influence the subsequent growth of the deposited material.

Analysis of the sample facet by SEM using the BSD, seen in figure 7.3, reveals columns through the grown layer. These are likely to be due to grain boundaries between different rotational orientations of the <111> growth, and the mixture of other orientations also present (as identified in figure 7.1). The YAG substrate is below the waveguide structure in the image, but appears black using the contrast and brightness levels required to see the detail in the waveguide layer.

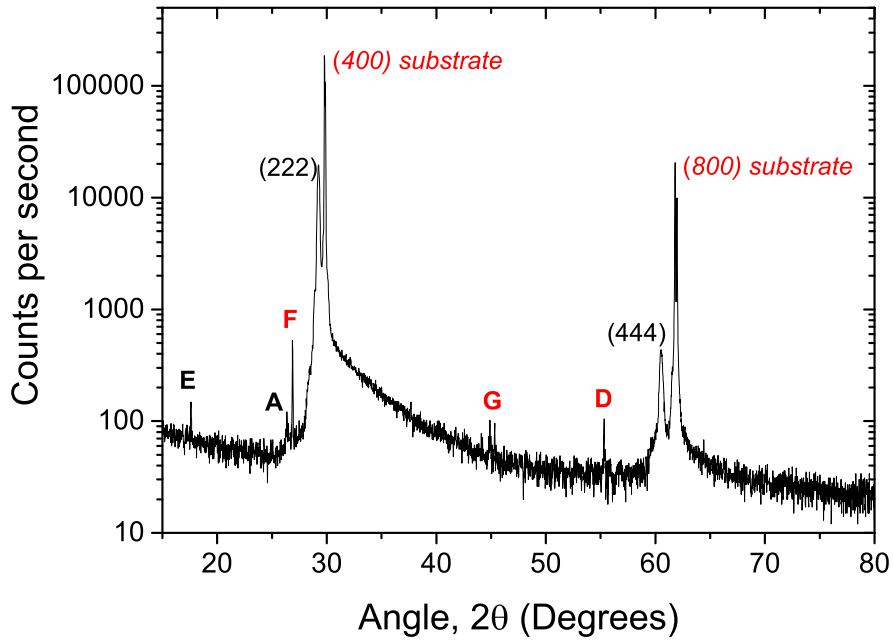

Figure 7.2: XRD spectrum of the ~50 nm-thick Tm:Y_2O_3 sample on YAG, deposited under the same conditions as the 12 μm-thick film for study of the initial growth.

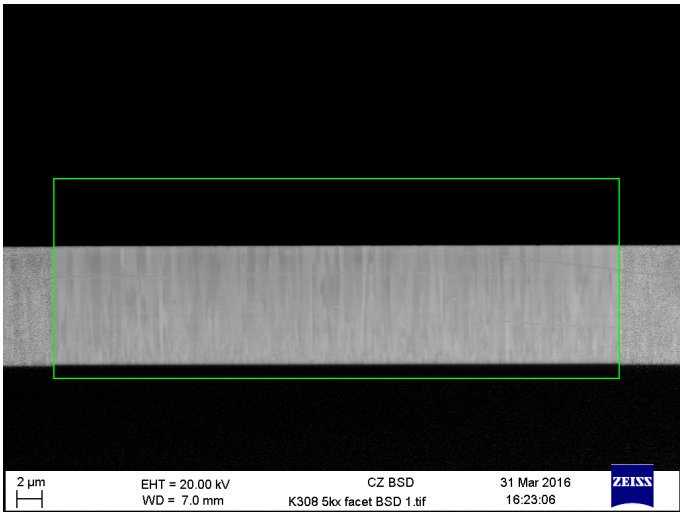

Figure 7.3: SEM BSD image of an end facet of the Tm:Y_2O_3 waveguide. The substrate is below the grown waveguide layer in this image, and nothing above.

7.3.2 Waveguide Characterisation

Considering the refractive indices of the YAG substrate and undoped yttria (1.82 and 1.91 respectively at 800 nm) and noting that the increase in refractive index due to the Tm doping is likely to be negligible, the NA of the waveguide at the pump and lasing wavelengths was calculated to be 0.58 and 0.57 respectively. The 12 μm-thick film should support up to 50 modes at the pump wavelength and 20 modes at the lasing wavelength, and is therefore a highly multi-mode structure.

Propagation losses of the waveguide were estimated from transmission measurements using light from a tunable Ti:sapphire laser, tuned to wavelengths of 730 nm and 850 nm, outside the absorption band of the Tm^{3+} $^3H_4$ manifold. Assuming 100% launch efficiency, the loss coefficient, α, can be calculated using equation 7.1:

$$\alpha = ln\left(\frac{P_{out}}{P_{in}(1-R)^2}\right)/l_w \tag{7.1}$$

where l_w is the waveguide length, R is the Fresnel reflectance at each waveguide facet and $P_{in/out}$ are the respective incident and out-coupled powers of the probe beam. For this 8 mm long waveguide, assuming the Fresnel reflectance is the same as that of pure yttria, R = 9.9%, an estimate of ~2 dB/cm loss at the probe wavelength is obtained (losses at longer wavelengths are expected to be lower due to a smaller Rayleigh scattering coefficient). By comparison of results from Barrington et al [102] on how particulate density affects propagation loss and the particulate density reported in section 7.3.1 for this work, we would expect losses to be below 1 dB/cm. This suggests there are other sources of loss in our waveguide that we cannot quantify, which may include local areas of poor-quality facet polishing, strain-induced birefringence, and scattering at grain boundaries and/or areas of non-cubic growth.

7.3.3 Spectroscopic Characterisation

An absorption spectrum of the Tm:Y_2O_3 was determined by measurement of light from a Ti:sapphire laser through the waveguide, using a wavelength tuning range of 790-810 nm at intervals of 0.1 nm, as shown in figure 7.4. This allowed us to determine the optimum pump wavelength for laser experiments, which was found to be $\lambda_p = 796.5$ nm. The absorption coefficient, α, at this wavelength was determined to be 1.45 /cm, corrected for propagation losses determined at non-absorbing probe wavelengths, which is consistent with results obtained from bulk crystal [103,104]. Previously reported absorption cross section data is displayed in figure 7.4 for comparison.

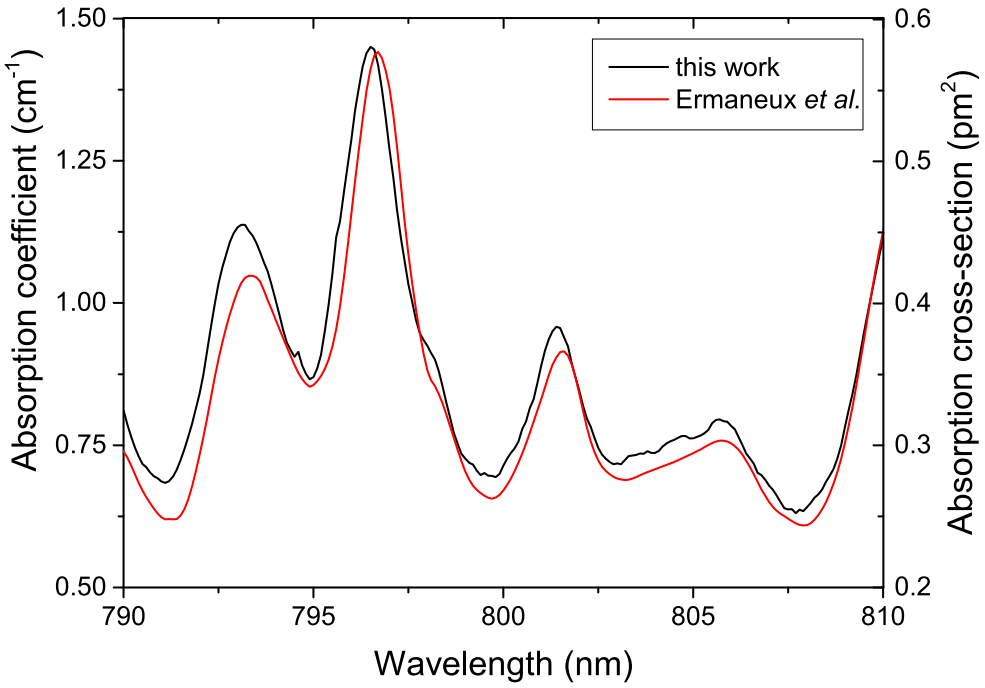

Figure 7.4: Absorption cross-section and corresponding absorption coefficient of Tm:Y_2O_3 across the wavelength range 790 - 810 nm. Data taken from the PLD-grown waveguide sample presented in this work is compared with data from the literature [104].

Measurement of the emission spectrum from the PLD-grown Tm:Y_2O_3 was performed at room temperature using a 793 nm fibre-coupled laser diode to excite the Tm^{3+} ions to their $^3H_4$ level. The pump beam was focussed onto the surface of the waveguide, perpendicular to the plane of the film and close to one edge, while the 2 μm fluorescence from the $^3F_4$ energy level, populated by cross-relaxation, was captured as it exited the waveguide facet. A peak pump power of 3 W was available, and when focussed down to a 600 μm diameter spot the irradiance was $I_p \simeq$ 1 kW/cm^2. The waveguide facet and emerging 2 μm emission were reimaged onto a Thorlabs DET10D InGaAs detector with a germanium filter covering the active area, allowing the 2 μm light to pass while blocking the pump light, connected to an ANDO AQ6375 optical spectrum analyser using a spectral bandwidth of 2 nm. The recorded emission spectrum is displayed in figure 7.5 along with data obtained from bulk crystal [105] for comparison, which are in good agreement with each other.

To determine the lifetime of the upper laser level the pump beam was modulated with 5 ms pulses at a 10% duty cycle (5 ms pulse at a period of 50 ms), allowing enough time for the system

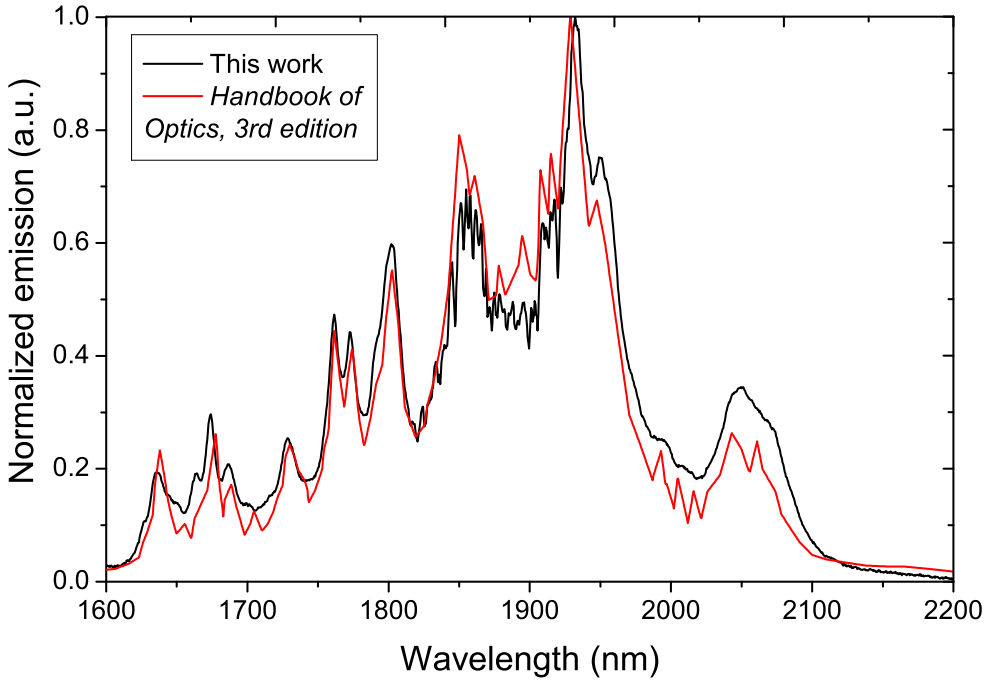

Figure 7.5: Normalised emission spectrum from the PLD-grown Tm:Y_2O_3 sample, plotted with data from the literature for comparison [105].

to reach steady-state conditions. The exponential decaying signal was recorded using an Agilent MSO6104A digital oscilloscope, from which a fluorescence lifetime of $\tau = 3.44 \pm 0.01$ ms was determined. This is in good agreement with reported values of bulk Tm:Y_2O_3 of 4.15 ms for a 1 at. % Tm^{3+} [103] and 3.2 ms for a 2 at. % Tm^{3+} [106]. However, with our measured lifetime value being in between these two, it suggests the Tm^{3+} concentration should be slightly less than 2 at. %, but measurement by EDX suggests the Tm concentration is 2.3 at. %. This discrepancy could be due to not all of the Tm in the sample being in the Tm^{3+} state, which would mean it is detected by EDX but is not contributing to the signal in the lifetime measurement, or other undetermined errors in these reported lifetime results.

7.4 Laser Experiments

The setup used for the lasing experiments is shown in figure 7.6. The tunable Ti:sapphire laser had a maximum output power of 600 mW at 797 nm. The incident pump power was adjusted by use of a neutral density filter wheel before entering the lens system to be launched into the

waveguide. The optics used for launching the pump beam were a 100 mm focal length cylindrical lens, an 11 mm focal length aspheric lens and a thin pump input coupling mirror. The laser cavity was formed by a thin incoupling mirror, the waveguide and various interchangeable bulk outcoupling mirrors, and the output beam collected with a lens (NA = 0.16) to transfer the 2 μm light to a thermal detector covered by a 3 mm-thick longpass filter to block the transmitted pump light.

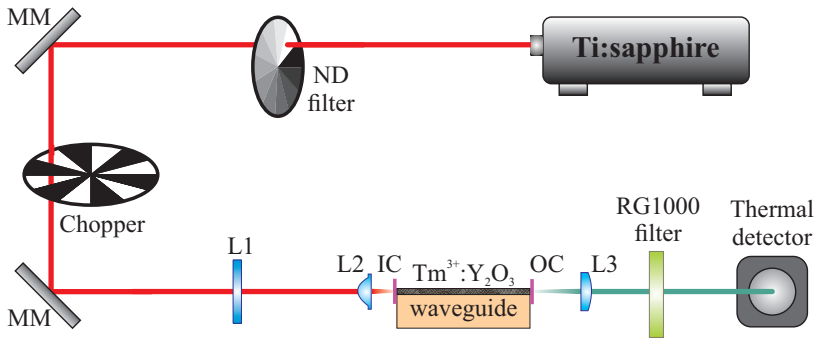

Figure 7.6: $Tm:Y_2O_3$ waveguide laser setup. Abbreviations are as follows: MM - metal mirror, L1 - in-plane collimating cylindrical lens, L2 - aspheric lens, IC - input coupling mirror, OC - interchangeable output coupling mirror, L3 - collection lens.

The pump beam was focussed to a beam waist of 3.6 μm in the waveguide's fast axis (guiding direction), which is smaller than half the thickness of the waveguide, with an input lens with an NA of 0.25, giving an input beam well within the acceptance angle of the waveguide. A launch efficiency of 100%, neglecting interface reflections, is therefore assumed. In the unguided direction two configurations were tested. The beam was either collimated through the waveguide by placing a cylindrical lens before the incoupling aspheric resulting in a beam waist of 90 μm positioned approximately midway along the waveguide, the results of which are displayed in figure 7.7, or alternatively focussed to a beam waist of 3.6 μm (by the incoupling aspheric alone) at the input facet and allowed to diverge through the waveguide, results of which are displayed in figure 7.8. The beam radius at the exit facet was calculated (assuming no lensing effects in the plane) to have spread to $\sim$350 μm, which is significantly larger than the $\sim$75 μm cavity mode radius. This configuration therefore provided a higher inversion density at the input facet but worse overlap between pump and cavity modes throughout the waveguide than the collimated configuration.

As can be seen in figures 7.7 and 7.8, a variety of output coupling mirrors were investigated. The

input coupling mirror had 92% transmittance at the pump wavelength and was highly reflective (HR) at the lasing wavelength. Both input and output coupling mirrors were thin and able to be butt-coupled to the waveguide facets using Fluorinert FC-70 liquid to form a quasi-monolithic optical resonator. Due to the high transmission of the mirrors at the pump wavelength, the pump light saw a single pass through the cavity. The waveguide was secured to an aluminium pedestal on a 3-axis translation stage and was not actively cooled.

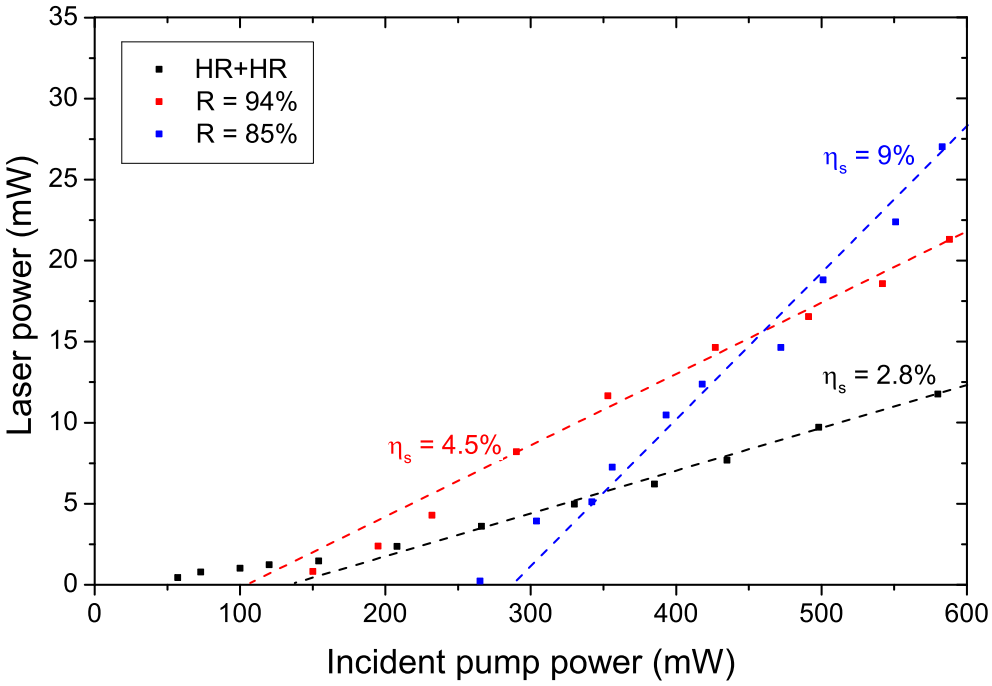

Figure 7.7: Laser input-output plots for the first pump configuration, where the input beam was collimated in the non-guided axis, with the focus approximately midway along the waveguide.

Lasing was observed at ∼1950 nm in both configurations, with the lowest threshold of 50 mW achieved using the setup including the cylindrical collimating lens and a HR+HR cavity. This result can be seen in figure 7.7 along with results obtained using 94% and 85% reflective output couplers. Further results with higher output powers were acheived in the configuration with only the aspheric incoupling lens. These results are shown in figure 7.8, including the maximum output power of 35 mW for 600 mW input pump power, threshold of 135 mW and a slope efficiency of ∼9% for an 85% reflective output coupler. The slope efficiency with this output coupler was the same for both configurations, but with different thresholds and therefore maxiumum output powers. The beam quality parameter (M^2) of the optimum laser setup at maximum output power

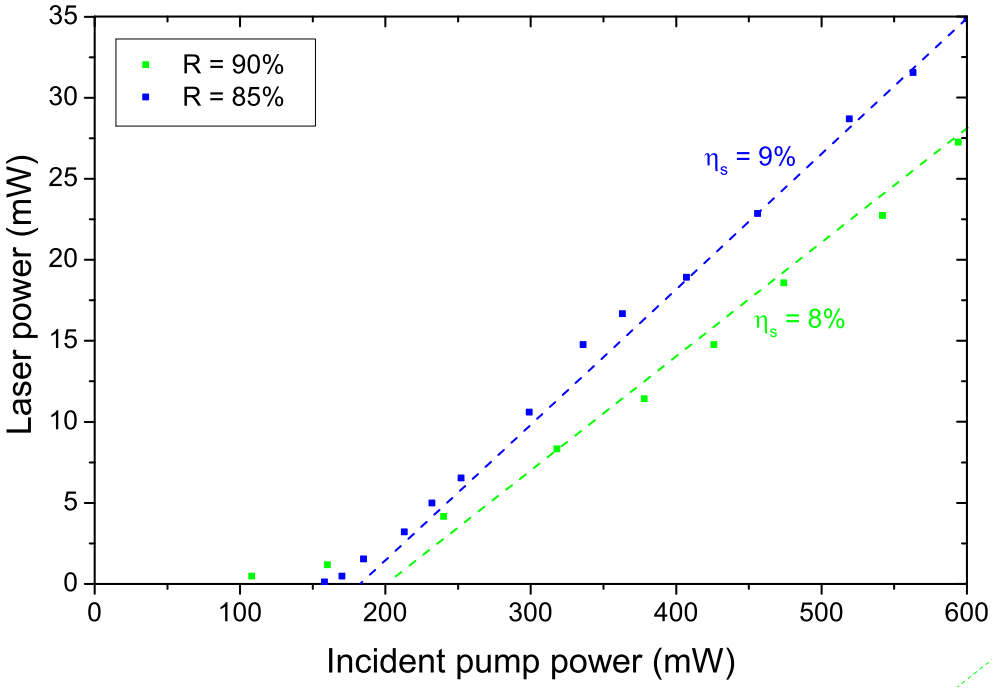

Figure 7.8: Laser input-output plots for the second pump configuration, where the pump beam was focused in both axes at the input facet.

was measured in the guided direction using a scanning slit beam profiler (Datarays Beam Scope P8, InAs detector with a single 5 μm slit). A value of 5 $\pm$ 2.9 was obtained.

Estimates of the round trip losses in the cavity, including reabsorption at the laser wavelength, were made by measuring the relaxation oscillation frequency as a function of pump power with respect to threshold power [107], the results of which are displayed in figure 7.9. The experimental setup used was similar to that in figure 7.6. A mechanical chopper in the setup before the incoupling lens was used to modulate the input signal and the thermal detector was replaced by a biased InGaAs detector connected to a digital oscilloscope to measure the relaxation oscillation frequency.

For a system with reabsorption losses, the relaxation oscillation angular frequency ω_{RO} is given by equation 7.2 [107]:

$$\omega_{RO}^2 = \gamma_c \gamma_\tau \left(1 + \frac{N\sigma_{al}c}{n\gamma_c}\right)\left(\frac{P_p}{P_{pth}} - 1\right) \tag{7.2}$$

where γ_c is the cavity decay rate, γ_τ is the fluorescence decay rate, P_p is the pump power, P_{pth} is the threshold pump power, N is the thulium concentration, σ_{al} is the absorption cross section at the laser wavelength, c is the speed of light in vacuum, and n is the refractive index of the active medium at the laser wavelength. The loss can then be obtained from the gradient of the linear

fit to the angular frequencies, as shown in figure 7.9, the cavity decay rate γ_c, and other physical parameters via equation 7.3:

$$L = 1 - \frac{1}{R_{in}R_{out}\exp\left(\frac{2\gamma_c l_{opt}}{c}\right)} \tag{7.3}$$

where R_{in} and R_{out} are reflectance values for the input coupling and output coupling mirrors and l_{opt} is the optical path length of the cavity. A round trip loss value of L = 5.8 ± 0.7 dB was obtained using equation 7.3 for the HR + HR cavity, highlighting additional losses were incurred at mirror/facet interfaces by comparison with the simple propagation loss measurement of ∼2 dB, as in section 7.3.2. Even higher round trip losses were obtained from the bulk output couplers trialled due to the small gap between the waveguide facet and the mirror.

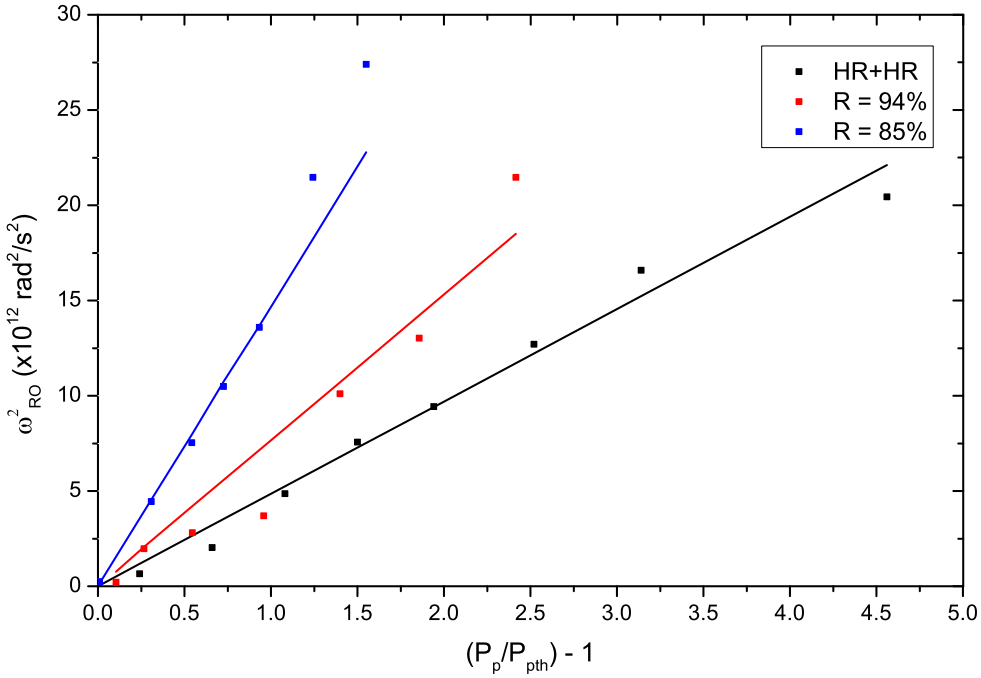

Figure 7.9: Relaxation oscillations plotted to use to determine the round trip cavity losses of the Tm:Y_2O_3 planar waveguide laser.

7.5 Conclusion

We have demonstrated, to the best of our knowledge, the first Tm:Y_2O_3 planar waveguide laser, grown by PLD. A maximum output power of 35 mW was achieved at a wavelength of 1.95 μm, with a slope efficiency of 9%. XRD revealed the PLD-grown yttria was highly crystalline, predominantly

in the <111> orientation. Various other peaks were present in the XRD spectrum, most of which could be assigned to other cubic orientations of yttria. Moderate propagation and mirror coupling losses limited the laser performance, and output power was limited by the available pump power as there was no sign of thermal rollover, despite the lack of active cooling of the waveguide.

Chapter 8

Yb:Y_2O_3 Planar Waveguide lasers

8.1 Introduction

Yb-doped samples have been the main focus in this thesis, due to the low quantum defect and ease of pumping with commercially available high power diode lasers. Both single layer and multilayer samples have been deposited on YAG <100> substrates, which have been analysed and polished for laser experiments. This chapter examines some of the better Yb:Y_2O_3 samples grown, from the material analysis through to the best laser results achieved, including those published in reference [108].

8.2 Yb:Y_2O_3

8.2.1 Single layer samples

Following the yttria optimisation experiments in section 5.3, longer depositions were carried out using the ablation fluence and background pressure found to produce samples with the fewest particulates, which was 1.3 J/ cm^2 and 2x10^{-2} mbar, respectively. These samples were grown in depositions of 288000 excimer laser shots at 20 Hz, lasting 4 hours each. The substrate temperature used for these growths was varied slightly; the first is estimated to have been a little below 900°C, and the second and third around 950°C (the last of which was heated with slightly more CO_2 laser power but held in a different substrate holder with more contact with the substrate, and therefore likely to be more heat sunk). The results of XRD scans of these samples are displayed in figure 8.1. Each of these XRD spectra show the (400) and (800) peaks from the <100>-oriented

YAG substrate, the dominant (222) and (444) peaks of Y_2O_3, and some other smaller peaks that correspond to other orientations of yttria. There are also peaks that arise as artefacts of kβ radiation from the x-ray source, which normally are not noticable due to them being several orders of magnitude smaller than the main peaks. In figures 8.1(b) and 8.1(c) the kβ peak corresponding to the YAG (800) peak is present, as well as the kβ peaks coresponding to (222) and (444) yttria.

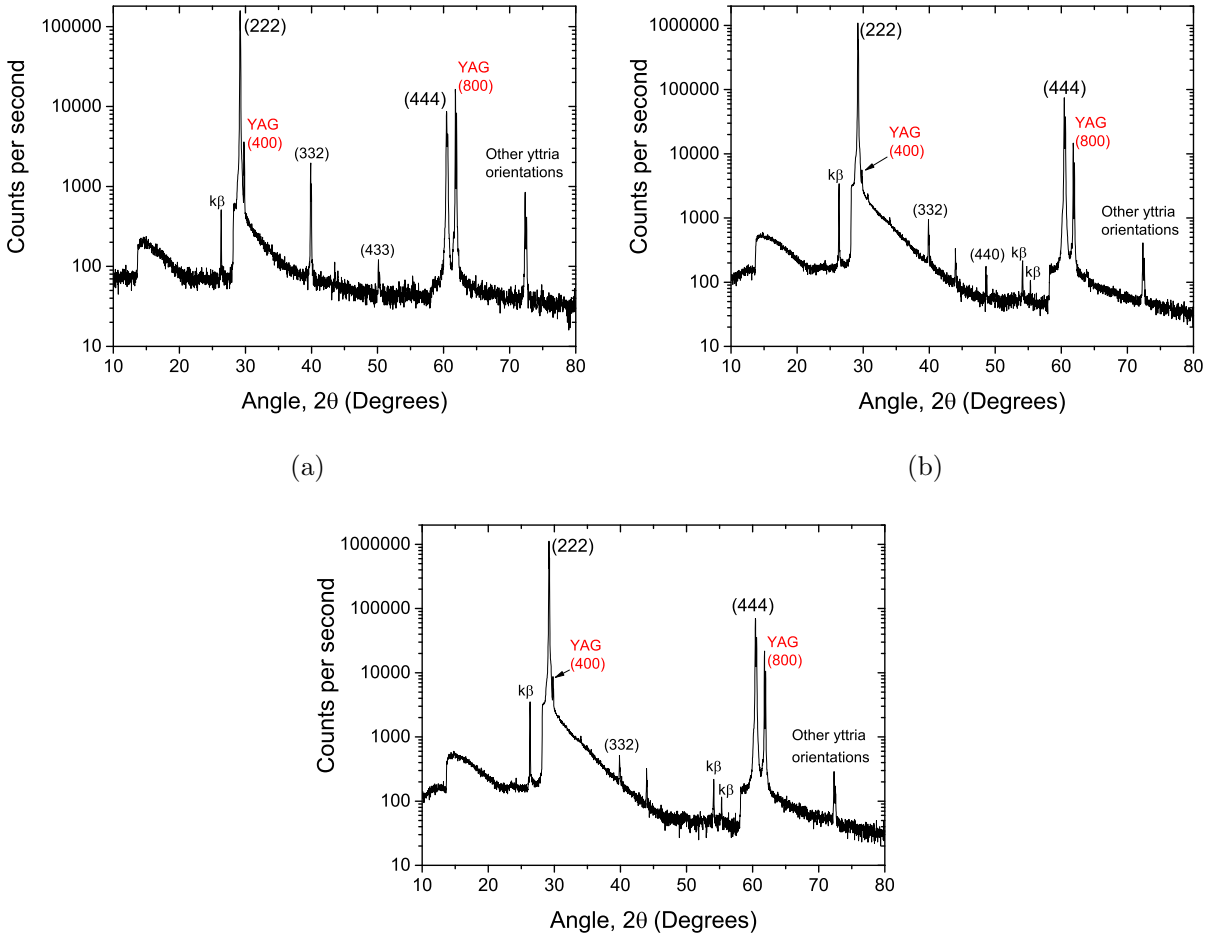

Figure 8.1: XRD spectra of growth of Yb:Y_2O_3 on YAG <100> substrates, grown under optimised conditions. Results of laser experiments using the sample whose XRD spectrum is shown in (a) can be found in section 10.3, and laser results achieved using the samples whose XRD spectra are displayed in (b) and (c) are given in this section.

The first of these samples, with its XRD spectrum shown in figure 8.1(a), was used for the experiments detailed later in this thesis, in the chapter on pulsed laser operation, section 10.3.

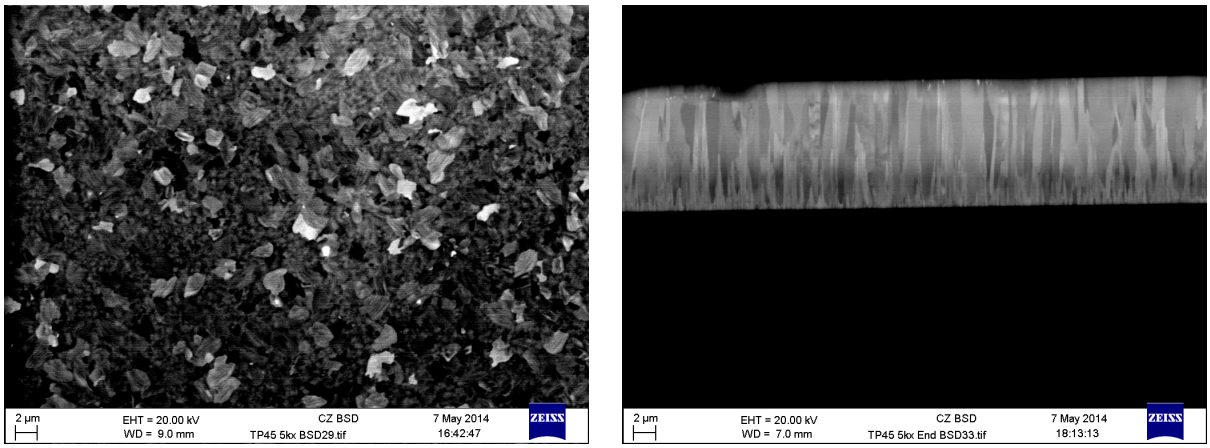

(a) (b)

Figure 8.2: SEM BSD images of (a) the surface of and (b) a polished end facet of an Yb:Y_2O_3 sample deposited on YAG <100>, the XRD spectrum of which is displayed in figure 8.1(b).

The samples whose XRD spectra are seen in figures 8.1(b) and 8.1(c) were trialled as planar waveguide lasers in a quasi-monolithic plane-plane cavity setup, as shown later in figure 10.1. A single-mode diode laser was used as the pump source and input and output coupling mirrors were attached to the waveguide end facets using fluorinated liquid. These samples shall be referred to as sample 1 and sample 2 in the following description of the laser experiments conducted with them, corresponding to the XRD spectra in figures 8.1(b) and 8.1(c), respectively.

As surface particulates can lead to the adverse affect of scattering light that is propagating through a waveguide, sample 1 was briefly surface-polished prior to conducting laser experiments. The results obtained with four different output coupling mirrors are displayed in figure 8.3, but no laser operation was seen using the Fresnel reflections to output couple light, suggesting the polished end facets were not quite plane and parallel to each other. Sample 1 was then removed from the laser setup to have its surface re-polished.

Sample 1 was put back into the laser setup for further testing, the results of which are displayed in figure 8.4. The results achieved here have a higher slope efficiency for each output coupler trialled as well as higher output powers when compared to the previous set of results obtained from sample 1. Given the improvement seen here, this suggests the surface polishing did improve the quality of the waveguide surface, making it smoother, flatter and consequently a better waveguide with fewer scattering centres. While there is evidence of this in the laser results, before and after

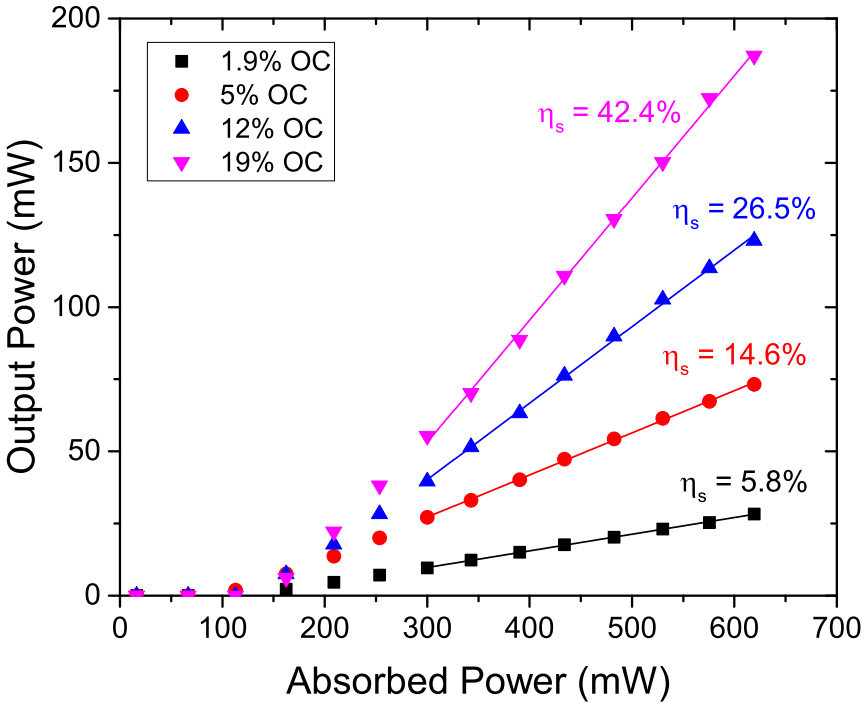

Figure 8.3: Initial laser characterisation results obtained from sample 1, deposited at the optimised conditions from section 5.3.

images were not taken for comparison on either the SEM or ZeScope (which could have provided a particlate count and roughness comparison). As this method gave improved results, it should be used again for future samples and further analysis performed on the sample surface before and after the polishing process.

Sample 2 was inserted into the laser setup and a similar set of experiments performed to those with sample 1. The slope efficiencies achieved were lower than for sample 1 (even compared to the first set of results), for every output coupler trialled, suggesting higher loss. This could be due to the propagation losses through the sample, which in theory should be very similar to that in sample 1 due to the similar growth conditions, or potentially due to the facet polishing. The other differences were that sample 2 did not undergo any surface polishing, so the scattering loss at the waveguide surface may have been higher, and a different substrate holder was used during the deposition. The heat sinking of the substrate to the ceramic posts holding it and the effects this has on the temperature distribution across the substrate have not been studied for either substrate

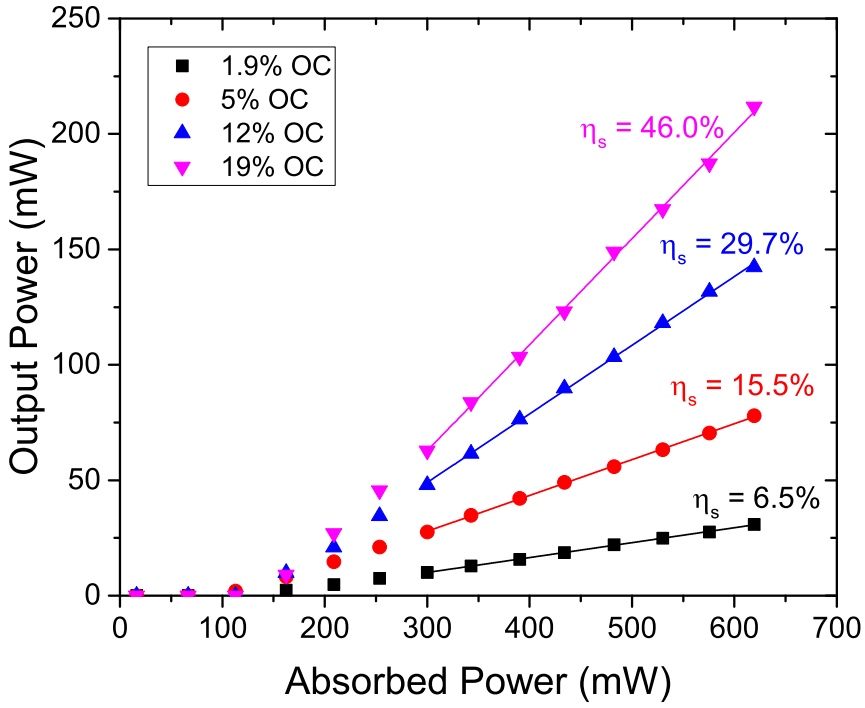

Figure 8.4: Laser characterisation results obtained from sample 1 following further surface polishing.

holder, so cannot be compared.

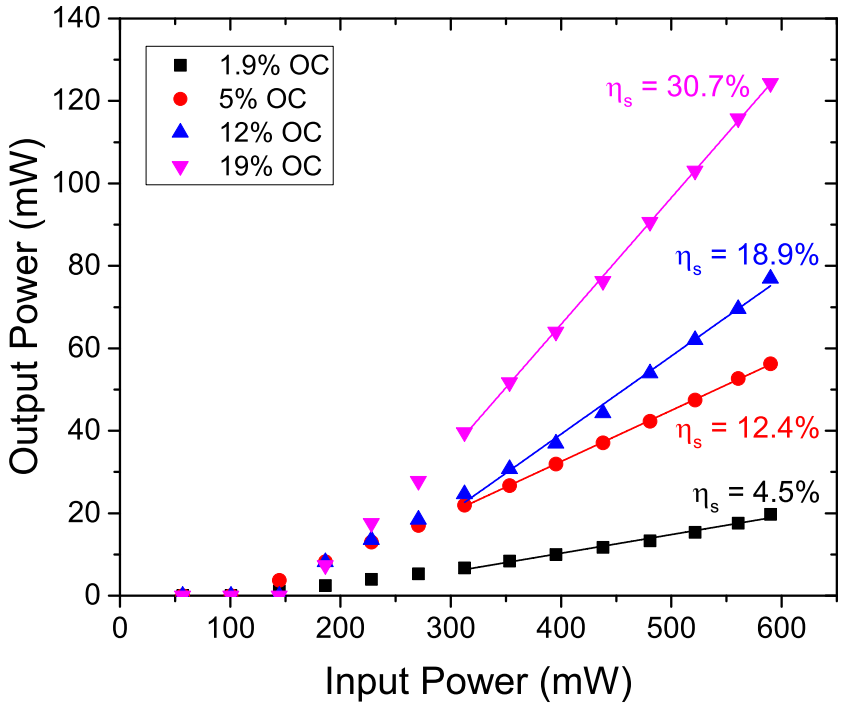

Figure 8.5: Laser characterisation results achieved using sample 2, deposited at the optimised conditions from section 5.3.

8.2.2 Multilayer sample

8.2.2.1 Design and Fabrication

In 2000 Bonner *et al.* demonstrated that near diffraction-limited laser performance can be achieved by structuring a highly multimode waveguide such that the dopant region has a much better overlap fundamental mode than higher order modes [14]. This idea was implemented in the design of the waveguide reported below, where a doped core layer was sandwiched in between two almost index-matched undoped layers. Assuming the growth rate from ablation of the 2 at. % Yb:Y_2O_3 target and undoped Y_2O_3 sintered ceramic targets are approximately equal, the central doped region was set to deposit for twice as long as each of the individual undoped regions, such that the central region is 50% of the entire waveguide thickness. From previous depositions performed under the same conditions, the deposition rate was known and used to select deposition times for each of the layers to form a 12 μm-thick waveguide with internal structure of 3 μm undoped Y_2O_3,

6 μm Yb:Y_2O_3 and another 3 μm undoped Y_2O_3 layer. This structure was deposited onto a YAG <100> substrate of dimensions 10 x 10 x 1 mm, using the PLD setup detailed in section 4.2.1.

The Yb:Y_2O_3 and Y_2O_3 targets were ablated at an ablation fluence of 1.7 J /cm^2 on the target surface. The targets were alternated for each stage of the growth (Y_2O_3, then Yb:Y_2O_3 and back to Y_2O_3), and were rotated. The depositions for production of this waveguide were conducted in an oxygen atmosphere at a pressure of 4x10^{-2} mbar.

8.2.2.2 Sample Characterisation

X-ray diffraction was performed on the multilayer waveguide structure over a 2θ range 10-80°, the results of which are displayed in figure 8.6. These results indicate that the film has grown in a highly ordered crystalline phase. The largest peaks correspond to the <222> and <444> orientations of cubic yttria and the <400> and <800> peaks from the YAG substrate. As the lattice plane match between the yttria <222> and YAG <400> is so close their XRD peaks are only just distinguishable, as can be seen in figure 8.6. The lattice constants as calculated from data from the crystal database are 10.59 Å and 11.99 Å, translating to plane spacing of 3.06 Å and 2.99 Å for the yttria <222> and YAG <400> planes, respectively. The corresponding 2θ values obtained from the XRD data suggest lattice constants of 10.58 Å and 11.98 Å, plane spacing 3.05 Å and 2.99 Å, essentially the same as those calculated from the crystal database data. Other peaks present in the XRD data, at least three orders of magnitude smaller, have been identified as other cubic orientations of yttria, by comparison with crystal database data, and two peaks as Kβ artefacts from the XRD source corresponding to the <222> and <444> yttria peaks respectively.

EDX was used to characterise the dopant concentration and profile though the multilayer waveguide by taking measurements across a facet. Ytterbium was only detected in the waveguide core, and at a dopant concentration of 1.85 at.%. Following material characterisation, the sample had two opposing facets polished plane-parallel for laser experiments.

Spectroscopic experiments were not performed on the multilayer sample as the undoped cladding layer would reduce the signal, as it is detected through the top of the guide (as seen in the configurations in figures 4.6 and 4.5. Instead, spectroscopic data were collected using a single layer Yb:Y_2O_3 sample grown under similar conditions to the multilayer, also 12 μm thick on a YAG <100> substrate. In experiments conducted with S. J. Beecher, light from a 965 nm diode laser was loosely focused to a 0.5 mm radius spot on the face of the sample and pulsed at a repetition

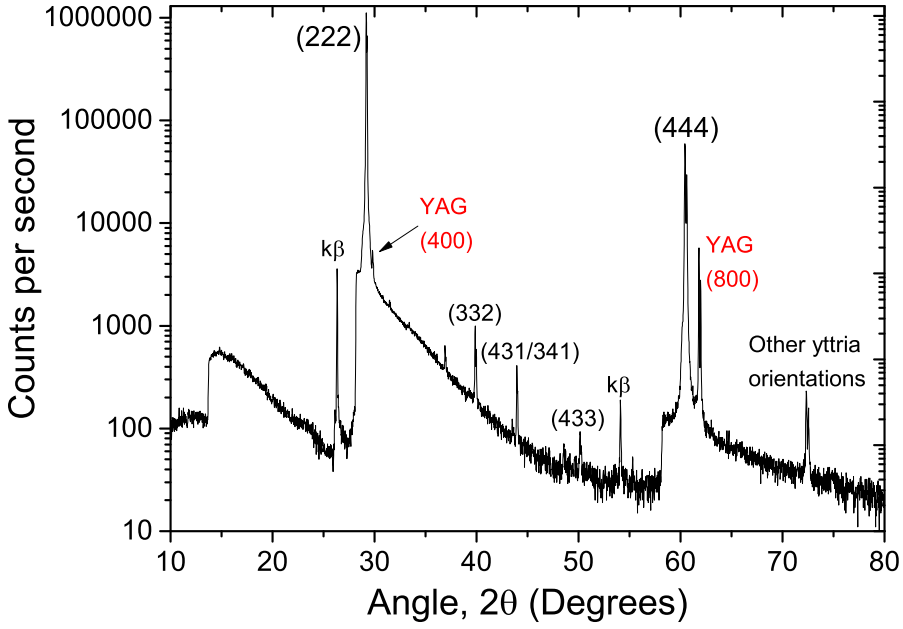

Figure 8.6: XRD spectrum collected from the multilayer sample.

rate of 10 Hz, with a peak power of 1 W. This resulted in a peak irradiance of ~125 W/cm^2, which is significantly below the saturation intensity for the material. Fluorescence from the Yb:Y_2O_3 film was collected and refocused onto a photodiode with a 1 μm long pass filter used to remove pump light. The decay of the fluorescence was exponential with a lifetime of 860 μs, as shown in figure 8.7, which is consistent with the measured lifetime of this material grown by other methods [40].

For measurement of the fluorescence spectrum, the 965 nm diode laser was focused to a spot, with second moment beam widths of 10 μm x 800 μm, at one facet of the waveguide. Fluorescence emerging from the top face of the sample, adjacent to the facet through which the incident pump light was coupled, was captured by a proximity-coupled 62.5 μm core diameter 0.22 NA multimode fiber connected to an optical spectrum analyzer (ANDO AQ6317B). This collection configuration minimizes the distance the fluorescence signal must travel through doped material, reducing spectral-dependent reabsorption. The Füchtbauer-Ladenberg equation was used to calculate the emission cross section, and McCumber analysis was then used to calculate the absorption cross section for the material using Stark levels calculated from the data in [109], as shown in figure 8.8. Some of the pump light scattered from the guide was visible in the fluorescence spectrum, so this 3 nm spectral region on the blue side of the zero phonon line was removed from the

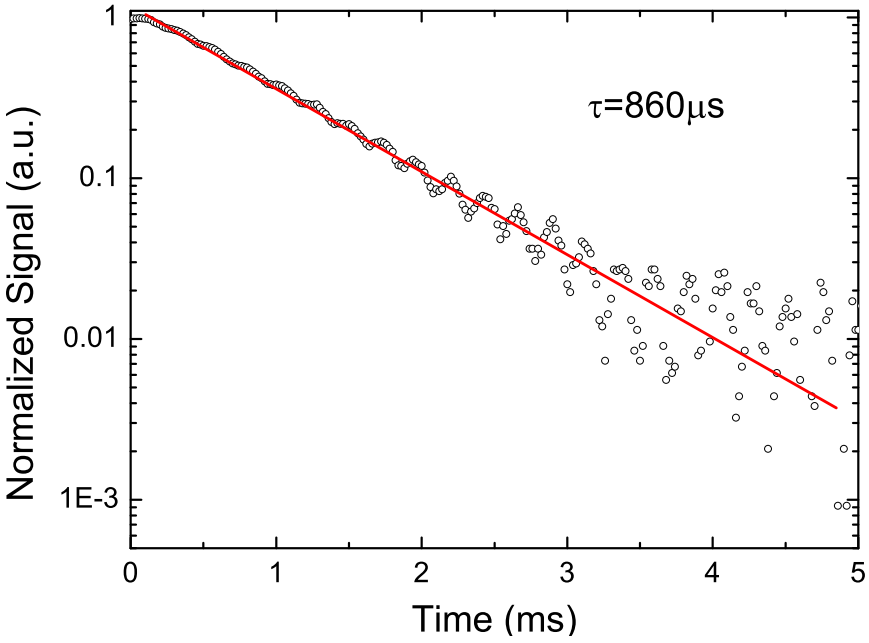

Figure 8.7: Yb:Y_2O_3 lifetime

fluorescence data and then linearly interpolated before analysis.

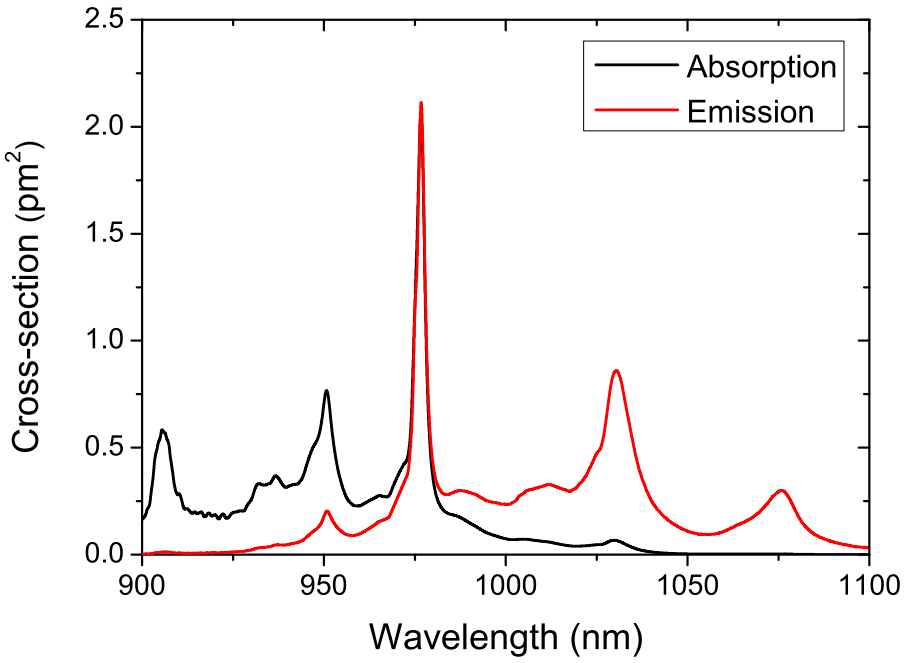

Figure 8.8: Absorption and emission spectra of Yb:Y_2O_3

8.2.2.3 Laser Experiments

The waveguide was mounted on a 5-axis translation stage (3 spatial dimensions, roll and yaw) and mirrors brought close to the opposing polished facets to form a quasi-monolithic plane-plane cavity. The pump input mirror was HT 950-990 nm, HR 1020-1100 nm, and a range of output couplers were trialled at the output facet. Light from the broad area laser diode was focused to a spot of radius 5 μm in the fast axis to allow it to be coupled into the waveguide, and quasi-collimated at a radius of 400 μm in the slow axis. The broad area laser diode was run at maximum power and its wavelength tuned by temperature control via a Peltier patch and feedback loop to stabilise the operating temperature and therefore wavelength. The pump power was then controlled using a half waveplate and polarizing beam splitter and the laser output was reflected from a HT 950-990 nm, HR 1020-1100 nm mirror to remove any unabsorbed pump light before being measured by a thermal power meter. The pump reflectivity at the angle of incidence on this mirror was measured to be significantly below 1%. The setup used is illustrated in figure 8.9.

Laser operation was obtained using three different output couplers with reflectivities of 95%, 75% and 30%, the results of which are displayed in figure 8.10. In all cases, the laser wavelength was 1030 nm, with spectrum as shown in figure 8.11(a), and laser thresholds were 2.0, 2.25 and

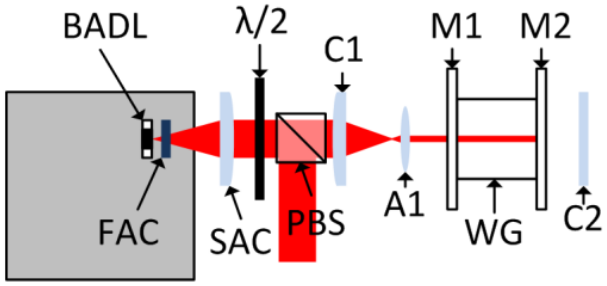

Figure 8.9: Schematic of the optical system: BADL - broad area diode laser, FAC - fast axis collimator, SAC - slow axis collimator, $\lambda/2$ - half-wave plate, PBS - polarising beam splitter, C1 & C2 - cylindrical lenses, A1 - aspheric lens, M1 - pump input mirror, WG - waveguide, M2 - output coupler.

2.5 W respectively. A laser threshold analysis was performed, based on the formalism reported by Taira *et al.* [110], the results of which suggest a parasitic cavity loss of 2.2 dB per round trip. If it is assumed that this is entirely due to waveguide propagation loss, an estimate of 1.4 dB/ cm is obtained. The highest output power was achieved using the 30% reflectivity output coupler and with the polarizing beam splitter removed, giving a maximum incident pump power of 8.5 W (after lenses and pump input mirror), which yielded a maximum waveguide laser output of 1.2 W, as in figure 8.11(b).

Following power characterisation, the laser output was imaged onto a CMOS detector array. The intensity distribution in the guided axis displayed a Gaussian profile and was close to diffraction limited, with an M^2 value of 1.2. The unguided axis showed uneven intensity across the beam, which was also seen when a HeNe laser beam was launched into the waveguide and the transmitted beam reimaged onto the same CMOS camera. This variation in intensity across the beam is likely caused by the internal structure of the grown crystal. Figure 8.12 shows a backscatter detector image of one of the polished end facets of the sample that displays internal structure in the form of columns through the thickness of the waveguide, which fits with the horizontal intensity variation of light exiting the waveguide. The top edge of the waveguide also appears chipped; this may have happened during the polishing process or could be damage occuring at a later stage. XRD spectra such as those in figures 8.1 and 8.6 show that PLD-grown Y_2O_3 grows predominantly in the <222> orientation, and the use of a <100>-oriented YAG substrate allows for four potential

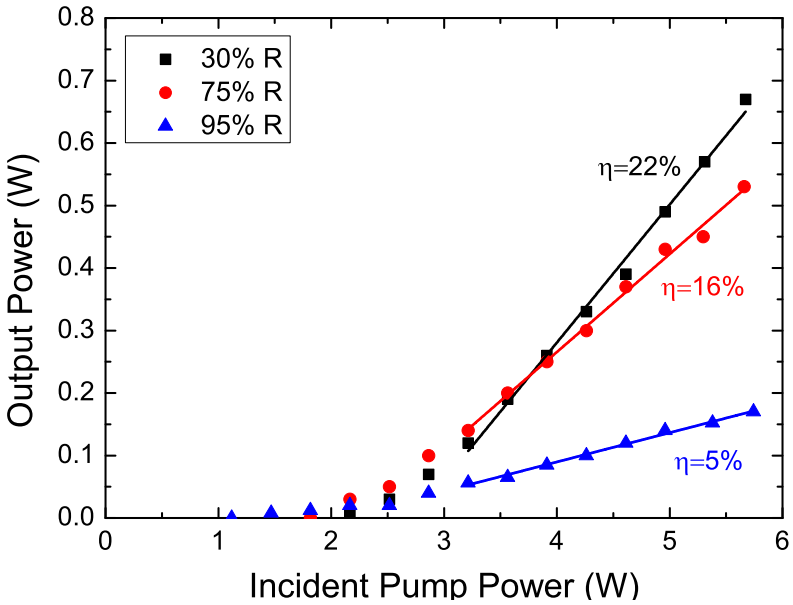

Figure 8.10: Slope efficiencies obtained from experiments with the Yb-doped multilayer yttria sample, TP1.

growth directions of this orientation, as discussed in section 6.3.1. We believe that islands of differently orientated epitaxially grown yttria are merging during the growth process and defects, porosity and strain occur at the grain boundaries leading to the significant value of propagation loss, and the resultant observed poor beam quality in the non-guided axis, pictured in figure 8.13.

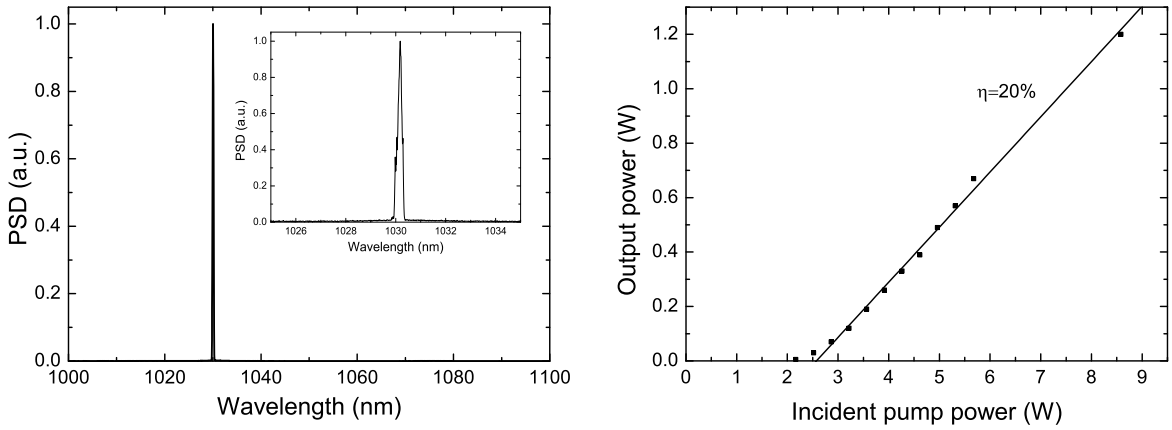

(a) (b)

Figure 8.11: (a) Laser spectrum showing laser operation only around 1030 nm. Inset: zoomed in version of laser spectrum.(b) Highest power obtained from laser experiments with the multilayer Yb:Y_2O_3 sample (TP1).

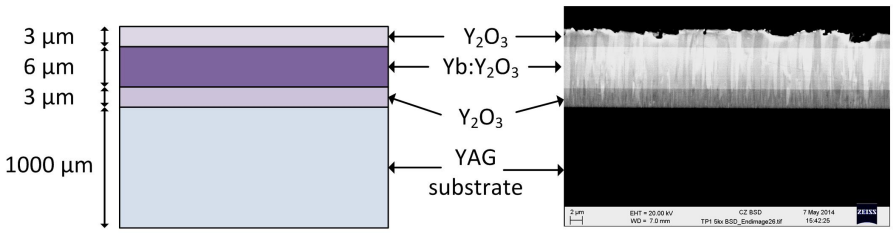

Figure 8.12: A schematic of the multilayer waveguide design, marked with the thickness of each layer, side by side with an SEM BSD image of the actual sample.

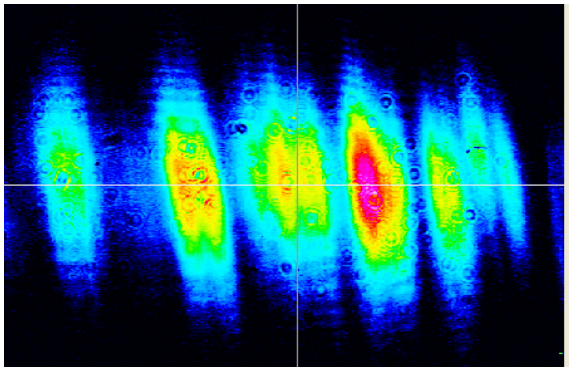

Figure 8.13: Image of the propagting laser mode output from the multilayer sample, some distance from the facet. A cylindrical lens was used in the fast axis to capture the rapidly diverging light, while the slow axis was allowed to continue to gradually diverge.

8.2.2.4 Conclusions

A Watt-level output from a PLD-grown crystalline Yb:Y_2O_3 on YAG waveguide has been demonstrated, with no negative thermal effects observed up to the maximum pump power available of 8.5 W. The multilayer structure designed to promote fundamental mode operation appears to have been successful, as a beam quality factor of $M^2 = 1.2$ was achieved in the guided axis. However, the beam quality in the unguided axis is poor, with varying intensity across the beam. We believe this to be due to the four directional orientations the <222> Y_2O_3 can grow on <100>-oriented YAG, which lead to defects in the crystal as the domains join. This effect may be able to be improved with further optimisation of the growth process, but so far seems to be an intrinsic property of Y_2O_3 growth on <100>-oriented YAG. This is not helped by using a <111>-oriented YAG substrate instead, to match the crystal orientation throughout the structure, as the lattice mismatch between the two materials with the same cut is far larger (see section 6.3.2 for more on growth on <111>-oriented YAG substrates).

Chapter 9

Yb:Lu_2O_3 Planar Waveguide Laser

This chapter continues to investigate ytterbium lasers as we study the growth by PLD of Yb:Lu_2O_3 planar waveguides. The growth conditions are outlined and the analysis of the deposited film reported, followed by spectral analysis and the highest power laser results in this thesis, which were published in reference [111].

9.1 Single Layer Sample

9.1.1 Fabrication

An Yb:Lu_2O_3 layer of approximately 8 μm in thickness was deposited on a 10 x 10 x 1 mm YAG <100>-oriented substrate. A fluence of 1.3 J/cm^2 was incident on the Yb:Lu_2O_3 target for ablation, in an oxygen atmosphere at a pressure of 2x10^{-2} mbar. The YAG substrate was heated to around 900°C from the rear by a CO_2 laser beam to aid crystalline growth. An interfacial layer of $\sim$ 2 nm Yb:Lu_2O_3 was deposited and annealed at >1000°C for 5 hours prior to the main deposition to promote subsequent epitaxial growth at the YAG-Lu_2O_3 interface.

9.1.2 Sample Characterisation

The sample was analysed with XRD to characterise the crystallography, a stylus profiler to measure the film thickness and an optical interferometric microscope to determine the surface morphology. Following initial characterisation of the deposited material, the sample was end-polished such that the opposing facets were plane and parallel, resulting in a waveguide length of

~8 mm.

For Yb:Lu_2O_3 growth on <100>-oriented YAG, the XRD analysis, performed using a Bruker D2 Phaser diffractometer, contains sharp peaks, as shown in figure 9.1, indicating highly crystalline material. However, the Yb:Lu_2O_3 grows preferentially in the <111> orientation on the YAG <100> substrate due to lattice matching considerations. This is illustrated by the (222) and (444) peaks detected for the Lu_2O_3 overlapping the (400) and (800) peaks of YAG in the XRD spectra, making them practically indistinguishable, which is in agreement with spectra obtained from the crystal database [10] that has been used to identify the peaks present in figure 9.1, along with PDXL2 Version 2.1.3.4, Rigaku Corporation (2007-2013) software. Looking at the first 5 results on the crystal database for Lu_2O_3 (Ia-3 space group) and YAG, the (222) Lu_2O_3 peak 2θ values range from 29.78° to 29.88° and the (400) YAG from 29.78° to 29.80°, while the peak in our data sits at 29.78°.

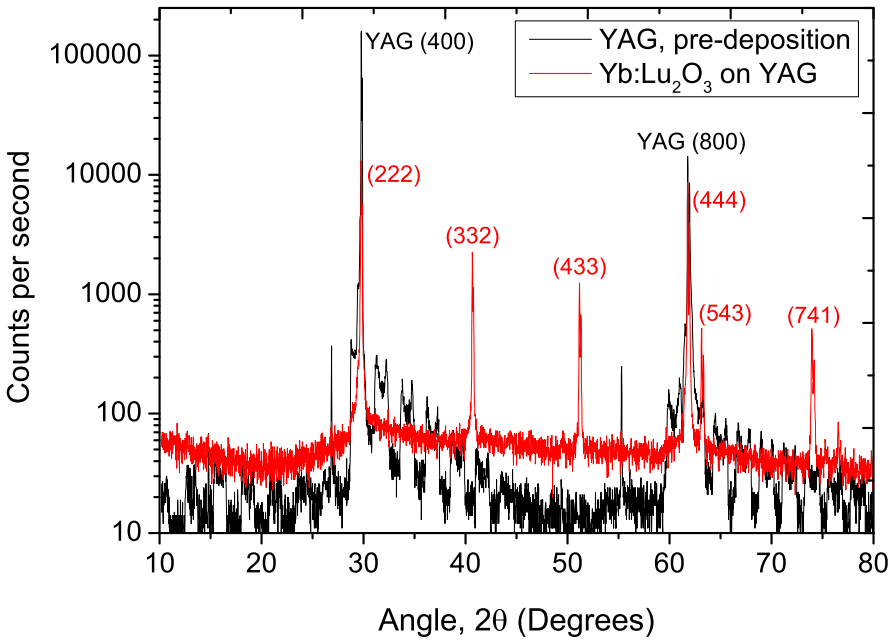

Figure 9.1: XRD spectrum of Yb:Lu_2O_3 on YAG, displayed with the XRD specturm obtained from the YAG substrate prior to deposition.

The sample thickness was measured to be 8 μm, and the number of surface particulates was counted at five positions over the sample by an optical interferometric microscope and associated

software. Using the mean of these readings, the particulate density for this sample has been calculated to be approximately 1.5x10^4 cm^{-2} for particulates >100 nm and 2.2x10^4 cm^{-2} for particulates >50 nm; these values are roughly comparable to those reported in [101] for particulates >100 nm and around a factor of 7x fewer for those >50 nm.

To determine the emission characteristics, light from a broad-stripe diode laser operating close to the zero-phonon line, at 976 nm, was focussed into the Yb:Lu_2O_3 waveguide through one of the polished end facets. Fluorescence was captured from the top surface of the waveguide by a 62.5 μm core-diameter, 0.22 NA optical fiber positioned above the excited region of the waveguide. This collection geometry minimises the distance through doped material that fluorescence must travel before being collected, effectively reducing the spectrally dependent re-absorption loss of the Yb ions. The light captured by the fiber was measured using an optical spectrum analyser (ANDO AQ6317B), with a resolution of 0.2 nm. Due to an overlap of the fluorescence and pump spectra, pump light either scattered from the waveguide or not fully coupled into the guide can distort the measured spectra. To obtain a clean fluorescence spectrum two different measurements were made, with the pump laser wavelength-tuned, by adjusting the operation temperature and current, either side of the zero phonon line, at 959 nm and 981 nm. The two spectra had their pump-contaminated regions removed, were normalised to the 1033 nm emission peak and then averaged, resulting in a spectrum with negligible pump contamination and minimal influence from reabsorption losses. The fluorescence lifetime of the sample was measured under low excitation density, resulting in a measured lifetime of 785 μs, as displayed in figure 9.2, slightly below the low concentration limit of the lifetime of 820 μs [4], evidencing a slight quenching.

An emission cross section for the sample was calculated using the Füchtbauer-Ladenburg equation assuming a unity quantum efficiency, a constant refractive index of 1.911 [69] and the reported low concentration lifetime of 820 μs [4]. The calculated emission cross section is shown in figure 9.3 and shows no significant differences from bulk crystals [112]. To calculate the absorption cross section the reciprocity technique was used in combination with McCumber analysis and the electronic Stark levels of the ground and excited state manifolds as reported by Peters [112].

To measure the Yb ion concentration in the sample two methods were used; energy dispersive X-ray analysis (EDX), which resulted in a value of 3.6 $\pm$ 0.4 at. %, and a method, as follows, that relies on the absorption of laser light from a tunable source by the Yb ions. Transmission measurements for the waveguide were taken for a range of wavelengths using a narrowband (<0.1

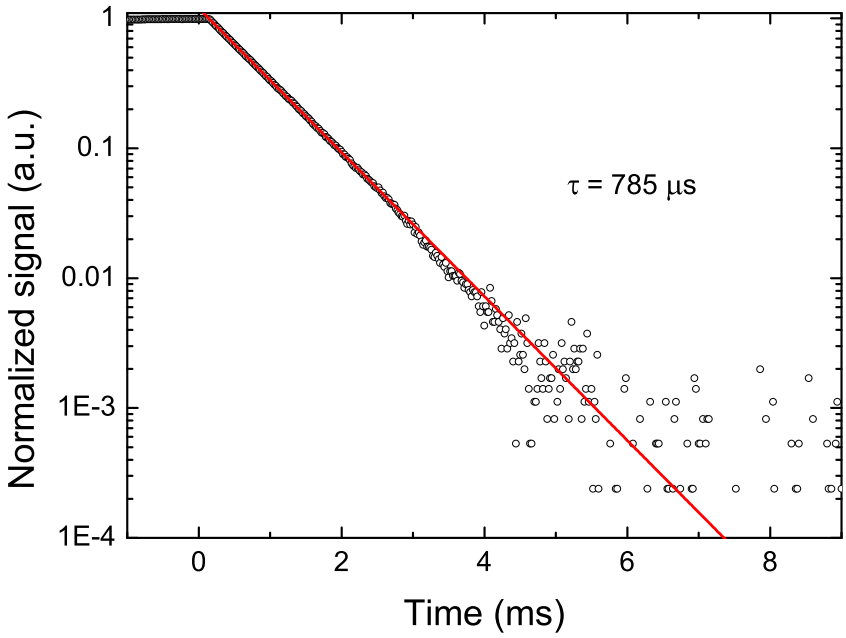

Figure 9.2: Yb:Lu_2O_3 fluorescence lifetime.

nm FWHM) tunable Yb:fiber laser. The laser was focussed to a spot of 7 μm diameter and coupled into the waveguide, and the output facet of the waveguide was imaged after magnification on to a narrow slit arranged to remove any potential contributions from light emerging from regions outside the waveguide core. Using this setup, the transmission through the system was measured for a range of wavelengths close to the 1033 nm absorption line. The transmission through the guide can be modelled well by assuming a broadband background insertion loss (IL) and a spectrally dependent loss due to absorption from the Yb^{3+} ions. Figure 9.4 presents the measured transmissions and the expected transmission for a background IL of 2.35 dB and an Yb^{3+} density of 9.0 x 10^{20} cm^{-3}. The background insertion loss includes a contribution of 0.9 dB from the two Fresnel reflections, 0.45 dB from each of the two uncoated facets, and a further 0.1 dB from residual reflections from AR coated coupling optics, thus resulting in an estimated upper limit on the propagation loss of 1.35 dB, or 1.7 dB cm^{-1}. The Yb ion density of 9.0 x 10^{20} cm^{-3} corresponds to a doping level of 3.2 $\pm$ 0.3 at.% assuming a cation density identical to bulk, which is in agreement (within the quoted errors) with the value obtained by EDX.

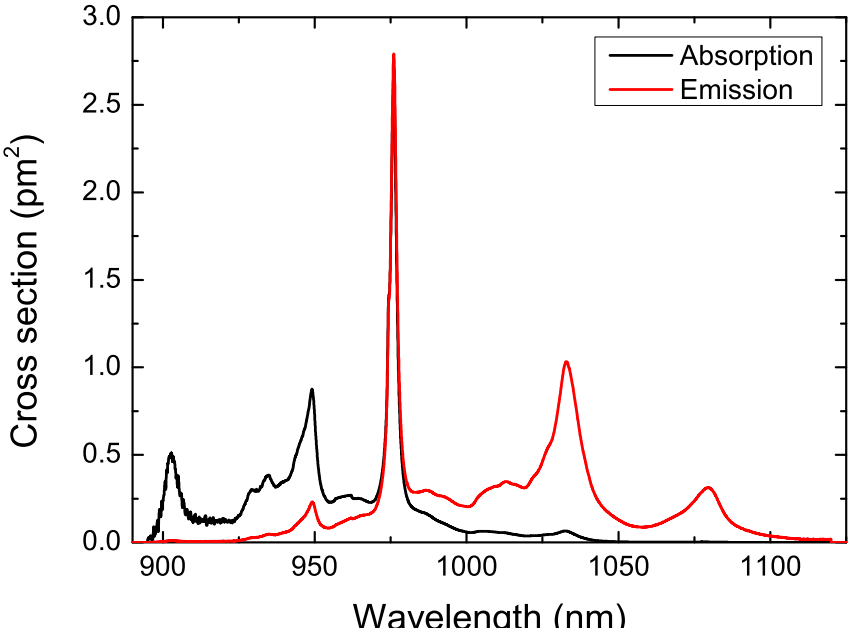

Figure 9.3: Absorption and emission cross-sections of Yb:Lu_2O_3.

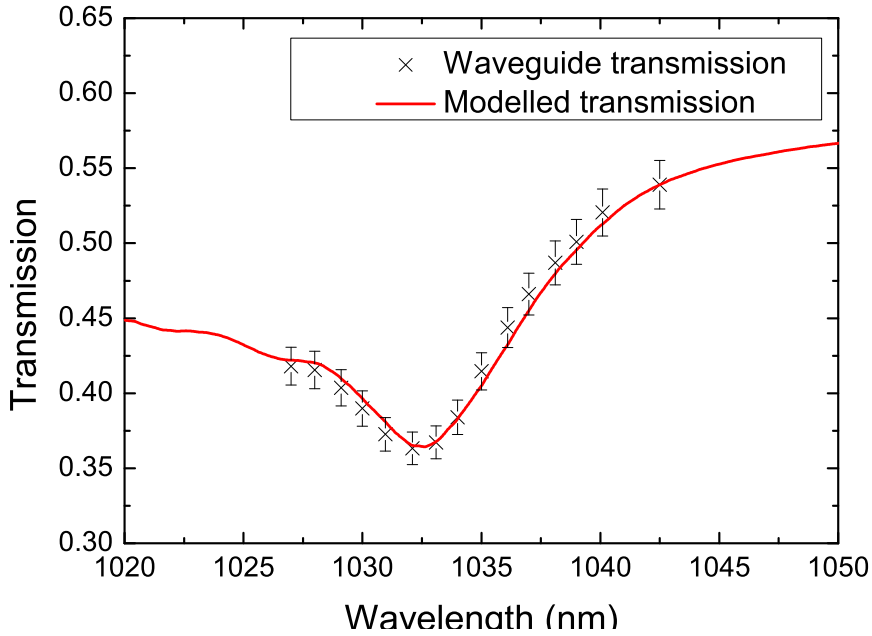

Figure 9.4: Transmission of a tunable Yb:fiber laser through the Yb:Lu_2O_3 sample to measure the Yb concentration.

9.1.3 Laser Experiments

The waveguide was mounted on a water-cooled heatsink attached to a 5-axis translation stage and a pump input mirror (HT 950-990 nm, HR 1020-1100 nm) brought into close proximity to the pump input facet. The other facet was either used as the output mirror, relying on the Fresnel reflection of 9.8% from the Lu_2O_3-air interface to provide feedback, or had an output coupling (OC) mirror brought into close proximity to the output facet. The Yb:Lu_2O_3 waveguide laser was pumped by a beam from a diode-laser bar operating around 976 nm that was focused by an acylindrical lens (AC1) to a diameter estimated to be 10 μm in the fast axis, at the input facet, and 1.2 mm in the slow axis, approximately half-way through the guide, with a system of cylindrical lenses as shown in Fig. 9.5. Cylindrical lenses C1 and C2 formed a telescope in the fast axis with a magnification of 6x and C3 loosely focused the beam in the slow axis.

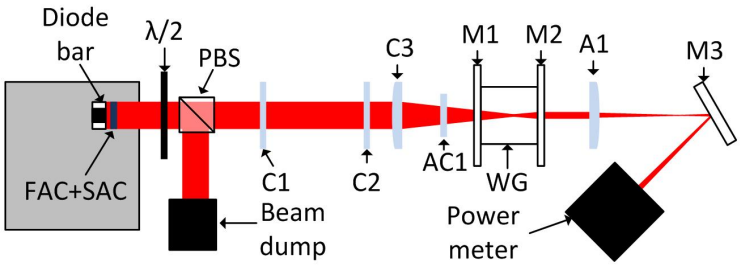

Figure 9.5: Schematic of the optical system: FAC - fast axis collimator, SAC - slow axis collimator, PBS - polarising beam splitter, C1, C2 & C3 - cylindrical lenses, AC1 - acylinder, M1 - pump input mirror, WG - waveguide, M2 - output coupler, A1 - aspheric lens, M3 - dichroic mirror.

To avoid shifts to the diode central wavelength when changing pump power the diode current and heatsink temperature were kept constant, and the pump power varied using a half-wave plate and polarising beam splitter. The output from the waveguide was collected with an aspheric lens (f=18 mm, NA=0.54) and the laser light reflected by a dichroic mirror (HT 900-990 nm, HR 1020-1100 nm) onto a power meter. Pump light transmitted through the dichroic mirror, mainly from the extremes of the diode spectrum that have poor overlap with the Yb:Lu_2O_3 absorption spectrum, was recorded with another power meter, to assess the pump absorption efficiency. The laser output performance as a function of absorbed pump power for the different laser configurations trialled is presented in figure 9.6(a). The absorbed pump power plotted in figure 9.6(a) is an over estimate as not all of the incident pump light was coupled into the waveguide or captured by the collection

lens, therefore, it could not be accounted for in the determination of the absorption, derived from the transmitted pump power subtracted from the incident pump power.

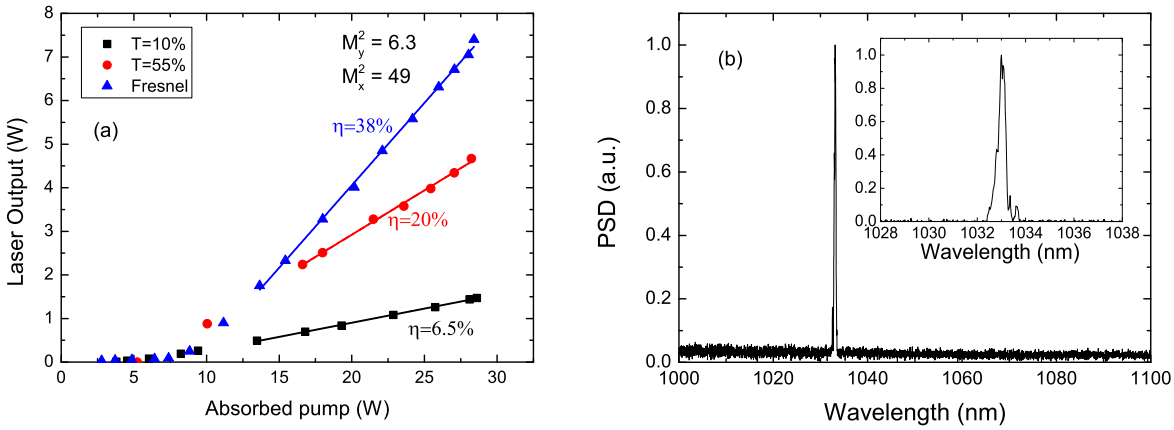

Figure 9.6: (a) Slope efficiencies and (b) Yb:Lu_2O_3 laser spectrum.

The best performance obtained was from the laser setup using the Fresnel reflection of the output facet, which gave a maximum output power of 7.4 W and a slope efficiency of 38% with respect to estimated absorbed pump power. A Caird analysis [82] of the laser performance gives an upper estimate of the parasitic waveguide loss to be 4.6 dB per round trip. The laser output wavelength was 1033 nm for all output couplers trialled, showing a high inversion density was required to reach threshold, consistent with moderate to high round-trip losses. The recorded spectrum is shown in Fig. 9.6(b), showing no lasing at other wavelengths and a zoomed-in view around 1033 nm. A waveguide of this thickness, 8 μm, operating at 1033 nm theoretically supports 9 modes, and second-moment beam-quality measurement established the laser output to be highly multimode with an M^2 of 6.3 in the guided axis and 49 in the unguided axis, at full power. The output mode of the laser is consistent with the inhomogeneous sample structure previously seen in PLD-grown sesquioxides, as reported in [108] for Yb:Y_2O_3. This laser mode in the unguided axis is visibly improved compared to that seen in Y_2O_3 growth on <100>-oriented YAG, which we believe is due to the closer lattice match between the Lu_2O_3 and <100>-oriented YAG.

Further experiments were later conducted by S. J. Beecher to see how laser results compared when using a 940 nm diode bar laser as the pump source. The setup was similar to that used for the 976 nm diode pumping, but simpler as the half-wave plate and polarising beam splitter could be excluded because the wavelength dependance on the pump current was less crucial as the absorption peak around 940 nm is far broader and therefore more tolerant to small changes in

pump wavelength and a broader pump spectrum. Laser operation was again achieved using the Fresnel reflection at the output coupling facet. The results of this laser characterisation experiment are displayed in figure 9.7, along with the results obtained using Fresnel reflections for output coupling when the 976 nm pump was employed for comparison. It can be seen that although the slope efficiency achieved with the 940 nm pumping was slightly lower, the laser threshold was also slightly lower and the maximum output power exceeded that achieved with 976 nm pumping, with a maximum output of 7.9 W. As for the 976 nm pumped laser, there was no sign of thermal rollover. In the case of 976 nm pumping the quantum defect limit is higher as the pump wavelength is closer to the output laser wavelength, at 94.4%, compared to 91.0% for 940 nm pumping. In these experiments, 40% of the quantum defect limit was reached when using 976 nm pumping and 37% in the case of 940 nm pumping.

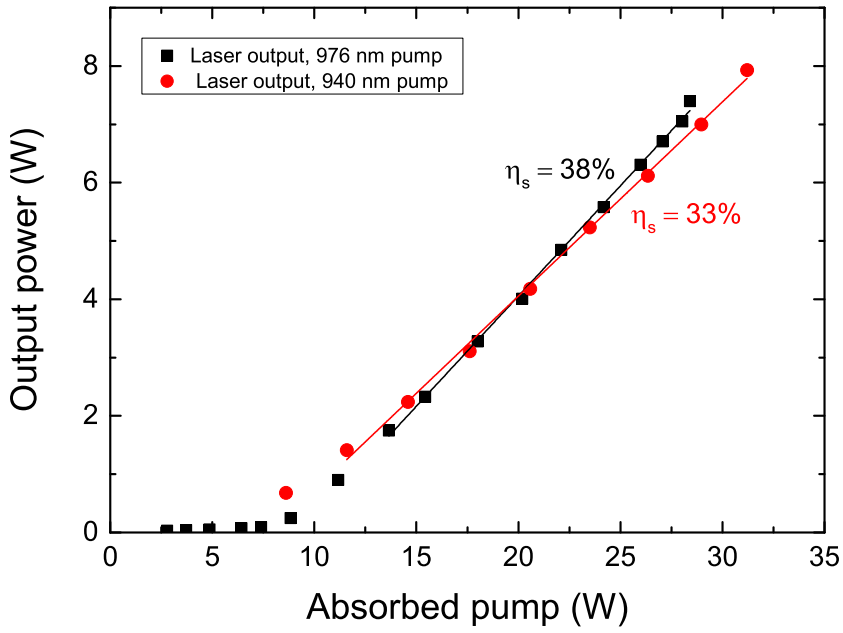

Figure 9.7: Comparison of laser results achieved with 976 nm (black squares) and 940 nm (red circles) pumping, using Fresnel reflections to outcouple the laser light.

9.2 Conclusions

7.4 W of laser power has been obtained from a PLD-grown Yb:Lu_2O_3 waveguide on a <100>-oriented YAG substrate, with a slope efficiency of 38% with respect to absorbed pump power when pumped at 976 nm. A slightly higher maximum output power of 7.9 W was acheived using a 940 nm pump source, but with slightly lower slope efficiency. In both cases, there was no sign of thermal rollover, even at the highest pump powers used so far, despite minimal thermal management; this is a good indicator of the excellent thermal properties of these sesquioxide hosts. The output power obtained is currently limited by the available pump power, its launch conditions and absorption. In our setup using the 976 nm pump source, around 10 W of pump power was lost due to the spectral width of typical free-running diode bars exceeding that of the zero-phonon line of Yb:Lu_2O_3. Further improvements in the performance using a 976 nm pump source are expected by wavelength-narrowing the pump diode e.g. using a volume Bragg grating, polarisation multiplexing two diode bars together and by growing thicker waveguides capable of accepting the light from diode stacks or spatially multiplexed diode bars.

Chapter 10

Pulsed operation of rare-earth-doped sesquioxide planar waveguides

10.1 Introduction

In addition to the main work in this thesis on the growth and characterisation of sesquioxides by PLD and their application as cw planar waveguide lasers, this chapter outlines work, performed by Amol Choudhary, showing that Q-switched operation of my Yb:Y_2O_3 waveguides is also possible. These experiments were in collaboration with researchers at the University of Pittsburgh, who provided the graphene coatings using atmospheric pressure chemical vapour deposition (APCVD). Two configurations of the graphene saturable absorber were trialled. Firstly, a graphene-coated output coupler was used for experiments with the multilayer sample from section 8.2.2, and following this a graphene layer was deposited onto the top surface of an uncapped Yb:Y_2O_3 waveguide to take advantage of evanescent-field interactions. Results obtained were published in references [113] and [114], respectively.

10.2 Q-Switched Operation using Graphene as a Saturable Absorber

Following experiments outlined in section 8.2.2, the multilayer Yb:Y_2O_3 sample underwent further testing. This began with cw characterisation using a single-mode fiber-coupled laser diode (3S Photonics) with a maximum output power of 750 mW and a grating-stabilised wavelength of

975.1 nm as the pump source, and a selection of output couplers. The setup for these experiments is shown in figure 10.1. The laser diode output from the fiber was collimated by an aspheric lens of focal length 8 mm, and launched into the waveguide by using another f = 8 mm aspheric lens to focus the beam. A half-wave plate and faraday rotator were inserted into the path of the pump beam, between the two aspheric lenses, to block back reflection from the waveguide facet. The waveguide was mounted onto a copper block that was thermoelectrically cooled to 18°C and mounted on a multi-axis stage to allow optimisation of the pump beam coupling into the waveguide. The laser cavity was formed by end-butting a 200 μm-thick dielectric mirror with high reflectivity of >99% at the laser wavelength and high transmission at the pump wavelength to the input facet and a 200 μm-thick dielectric mirror at the end facet, of which a range of different output coupling percentages were trialled, using a fluorinated liquid (Fluorinert FC-70). The output from the laser was collected using an f = 11 mm aspheric lens, and a long-pass filter was inserted into the beam path to prevent the pump beam from reaching the thermal detector (Melles Griot) used for measuring the laser output power.

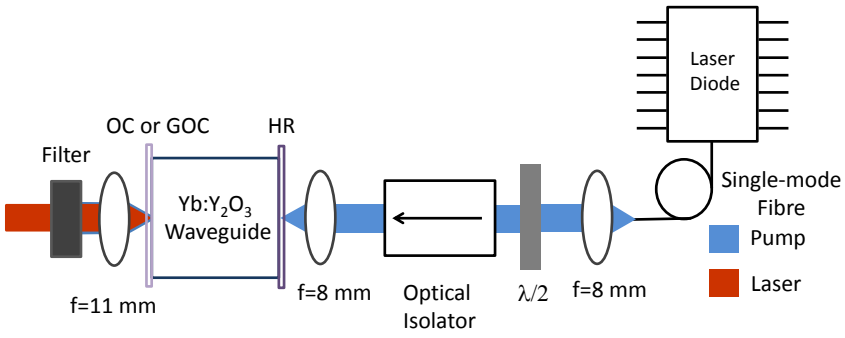

Figure 10.1: Setup used for cw laser characterisation of the Yb:Y_2O_3 waveguide sample.

Using an output coupler with 0.8% transmission, a lowest absorbed threshold power of 123 mW was obtained, with the output power reaching 5.7 mW for the maximum available pump power, corresponding to an absorbed power of 528 mW, giving a slope efficiency of 1.6%. The output coupling was increased to 2%, causing an increase in threshold to 136 mW of absorbed power and a slope efficiency of 4.9%. Further increases in output coupling to 5% and 13% gave absorbed pump power thresholds and slope efficiencies of 155 mW and 9.8%, and 167 mW and 14.5% respectively. The largest output coupling trialled was 19.5% and had the highest threshold of 171 mW, but also the highest maximum output power of 83 mW and slope efficiency of 25%.

These results are displayed in figure 10.2, and the laser mode profile, taken by imaging the output from the waveguide onto a camera (WinCamD from Dataray Inc.) is shown in figure 10.3. The measured mode diameters were 6.3 and 86 μm in the guided and unguided directions, respectively.

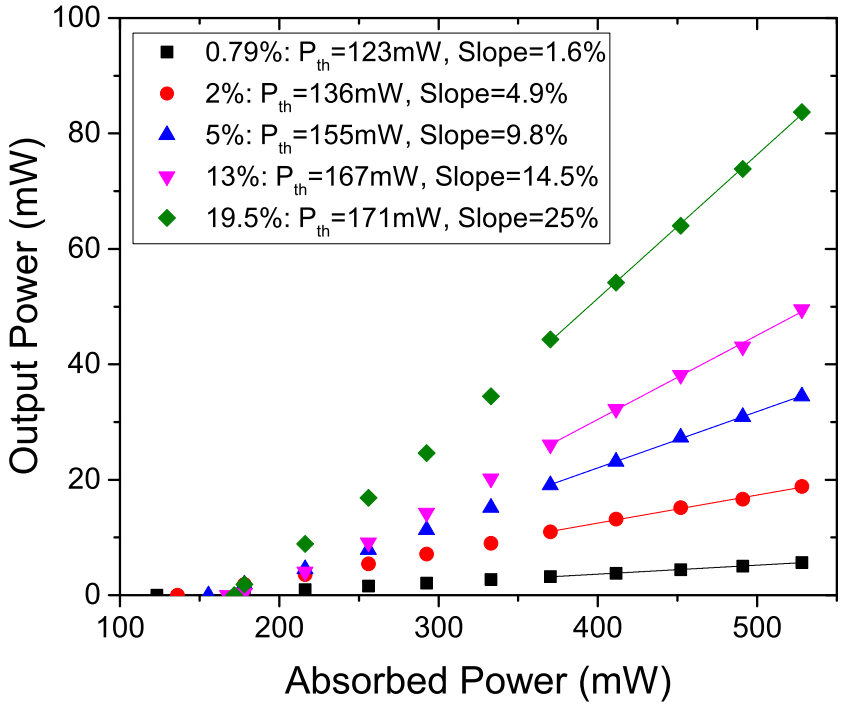

Figure 10.2: CW characterisation results

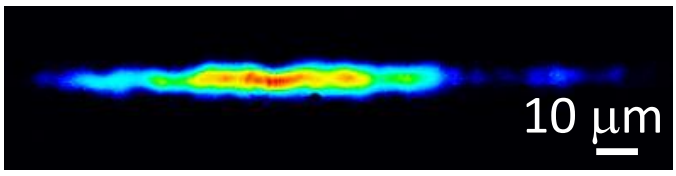

Figure 10.3: Mode profile.

The waveguide loss can be estimated from the measured slope efficiencies, by plotting the inverse of the slope efficiencies against the inverse of the transmission of the output coupler, using a Caird analysis (see section 3.3), as shown in figure 10.4. This plot give a loss estimate of 1.9 dB/cm for this waveguide.

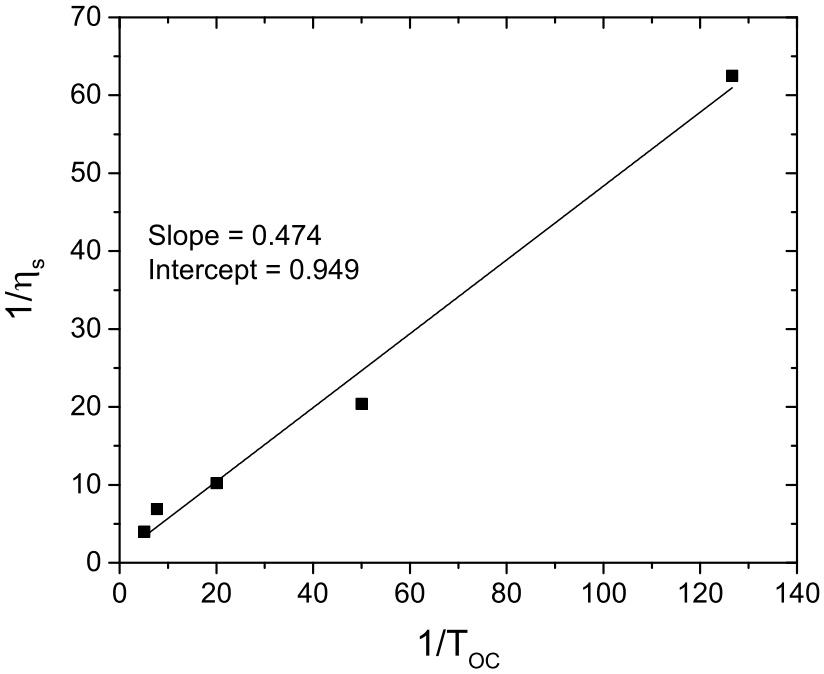

Figure 10.4: Caird plot used for estimation of the waveguide loss by comparison of the slope and intercept values when compared with equation 3.13.

Following the cw characterisation, the output coupling mirror was replaced by a 1 mm-thick mirror with 2% transmission at 1030 nm, coated with graphene to act as a saturable absorber for pulsed laser operation. The relatively low output coupling was chosen to ensure high intracavity power and hence enable saturation of the graphene layer. The graphene layer was grown by atmospheric pressure chemical vapour deposition at 1050°C on 1 inch diameter ultraflat large-domain copper substrates [115]. The quality of the deposited graphene was verified by Raman microscopy and found to be mostly single layer, as indicated by the position of the 2D and G peaks and the Lorentzian shape of the 2D peak [116]. A thin layer ($\sim$ 300 nm) of poly-(methyl methacrylate) (PMMA) was spun onto the graphene, and the underlying copper substrate was removed using mechanical cutting and chemical etching with ammonium persulfate. This stack of graphene and PMMA was washed several times by being transferred into clean baths of deionized water. The stack was then transferred to the output coupling mirror, with the graphene against the surface, and left to dry for $\sim$2 hours before baking at 180°C for 30 minutes to relax the PMMA and, in turn, improve the adhesion of the graphene layer to the output coupler. The graphene-

coated output coupler was then left to soak in acetone for 12 hours to remove the PMMA, after which is was blown dry with air.

For the pulsed laser operation experiments, the graphene-coated output coupler was mounted on a 3-axis stage to allow it to be aligned with respect to the waveguide. The absorbed threshold power for cw laser operation in this setup was 139 mW, and a transition to Q-switched operation occurred at an absorbed pump power of 370 mW. The output power is plotted with respect to absorbed pump power in figure 10.5, and displays a maximum output power of 12.8 mW for 528 mW of absorbed power. This is less than the 18 mW achieved with the 2% output coupler for the cw operation experiments, as well as achieving a lower slope efficiency of 3.3% compared to the 4.9% obtained during cw operation. These differences indicate higher round trip losses of ∼20% in the Q-switched setup, estimated by comparison of the slope efficiencies and taking into account the propagation loss and output coupling. The transmission of the graphene output coupler was measured before and after the application of the graphene layer and a decrease in transmission of ∼2.3% was found over a broad wavelength range; this is consistent with what is expected from a single layer of graphene [117]. Additional loss is therefore attributed to the alignment of the graphene output coupler with respect to the waveguide facet, as additional care was taken to not press the graphene-coated output coupler against the waveguide to prevent damage to the graphene layer. No mode-locked pulses could be achieved with the available pump power, suggesting that the pulse intensity would be insufficient to saturate the graphene saturable absorber at the high repetition rate of mode-locked pulses (∼10 GHz for this 8 mm long waveguide).

The operating wavelength of the laser was measured to be 1030.8 nm, using an optical spectrum analyser (Ando). The Q-switched pulses were measured using a DET-10 detector (Thor labs) connected to a 1 GHz oscilloscope (Agilent). The pulse repetition rate was found to increase from 877 kHz to 1.04 MHz when the absorbed pump power was increased from 370 mW to 528 mW, as shown in figure 10.5. Over the absorbed pump power increase of 370 mW to 528 mW the pulse duration decreased from 230 ns to as short as 98 ns and the pulse energy increased from 8.8 nJ to 12.3 nJ. The variation in pulse width and pulse energy with respect to absorbed pump power is displayed in figure 10.6, and the measured pulse and pulse train at the maximum pump power are shown in figures 10.7 and 10.8, respectively.

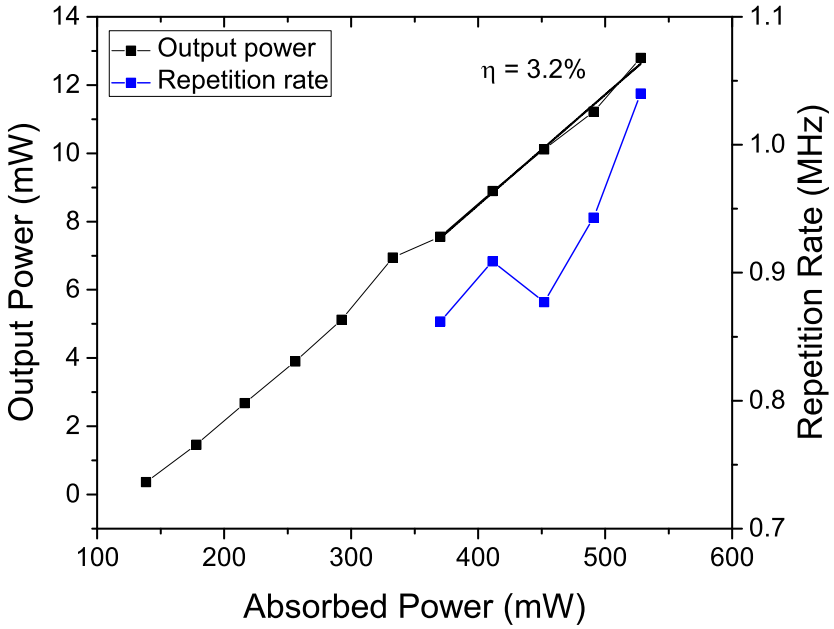

Figure 10.5: Results of Q-switching using graphene-coated output coupler and variation in pulse repetition rate with increasing absorbed pump power.

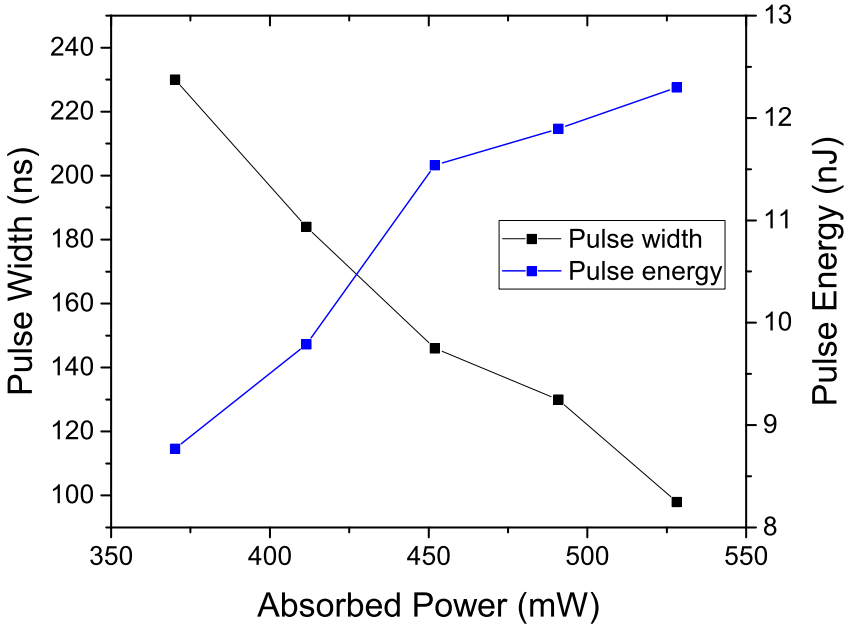

Figure 10.6: Variation in pulse width and pulse energy with respect to absorbed pump power.

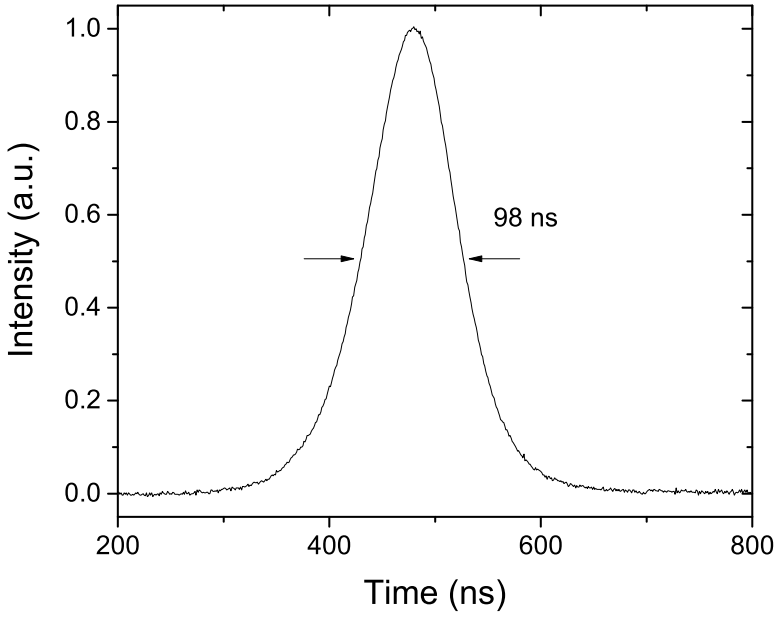

Figure 10.7: Measured pulse profile, showing a FWHM pulse width of 98 ns.

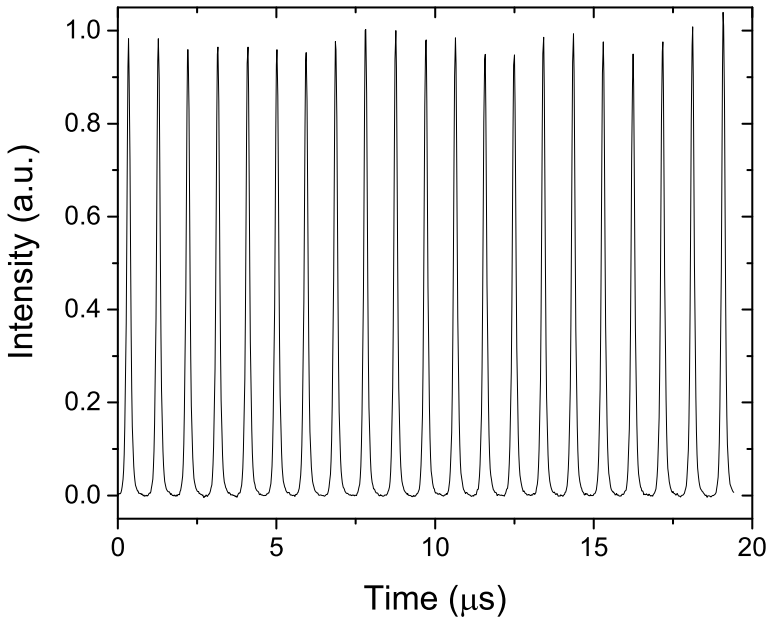

Figure 10.8: Measured pulse train at maximum pump power.

10.3 Q-switched Operation by Evanescent-Field Interaction with Graphene

A second set of experiments looking at pulsed operation of a PLD-grown waveguide were performed, this time with a 12 μm-thick single layer Yb:Y_2O_3 sample on a YAG <100> substrate and using evanescent-field interaction with a graphene saturable absorber. This configuration, with a single layer of graphene on the top surface of the waveguide, is more suitable for higher power laser operation than the previously trialled setup with the graphene saturable absorber on the output coupling mirror. Having the graphene layer on the output coupler puts it in the path of the laser beam where it's susceptible to damage so the power that can be used is quite limited. However, using evanescent-field coupling means the graphene layer isn't directly in the laser beam and therefore much higher pump powers can be used without damaging it. Another advantage of this positioning of the graphene saturable absorber is that the output coupling mirrors can easily be butted against the waveguide facets using a fluorinated liquid, unlike for the Q-switched experiments with the graphene output coupler in the previous section, 10.2. Graphene is also easy to produce and transfer onto a variety of substrates and has a zero bandgap [118], so is therefore suitable to be used as a saturable absorber for a broad range of wavelengths.

As in the previous section, the graphene was initially grown onto an ultra-flat large-domain copper substrate at 1050°C by atmospheric pressure chemical vapour deposition [115]. A thin (∼300 nm) layer of PMMA was again spun onto the deposited graphene and used as a support layer to transfer a piece of the graphene layer of the desired size onto the top surface of the waveguide. The waveguide was then heated above the glass transition temperature of PMMA to remove residual stress in the graphene and flatten it on the surface of the waveguide. The sample was then submerged in acetone for 10-12 hours to remove the PMMA. This left an area of ∼6 x 6 mm on the top of the waveguide covered with a layer of graphene.

The graphene-coated Yb:Y_2O_3 waveguide was pumped in two configurations, for different average power regimes. The first setup, shown in figure 10.10, used two polarized fibre-coupled single-transverse-mode diode lasers (3S photonics) with an operating wavelength of 975 nm and maxmimum output power of 750 mW each, which combined to give a power of 1.1 W . The output from each fiber was collimated by an aspheric lens of focal length 8 mm and a combination of a $\lambda/2$-plate and an isolator in each beam path protected the laser diodes from back-reflections. The

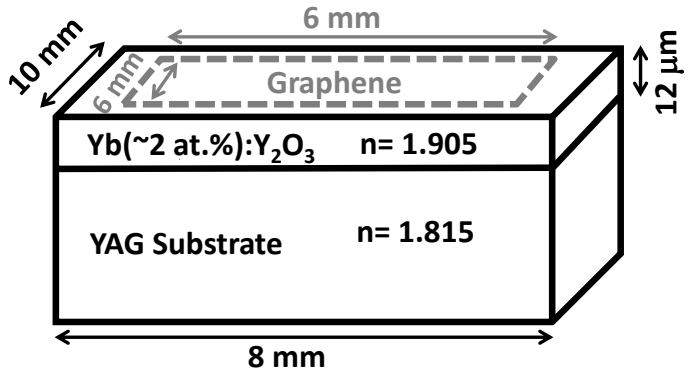

Figure 10.9: Schematic of the graphene-coated waveguide.

beams from the two laser diodes were combined using a polarizing beam splitter and coupled into the waveguide using an f = 15.3 mm aspheric lens. As for the cw experiments in section 10.2, the laser cavity was formed by end-butting thin (200 μm-thick) mirrors to the waveguide end facets using Flourinert FC-70. The input coupling mirror was highly reflective (R>99%) at the laser wavelength and the output coupling mirrors used were 12% and 19.5% transmissive at the laser wavelength. The laser output was collimated by an f = 11 mm aspheric lens and the pump and laser beams separated by a dichroic mirror so that only the generated laser power reaches the power meter.

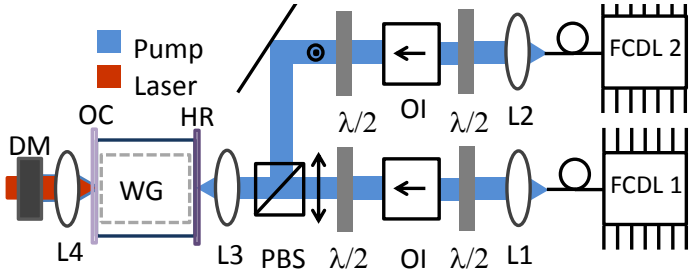

Figure 10.10: First configuration used for evanescent Q-switching experiments, using two polarized fibre-coupled single-transverse-mode diode lasers as the pump source.

The second configuration used is as shown in figure 10.11. A broad area diode laser (BADL) (with a 90 μm emitter width) is mounted on a water-cooled copper heat sink, kept at 25°C, and could deliver a maximum of 6 W of pump power. The bandwidth of the BADL was 4.1 nm and had a central wavelength of 976.5 nm. Cylindrical lenses were used to collimate the fast and slow axes of the BADL output, and the power incident on the waveguide was controlled using a half-

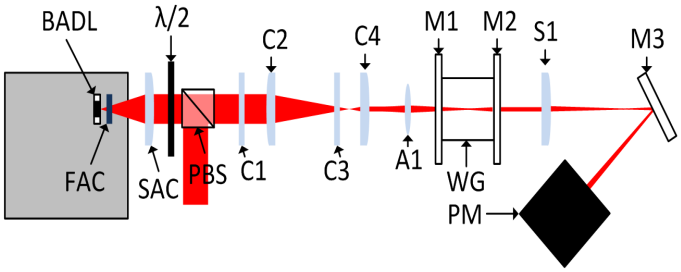

Figure 10.11: Second configuration used for evanescent Q-switching experiments, using a broad-area diode laser as the pump source.

wave plate and polarizing beam splitter, as for the laser experiments in sections 8.2.2 and 9.1.3. C1 and C3 are vertically orientated cylindrical lenses with focal lengths of 25 mm and 130 mm, respectively. C1 focused the fast axis and formed an afocal telescope with C3, giving a magification of 5.2x. For the slow axis, cylindrical lenses C2 (f =70 mm) and C4 (f = 10 mm) formed a near afocal telescope that reduced the beam size by ∼7x. An aspheric lens of focal length 15 mm was then used to launch the pump light into the waveguide that was secured, using silver paint, to a water-cooled copper heat sink, held at 19°C. The spot produced had a 4σ diameter of 10 μm in the fast axis and 190 μm in the slow axis. The position of the slow axis focus relative to the fast axis focus was adjusted by tuning the spacing of lenses C2 and C4. The spacing was selected such that the slow axis focus was positioned 2 mm after the fast axis focus in free space, which corresponded to it being approproximately in the longitudinal centre of waveguide. The laser cavity was formed by dielectric mirrors, similar to those used in the previous configuration, end-butted to the input and output facets with a fluorinated liquid. The laser output was collected by a spherical lens, S1 (f = 25 mm), and was then incident on a dichroic mirror, M3, with high transmission for <1000 nm and high reflectivity for 1020-1050 nm (at an angle of 30°), which therefore reflected the laser output to a thermal power meter and rejected unabsorbed pump light. During Q-switched operation the pulses were incident on a DET-10 detector (Thor Labs) and observed on a 1 GHz digital oscilloscope (agilent MSO6104A).

For the setup shown in figure 10.10 using the combined power of two polarized fibre-coupled single-transverse-mode diode lasers, the $1/e^2$ pump diameter at the input facet of the waveguide laser was 12.6 μm. Using a mirror with 12% output coupling, a maximum average output power of 85 mW was achieved for 1052 mW of absorbed pump power, with a slope efficiency of 16.2%,

shown in figure 10.12. Q-switching was observed at an absorbed pump power of 778 mW, at which the repetition rate was 912 kHz, up to the maximum absorbed pump power of 1052 mW, for which the repetition rate increased up to 1282 kHz, also displayed in figure 10.12. The pulse duration and calculated pulse energies are plotted with respect to absorbed pump power in figure 10.13 and range from 235 ns down to 121 ns and from 43 nJ up to 63 nJ, respectively. The pulse profile and pulse train were recorded for maximum power operation, and are displayed in figures 10.14 and 10.15, and the standard deviation of the pulse power calculated to be 6%.

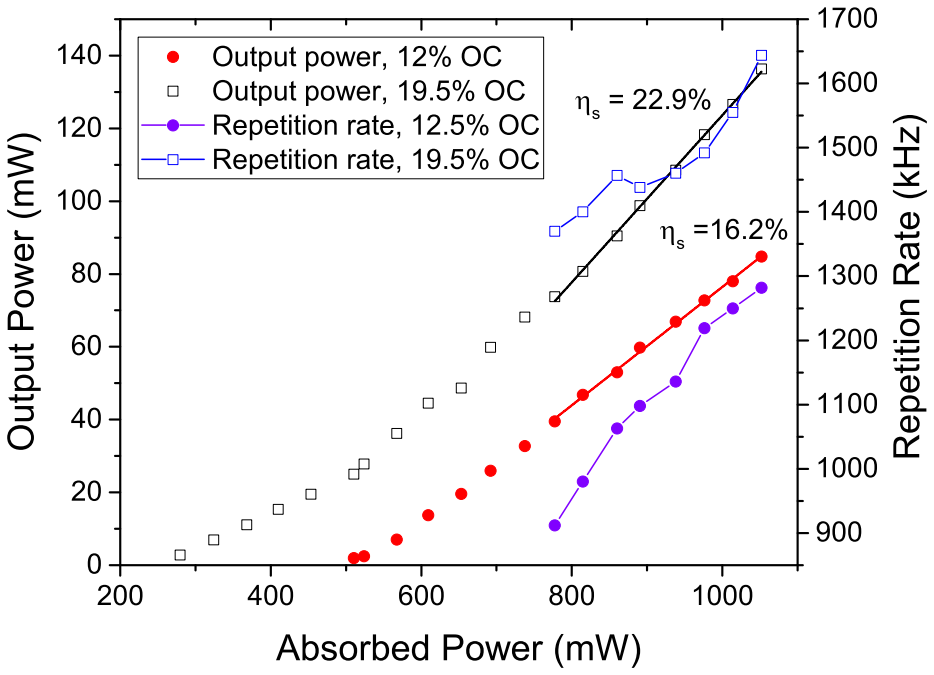

Figure 10.12: Output power and repetition rates achieved using a 12% and a 19.5% OC in configuration 1.

The output coupling mirror was replaced by another of 19.5% transmission and experiments repeated. Q-switched operation was again observed at an absorbed pump power of 778 mW, this time with the maximum average output power reaching 136 mW at full pump power. A slope efficiency of 22.9% with respect to absorbed pump power was acheived, which is considerably higher than that for the 12% output coupling mirror, highlighting relatively high cavity losses of the device. Over the absorbed pump power range of 778 mW to 1052 mW, the repetition rate increased from 1370 kHz to 1640 kHz and the pulse duration decreased from 215 ns down to 124

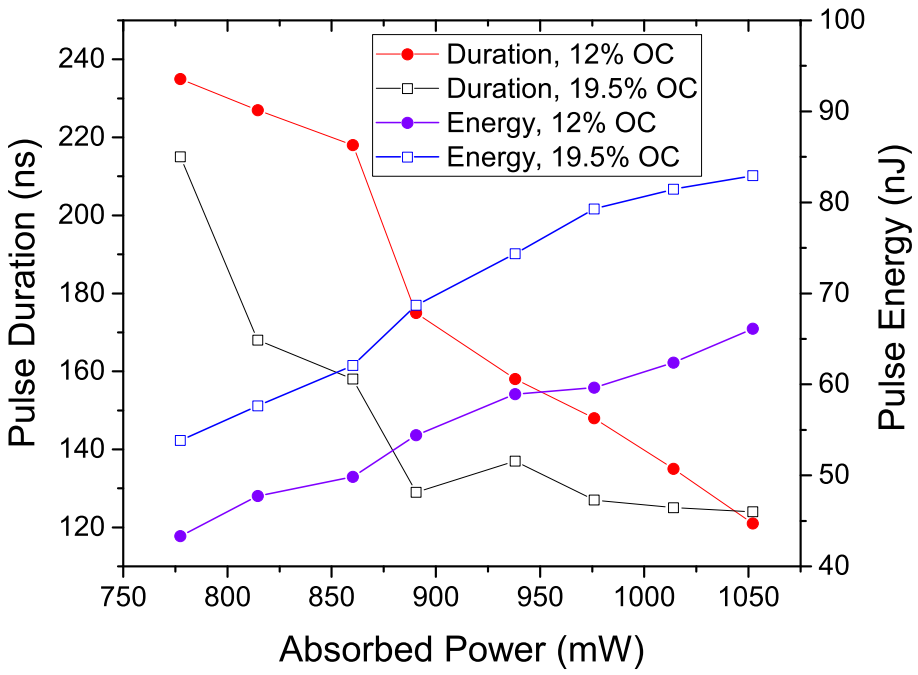

Figure 10.13: Pulse duration and calculated energies displayed with respect to absorbed pump power.

ns. The corresponding calulated pulse energies went from 54 nJ up to 83 nJ. These results can be found in figures 10.12 and 10.13. The mode profile seen in figure 10.16 was found to have a 4σ mode diameter of 9 μm in the guided direction. The pulse energy obtained here is more than 6x higher than in the previous work with the graphene output coupler (section 10.2), demonstrating the advantage of evanescent-field coupling. The quasi-monolithic cavity configuration used here with thin mirrors held against the waveguide facets with fluorinated liquid also allows for easy alignment, whereas the performance of the laser with the graphene output coupler appeared to suffer from misalignment of the graphene output coupler with respect to the waveguide output facet.

Moving on to the second pump configuration, using a broad area laser diode as the pump source, similar experiments were performed. Using the 12% output coupler, the output power increased and the repetition rate reduced slightly in comparison with results from the previous pump configuration, as can be seen by comparing figures 10.18 and 10.12. Threshold for laser operation was found to be at an absorbed pump power of 1.33 W, and Q-switched operation began

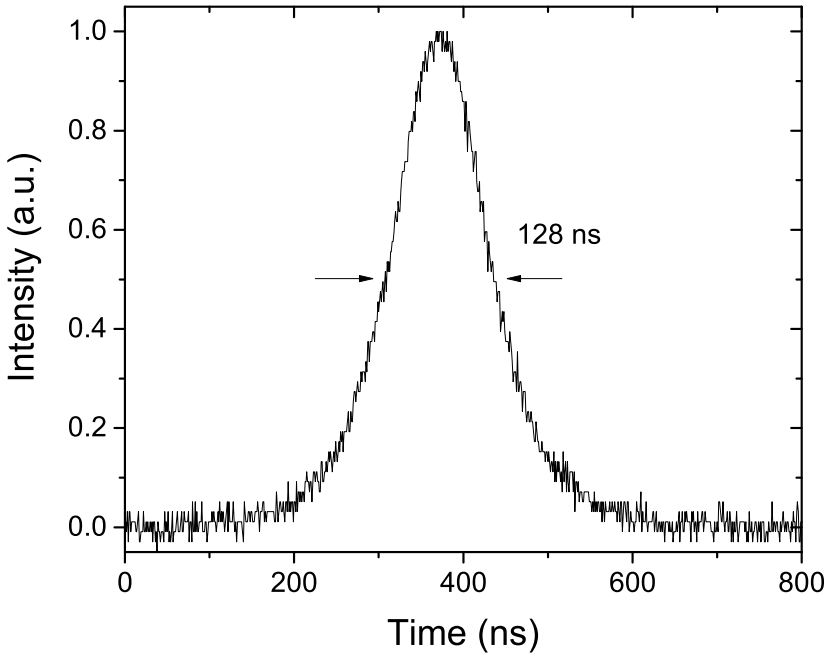

Figure 10.14: Pulse profile for maxium power operation using the 12% OC.

when the absorbed pump power was increased to 2.8 W. The output power at this pump power was 123 mW, while the pulse duration and repetition rate were 270 ns and 934 kHz, respectively. When the absorbed pump power was increased to a maximum of 4.1 W the average output increased to 261 mW, with a slope efficiency of 12.6%. This decrease in slope efficiency is likely to be due to the larger mode size of the pump beam in the unguided axis, which therefore samples more of the structural variation seen in the waveguide, see figure 8.2(b). At full pump power the pulse repetition rate increased to 1149 kHz and the shortest pulse duration was 160 ns. Pulse energies were found to increase from 132 nJ up to 227 nJ when the pump power was increased from 1.33 W to 4.1 W. The pulse duration and energy as a function of absorbed pump power are displayed in figure 10.18. The absorbed power was calculated by comparing the power incident on the waveguide and the power transmitted through it. These measurements were taken at laser threshold and translated to an absorption of 70%. It was expected that not all pump power would be absorbed as the emission spectrum of the broad area laser diode is broad in comparison to the absorption peak of the Yb:Y_2O_3. The mode profile is displayed in figure 10.19 and has a 4σ mode diameter of 10 μm in the guided direction. The mode is not uniform in the unguided direction due

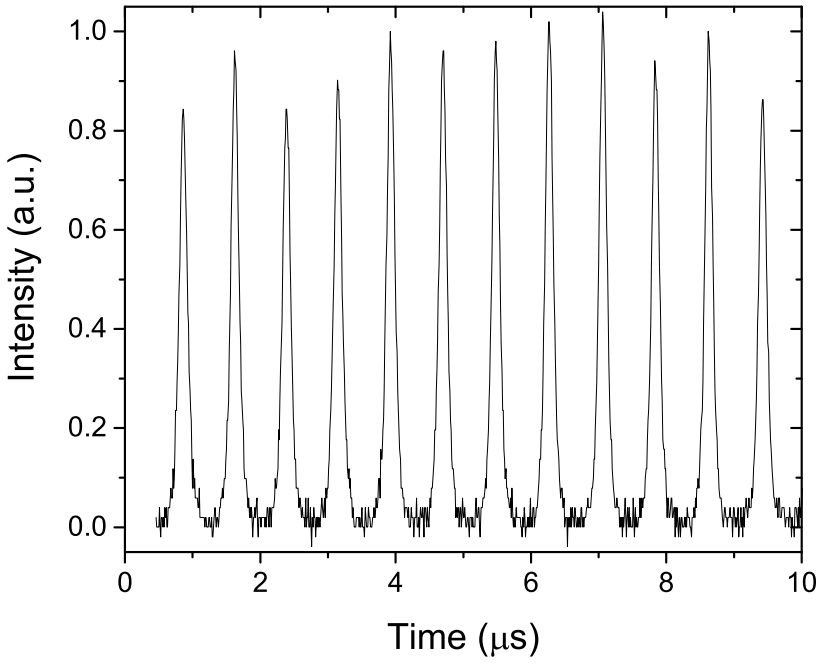

Figure 10.15: Pulse train for maxium power operation using the 12% OC.

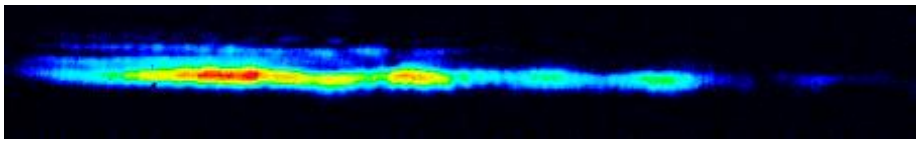

Figure 10.16: Mode profile obtained from pump configuration 1.

to the internal structure of the PLD-grown film.

Finally, the 19.5% output coupler was used in the second pump configuation, which increased the maximum average output power to 456 mW. The pulses had a duration of 158 ns and repetition rate of 1470 kHz. The pulse energy was 310 nJ and the peak power calculated to be 1.96 W, with a standard deviation of 4% for the pulse-to-pulse power. When the pump power was reduced, Q-switched operation was only obtained when the cavity was realigned, which is likely to be due to thermal effects. No damage to the graphene was observed, even at maximum pump power, and an improvement of more than 25 x in average power and pulse energy was observed compared to previous work with the end-butted graphene output coupler, demonstrating the capability of evanescent-field interaction with graphene for high-power operation.

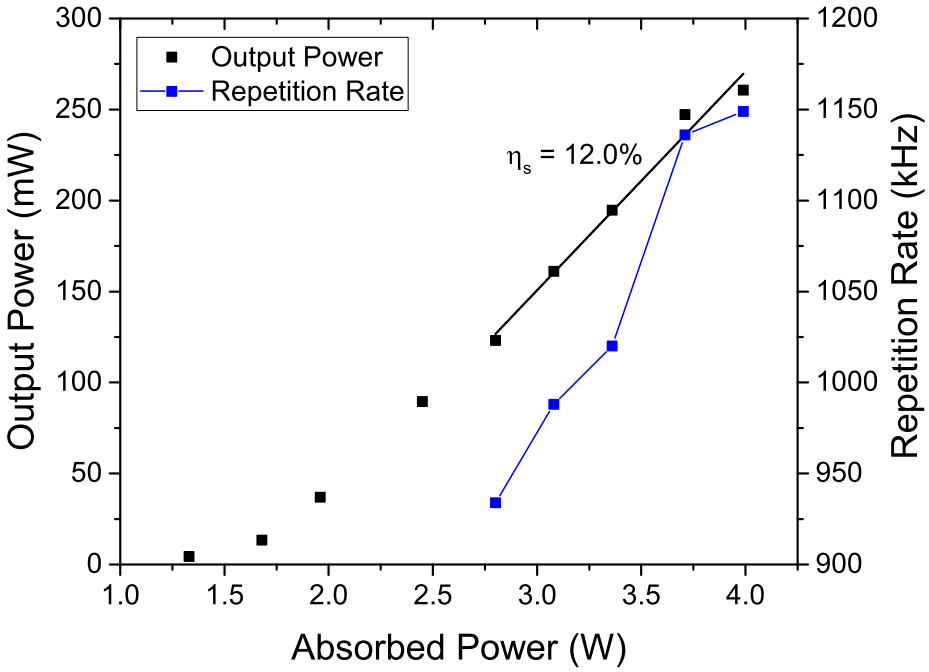

Figure 10.17: Output power and pulse repetition rate achieved using pump configuration 2 and the 12% OC.

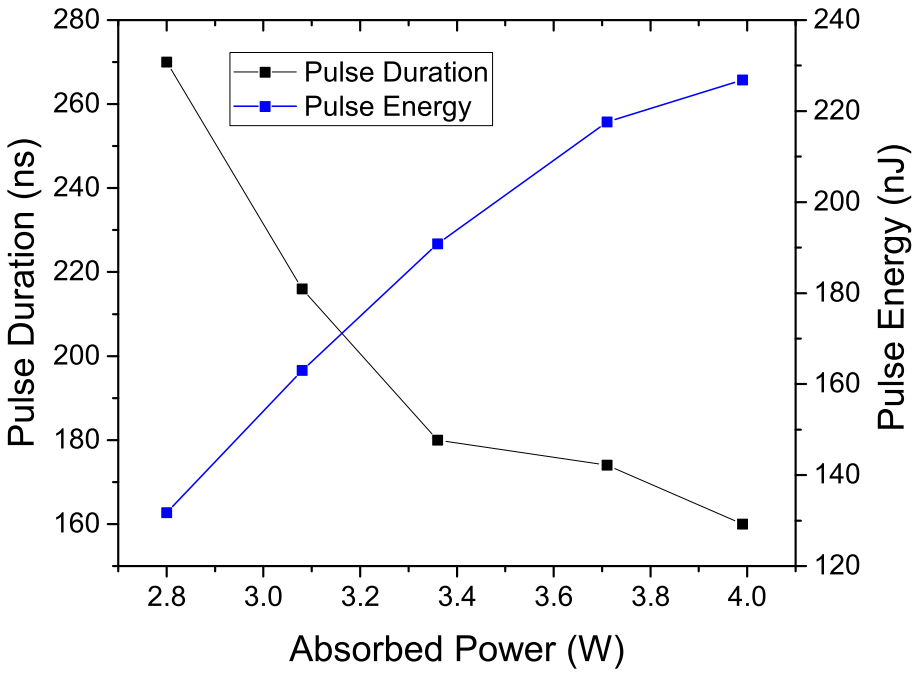

Figure 10.18: Pulse duration and pulse energy achieved using pump configuration 2 and the 12% OC.

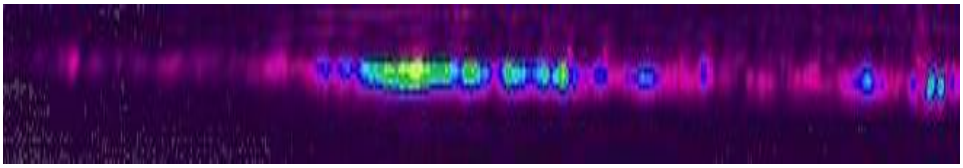

Figure 10.19: Mode profile obtained from pump configuration 2.

10.4 Conclusions

This chapter has reported Q-switched laser results obtained using PLD-grown planar waveguides and graphene saturable absorbers. The first section gives details of the first, to the best of our knowledge, PLD-grown Q-switched planar waveguide laser, which used a 2% transmission output coupler with a single layer of graphene, grown by APCVD, as a saturable absorber. This multilayer, Yb:Y_2O_3 core, waveguide output pulses as short as 98 ns with a pulse energy of 12.3 nJ at the maximum absorbed pump power of 528 mW. A maximum average output power of 12.8 mW was achieved with a slope efficiency of 3.3% for Q-switched operation. Prior to this, cw characterisation was performed with a variety of thin dielctric mirrors with different transmission values of the laser wavelength, providing different output coupling. The maximum output power achieved in cw operation was 83 mW with a slope efficiency of 25%, using a 19.5% output coupler. Propagation losses were estimated to be 1.6 dB/cm from a Caird analysis of the results of the cw characterisation.

The second part of this chapter reports higher power Q-switched operation of a single layer Yb:Y_2O_3 waveguide using evanescent-field interaction with graphene. A layer of graphene was again grown by APCVD, but this time transferred onto the top surface of the waveguide. Two pump configurations were trialled for this waveguide. Combining two single mode diodes to pump the waveguide gave an average output power of 136 mW, with a slope efficiency of 23% with respect to absorbed pump power, and pulses with energy of up to 83 nJ and a duration of 120 ns were obtained. Pumping with a broad area diode laser provided more pump power which allowed an average output power of 456 mW, with the pulse energy reaching 310 nJ, delivered in 160 ns pulses. This is the highest power and pulse energy to be obtained from any graphene Q-switched waveguide laser. No damage to the graphene layer was observed, suggesting this method of using evanescent-field interaction with graphene is suitable for higher power experiments in the future.

Chapter 11

Conclusions and Future work

11.1 Introduction

This final chapter provides some ideas of further similar work and future directions for this project, ranging from further optimisation of the waveguide sample to exploring new sample possibilities due to the extra capabilties available with the updated PLD system, before some concluding remarks.

11.2 Further optimisation of growth conditions

In this thesis the growth optimisation experiments have focused mainly on achieving samples with few particulates, while maintaining a reasonably high growth rate (often around 4 μm per hour). This was done by adjustment of the ablation fluence and background gas pressure. As PLD has many variables, there are lots more studies that could be carried out to see how the growths are affected and then be able to choose a set of growth conditions that are optimal for the most important qualities of the crystal; in this case, for making planar waveguide lasers, low loss crystals are desirable. To achieve this, aiming for flat, particulate-free samples is a good starting place. The flatness of the film will be dependent on multiple variables (fluence, background pressure and substrate-target distance), but can also be improved upon by polishing of the sample surface following a deposition, providing the stress in the film is sufficiently low. The stress in a PLD-grown film has previously been found to depend most strongly on the growth temperature and ablation fluence [62]. Keeping these factors in mind, and the results already presented in this thesis, I would

next focus more on how the substrate temperature affects the growth, paying particular attention to the crystallinity, sample curvature and the structure through the deposited layer. The columnar structure seen in the samples presented in this thesis, as seen by SEM BSD images, clearly have an affect on the beam quality of the laser output of these samples in the unguided axis, so observing how this internal structure changes with temperature, and perhaps other variables, should also be analysed with the aim of minimising (and perhaps eliminating) it.

As well as studying how the samples differ when grown over a range of temperatures and ablation fluences, further work should be conducted to see how the thickness affects the quality of the film growth, and whether the optimum conditions found for thin films (<10 μm) hold for thicker growths (ideally >40 μm) or if different conditions are required for improved quality thick films. To conduct optimisation of thick film growth, however, would be very time-consuming.

The surface polishing of samples to both ensure the flatness of the surface and reduce the number of particulates present that act as scattering centres that increase the waveguide loss should be pursued, following the improvement found through this post-processing in this work. This could prove particularly beneficial for thicker growths where the curvature has gradually increased due to the material distribution in the plume.

11.3 Multilayers

Following the experiments reported in section 8.2.2 of this thesis, inspired by work presented in reference [13], it appears that there is further research to be done here. PLD has proved to be an effective method of producing multilayer waveguides, where the central layer (waveguide core) is the same material as that deposited before and after it, but doped with RE-ions. The output in the guided direction was very close to being diffraction limited, as predicted by the theory reported in the literature. However, the mode profile in the unguided direction requires some work, as stated in the previous section of this chapter. If the growth defect causing these fluctuations across the waveguide can be reduced or eliminated, multilayer samples will be a worthwhile investment of time to routinely produce lasers with good beam quality, much higher than that of the diode lasers used for pumping. The maximum thickness without sample degredation found through optimisation of single layer growth should also apply for these multilayers. Therefore, with improved growth, multilayers of RE-doped Y_2O_3 and Lu_2O_3 (possibly Sc_2O_3, but growth of this material by PLD

has so far been less promising) should be produced and tested as diode-pumped planar waveguide lasers. There is scope here to use different RE-ions to produce lasers of a variety of different wavelengths and therefore broaden their potential application.

11.4 Multi-beam and mixed sesquioxide growths

There have been reports of mixed sesquioxide crystal growth in the literature [28, 43, 44], the aim of which has been to cause variation in the crystal lattice and therefore the crystal field seen by the dopant ions, causing the emission spectrum to be broadened. This broadening is useful for producing tunable lasers with a larger tuning range and to reduce the minimum pulse duration obtainable in pulsed laser operation.

In this thesis, depositions have been restricted to growths from one target at a time and the dopant concentration determined by the quanity included in the sesquioxide target being ablated. Using multiple laser beams for ablation greatly expands the possibilities of sample growth, and while a mulit-beam PLD setup has been available there was only one excimer laser beam entering it, with the others being frequency quadrupled Nd:YAG lasers operating at the slightly longer wavelength of 266 nm. Early on in our work with sesquioxides, ablation using one of the Nd:YAG lasers was trialled with a selection of sesquioxide targets, but it proved to be ineffective. However, a second excimer laser is now available, opening up lots of new possibilities with these materials. Some ideas of what could be done with this system are listed below:

- Use of an undoped host sesquioxide target (eg. pure Y_2O_3) and a target from which the dopant is obtained (eg. Yb_2O_3). Instead of having a fixed dopant concentration, as has been the case when growing samples from a doped sesquioxide target, samples with a range of dopant concentrations can be produced by altering the frequency of the laser pulses being used for ablation. Fewer shots on the dopant target would result in a low dopant concentration, and a higher frequency of laser shots on the dopant target would give a higher dopant concentration. Investigations could be carried out into how the dopant concentration affects the quality of crystal growth.

- Again using an undoped sesquioxide host target and another of the dopant oxide, multilayer samples could be formed without the necessity of cooling the sample and opening the deposition chamber to change targets mid-way through a growth, making the process easier and

much quicker. This would also have the added versatility of controlling the dopant concentration in the core region. Further to this, instead of having defined layers (undoped, doped core, undoped) the amount of dopant included can gradually be increased and decreased again through the growth to create a graded dopant profile, which isn't possible through other more conventional crystal growth techniques, to suppress the laser action of higher order modes [119]. The laser mode output from such samples can then be investigated and compared to step profile waveguides.

- Using two different host sesquioxide targets, one or both of which could be doped with RE-ions. This would allow a mixed host crystal to be grown with either one type of active ion or for co-doping. The proportion of each host material could be varied to see how the quality of crystal growth and spectroscopic properties of the grown material is affected. Mixed growth also changes the lattice constant of the crystal, which may be able to be used to our advantage, to improve lattice matching between the substrate and grown crystal. For example, mixing Sc_2O_3 with Lu_2O_3 (both <111>-oriented) in the proportion of 55% to 45%, respectively, matches with three unit cells of sapphire (14.28 Å).

11.5 PLD-grown Yb:Al_2O_3 lasers

Some initial experiments have been performed to investigate the growth by PLD of Yb:sapphire, with the intention to be able to use it as an active laser medium, also in the planar waveguide configuration. This was in collaboration with the University of Hamburg, who provided the target for this trial. A Yb:Al_2O_3 sample was deposited on a c-cut sapphire substrate and viewed with the ZeScope. Most of the sample appeared quite rough, but one corner was smoother and the hexagonal structure of the sapphire could be viewed, which is shown in figure 11.1. This suggests we may be able to grow crystalline Yb-doped sapphire films via PLD, but optimisation experiments need to be carried out to improve the crystal growth.

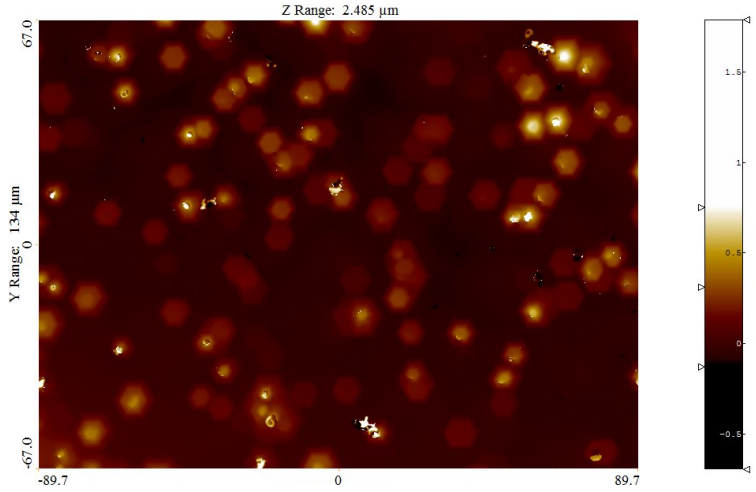

Figure 11.1: ZeScope image of Yb:sapphire on sapphire, showing hexagons due to the crystal orientation.

11.6 Conclusions

Pulsed laser deposition has been employed for the growth of thin crystalline films of the sesquioxides Y_2O_3, Lu_2O_3 and Sc_2O_3, doped with RE ions for use as planar waveguide lasers. This deposition technique is good for sesquioxide growth as it does not require forming a melt of the material, as many crystal growth techniques do, which is problematic for the sesquioxides due to their high melting points of ~2500°C. The excellent thermo-mechanical properties of the sesquioxides and their ability to doped with RE-ions make them ideal host materials for high power laser operation, particularly in planar waveguide or thin disk laser configurations that have large aspect ratios that also allow for effective thermal management.

Optimisation of the growth of these sesquioxides has been performed, looking mainly at reducing the number of particulates present in the crystal (an inherent problem in PLD-grown materials) whilst maintaining a reasonable growth rate and achieving crystalline films. The variables studied for this were restricted to the ablation fluence, background pressure and temperature. As PLD has so many variables, further optimisation would be desirable, particularly further study into optimal substrate temperature for the crystalline growth of these materials.

Depositions onto different substrates were trialled, and it was found that the sesquioxides grow preferentially in the <111> orientation in almost all cases, even on amorphous substrates, with the exception being for epitaxial growth on <100>-oriented sesquioxide substrates. The majority

of growths in this thesis were on <100>-oriented YAG substrates as they proved most suitable and are readily and cheaply available.

The first laser result reported in this thesis was from a PLD-grown Tm:Y_2O_3 waveguide, which, to the best of our knowledge, was the first reported in the literature. A maximum output power of 35 mW was obtained at a wavelength of 1.95 μm, with a slope efficiency of 9%.

Several Yb:Y_2O_3 samples were inserted into laser setups for testing. The highest slope efficiency achieved was 46%, which was from the sample that was surface polished and pumped with a single-mode fibre-coupled diode laser. This suggests that surface polishing of samples would be advisable to routinely pursue in future. The highest laser output power from a Yb:Y_2O_3 waveguide sample was from the multilayer sample; a maximum of 1.2 W output power was recorded at a slope efficiency of 20%, operating at a wavelength of 1030 nm. The multilayer sample also provided improved beam quality (M^2 = 1.2) in the guided direction via preferential fundamental mode selection due to the structure of the waveguide.

<111>-oriented Lu_2O_3 has the best lattice match to <100>-oriented YAG and was the host used for the highest power Yb laser reported in this thesis. An 8 μm-thick single layer Yb:Lu_2O_3 waveguide gave a maximum output power of 7.4 W with a slope efficiency of 38% when pumped with a diode-laser bar operating around 976 nm, using the Fresnel reflection at the output facet to outcouple the laser light. Laser experiments were repeated using a 940 nm diode bar as the pump source, which resulted in a slightly lower slope efficiency of 33%, but also a lower threshold, resulting over all in a higher a maximum output power of 7.9 W. No signs of thermal rollover were observed in any of the laser experiments reported here, the maximum output power was always restricted by the pump power available, demonstrating that RE-doped sesquioxides are suitable for further power scaling.

The last experimental chapter of this thesis reports on work showing that these PLD-grown RE-doped sesquioxides are also suitable for Q-switched operation.

Appendices

Publications

Peer-Reviewed Journal Articles

- **T. L. Parsonage**, S. J. Beecher, A. Choudhary, J. A. Grant-Jacob, P. Hua, J. I. Mackenzie, D. P Shepherd and R. W. Eason, "Pulsed Laser Deposited Diode-Pumped 7.4 W Planar Waveguide Laser," *Optics Express* vol. 23 (25) pp.31691-31697 (2015).

- A. Choudhary, S. J. Beecher, S. Dhingra, B. D'Urso, **T. L. Parsonage**, J. A. Grant-Jacob, P. Hua, J. I. Mackenzie, R. W. Eason and D. P Shepherd, "456 mW graphene Q-switched Yb:Yttria waveguide laser by evanescent-field interaction" *Optics Letters*, vol. 40(9) pp.1912-1915 (2015).

- S. J. Beecher, **T. L. Parsonage**, J. I. Mackenzie, K. A. Sloyan, J. A. Grant-Jacob and R. W. Eason, "Diode-end-pumped 1.2 W Yb:Y_2O_3 planar waveguide laser," *Optics Express*, vol. 22(18), pp.22056-22061 (2014).

- A. Choudhary, S. Dhingra, B. D'Urso, **T. L. Parsonage**, K. A. Sloyan, R. W. Eason and D. P Shepherd, "Q-switched operation of a pulsed-laser-deposited Yb:Y_2O_3 waveguide using graphene as a saturable absorber," *Optics Letters*, vol. 39(15), pp.4325-4328 (2014).

- J. I. Mackenzie, J. W. Szela, S. J. Beecher, **T. L Parsonage**, R. W. Eason and D. P Shepherd, "Crystal planar waveguides, a power scaling architecture for low-gain transitions," *IEEE Journal of Selected Topics in Quantum Electronics*, vol. 21(1) pp.10, art. no. 1601610 (Invited) (2014).

- J. W. Szela, K. A. Sloyan, **T. L. Parsonage**, J. I. Mackenzie, R. W. Eason, "Laser operation of a Tm:Y_2O_3 planar waveguide", Optics Express, **21**, 12460-12468 (2013)

- R. W. Eason, T. C. May-Smith, K. A. Sloyan, R. Gazia, M. S. B. Darby, A. Sposito, **T. L. Parsonage**, "Multi-beam pulsed laser deposition for advanced thin film optical waveguides", Journal of Physics D: Applied Physics, **47**, 034007 (2013)

Conference Proceedings

- R. W. Eason, J. I. Mackenzie, D. P. Shepherd, **T. L. Parsonage**, S. J. Beecher, P. Hua and J. Grant-Jacob, "Pulsed laser deposited crystalline optical waveguides for thin-film lasing devices," *International High Power Laser Ablation and Directed Energy*, Santa Fe, New Mexico, 4-7 April 2016.

- **T. L. Parsonage**, S. J. Beecher, A. Choudhary, J. A. Grant-Jacob, P. Hua, J. I. Mackenzie, D. P Shepherd and R. W. Eason, "7 W diode-end-pumped PLD-grown Yb:Lu_2O_3 planr waveguide laser," *Advanced Solid State Lasers Conference* (ASSL), Berlin, Germany, 4-9 October 2015. Accepted for **oral presentation**.

- S. J. Beecher, J. A. Grant-Jacob, **T. L. Parsonage**, P. Hua, A. Choudhary, J. I. Mackenzie, D. P. Shepherd and R. W. Eason, "Growth and initial experiments demonstrating watt level output from Yb:YAG planar waveguides grown by pulsed laser deposition," *Advanced Solid State Lasers Conference* (ASSL), Berlin, Germany, 4-9 October 2015.

- **T. L. Parsonage**, A. Choudhary, S. J. Beecher, J. A. Grant-Jacob, P. Hua, J. I. Mackenzie, D. P Shepherd and R. W. Eason, "Comparative study of rare-earth doped sesquioxides grown by pulsed laser deposition and their performance as planar waveguide lasers," *CLEO Europe -EQEC*, Munich, Germany, 21-25 June 2015. Accepted for **oral presentation**.

- A. Choudhary, S. J. Beecher, S. Dhingra, B. D'Urso, **T. L. Parsonage**, J. A. Grant-Jacob, P. Hua, J. I. Mackenzie, R. W. Eason and D. P Shepherd, "Graphene Q-Switched Yb:Yttria waveguide laser by evanescent-field interaction delivering an average output power of 0.5 W," *CLEO Europe -EQEC*, Munich, Germany, 21-25 June 2015.

- J. Grant-Jacob, **T. L. Parsonage**, S. J. Beecher, A. Choudhary, P. Hua, J. I. Mackenzie, D. P Shepherd and R. W. Eason, "Towards fabrication of 10 W class planar waveguide lasers: analysis of crystalline sesquioxide layers fabricated via pulsed laser deposition," *CLEO Europe -EQEC*, Munich, Germany, 21-25 June 2015.

- S. J. Beecher, **T. L. Parsonage**, J. I. Mackenzie, K. A. Sloyan, J. A. Grant-Jacob, and R. W. Eason, "1.2 W Yb:Y_2O_3 planar waveguide laser," *Advanced Solid State Lasers Conference* (ASSL), Shanghai, 16-21 November 2014.

- A. Choudhary, S. Dhingra, B. D'Urso, **T. L. Parsonage**, K. A. Sloyan, R. W. Eason and D. P Shepherd, "PLD-grown Yb:Y_2O_3 waveguide laser Q-switched by a graphene saturable absorber," *ECIO*, Nice, France, 24 -27 June 2014.

- **T. L. Parsonage**, S. J. Beecher, K. A. Sloyan, J. I. Mackenzie and R. W. Eason, "Pulsed laser deposition of Yb:Y_2O_3 planar waveguide lasers," *E-MRS*, Spring meeting, Lille, France, 26-30 May 2014. Accepted for **poster presentation**.

- **T. L. Parsonage**, K. A. Sloyan, J. W. Szela, J. I. Mackenzie and R. W. Eason, "Doped sesquioxide growth by pulsed laser deposition for planar waveguide lasing applications," *Conference on Laser Ablation (COLA)*, Ischia, Italy, 6-10 October 2013. Accepted for **oral presentation**.

- J. W. Szela, K. A. Sloyan, **T. L. Parsonage**, J. I Mackenzie and R. W. Eason, "Thulium-doped yttria planar waveguide laser grown by pulsed laser deposition," *CLEO Europe - EQEC*, Munich, Germany, 12-16 May 2013.

Bibliography

[1] Daniel-Dennis McAlevy Bubb and Richard F. Haglund, Jr., "Resonant infrared pulsed laser ablation and deposition of thin polymer films" in *Pulsed Laser Deposition of Thin Films: applications-led growth of functional materials* (R. Eason, ed.), Wiley (2007).

[2] Jeffrey T. Cheung, "History and fundamentals of pulsed laser deposition" in *Pulsed Laser Deposition of Thin Films* (D. Chrisey and G. Hubler, eds.), Wiley (1994).

[3] David P. Norton, "Pulsed laser deposition of complex materials: progress towards applications" in *Pulsed Laser Deposition of Thin Films: applications-led growth of functional materials* (R. Eason, ed.), Wiley (2007).

[4] R. Peters, C. Kränkel, K. Petermann, G. Huber, "Broadly tunable high-power Yb:Lu_2O_3 thin disk laser with 80% slope efficiency," Optics Express, **15**(11), 7075 – 7082 (2007).

[5] U. Griebner, V. Petrov, K. Petermann, and V. Peters, "Passively mode-locked Yb:Lu_2O_3 laser," Optics Express, **12**(14), 3125 – 3130 (2004).

[6] P. Klopp, V. Petrov, U. Griebner, K. Petermann, V. Peters, and G. Erbert, " High efficient mode-locked Yb:Sc_2O_3 laser," Opt. Lett. **29**(4), 391–393 (2004).

[7] A. Brenier and G. Boulon, "Overview of the best Yb^{3+}-doped laser crystals," Journal of alloys and compounds, **323 - 324** 210-213 (2001).

[8] L. Fornasiero, E. Mix, V. Peters, K. Petermann and G. Huber, "New oxide crystals for solid state lasers," Cryst. Res. Technol. **34**(2) 255 – 260 (1999).

[9] V. Peters, A. Bolz, K. Petermann and G. Huber, "Growth of high-melting sesquioxides by the heat exchanger method," Journal of Crystal Growth, **237 - 239**, 879 - 883 (2002).

[10] "Inorganic Crystal Structure Database," http://icsd.cds.rsc.org/

[11] J. I Mackenzie, "Dielectric solid-state planar waveguide lasers: a review," IEEE Journal of Selected Topics in Quantum Electronics, **13**(3), 626 – 637 (2007).

[12] M. Pollnau and Y. E. Romanyuk, "Optical waveguides in laser crystals," C. R. Physique **8**, 123 – 137 (2007).

[13] T. Bhutta, J. I. Mackenzie, and D. P Shepherd, "Spatial dopant profiles for transverse-mode selection in multimode waveguides," J. Opt. Soc. Am. B, **19**(7), 1539 – 1543 (2002).

[14] C. L. Bonner, T. Bhutta, D. P. Shepherd, and A. C. Tropper, "Double-clad structures and proximity coupling for diode-bar-pumped planar waveguide lasers," IEEE Journal of Quantum Electronics, **36**(2), 236 –242 (2000)

[15] S. Franssila, "Thin-Film Materials and Processes" in *Introduction to Microfabrication*, second edition, Wiley (2010).

[16] R. Hunsperger, "Waveguide fabrication techniques" in *Integrated Optics: Theory and Technology*, Edition 4, Springer Science & Business Media (2013).

[17] S. J. Pearce, M. D. B. Charlton, J. Hiltunen, J. Puustinen, J. Lappalainen, and J. S. Wilkinson, "Structural characteristics and optical properties if plasma assisted reactive megnetron sputtered dielectric thin films for planar waveguiding applications," Surface & Coatings Technology, **206**, 4930 – 4939 (2012).

[18] L. Rabisch, S. Bär, and H. Scheife, " Eu-doped $(Lu/Sc)_2O_3$ thin films grown by thermal evaporation," Optical Materials, **28**, 665 – 670 (2006).

[19] *Thin Film Processes II*, John L. Vossen and Werner Kern eds., Gulf Professional Publishing (1991).

[20] B. Ferrand, B. Chambaz and M. Couchaud, Liquid phase epitaxy: A versatile technique for the development of miniature optical components in single crystal dielectric media, Optical Materials **11**, 101 - 104 (1999).

[21] J. R. Creighton and P. Ho, *Chemical vapour deposition*, (Jong-Hee Park and T. S. Sudarshan eds.), ASM international, 2001.

[22] N. J. Archer, "Chemical vapour deposition," Phys. Technol. **10**, 152 – 161 (1979).

[23] C. T. A. Brown, C. L . Bonner, T. J. Warburton, D. P. Shepherd, A. C. Tropper and D. C. Hanna, Thermally bonded planar waveguide lasers, Appl. Phys. Lett. **71**(9), 1139 – 1141 (1997).

[24] D. Kip, "Photorefractive waveguides in oxide crystals: fabrication, properties, and application," Appl. Phys. B, **67**, 131-150 (1998).

[25] T. Suhara and M. Fujimura, "Waveguide fabrication and Characteristics" in *Waveguide Nonlinear-Optic Devices*, Volume 11 of Springer Series in Photonics, Springer Science & Business Media, 2013.

[26] Robert S. Feigelson, "Crystal growth through the ages: a historical perspective," in *Handbook of Crystal Growth: Fundamentals*, vol. 1, second edition (T. Nishinaga ed.), Elsevier (2014).

[27] M. Eagleson (Translator), *Concise Encyclopedia Chemistry*, Walter de Gruyter & Co. (1994).

[28] F. Reichert, M. Fechner, P. Koopman, C. Brandt, K. Petermann, and G. Huber, "Spectroscopy and laser operation of Nd-doped mixed sesquioxides $(Lu_{1-x}Sc_x)_2O_3$," Appl. Phys. B, **108**, 475 – 478 (2012).

[29] L. Fornasiero, E. Mix, V. Peters, K. Petermann, and G. Huber, "Czochralski growth and laser parameters of RE^{3+}-doped Y_2O_3 and Sc_2O_3," Ceramics International, **26**, 589 – 592 (1999).

[30] K. Petermann, L. Fornasiero, E. Mix, and V. Peters, "High melting sesquioxides: crystal growth, spectroscopy, and laser experiments," Optical Materials, **19**, 67 – 71 (2002).

[31] P. Veber, M. Velazquez, V. Jubera, S. Pechev, and O. Viraphong, "Flux growth of Yb^{3+}-doped RE_2O_3 (RE = Y, Lu) single crystals at half their melting point temperature," Cryst. Eng. Comm., **13**, 5220 – 5225 (2011).

[32] J. J. Carvajal, M. C. Pujol, F. Díaz, "High-Temperature Solution Growth: Application to Laser and Nonlinear Optical Crystals," in *Handbook of Crystal Growth: Fundamentals*, vol. 1, second edition (T. Nishinaga ed.), Elsevier (2014).

[33] D. B. Gasson and B. Cockayne, "Oxide crystal growth using gas lasers," Journal of Materials Science, **5**, 100 – 104 (1970).

[34] H. Li and J. Xu, "Crystal growth of laser host fluorides and oxides," in *Handbook of Crystal Growth*, Part B (G. Dhanaraj, K. Byrappa, V. Prasad, M. Dudley, eds.) Springer (2010).

[35] B. M. Tissue and L. Lu, "Laser-heated pedestal growth of laser and IR-upconverting materials," Journal of Crystal Growth, **109**, 323 – 328 (1991).

[36] V. I. Chani, "Micro-pulling-down (μm-PD) and related growth methods," in *Shaped Crystals: Growth by Micro-Pulling-Down Technique* (T. Fukuda and V. I. Chani, eds.), Springer (2007).

[37] A. Novoselov, J. H. Mun, R. Simura, A. Yoshikawa, and T. Fukada, "Micro-pulling-down: a viable approach to the crystal growth of refractory rare-earth sesquioxides," Inorganic Materials, **43**(7), 729 – 734 (2007).

[38] A. Fukabori, V. Chani, K. Kamada, A. Yoshikawa, "Growth of Yb-doped Y_2O_3, Sc_2O_3 and Lu_2O_3 single crystals by the micro-pulling-down technique and their opitcal and scintillation properties," Journal of Crystal Growth, **352**, 124 –128 (2012).

[39] M. Guzik, J. Pejchal, A. Yoshikawa, A. Ito, T. Goto, M. Siczek, T. Lis, and G. Boulon, "Structural investigations of Lu_2O_3 as single crystal and polycrystalline transparent ceramic," Cryst. Growth Des., **14**, 3327 – 3334 (2014).

[40] K. Petermann, G. Huber, L. Fornasiero, S. Kuch, E. Mix, V. Peters, and S. A. Basun, "Rare-earth-doped sesquioxides," Journal of Luminescence, **87 − 89**, 973 – 975 (2000).

[41] Y. Xu, Z. Gu, and W. Y. Ching, "Electronic, structural, and optical properties of crystalline yttria," Phys. Rev. B, **56**(23), 14993 – 15000 (1997).

[42] P.A. Loiko, K. V. Yumashev, R. Schödel, M. Peltz, C. Liebald, X. Mateos, B. Deppe, and C. Kränkel, "Themo-optic properties of Yb:Lu_2O_3 single crystals," Appl. Phys. B, **120**(4), 601 – 607 (2015).

[43] A. Schmidt, V. Petrov, U. Griebner, R. Peters, K. Petermannm G. Huber, C. Fiebig, K. Paschke, and G. Erbert, "Diode pumped mode-locked Yb:$LuScO_3$ single crystal laser with 74 fs pulse duration," Optics Letters, **35**(4), 511 – 513 (2010).

[44] K. Beil, C. J. Saraceno, C. Schriber, F. Emaury, O. H. Heckl, C. R. E. Baer, M. Golling, T. Südmeyer, U. Keller, C. Kränkel, and G. Huber, "Yb-doped mixed sesquioxides for ultrashort pulse generation in the thin disk laser setup," Appl. Phys. B, **113**(1), 13 – 18 (2013).

[45] H. Kühn, S. T. Fredrich-Thornton, C. Kränkel, R. Peters, and K. Petermann, "Model for the calculation of radiation trapping and description of the pinhole method," Optics Letters, **32**(13), 1908 – 1910 (2007).

[46] P. Koopmann, S. Lamrini, K. Schollo, P. Fuhrberg, K. Petermann, and G. Huber, "Long wavelength laser operation of Tm:Sc_2O_3 at 2116 nm and beyond," in *Advances in Optical Materials*, OSA Technical Digest (CD) (Optical Society of America, 2011), paper ATuA5.

[47] C. Kränkel, R. Peters, O. H. Heckl, C. R. E. Baer, C. J. Saraceno, K. Beil, T. Südmeyer, K. Petermann, U. Keller, and G. Huber, "Yb-doped sesquioxide thin disk lasers exceeding 300 W of output power in continuous-wave operation," in *Conference on Lasers and Electro-Optics 2010*, OSA Technical Digest (CD) (Optical Society of America, 2010), paper CTuQQ2.

[48] R. Peters, C. Kränkel, S. T. Fredrich-Thornton, K. Beil, K. Petermann, G. Huber, O. H. Heckl, C. R. E. Baer, C. J. Saraceno, T. Südmeyer, and U. Keller, "Thermal analysis and efficient high power cw and mode-locked thin disk laser operation of Yb-doped sesquioxides," App. Phys.B, **102**(3), 509 – 514 (2011).

[49] C. R. E Baer, C. Kränkel, O. H. Heckl, M. Golling, T. Südmeyer, R. Peters, K. Petermann, G. Huber and U. Keller, "227-fs pulses from a mode-locked Yb:$LuScO_3$ thin disk laser," Optics Express, **17**(13), 10725 – 10730 (2009).

[50] C. Schriber, F. Emaury, A. Diebold, S. Link, M. Golling, K. Beil, C. Kränkel, C. J. Saraceno, T. Südmeyer, and Ursula Keller, "Dual-gain SESAM modelocked thin disk laser based on Yb:Lu_2O_3 and Yb:Sc_2O_3," Optics Express, **22**(16), 18979-18986 (2014).

[51] A. Kahn, S. Heinrich, H. Kühn, K. Petermann, J. D. B. Bradley, K. Wörhoff, M. Pollnau, and G. Huber, " Low threshold monocrystalline Nd:(Gd, $Lu)_2O_3$ channel waveguide laser," Optics Express, **17**(6), 4412 – 4418 (2009).

[52] J. D. B. Bradley, F. Ay, K. Wörhoff, and M. Pollnau,"Fabrication of low-loss channel waveguides in Al_2O_3 and Y_2O_3 layers by inductively coupled plasma reactive ion etching," Appl. Phys. B, **89**, 311 – 318 (2007).

[53] H. Kühn, S. Heinrich, A. Kahn, K. Petermann, J. D. B. Bradley, K. Wörhoff, M. Pollnau, and G. Huber," Monocrystalline Yb^{3+}:$(Gd, Lu)_2O_3$ channel waveguide laser at 976.8 nm," Optics Letters, **34**(18), 2718 – 2720 (2009).

[54] T. May-Smith, *Pulsed Laser Deposition of Thick Multilayer Garnet Crystal Films for Waveguide Laser Devices*. PhD thesis, University of Southampton, 2005.

[55] K. A. Sloyan, *Multi-beam pulsed laser deposition for engineered crystal films*. PhD thesis, University of Southampton, 2012.

[56] R. Stoian, A. Rosenfeld, D. Ashkenasi, I. V. Hertel, N. M. Bulgakova, and E. E. B. Campbell, "Surface charging and impulsive ion ejection during ultrashort pulsed laser ablation," Phys. Rev. Lett., **88**(9), 097603-1 – 097603-4 (2002).

[57] Roger Kelly and Antonio Miotello, "Mechanisms of Pulsed Laser Sputtering" in *Pulsed Laser Deposition of Thin Films* (D. Chrisey and G. Hubler, eds.), Wiley (1994).

[58] Katherine L. Saenger, "Angular distribution of ablated material" in *Pulsed Laser Deposition of Thin Films* (D. Chrisey and G. Hubler, eds.), Wiley (1994).

[59] James S. Horwitz and James A. Sprague, "Film Nucleation and Film Growth in Pulsed Laser Deposition of Ceramics" in *Pulsed Laser Deposition of Thin Films* (D. Chrisey and G. Hubler, eds.), Wiley (1994).

[60] L. V. Zhigilei, "Crystal defects." Lecture notes, Department of Materials Science and Engineering, University of Virginia (2011).

[61] M. Ohring, "Epitaxy" in *The materials science of thin films*, Academic Press (1992).

[62] T. C. May-Smith, K. A. Sloyan, R. Gazia, and R. W. Eason, "Stress engineering and optimization of thick garnet crystal films grown by pulsed laser deposition," Cryst. Growth Des., **11**, 1098 – 1108 (2011).

[63] K. H. Wong, S. K. Hau, P. W. Chan, L. K. Leung, C. L. Choy, and H. K. Wong, "XeCl excimer laser interaction with partially stabilized zirconia target," J. Mater. Sci. Lett., **10**(14), 801 – 803 (1991).

[64] Stephen R. Foltyn, "Surface Modification of Materials by cumulative Laser Irradiation" in *Pulsed Laser Deposition of Thin Films* (D. Chrisey and G. Hubler, eds.), Wiley (1994).

[65] James S. Horwitz and James A. Sprague, "Particulates generated by pulsed laser ablation" in *Pulsed Laser Deposition of Thin Films* (D. Chrisey and G. Hubler, eds.), Wiley (1994).

[66] R. W. Eason, S. J. Barrington, C. Grivas, T. C. May-Smith, and D. P Shepherd, "Optical Waveguide Growth and Applications" in *Pulsed Laser Deposition of Thin Films: applications-led growth of functional materials* (R. Eason, ed.), Wiley (2007).

[67] K. Murakami, in *Laser Ablation of Electronic Materials*, (E. Fogarassy and S. Lazare, eds.), Elsevier, The Netherlands (1992).

[68] P. Koopman, S. Lamrini, K. Scholle, M. Schäfer, P. Fuhrberg, and G. Huber, "Holmium-doped Lu_2O_3, Y_2O_3 and Sc_2O_3 for lasers above 2.1 μm," Optics Express, **21**(3), 3926 – 3931(2013).

[69] C.Kránkel,"Rare-earth-doped sesquioxides for diode-pumped high-power Lasers in the 1-, 2-, and 3-μm spectral range," IEEE J. Sel. Top. Quant., **21**(1), 1602013 – 1602013 (2015).

[70] C. Ladam, T. Mongstad, K. Valset, T. Mokkelbost, I. Kaus, A. Fossdal, and R. Fagerberg, " Optical up-conversion in Er^{3+} and YB^{3+} co-doped Y_2O_3 films prepared by pulsed laser deposition for enhanced solar cell efficiency," *23rd European Photovoltaic Solar Energy Conference and Exhibition*, session 1CO.3.2, 181 – 185 (2008).

[71] W. Koechner, "Properties of solid-state laser materials" in *Solid-State Laser Engineering*, sixth revised and updated edition, Springer (2006).

[72] A. Huignard, A. Aron, P. Aschehoug, B. Viana, J. Théry, A. Laurent, and J. Perrière, "Growth by laser ablation of Y_2O_3 and Tm:Y_2O_3 thin films for optical application," J. Mater. Chem. **10**, 549 – 554 (2000).

[73] G. B. Venus, A. Sevian, V. I. Smirnov, and L. B. Glebov, "High-brightness narrow-line laser diode source with colume Bragg grating feedback," *Conference on High-Power Diode Laser Technology and Applications III*, Talk 166-176 (2005).

[74] B. E. A. Saleh and M. C. Teich, "Guided-wave optics" in *Fundamentals of Photonics* (J. W. Goodman, ed.), Wiley (1991).

[75] C. Grivas, "Optically pumped planar waveguide lasers, part 1: fundamentals and fabrication techniques," Progress in Quantum Electronics, **35**, 159 – 239 (2011).

[76] H. P. Weber, F. A. Dunn, and W. N. Leibolt, "Loss Measurements in Thin-Film Optical Waveguides," Appl. Opt. **12**, 755 – 757 (1973).

[77] Y. Okamura, S. Yoshinaka, and S. Yamamoto, "Measuring mode propagation losses of integrated optical waveguides: a simple method," Appl. Opt. 22, 3892 – 3894 (1983).

[78] A. Kahn, Y. Kuzminykh, H. Scheife, and G. Huber, "Nondestructive measurement of the propagation losses in active planar waveguides," J. Opt. Soc. Am. B 24, 1571 – 1574 (2007).

[79] D. Findlay and R. A. Clay, "The measurement of internal losses in 4-level lasers," Physics Letters, **3**(3), 277 –278 (1966).

[80] RP Photonics Enclycopedia, https://www.rp-photonics.com/encyclopedia.html.

[81] O. Svelto, "Continuous wave laser behavior" in *Principles of Lasers*, 5^{th} edition (D. C. Hanna, ed.), Springer (2009).

[82] J. A. Caird, S. A. Payne, P. Randall Staver, A. J. Ramponi, L. L. Chase, and W. F. Krupke, "Quantum electronic properties of the $Na_3Ga_2Li_3F_{12}$:Cr^{3+} laser," IEEE Journal of Quantum Electronics, **24**(6), 1077 –1099 (1988).

[83] W. P. Risk, "Modeling of longitudinally pumped solid-state lasers exhibiting reabsorption losses," J. Opt. Soc. Am. B, **5**(7), 1412 – 1423 (1988)

[84] A. Giesen and J. Speiser, "Fifteen years of work on thin-disk lasers: results and scaling laws," IEEE Journal of selected topics in quantum electronics, **13**(3), 598 – 609 (2007).

[85] O. Svelto, "Transient wave laser behavior" in *Principles of Lasers*, 5^{th} edition (D. C. Hanna, ed.), Springer (2009).

[86] W. Koechner, "Q-switching" in *Solid-State Laser Engineering*, sixth revised and updated edition, Springer (2006).

[87] Q. Bao, H. Zhang, Y. Wang, Z. Ni, Y. Yan, Z. X. Shen, K. P. Loh, and D. Y. Tang, "Atomic-layer graphene as a saturable absorber for ultrafast pulsed lasers," Advanced Functional Materials, **19** 3077 – 3083 (2009).

[88] S. Y. Set, H. Yaguchi, Y. Tanaka, and M. Jablonski, "Laser Mode Locking Using a Saturable Absorber Incorporating Carbon Nanotubes," J. Lightwave Technol. **22**(1), 51 – (2004).

[89] H. Zhang, D. Y. Tang, L. M. Zhao, Q. L. Bao, and K. P. Loh, "Large energy mode locking of an erbium-doped fiber laser with atomic layer of graphene," Optics Express, **17**(20), 17630 – 17635 (2009).

[90] J. E. Midwinter, "Evanescent field coupling into a thin-film waveguide," IEEE Journal of Quantum Electronics,QE-6, **10**, 583 – 590 (1970).

[91] J. W. Kim, S. Y. Choi, D. Yeom, S. Aravazhi, M. Pollnau, U. Griebner, V. Petrov, and F. Rotermund, "Yb:KYW planar waveguide laser Q-switched by evanescent-field interaction with carbon nanotubes," Opt. Lett. **38**(23), 5090 – 5093 (2013).

[92] http://chemwiki.ucdavis.edu/

[93] K. Nagao and E. Kagami, X-ray thin film measurement techniques VII. Pole figure measurement, The Rigaku Journal **27**(2), 6 – 14 (2011).

[94] T. C. May-Smith, A. C. Muir, M. S. B. Darby, and R. W. Eason, "Design and performance of a ZnSe tetra-prism for homogeneous substrate heating using a CO_2 laser for pulsed laser deposition experiments," Applied Optics, **47**(11), 1767 – 1780 (2008).

[95] https://www.webelements.com

[96] A. R. Denton and N. W. Ashcroft, "Vegard's Law," Physical Review A, **42**(6), 3161 – 3164 (1991).

[97] http://www.goodfellow.com/E/Yttrium-Oxide.html

[98] W. Souder and P. Hidnert, "Meaurements on the thermal expansion of fused silica," Scientific Papers of the Bureau of Standards, **21**, S524 (1926).

[99] E. R. Dobrovinskaya, L. A. Lytvynov, and V. Pishchik, "Properties of Sapphire," in *Sapphire: Material, Manufacturing, Applications*, Springer (2009).

[100] http://refractiveindex.info

[101] J. W. Szela, K. A. Sloyan, T. L. Parsonage, J. I. Mackenzie, R. W. Eason, "Laser operation of a Tm:Y_2O_3 planar waveguide", Optics Express, **21**, 12460-12468 (2013).

[102] S. J. Barrington, T. Bhutta, D. P. Shepherd, and R. W. Eason, "The effect of particulate density on performance of Nd:$Gd_3Ga_5O_{12}$ waveguide lasers grown by pulsed laser deposition," Optics Communications, **185**, 145 – 152 (2000).

[103] L. Fornasiero, N. Berner, B. -. Dicks, E. Mix, V. Peters, K. Petermann, and G. Huber, "Broadly Tunable Laser Emission from Tm:Y_2O_3 and Tm:Sc_2O_3 at 2 μm," in *Advanced Solid State Lasers* (M. Fejer, H. Injeyan, and U. Keller, eds.) Vol. 26 of OSA Trends in Optics and Photonics (Optical Society of America, 1999), paper WD5.

[104] F.S. Ermeneux, Y. Sun, R.L. Cone, R.W. Equall, R.L. Hutcheson, and R. Moncorge, "Efficient CW 2 μm Tm^{3+}:Y_2O_3 laser," in *Advanced Solid State Lasers* (M. Fejer, H. Injeyan, and U. Keller, eds.) Vol. 26 of OSA Trends in Optics and Photonics (Optical Society of America, 1999), paper TuB8.

[105] W. J. Tropf, M. E. Thomas, and E. W. Rogala, "Properties of crystals and glasses," in *Handbook of Optics, 3rd edition* (M. Bass, ed.), McGraw Hill Professional (2010).

[106] Y. Guyot, R. Moncorgé, L. D. Merkle, A. Pinto, B. McIntosh, and H. Verdun, "Luminescence properties of Y_2O_3 single crystals doped with Pr^{3+} or Tm^{3+} and codoped with Yb^{3+}, Tb^{3+} or Ho^{3+} ion," Optical Materials, **5**, 127 –136 (1996).

[107] J. R. Salcedo, J. M. Sousa, and V. V. Kuzmin, "Theoretical treatment of relaxation oscillations in quasi-three-level systems," Appl. Phys. B, **62**, 83 – 85 (1996).

[108] S. J. Beecher, T. L. Parsonage, J. I. Mackenzie, K. A. Sloyan, J. A. Grant-Jacob and R. W. Eason, "Diode-end-pumped 1.2 W Yb:Y_2O_3 planar waveguide laser," Optics Express, **22**(18), 22056 – 22061 (2014).

[109] F. Druon, M. Velázquez, P. Veber, S. Janicot, O. Viraphong, G. Bue, Marwan A. Ahmed, T. Graf, D. Rytz, and P. Georges, "Laser demonstration with highly doped Yb:Gd_2O_3 and Yb:Y_2O_3 crystals grown by an original flux method," Opt. Lett. **38**, 4146-4149 (2013).

[110] T. Taira, W. M. Tulloch, and R. L. Byer, "Modeling of quasi-three-level lasers and operation of cw Yb:YAG lasers," Applied Optics, **36**(9), 1867 – 1874 (1997).

[111] T. L. Parsonage, S. J. Beecher, A. Choudhary, J. A. Grant-Jacob, P. Hua, J. I. Mackenzie, D. P Shepherd and R. W. Eason, "Pulsed Laser Deposited Diode-Pumped 7.4 W Planar Waveguide Laser," Optics Express, **23**(25) 31691 – 31697 (2015).

[112] V.Peters, *Growth and spectroscopy of ytterbium doped sesquioxides*, PhD thesis, University of Hamburg (2001).

[113] A. Choudhary, S. Dhingra, B. D'Urso, T. L. Parsonage, K. A. Sloyan, R. W. Eason and D. P Shepherd, "Q-switched operation of a pulsed-laser-deposited Yb:Y_2O_3 waveguide using graphene as a saturable absorber," Optics Letters, **39**(15), 4325-4328 (2014).

[114] A. Choudhary, S. J. Beecher, S. Dhingra, B. D'Urso, T. L. Parsonage, J. A. Grant-Jacob, P. Hua, J. I. Mackenzie, R. W. Eason and D. P Shepherd, "456 mW graphene Q-switched Yb:Yttria waveguide laser by evanescent-field interaction" Optics Letters, **40**(9) 1912-1915 (2015).

[115] S. Dhingra, J. Hsu, I. Vlassiouk, and B. D'Urso, "Chemical vapor deposition of graphene on large-domain ultra-flat copper," Carbon, **69**, 188 – 193 (2014).

[116] D. Graf, F. Molitor, K. Ensslin, C. Stampfer, A. Jungen, C. Hierold, and L. Wirtz, "Spatially Resolved Raman Spectroscopy of Single- and Few-Layer Graphene," Nano Lett., **7**(2), 238 – 242 (2007).

[117] R. Mary, G. Brown, S. J. Beecher, F. Torrisi, S. Milana, D. Popa, T. Hasan, Z. Sun, E. Lidorikis, S. Ohara, A. C. Ferrari, and A. K. Kar, "1.5 GHz picosecond pulse generation from a monolithic waveguide laser with a graphene-film saturable output coupler," Optics Express, **21**(7), 7943 – 7950 (2013).

[118] A. K. Giem and K. S. Novoselov, "The rise of graphene," Nature Materials, **6**, 183 – 191 (2007).

[119] M. Hotoleanu, M. Söderlund, D. Kliner, J. Koplow, S. Tammela, and V. Philipov, "High order modes suppression in large mode area active fibres by controlling the radial distribution of the rare earth dopant," in fibre lasers III, (A. J. W. Brow, J. Nilsson, D. J. Harter, A. Tünnerman, eds.), Proc. SPIE 6102, 61021T1 – 61021T8 (2006).